

Characterization and Cancellation of High-Frequency Parasitics for
EMI Filters and Noise Separators in Power Electronics
Applications

Shuo Wang

Dissertation submitted to the Faculty of the Virginia Polytechnic Institute
and State University in partial fulfillment of the requirements for the degree of

DOCTOR OF PHILOSOPHY
in
ELECTRICAL ENGINEERING

APPROVED:

Prof. Fred C. Lee, Chair

Prof. W. G. Odendaal

Prof. Dushan Boroyevich

Prof. Douglas K. Lindner

Prof. Douglas J. Nelson

May 11, 2005
Blacksburg, Virginia

Keywords: EMI Filter, Parasitic Couplings, Equivalent Series Inductance (ESL), S-Parameters, Parasitic Cancellation, Unbalance, Mode Transformation, Transmission Lines, Impedance Transformation, Noise separator, Conducted EMI

Copyright 2005, Shuo Wang

Characterization and Cancellation of High-Frequency Parasitics for EMI Filters and Noise Separators in Power Electronics Applications

by

Shuo Wang

ABSTRACT

Five chapters of this dissertation concentrate on the characterization and cancellation of high frequency parasitic parameters in EMI filters. One chapter addresses the interaction between the power interconnects and the parasitic parameters in EMI filters. The last chapter addresses the characterization, evaluation and design of noise separators. Both theoretical and experimental analyses are applied to each topic.

This dissertation tries to explore several important issues related to EMI filters and noise separators. The author wishes to find some helpful approaches to benefit the understanding and design of EMI filters. The contributions of the dissertation can be summarized below:

- 1) Identification of mutual couplings and their effects on EMI filter performance
- 2) Extraction of mutual couplings using scattering parameters
- 3) Cancellation of mutual couplings to improve EMI filter performance
- 4) Cancellation of equivalent series inductance to improve capacitor performance

- 5) Analysis of mode transformations due to the imperfectly balanced parameters in EMI filters
- 6) Analysis of interaction between power interconnects and EMI filters on filter high-frequency performance
- 7) Modeling and design of high-performance noise separator for EMI diagnosis
- 8) Identification of the effects of parasitics in boost PFC inductor on DM noise

Although all topics are supported by both theory and experiments, there may still be some mistakes in the dissertation. The author welcomes any advice and comments. Please send them via email to shuowang@ieee.org. Thanks.

ACKNOWLEDGEMENT

I would like to first thank my family for their great and important support on my Ph. D. study. I especially want to appreciate my advisor, Dr. Fred C. Lee. Your strictness, wisdom and foresight deeply impressed me. Under your instruction, I am learning the correct approaches to research. I know it is most important for a man to be a successful researcher. Thank you very much. I would like to thank Dr. J. D. van Wyk for your knowledge, wisdom and insight. It is you who helped me find pleasure in doing research. I would also want to thank Dr. W. G. Odendaal for your helpful advice in our weekly meetings.

Finally, I would like to express my appreciation to all the professors and colleagues in CPES who gave me knowledge in my 52-month Ph. D. study.

Best regards

Shuo Wang

May, 2005

TABLE OF CONTENTS

Abstract -----	ii
Acknowledgement -----	iv
Table of Contents -----	v
List of Figures -----	xi
List of Tables -----	xxiv
Chapter1: Introduction to EMI and EMI Filters in Switch Mode Power Supplies --	1
1.1 Introduction to Conducted EMI -----	1
1.1.1 Introduction to EMI and EMC-----	1
1.1.2 Differential Mode and Common Mode Noise-----	2
1.1.3 Measurement of Conducted EMI Noise-----	4
1.1.4 EMI Standards-----	6
1.2 Conducted EMI Noise in a Power Factor Correction Circuit-----	7
1.2.1 Noise Paths of DM, CM and Mixed Mode Noise-----	7
1.2.2 Effects of Boost Inductors on DM Noise-----	15
1.3 EMI Filters for Switch Mode Power Supplies Circuit-----	20
1.4 Objective of This Work-----	24
Chapter2: Effects of Parasitic Parameters on EMI Filter Performance -----	25
2.1 Introduction-----	25
2.2 Parasitic Couplings Existing in an EMI Filter-----	26
2.3 Identifying, Analyzing and Extracting Parasitic Couplings-----	28

2.3.1 Inductive Couplings Existing between DM Inductor L_{dm} and Capacitor Branches, between DM Inductor L_{dm} and In and Out Trace Loops-----	28
2.3.2 Inductive Couplings Existing between Capacitor Branches-----	35
2.3.3 Capacitive Coupling and the Effects of Ground Plane-----	37
2.3.4 Inductive Coupling between In and Out Trace Loops-----	40
2.3.5 Inductive Coupling between Two Inductors in a Two-stage Filter-----	40
2.4 Simulation Verification, Discussion and Recommendations-----	43
2.4.1 Simulation Verification on the Extracted Model-----	43
2.4.2 Discussion-----	44
2.4.3 Measures Used to Improve Filter Performance-----	47
2.5 Summary-----	48
Chapter3: Characterization and Extraction of Parasitic Parameters Using Scattering Parameters-----	50
3.1 Introduction-----	50
3.2 Using S-parameters to Characterize EMI filters-----	53
3.2.1 Characterization of EMI Filters Using S-parameters-----	53
3.2.2 Experiments-----	55
3.3 Using S-parameters to Extract Parasitic Parameters-----	58
3.3.1 Network Theory-----	58
3.3.2 Extraction of Parasitic Parameters for a One-stage EMI Filter-----	60
3.3.2.1 Extraction of M_1 , M_2 , M_4 and M_5 in Fig. 3-3-----	61
3.3.2.2 Extraction of M_3 and M_6 in Fig. 3-3-----	65

3.3.2.3 Extraction of M_7 and C_p in Fig. 3-3-----	67
3.3.3 Extraction of Parasitic Parameters for a Two-stage EMI Filter-----	68
3.4 Experimental Verification-----	70
3.4.1 One-stage EMI Filter-----	70
3.4.2 Two-stage EMI Filter-----	72
3.5 Summary-----	73
Chapter4: Mutual Parasitic Parameter Cancellation Technique-----	76
4.1 Introduction-----	76
4.2 Parasitic Coupling Cancellation-----	82
4.2.1 First Approach-----	83
4.2.2 Second Approach-----	86
4.3 Implementation-----	87
4.3.1 Internal Structure of Film Capacitors-----	87
4.3.2 First Approach-----	88
4.3.3 Second Approach-----	91
4.4 Experimental Results-----	92
4.4.1 Applying to a One-stage EMI Filter-----	93
4.4.2 Applying to a Two-stage EMI Filter-----	97
4.5 Summary-----	100
Chapter5: Self-parasitic Parameter Cancellation Technique-----	103
5.1 Introduction-----	103
5.2 Network Theory of ESL and ESR Cancellation-----	105

5.3 Experimental Results-----	107
5.3.1 Implementation on PCB-----	108
5.3.2 Measurement Results-----	109
5.3.3 Application for a Noise Filter-----	113
5.4 Summary-----	114
Chapter6: Mode Transformation due to the Imperfect of Balanced Structures---	116
6.1 Introduction-----	116
6.2 Analysis of Mode Transformation-----	118
6.2.1 Partition of the Filter-----	119
6.2.2 Analysis of DM Excitation-----	121
6.2.3 Analysis of CM Excitation-----	124
6.2.4 Summary of the Effects of Unbalances-----	126
6.3 Experiments-----	128
6.3.1 Effects of the Unbalance of CM Capacitors-----	130
6.3.2 Effects of the Unbalance of Inductors-----	133
6.4 Discussion-----	136
6.4.1 Mode Transformation on Different Directions-----	136
6.4.2 Effects of Cancellation Turn on Unbalance-----	137
6.4.3 The Bump on S_{CD21} and S_{DD21} -----	138
6.4.4 Effects of Unbalanced Mutual Couplings-----	139
6.5 Summary-----	140

Chapter7: Transmission Line Effects of Power Interconnects on EMI Filter High-Frequency Performance -----	141
7.1 Introduction-----	141
7.2 Electrical Parameters for Noise Propagation Path-----	142
7.3 Impedance Transformation-----	146
7.4 Interaction with EMI Filters-----	150
7.5 Effects on EMI Filter Performance-----	154
7.6 Experiments-----	162
7.7 Summary-----	167
Chapter8: Characterization, Evaluation and Design of Noise Separators -----	169
8.1 Introduction-----	169
8.2 Characterization of Noise Separator-----	174
8.3 Evaluation of Existing Noise Separators-----	179
8.4 Developing a High Performance Noise Separator-----	183
8.5 Noise Measurement Result-----	190
8.6 Summary-----	193
Chapter9: Conclusions and Future Work -----	196
9.1 Conclusions-----	196
9.2 Future Work-----	198
Appendix A -----	199
A.1 Characterization of EMI Filters Using S-parameters -----	199
A.1.1 Introduction-----	199

A.1.2 Using Scattering Parameters to Characterize EMI Filters-----	200
A.1.3 Insertion Voltage Gain with Arbitrary Source and Load Impedances-----	204
A.1.3.1 Insertion Voltage Gain under Small-signal Excitation Conditions-- -----	204
A.1.3.2 Experimental Verification-----	206
A.1.3.3 Insertion Voltage Gain with Current Bias-----	208
A.1.3.3.1 DM Current Bias-----	208
A.1.3.3.2 CM Current Bias-----	209
A.1.4 Filter Input /Output Impedance Requirement from the Standpoint of Waves- -----	212
A.1.5 Analyzing the Filter Performance with Practical Noise Source Impedances-- -----	214
A.1.6 Summary-----	216
A.2 Procedures of Extracting Parasitic Parameters for EMI Filters -----	218
Appendix B -----	227
B.1 Evaluation of Existing Noise Separators-----	227
Vita-----	235

LIST OF FIGURES

Fig. 1-1. Noise paths-----	1
Fig. 1-2. DM and CM noise-----	3
Fig. 1-3. Circuit of a LISN-----	5
Fig. 1-4. Equivalent circuit of LISN for HF noise-----	5
Fig. 1-5. Noise measurement using two LISNs and a spectrum analyzer-----	5
Fig. 1-6. FCC specified measurement setup-----	6
Fig. 1-7. EMI standards-----	6
Fig. 1-8. PFC Converter under Investigation-----	7
Fig. 1-9. Equivalent Noise source-----	7
Fig. 1-10. Conduction states of diode bridge-----	8
Fig. 1-11. Noise paths in state 1-----	9
Fig. 1-12. Noise paths in state 2-----	10
Fig. 1-13. Noise paths in state 1 in a balance structure-----	12
Fig. 1-14. Noise paths in state 2 in a balance structure-----	13
Fig. 1-15. Noise paths in state 1 in a balance structure-----	14
Fig. 1-16. Noise paths in state 2 in a balance structure-----	14
Fig. 1-17. DM noise equivalent circuit-----	15
Fig. 1-18. Equivalent DM noise voltage source-----	16
Fig. 1-19. Impedance of a boost inductor-----	16
Fig. 1-20. Measured DM noise spectrum-----	17
Fig. 1-21. Impedance of redesigned boost inductor-----	18

Fig. 1-22. Measured DM noise spectrums-----	19
Fig. 1-23. Attenuating DM noise using a DM filter-----	20
Fig. 1-24. Attenuating DM noise using a DM filter-----	21
Fig. 1-25. DM and CM filters for a power converter-----	21
Fig. 1-26. Equivalent circuit for CM noise-----	22
Fig. 1-27. Equivalent circuit for DM noise-----	22
Fig. 1-28. Input and output impedances of EMI filter, noise source and LISNs-----	23
Fig. 1-29. Impedance mismatch rule of EMI filter design-----	23
Fig. 2-1. Circuit of the investigated filter.- -----	26
Fig. 2-2. PCB layout of the filter: (a) Bottom side and (b) Top side-----	26
Fig. 2-3. DM filter model-----	27
Fig. 2-4. Inductive coupling between the inductor and the trace loop-----	29
Fig. 2-5. Inductive coupling between the inductor and the capacitor branch-----	29
Fig. 2-6. Calculated impedances for a capacitor branch with different mutual inductances- -----	32
Fig. 2-7. Different winding structures have different coupling polarities-----	33
Fig. 2-8. Equivalent circuits including self and mutual inductances-----	33
Fig. 2-9. Measured insertion voltage gains-----	34
Fig. 2-10. Equivalent circuit for the coupling between two capacitor branches-----	35
Fig. 2-11. Three cases in the experiment-----	36
Fig. 2-12. Comparison of insertion voltage gains-----	37

Fig. 2-13. Capacitive couplings between the in and out traces: (a) Equivalent capacitors on the bottom side. (b) Cross section view of the capacitive couplings-----	38
Fig. 2-14. Comparison of the measured inductor impedances-----	39
Fig. 2-15. Investigated Γ + Π filter: (a) Circuit of the filter and (b) Prototype of the filter-----	41
Fig. 2-16. Inductive couplings between two inductors-----	41
Fig. 2-17. Equivalent circuits for two inductors and C_2 -----	42
Fig. 2-18. Insertion voltage gain comparison-----	42
Fig. 2-19. EMI filter model for positive coupling-----	43
Fig. 2-20. Simulated insertion voltage gain for positive-----	44
Fig. 2-21. Measured insertion voltage gain for positive-----	44
Fig. 2-22. Equivalent circuit when the inductor is disconnected-----	45
Fig. 2-23. Insertion voltage-gain comparison: (a) Insertion voltage gain and (b) Phase-----	46
Fig. 3-1. The investigated one-stage DM EMI filter-----	50
Fig. 3-2. Comparison of insertion voltage gains when both source and load are 50Ω -----	50
Fig. 3-3. Parasitic couplings in an EMI filter-----	52
Fig. 3-4. EMI filters are treated as linear, passive, two-port networks under small-signal excitation conditions-----	54
Fig. 3-5. The impedance of the inductor used as DM source-----	57
Fig. 3-6. Comparison of the predicted insertion voltage gain, the measured insertion voltage gain, and the measured 50Ω -based transfer gain-----	57
Fig. 3-7. S-parameter measurement setup for the CM filter part-----	58

Fig. 3-8. Predicted insertion voltage gains for the CM filter part ($Z_S=100\text{pF}$, $Z_L=25\Omega$)--	58
Fig. 3-9. Calculation of M_2 through the impedance of the capacitor branch-----	59
Fig. 3-10. S-parameters of a Tee network-----	59
Fig. 3-11. PCB layout of the investigated one-stage DM EMI filter-----	61
Fig. 3-12. DM EMI filter is connected to a single-ended structure-----	61
Fig. 3-13. Calculated impedances for a capacitor branch with different mutual inductances-----	62
Fig. 3-14. Derived impedances for the C_1 branch from the measured S-parameters-----	64
Fig. 3-15. Calculation of M_5 through the impedance of the capacitor branch-----	64
Fig. 3-16. Derived impedances of the C_1 branch from measured S-parameters-----	65
Fig. 3-17. Equivalent circuit for the inductive coupling between two capacitors-----	66
Fig. 3-18. Impedance of the Z_3 branch, derived from measured S-parameters-----	66
Fig. 3-19. Equivalent circuit for the inductive couplings between two capacitors and between trace loops-----	66
Fig. 3-20. Derived impedances of the Z_3 branch-----	67
Fig. 3-21. Impedances of the inductor and the inductor branch-----	67
Fig. 3-22. The investigated two-stage DM EMI filter-----	68
Fig. 3-23. PCB layout of the investigated two-stage EMI filter-----	69
Fig. 3-24. Equivalent circuit for the inductive couplings between two inductors and between inductors and the capacitor C_2 -----	69
Fig. 3-25. Derived impedances of the C_2 branch from measured S-parameters-----	69
Fig. 3-26. EMI filter model for inductor winding direction1-----	70

Fig. 3-27. EMI filter model for inductor winding direction2-----	71
Fig. 3-28. Comparison of the measured and simulated insertion voltage gains for inductor winding direction1-----	71
Fig. 3-29. Comparison of the measured and simulated insertion voltage gains for inductor winding direction2-----	71
Fig. 3-30. Two-stage EMI filter model-----	72
Fig. 3-31. Comparison of the measured and simulated insertion voltage gains: (a) magnitude, and (b) phase-----	73
Fig. 4-1. One-stage EMI filter under investigation-----	78
Fig. 4-2. CM and DM filter models including parasitics of components-----	78
Fig. 4-3. Effects of parasitic parameters on EMI filter performance-----	79
Fig. 4-4. Parasitic couplings in a DM filter-----	79
Fig. 4-5. Reducing M1, M2, M3, M4 and M5 by rotating inductor windings and a capacitor-----	81
Fig. 4-6. HF model of the filter-----	84
Fig. 4-7. HF equivalent circuit for the filter-----	85
Fig. 4-8. Equivalent circuit for capacitor C_1 -----	85
Fig. 4-9. HF model of the filter-----	86
Fig. 4-10. HF equivalent circuit for the filter-----	87
Fig. 4-11. Internal structure and current flow of film capacitors-----	88
Fig. 4-12. Mutual coupling between two capacitors-----	88

Fig. 4-13. Mutual coupling between two capacitors and between C_2 and the cancellation turn-----	89
Fig. 4-14. Equivalent circuit of two capacitors when one is with a cancellation turn-----	90
Fig. 4-15. Equivalent circuit of the integrated capacitor-----	90
Fig. 4-16. Exploded view of the capacitor with an integrated cancellation turn-----	91
Fig. 4-17. Prototype of the integrated tubular film capacitor-----	92
Fig. 4-18. Equivalent circuit and structure of the integrated capacitor-----	92
Fig. 4-19. One-stage EMI filter using the capacitor with an integrated cancellation turn-----	93
Fig. 4-20. Comparison of impedances of the mutual inductances between two capacitors-----	94
Fig. 4-21. Comparison of impedances of capacitor C_1 -----	95
Fig. 4-22. Comparison of insertion voltage gains of a filter with and without mutual coupling cancellation for rectangular capacitors-----	95
Fig. 4-23. Comparison of insertion voltage gains of a filter with and without mutual coupling cancellation for tubular capacitors-----	96
Fig. 4-24. Comparison of insertion voltage gains of a filter with and without mutual coupling cancellation for the second approach-----	96
Fig. 4-25. Investigated two-stage DM EMI filter-----	98
Fig. 4-26. Parasitic model for a two-stage DM EMI filter-----	98
Fig. 4-27. Comparison of insertion voltage gains-----	99

Fig. 4-28. Comparison of insertion voltage gains of a two-stage EMI filter with and without mutual coupling cancellation-----	99
Fig. 5-1. Setup for evaluating the insertion voltage gain of a capacitor-----	103
Fig.5-2. Insertion voltage gain curves of capacitors-----	104
Fig.5-3. Network 1-----	105
Fig. 5-4. Network 2-----	105
Fig. 5-5. ESL and ESR cancellation for capacitors-----	106
Fig. 5-6. One turn rectangular PCB winding-----	107
Fig. 5-7. Implementation of ESL and ESR cancellation on PCB-----	108
Fig. 5-8. Implementation for two 0.47uF/400V film capacitors: (a) prototype and (b) PCB layout-----	109
Fig. 5-9. Implementation for two 220uF/250V electrolytic capacitors-----	109
Fig. 5-10. Equivalent measurement setup in time domain-----	109
Fig. 5-11. Comparison of measured results-----	110
Fig. 5-12. Equivalent measurement setup in frequency domain-----	111
Fig. 5-13. Comparison of insertion voltage gains for film capacitors-----	111
Fig. 5-14. Comparison of insertion voltage gains for electrolytic capacitors-----	112
Fig. 5-15. Application for a Γ type EMI filter-----	113
Fig. 5-16. Comparison of insertion voltage gains for a Γ type filter-----	113
Fig. 6-1. EMI filter with balanced circuit structure-----	116
Fig. 6-2. Decoupling EMI filters to CM and DM filters-----	117
Fig. 6-3. Comparison of measured S_{CD21} and S_{CC21} -----	117

Fig. 6-4. EMI Filter including parasitic parameters-----	119
Fig. 6-5. Representing the right part using impedances-----	120
Fig. 6-6. Decoupling DM and CM inductors-----	120
Fig. 6-7. Representing the left part using impedances-----	121
Fig. 6-8. DM excitation on the right part-----	122
Fig. 6-9. CM excitation on right part-----	124
Fig. 6-10. Effects of unbalance on EMI filter Performance-----	126
Fig. 6-11. Impedances of two CM capacitors-----	128
Fig. 6-12. Unbalance of two CM capacitors-----	128
Fig. 6-13. PCB layout of the investigated EMI filter-----	129
Fig. 6-14. Mixed mode S-parameters-----	130
Fig. 6-15. Measured S-parameters-----	130
Fig. 6-16. Measured S-parameters-----	130
Fig. 6-17. Impedances of two CM capacitors-----	131
Fig. 6-18. Comparison of unbalance of two CM capacitors-----	131
Fig. 6-19. Measured S-parameters-----	132
Fig. 6-20. Measured S-parameters-----	132
Fig. 6-21. Comparison of transformation from DM to CM-----	132
Fig. 6-22. Measured S-parameters-----	135
Fig. 6-23. Measured S-parameters-----	135
Fig. 6-24. Mode transformations on different directions-----	136
Fig. 6-25. Measured S-parameters-----	137

Fig. 6-26. Measured S-parameters-----	138
Fig. 6-27. Resonances in the EMI filter-----	138
Fig. 6-28. Effects of resonances in the EMI filter-----	139
Fig. 7-1. Conducted EMI measurement setup for a PFC converter-----	142
Fig. 7-2. Distribution of electrical field-----	143
Fig. 7-3. Distribution of magnetic field-----	144
Fig. 7-4. Calculation of capacitance-----	144
Fig. 7-5. Decoupling the noise propagation paths-----	146
Fig. 7-6. Propagation of noise waves-----	147
Fig. 7-7. Impedance transformation analysis using smith chart-----	148
Fig. 7-8. Input impedance as a function of the length of power interconnects-----	149
Fig. 7-9. Investigated one-stage EMI filter-----	151
Fig. 7-10. Output impedance of the DM filter-----	151
Fig. 7-11. Measured output impedance of the DM filter-----	152
Fig. 7-12. Output impedance of the CM filter-----	152
Fig. 7-13. Measured output impedance of the CM filter-----	152
Fig. 7-14. EMI filter with noise source, power interconnects and load-----	153
Fig. 7-15. Noise peaks caused by the resonances propagate to LISNs-----	154
Fig. 7-16. Calculation process-----	155
Fig. 7-17. Effects of power interconnects on DM EMI filter performance: $Z_0 < 50\Omega$ ---	156
Fig. 7-18. DM noise analysis when $Z_0 > 50\Omega$ -----	156
Fig. 7-19. Effects of power interconnects on DM EMI filter performance: $Z_0=5\Omega$ -----	157

Fig. 7-20. DM noise analysis when $Z_0 = 500\Omega$ -----	157
Fig. 7-21. Effects of power interconnects on CM EMI filter performance: $Z_0 < 50\Omega$ --	158
Fig. 7-22. Effects of power interconnects on CM EMI filter performance: $Z_0 > 50\Omega$ ---	159
Fig. 7-23. CM noise analysis when $Z_0 = 10\Omega$ -----	160
Fig. 7-24. CM noise analysis when $Z_0 = 500\Omega$ -----	160
Fig. 7-25. Characterizing power interconnects and LISNs as a network-----	162
Fig. 7-26. Experiment setup-----	163
Fig. 7-27. Comparison of S21 on DM propagation-----	164
Fig. 7-28. Imaginary parts of the input and output impedances-----	164
Fig. 7-29. Comparison of S21 on CM propagation-----	164
Fig. 7-30. Phases of S21-----	165
Fig. 7-31. Imaginary parts of input and output impedances-----	166
Fig. 7-32. Comparison of S21 on CM propagation-----	166
Fig. 7-33. Phases of S21-----	166
Fig. 8-1. EMI noise measurement setup for a PFC converter-----	169
Fig. 8-2. Using noise separator to separate DM and CM noise-----	170
Fig. 8-3. Using a power splitter and a network analyzer to measure the noise separator may not yield accurate results-----	173
Fig. 8-4. Characterizing noise separator in terms of waves-----	174
Fig. 8-5. Characterizing the noise separator using a signal flow graph-----	175
Fig. 8-6. Signal-flow graph for a practical noise separator with a matched load at port3-- -----	176

Fig. 8-7. Signal-flow graph for an ideal noise separator with a matched load at port3-----	177

Fig. 8-8. Noise separator proposed by paper [1] -----	180
Fig. 8-9. Noise separator proposed by paper [16]-----	181
Fig. 8-10. Parasitic parameters in a noise separator-----	182
Fig. 8-11. Transmission line transformer-----	183
Fig. 8-12. Utilizing winding capacitance and leakage inductance to match DM load-----	184

Fig. 8-13. Utilizing winding capacitance and leakage inductance to match CM load-----	185

Fig. 8-14. Proposed noise separator-----	186
Fig. 8-15. Prototype of the proposed noise separator-----	187
Fig. 8-16. Measured S-parameters of the prototype-----	188
Fig. 8-17. Measured S-parameters of the prototype-----	188
Fig. 8-18. Input impedances of the prototype-----	189
Fig. 8-19. DMRR and CMTR of the prototype-----	189
Fig. 8-20. CMRR and DMTR of the prototype-----	189
Fig. 8-21. Conducted EMI measurement setup for a 1.1kW PFC converter-----	191
Fig. 8-22. Total noise and CM noise when the heat-sink is ungrounded-----	192
Fig. 8-23. Total noise and DM noise when heat-sink is ungrounded-----	192
Fig. 8-24. Total noise and CM noise after heat-sink is grounded-----	192
Fig. 8-25. Total noise and DM noise after heat-sink is grounded-----	193

Fig. A-1. EMI filters are treated as linear passive two-port networks under small-signal excitation conditions-----	200
Fig. A-2. Characterizing the filter circuit using a signal flow graph-----	202
Fig. A-3. The dual circuit for the measurement and calculation of insertion voltage gain-----	204
Fig. A-4. The schematic and the photo of an investigated-----	206
Fig. A-5. The measured S-parameters of the DM filter part-----	207
Fig. A-6. The comparison of calculated and measured DM insertion voltage gains when load is $1\text{meg}\Omega$ and source is 50Ω -----	207
Fig. A-7. The comparison of calculated and measured CM insertion voltage gains when source is $1\text{meg}\Omega$ and load is 50Ω -----	208
Fig. A-8. S-parameters measurement setup for the DM filter part-----	208
Fig. A-9. S-parameters measurement setup for the CM filter part-----	208
Fig. A-10. S-parameter measurement setup for the DM filter part-----	210
Fig. A-11. S-parameter measurement setup for the CM filter part-----	210
Fig. A-12. The magnitude of the measured S-parameters and the predicted insertion voltage gains for the CM filter part-----	211
Fig. A-13. The simplified signal flow graph for an EMI filter-----	212
Fig. A-14. Simplified boost PFC DM noise loop-----	215
Fig. A-15. The impedance of the boost inductor Z_{LB} -----	215
Fig. A-16. The measurement setup for the insertion voltage gains when the source impedance is the boost inductor Z_{LB} -----	215

Fig. A-17. The comparison of the predicted and the measured insertion voltage gains-----	
-----	215
Fig. A-18. The comparison of predicted insertion voltage gains with practical and ideal inductors-----	216
Fig. A-19. One-stage EMI filter model including parasitics-----	218
Fig. A-20. Two-stage EMI filter model including parasitics-----	218
Fig. A-21. Two-stage EMI filter model including parasitics-----	219
Fig. A-22. Two-stage EMI filter model including parasitics-----	219
Fig. B-1. Noise separator proposed by Clayton R. Paul-----	227
Fig. B-2. Noise separator proposed by Hsin-Lung Su-----	228
Fig. B-3. Noise separator proposed by M. Chiado Caponet -----	229
Fig. B-4. Noise separator proposed by Mark J. Nave-----	230
Fig. B-5. Noise separator proposed by Ting Guo-----	230
Fig. B-6. Noise separator proposed by K. Y. See-----	231
Fig. B-7. Noise measurement using current probes-----	231
Fig. B-8. Noise measurement using current probes and a spectrum analyzer-----	232

LIST OF TABLES

Table 2-I. Extracted mutual inductances-----	33
Table 2-II. Extracted inductance and parasitic capacitance-----	40
Table 7-I. Interaction between the filter and power lines-----	153

CHAPTER 1: INTRODUCTION TO EMI AND EMI FILTERS IN SWITCH

MODE POWER SUPPLIES

1.1. Conducted EMI in Switch Mode Power Supplies

1.1.1. Introduction to EMI and EMC

Electromagnetic interference (EMI) is a very important issue not only for the power electronics area but also for all electronic areas. In the United States, the Federal Communications Commission (FCC) has issued many EMI standards to specify both conducted EMI and radiated EMI limits in both industrial and residential environments.

The high di/dt loops and high dv/dt nodes in power stages are usually the source of noise. Typically, the noise source interferes with the victim circuit through four ways:

- 1) Conductive interference,
- 2) Radiated interference,
- 3) Capacitive interference,
- 4) Inductive interference.

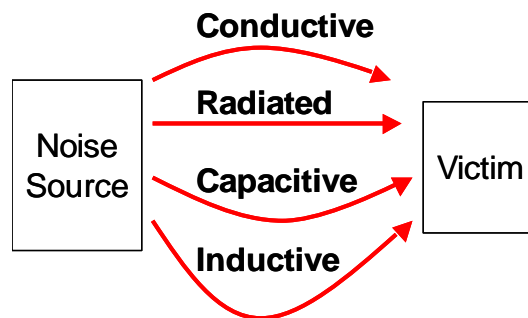


Fig. 1-1. Noise paths.

Conductive interference means the noise source interferes with the victim circuit through the conduction of conductors. Radiated interference means the noise source

interferes with the victim circuit through radiation. The capacitive and inductive interferences result from the near field couplings between the noise source and the victim circuit.

In contrast to EMI, electromagnetic compatibilities (EMC) mean the electronic equipment should not be affected by external EMI and should not be an EMI source. To achieve it, there are many approaches, such as filtering, shielding, grounding, isolation, separation and orientation.

For switch mode power supplies, EN55022 class A is one of the generic standards for conducted EMI for most of the AC/DC converters in both commercial and industrial applications in the United States. EN55022 class A specifies the conducted EMI frequency range from 150 kHz to 30 MHz and the limit is 66 dB μ V at 150 kHz, 56 dB μ V from 500 kHz to 5 MHz and 60 dB μ V from 5 MHz to 30 MHz. Most of the AC/DC power products need to meet this limit before coming to market. EMI filters have been used for this purpose for a long time.

1.1.2. Differential Mode and Common Mode Noise

The conducted EMI noise flows in both power lines and the ground. In order to measure and analyze it easily, it is usually decoupled to differential mode (DM) and common mode (CM) noise.

A simple case is shown in Fig. 1-2. V_N is noise source in the converter. Z_1 and Z_2 are impedances on noise paths (here are two power lines). Z_{C1} is the impedance between the converter and the ground. Two 50 Ω resistors are the load of noise. DM noise current i_{DM}

flows in the loop between two power lines and CM noise current i_{CM} flows in the loop including power lines and the ground. The actual noise current in two power lines are:

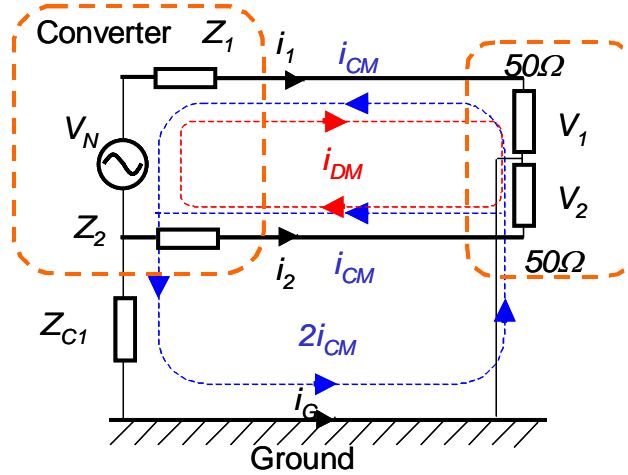


Fig. 1-2. DM and CM noise.

$$\begin{aligned} i_1 &= -i_{CM} + i_{DM} \\ i_2 &= -i_{CM} - i_{DM} \\ i_G &= 2i_{CM} \end{aligned} \quad (1-1)$$

The EMI standards specify the voltage limits of noise on a 50Ω resistance, which are:

$$\begin{aligned} v_1 &= 50(-i_{CM} + i_{DM}) \\ v_2 &= 50(-i_{CM} - i_{DM}) \end{aligned} \quad (1-2)$$

It should be pointed out that DM and CM concepts are just a shortcut for noise analysis. In an actual circuit, one path line may have no noise current, but DM and CM noise currents still exist. In that case, they are out of phase and have the same amplitude in the line.

Since v_1 and v_2 are the voltage drops resulting from both DM and CM noise currents, either of them is total noise. In a measurement, their amplitudes are almost same since

i_{DM} and i_{CM} are HF AC currents. In order to meet the standard, EMI filters are used to attenuate v_1 and v_2 to lower than the limits specified by related EMI standards.

The noise voltage drops due to DM or CM current are shown in (1-3).

$$\begin{aligned} v_{CM} &= -50i_{CM} = \frac{v_1 + v_2}{2} \\ v_{DM} &= 50i_{DM} = \frac{v_1 - v_2}{2} \end{aligned} \quad (1-3)$$

v_1 , v_2 and v_{CM} , v_{DM} satisfy:

$$\begin{aligned} v_1 &= v_{CM} + v_{DM} \\ v_2 &= v_{CM} - v_{DM} \end{aligned} \quad (1-4)$$

If both v_{CM} and v_{DM} are 6dB lower than the EMI standard, total noise must meet the standard.

1.1.3. Measurement of Conducted EMI

Since the conducted EMI flows in different paths and different paths have different characteristics, in order to measure noise under a constant condition, Line Impedance Stabilization Network (LISN) are introduced in Fig. 1-3.

In Fig. 1-3, the internal circuit of a LISN is factually a high-pass filter. The conducted noise comes from the converter side (AC out) and comes to a 50Ω termination or the input impedance of a spectrum analyzer. $1k\Omega$ resistor is used to discharge capacitors. The equivalent circuit for HF noise is shown in Fig. 1-4. The corner frequency of this high-pass filter is around 150 kHz. For 60Hz AC current, the inductor is short and capacitors are open, so it feeds the converter directly.

In a factual measurement, two LISNs are connected to power lines and a converter as shown in Fig.1-5. The total noise voltage is measured using a spectrum analyzer connected to one of the LISNs. Another LISN is terminated by a standard 50Ω terminator. The noise amplitude is displayed on the screen of the analyzer in dBμV.

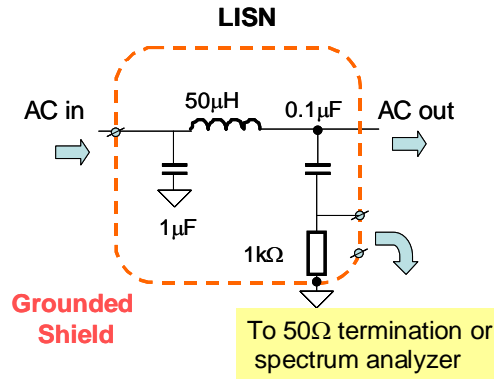


Fig. 1-3. Circuit of a LISN.

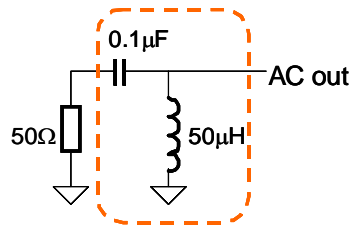


Fig. 1-4. Equivalent circuit of LISN for HF noise.

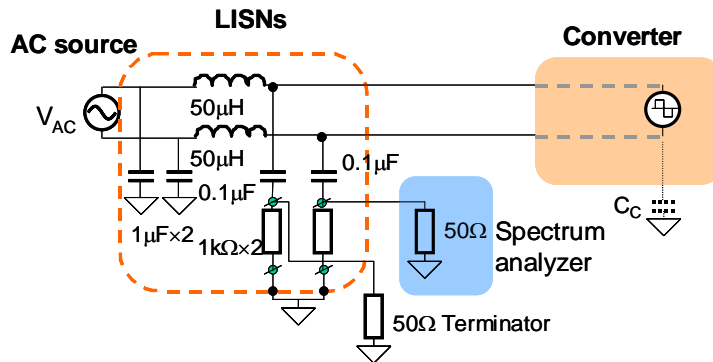


Fig. 1-5. Noise measurement using two LISNs and a spectrum analyzer.

1.2. Conducted EMI noise in a power factor correction circuit

1.2.1. Noise Paths of DM, CM and Mixed Mode Noise

For a typical power factor correction (PFC) converter shown in Fig. 1-8,

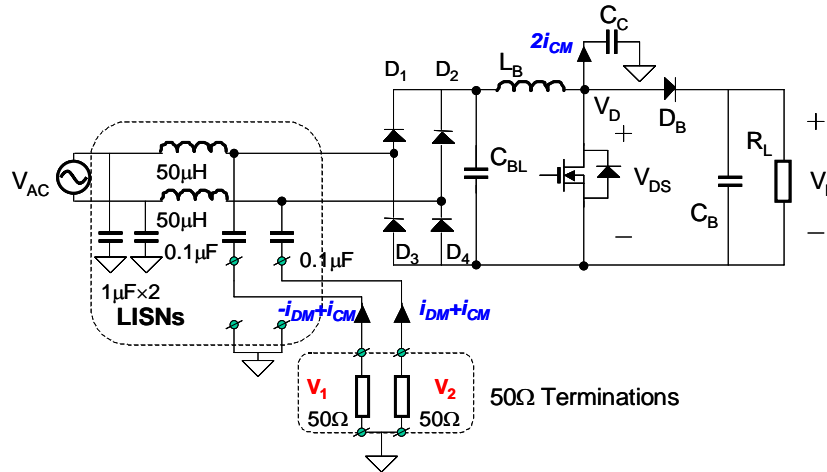


Fig. 1-8. PFC Converter under Investigation.

C_C is the parasitic capacitance between the drain of MOSFET and the ground. $1K\Omega$ resistors in LISNs in Fig. 1-5 are ignored here. When MOSFET turns off, V_{DS} equals V_L and when MOSFET turns on, V_{DC} equals zero. Since the behavior of MOSFET is like a voltage source to noise, the MOSFET and the D_B , C_B and R_L can be replaced by a voltage source V_N as shown in Fig.1-9.

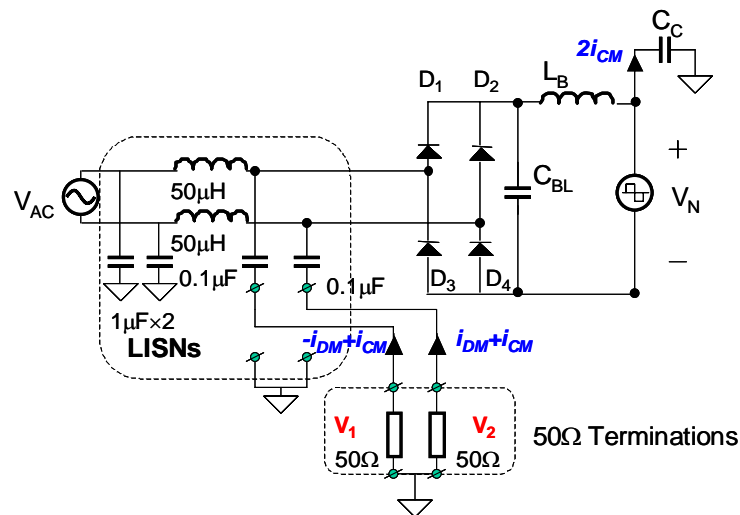


Fig. 1-9. Equivalent Noise source.

C_{BL} is a balance capacitor, whose effects will be illustrated below. If the C_{BL} does not exist, all conduction states of diode-bridge are shown in Fig. 1-10.

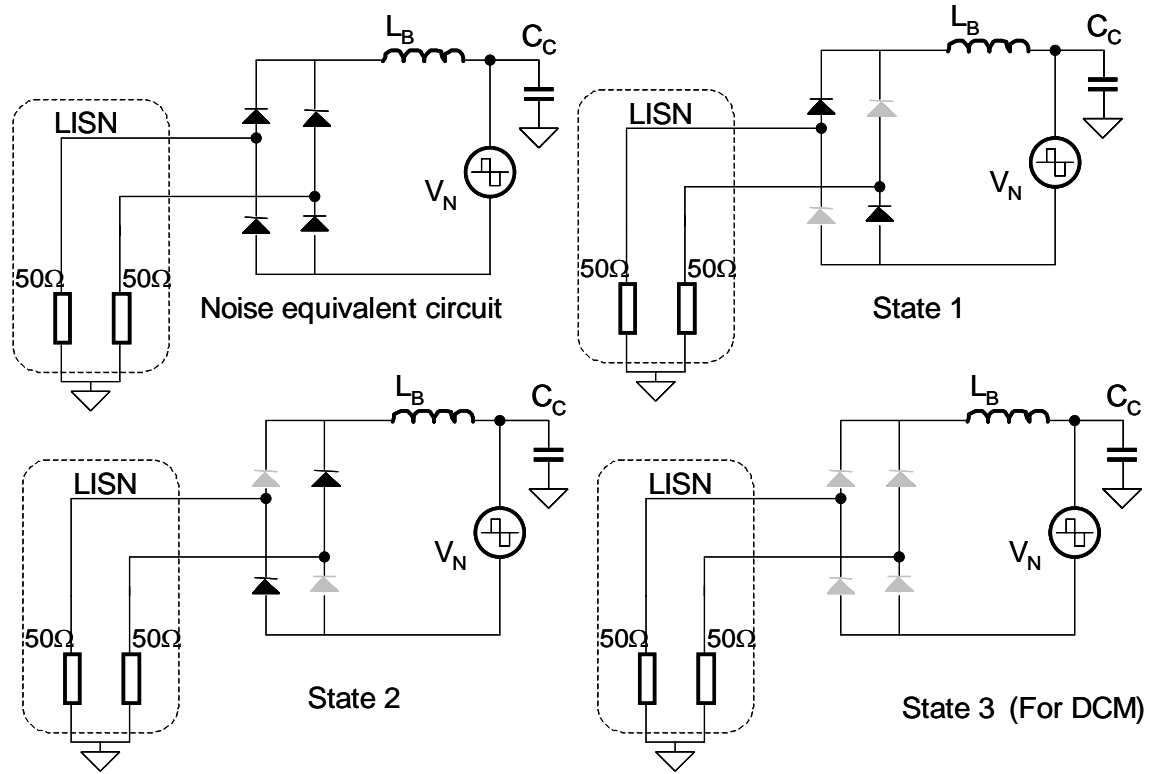


Fig. 1-10. Conduction states of diode bridge.

For CCM PFC, there is always one pair of diodes conducting current (State 1 and 2). For DCM PFC, four diodes can turn off at the same time (State 3). At state 1, the noise path is shown in Fig. 1-11.

In Fig. 1-11, DM noise always comes through the boost inductor L_B and two power lines. However, for $2i_{CM}$, the current due to parasitic capacitor C_C , comes through only one power line and does not come through L_B . The total noise including DM and CM

noise is also show in the figure. Two power lines conducting different currents and one line conducts $2i_{CM}$ more current than the other line.

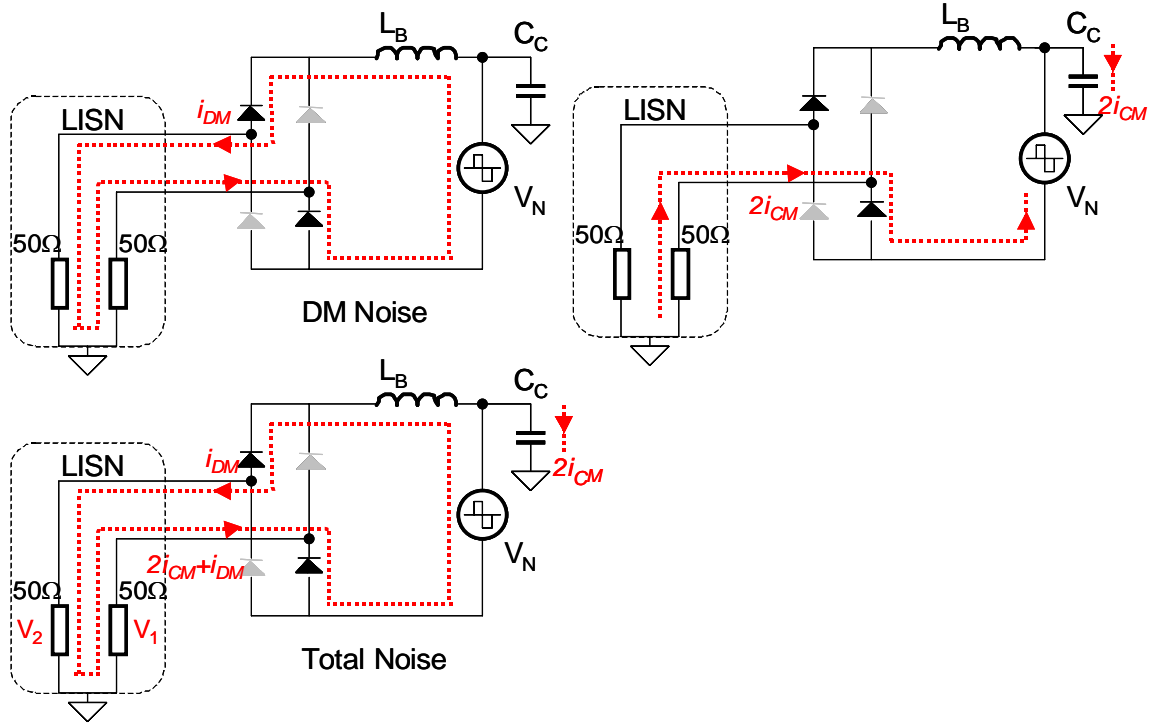


Fig. 1-11. Noise paths in state 1.

The measured noise voltages V_1 and V_2 on LISNs are:

$$\begin{aligned} V_1 &= -50(i_{DM} + 2i_{CM}) \\ V_2 &= 50i_{DM} \end{aligned} \quad (1-5)$$

If using (1-3, 1-4), then the measured DM and CM noise voltage on LISNs are:

$$\begin{aligned} V_{DM}^m &= \frac{V_1 - V_2}{2} = -50(i_{DM} + i_{CM}) \\ V_{CM}^m &= \frac{V_1 + V_2}{2} = -50i_{CM} \end{aligned} \quad (1-6)$$

It can be seen that V_{DM}^m is the voltage drop of $i_{DM} + i_{CM}$ on a 50Ω resistor instead of the voltage drop of current i_{DM} only. This is different from (1-3). For V_{CM}^m , it is the voltage drop of current i_{CM} on a 50Ω resistor, which is the same as (1-3) except the phase. The fact that $2i_{CM}$ comes through only one line causes this phenomenon. Some literature suggests that this is mixed mode (MM) noise, a third kind of noise besides DM and CM noise. For this MM noise, two equations in (1-3) are no longer both satisfied, just as shown in (1-6). Investigating Fig. 1-11, the reason for MM noise is the unbalance of the circuit.

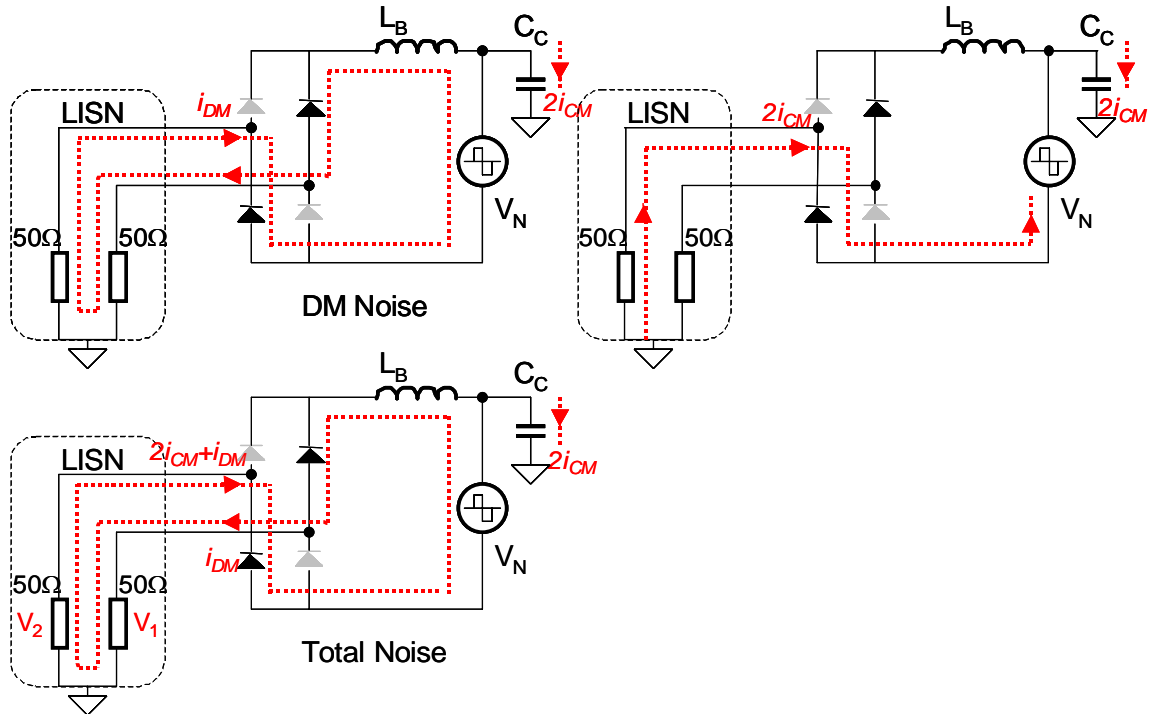


Fig. 1-12. Noise paths in state 2.

At state 2, the situation is similar to that of state 1. Fig. 1-12 shows noise paths in state 2.

The measured noise voltages V_1 and V_2 on LISNs are:

$$\begin{aligned} V_1 &= 50i_{DM} \\ V_2 &= -50(i_{DM} + 2i_{CM}) \end{aligned} \quad (1-7)$$

If using (1-3, 1-4), then the measured DM and CM noise voltage on LISNs are:

$$\begin{aligned} V_{DM}^m &= \frac{V_1 - V_2}{2} = 50(i_{DM} + i_{CM}) \\ V_{CM}^m &= \frac{V_1 + V_2}{2} = -50i_{CM} \end{aligned} \quad (1-8)$$

Comparing (1-8) with (1-6), the only difference is 180° phase of V_{DM}^m , so the measured noise amplitudes are same. MM noise still exists.

Although mixed mode noise is used to describe the unbalanced structure, a new definition on noise current can resolve the conflict between (1-3) and (1-6):

$$\begin{aligned} i_{DM}^m &= i_{DM} + i_{CM} \\ i_{CM}^m &= i_{CM} \end{aligned} \quad (1-9)$$

In (1-9), DM current i_{DM}^m and CM current i_{CM}^m are redefined. (1-5) and (1-6) can then be rewritten as:

$$\begin{aligned} V_1 &= -50(i_{DM}^m + i_{CM}^m) \\ V_2 &= 50(i_{DM}^m - i_{CM}^m) \end{aligned} \quad (1-10)$$

$$\begin{aligned} V_{DM}^m &= \frac{V_1 - V_2}{2} = -50i_{DM}^m \\ V_{CM}^m &= \frac{V_1 + V_2}{2} = -50i_{CM}^m \end{aligned} \quad (1-11)$$

(1-8) can also be rewritten as:

$$\begin{aligned} V_{DM}^m &= \frac{V_1 - V_2}{2} = 50i_{DM}^m \\ V_{CM}^m &= \frac{V_2 + V_1}{2} = -50i_{CM}^m \end{aligned} \quad (1-12)$$

Now they both are similar to (1-3). The unbalanced structure can therefore be described by redefining the noise current.

Now, if a balance capacitor C_{BL} is added after the diode bridge, the situation is much different as shown in Fig. 1-13.

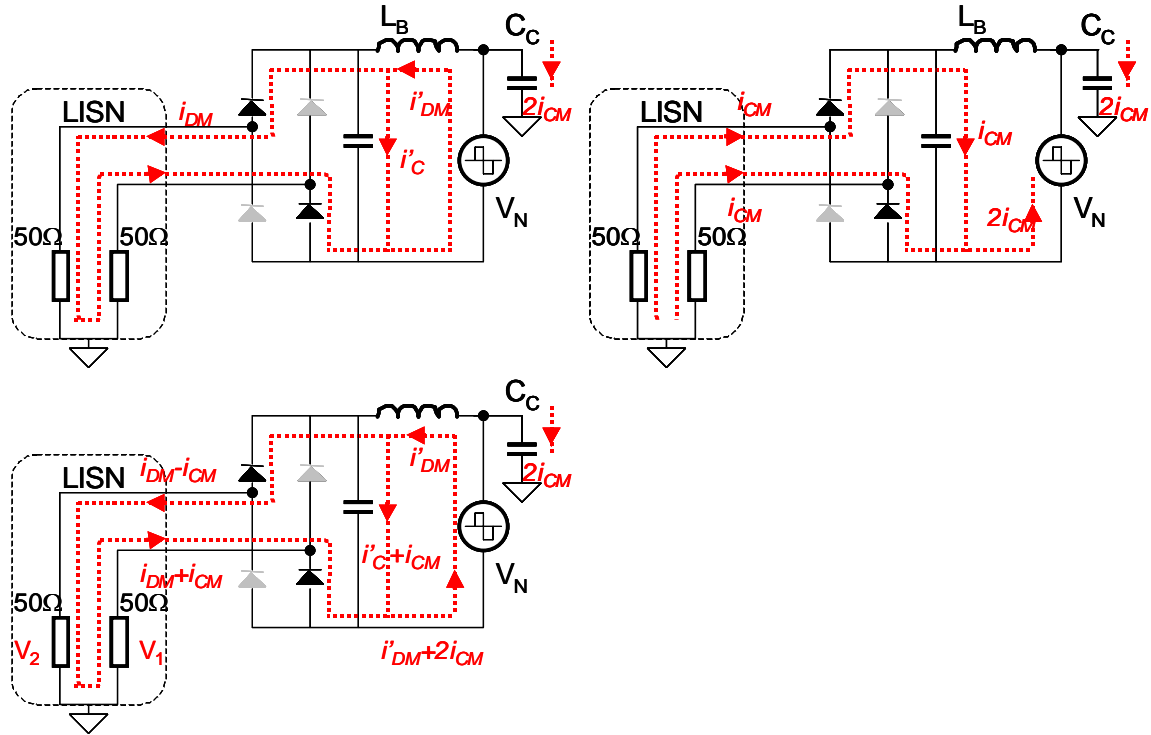


Fig. 1-13. Noise paths in state 1 in a balance structure.

In Fig. 1-13, the CM noise comes through both power lines because C_{BL} provides a path for CM currents, which are previously unbalanced. Because of this, the measured noise voltages on LISNs are:

$$\begin{aligned} V_1 &= -50(i_{DM} + i_{CM}) \\ V_2 &= 50(i_{DM} - i_{CM}) \end{aligned} \quad (1-13)$$

$$V_{DM}^m = \frac{V_2 - V_1}{2} = 50i_{DM} \quad (1-14)$$

$$V_{CM}^m = \frac{V_2 + V_1}{2} = -50i_{CM}$$

They agree with (1-3). Effects of C_{BL} on CM noise can then be described by comparing Fig. 1-11 with Fig. 1-13, and (1-5) with (1-13). It should be pointed out that the DM noise current in Fig. 1-13 is smaller than that in Fig. 1-11 because of the filtering effects of C_{BL} on DM noise.

For state2 the situation is similar to that shown in Fig. 1-14, (1-15) and (1-16).

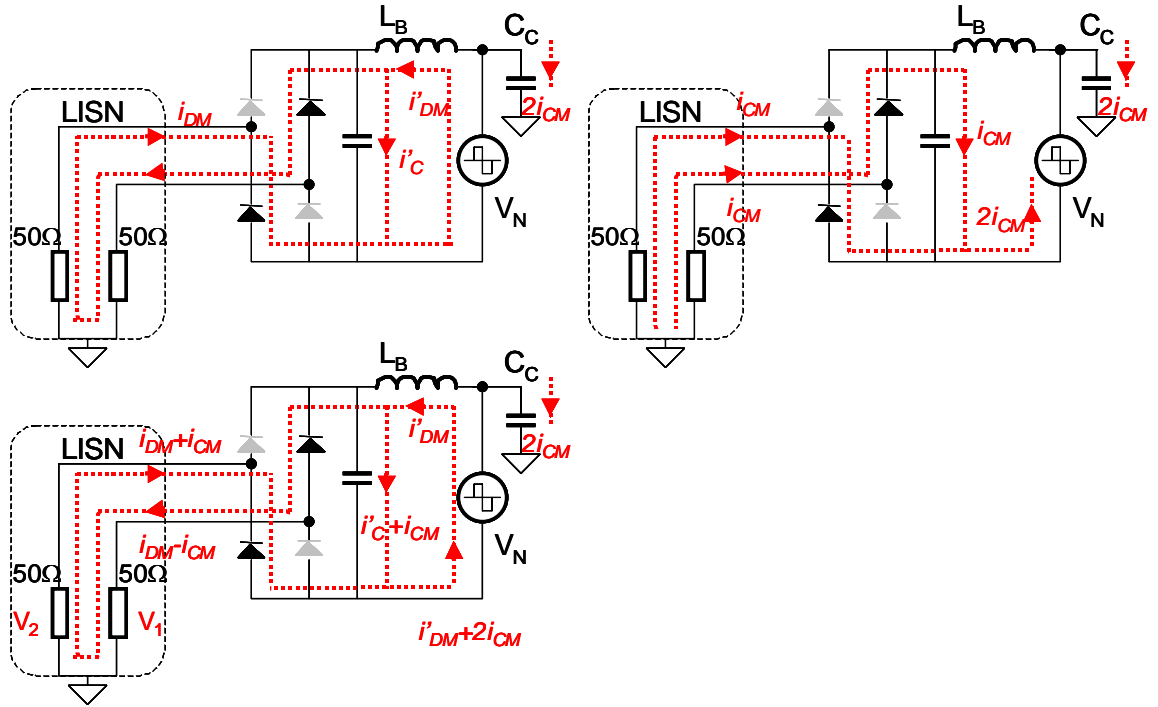


Fig. 1-14. Noise paths in state 2 in a balance structure.

$$\begin{aligned} V_1 &= 50(i_{DM} - i_{CM}) \\ V_2 &= -50(i_{DM} + i_{CM}) \end{aligned} \quad (1-15)$$

$$V_{DM}^m = \frac{V_2 - V_1}{2} = -50i_{DM} \quad (1-16)$$

$$V_{CM}^m = \frac{V_2 + V_1}{2} = -50i_{CM}$$

The balance capacitor can also be added before the diode bridge. Fig. 1-15 and 1-16 illustrate its effects on noise propagation.

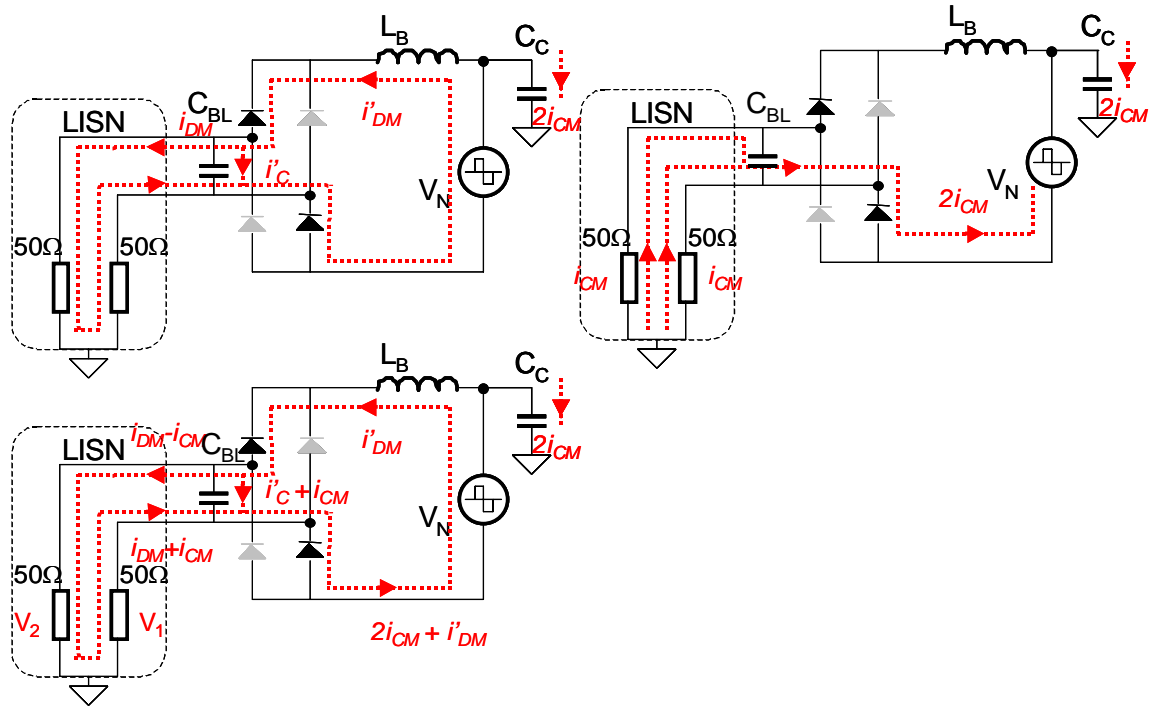


Fig. 1-15. Noise paths in state 1 in a balance structure.

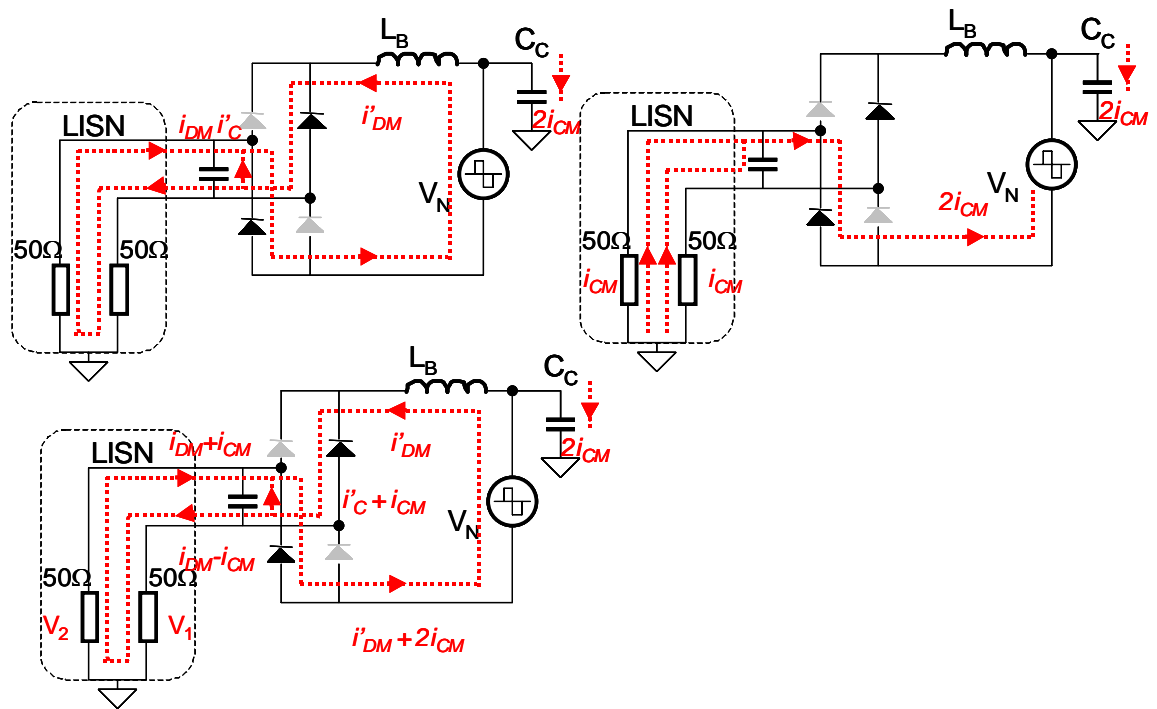


Fig. 1-16. Noise paths in state 2 in a balance structure.

1.2.2. Effects of Boost Inductor on DM Noise

As Figs. 1-11 to Figs. 1-16 show, DM noise always comes through the boost inductor L_B .

The equivalent circuit for the DM noise in Fig. 1-11 is shown in Fig. 1-17 if the parasitics in the loop are ignored.

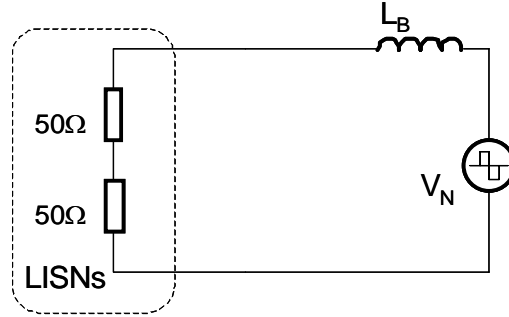


Fig. 1-17. DM noise equivalent circuit.

$$V_{DM} = \frac{50}{100 + j\omega L_B} V_N = \frac{V_N}{2 + Z_{LB}/50} \quad (1-17)$$

$$\text{If } |Z_{LB}| \gg 100$$

$$20 \log \left(\frac{|V_{DM}|}{1 \mu V} \right) = 20 \log V_N - 20 \log(|Z_{LB}|) + 154 (dB \mu V) \quad (1-18)$$

The measured DM noise using a spectrum analyzer is actually composed of three parts, as shown in (1-18). The first part is the spectrum of the equivalent noise voltage source i.e. the voltage transition across the drain and source of the main switch. The second part is the impedance of the boost inductor and the third part is a constant.

Since the spectrum of noise source is already determined for a PFC converter, the measured DM noise is therefore shaped by the impedance of the boost inductor. The typical waveform of V_N is shown in Fig. 1-18. The pulse width is modulated by a 120Hz

signal from control circuit. The switching frequency is usually much higher than 120Hz, so the effects of 120Hz modulation signal can be ignored when considering the spectrum from 150kHz to 30MHz.

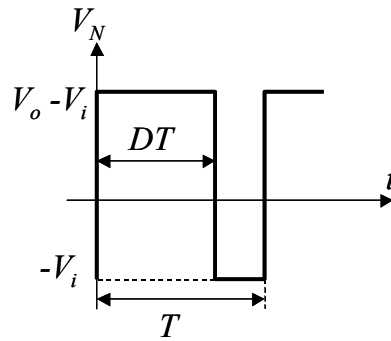


Fig. 1-18. Equivalent DM noise voltage source.

The spectrum for the periodical waveform in Fig. 1-18 has a -20dB spectrum. The investigated boost inductor has a cool μ core with a permeability of 60. Its impedance is shown in Fig. 1-19. It can be seen that due to the parasitics in inductor structure, in HF range, there are several impedance peaks and valleys. The inductor is no longer an inductor but a frequency dependent and coupled transmission line structure.

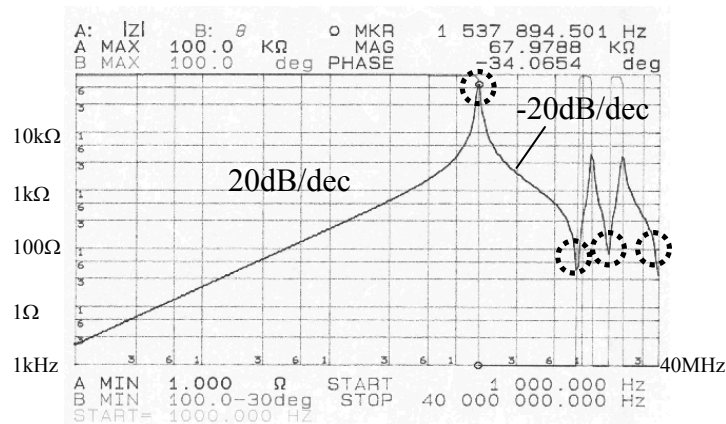


Fig. 1-19. Impedance of a boost inductor.

In Fig. 1-19, in low frequency range ($< 600\text{kHz}$), the impedance is dominated by the inductance, so the impedance Z_{LB} is 20dB/dec . The first impedance peak is caused by the parallel resonance between the inductance and the winding capacitance (first order). After that, the inductor acts like a capacitor so the impedance becomes -20dB/dec . The other impedance peaks and valleys can be explained by the related transmission line theory.

In (1-18), the first part is already known as -20dB/dec . The second part is the impedance of boost inductor, which is 20dB/dec in LF range. Then the spectrum of the measured DM noise should be -40dB/dec in LF range. At the frequency of impedance peak, the spectrum should have a corresponding valley. After the impedance peak, the impedance is -20dB/dec , so the measured DM spectrum should be 0dB/dec . On the other hand, at the frequency of the impedance valley, the spectrum should have a corresponding peak, and so on. The measured DM noise spectrum is shown in Fig. 1-20.

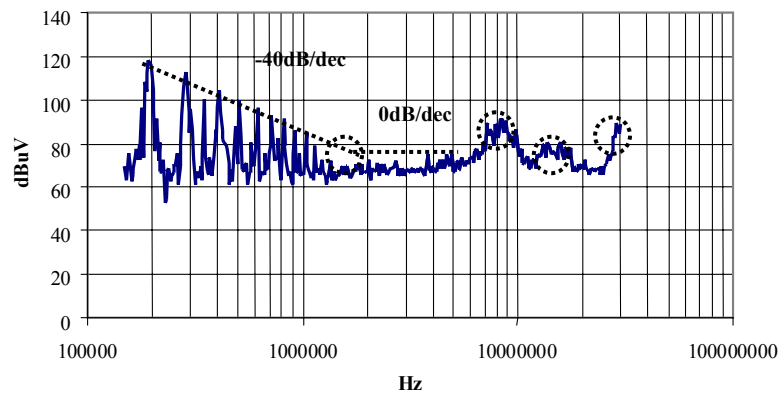


Fig. 1-20. Measured DM noise spectrum.

Just as we expected, the DM spectrum is -40dB/dec in LF range and 0dB/dec after the frequency of the first impedance peak. There are noise peaks and valleys corresponding

to impedance valleys and peaks. The inductor is redesigned using an iron powder core with permeability of 100. With an iron powder core, the HF loss is higher than the cool μ core, so the HF impedance is higher than the cool μ core. The DM noise is therefore expected to be lower than cool μ core in HF range. At the same time the Q is lower so that the impedance valley is higher than the cool μ core. As a result the noise peak is lower. Furthermore, due to the higher permeability, the turn number of winding is smaller than that of the cool μ core, so the winding capacitance can be smaller. The impedance peaks and valleys are therefore increased to higher frequency. The impedance of the redesigned boost inductor is shown in Fig. 1-21. Based on these comparisons, the iron powder core should have a lower DM noise in HF range than the cool μ core. The measured DM noise with two boost inductors is shown in Fig. 1-22.

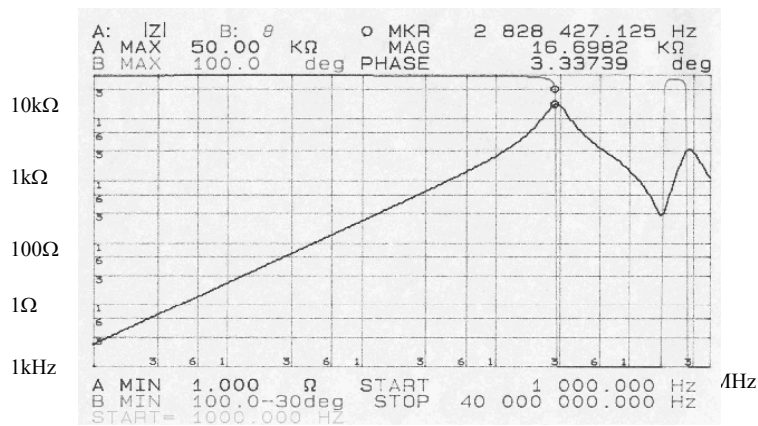


Fig. 1-21. Impedance of redesigned boost inductor.

Comparing Fig. 1-19 and Fig. 1-21, two inductors have same inductance in LF range. The impedance peaks of iron powder core inductor increased to around 3MHz compared with 1.5MHz of the cool μ core. Due to smaller parasitic parameters, there are fewer

peaks and valleys in HF range. Due to the higher core loss, the impedance in HF range is higher than the cool μ core. For the first impedance valley, the iron powder core is 300Ω , which is much higher than 50Ω of the cool μ core.

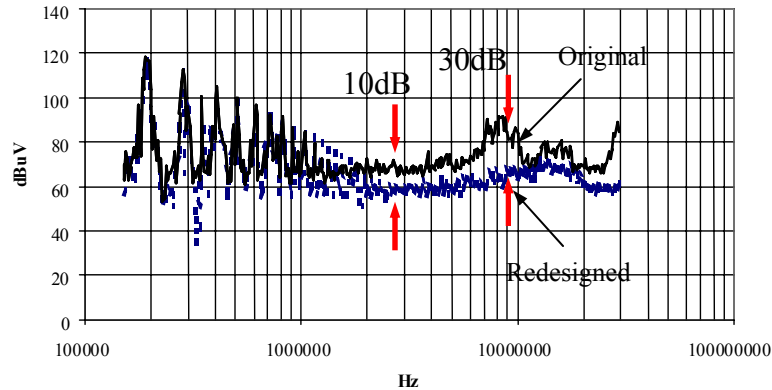


Fig. 1-22. Measured DM noise spectrums.

Two measured DM noise spectrums are compared in Fig. 1-22. It is shown that the redesigned boost inductor has a lower HF DM noise than the cool μ core inductor. The DM noise peak is also dampened by the core loss. Compared with the cool μ core inductor case, the DM noise has 10dB improvement above 2MHz and up to 30dB improvement at noise peaks.

It is shown that the HF DM noise is effectively reduced by redesigning the boost inductor. The general rule of designing an inductor with low DM noise is: 1) high HF core to get high HF impedance and high damping on parasitic resonance; 2) appropriately high permeability to get small number of turns and thus small parasitic parameters. Other structural parameters such as the thickness and permittivity of coating materials of core and wire are also important. The distance between turns is also a factor to be considered.

1.3. EMI Filters for Switch Mode Power Supplies Circuit

One or two stages of EMI filters are usually used for DM and CM noise attenuation in the power electronics area. The basic principle of filtering is to bypass noise using shunt capacitors and block noise using series inductors. The commonly used EMI filter topologies include LC low pass filters to attenuate HF noise, and sometimes, band reject filters to attenuate a certain frequency, which is usually the switching frequency. As an example, a DM filter used to attenuated DM noise in Fig. 1-2 is shown in Fig. 1-23.

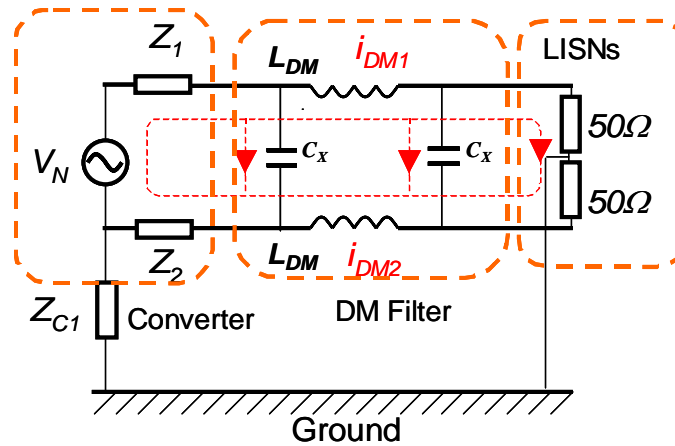


Fig. 1-23. Attenuating DM noise using a DM filter.

In Fig. 1-23, the left DM capacitor C_X bypasses most of the DM current because of the high impedance of L_{DM} . The right DM capacitor C_X bypasses most of the remained DM current because of the higher impedance of LISNs. Since the DM currents in two DM inductors are same, they can be considered in series.

A CM filter used to attenuate CM noise is shown in Fig. 1-24. CM capacitors C_Y have same capacitance and thus the same impedance to CM noise. The CM inductance L_{CM} is the same on two lines and at the same time, two inductors are closely coupled. Because of

this, the CM currents in two lines are evenly bypassed by two CM capacitors. The CM inductor and LISNs form a voltage divider. Since the impedance of CM inductor is much higher than the impedance of LISNs, the CM noise is further attenuated.

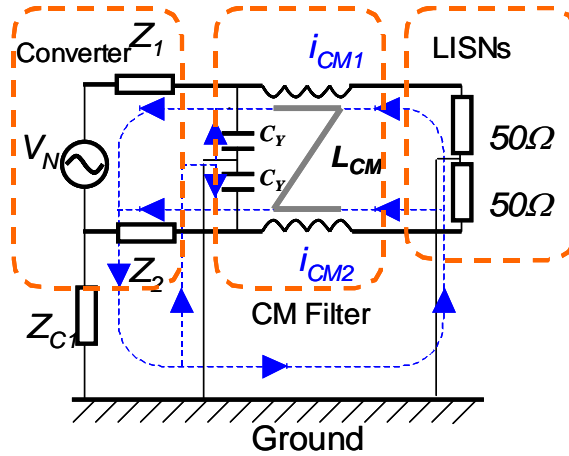


Fig. 1-24. Attenuating CM noise using a CM filter.

CM and DM filter are usually built together in power electronics applications as shown in Fig. 1-25, where the leakage part of coupled CM inductor acts as DM inductor.

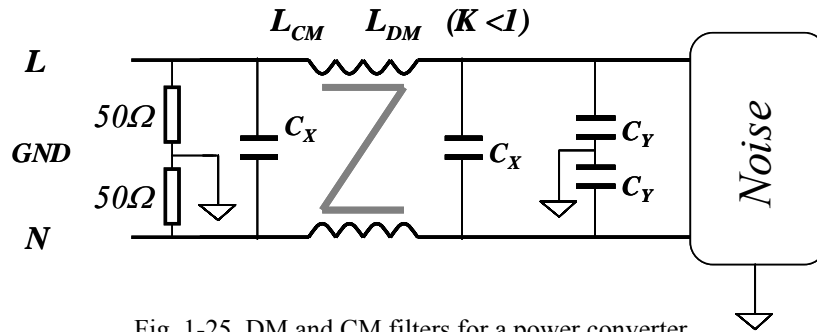


Fig. 1-25. DM and CM filters for a power converter.

The equivalent circuits for DM and CM filters are shown in Fig. 1-26 and Fig. 1-27. The leakage inductance of the inductor is the DM inductance of DM filter. The coupled inductance of the inductor is the CM inductance of CM filter.

Two CM capacitors are in series for DM noise, so the capacitance is only one half of the single capacitor. Two DM inductors are in parallel for CM noise, so the equivalent inductance is only half of one DM inductance. DM capacitors work like balance capacitors for CM noise. CM inductor is like a short circuit for DM noise because the magnetic fluxes generated by the DM current in two coupled windings are cancelled.

CM equivalent loop

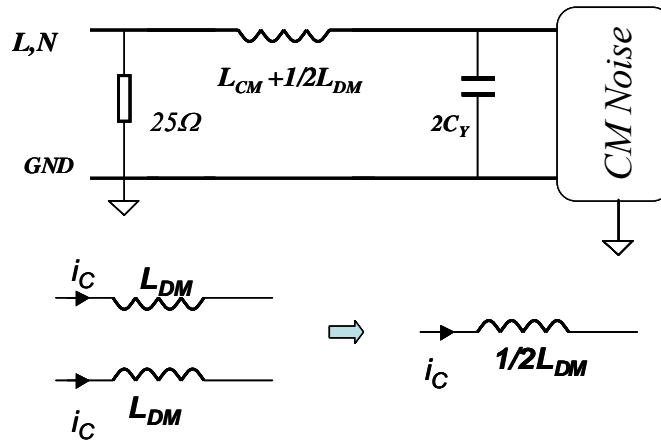


Fig. 1-26. Equivalent circuit for CM noise.

DM equivalent loop

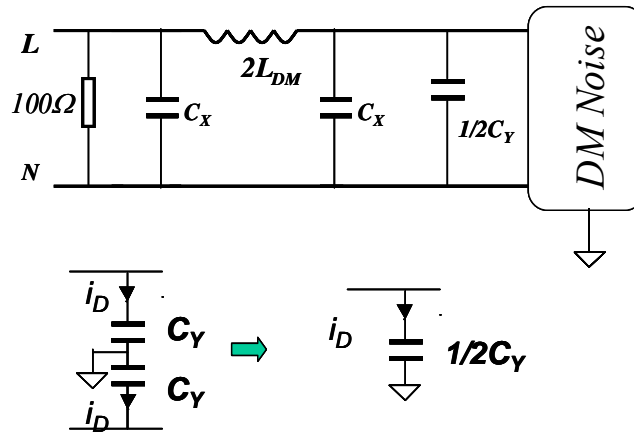


Fig. 1-27. Equivalent circuit for DM noise.

The general rule for EMI filter design is the so called impedance mismatch rule which is shown in Fig. 1-28 and 1-29. In Fig. 1-28, the input and output impedances of EMI

filter, power supply and LISN should satisfy the rule defined in Fig. 1-29. The impedance mismatch rule can be described as: the input impedance of EMI filter should be much higher or lower than the output impedance of noise source. The output impedance of the EMI filter should be much higher or lower than the input impedance of LISNs.

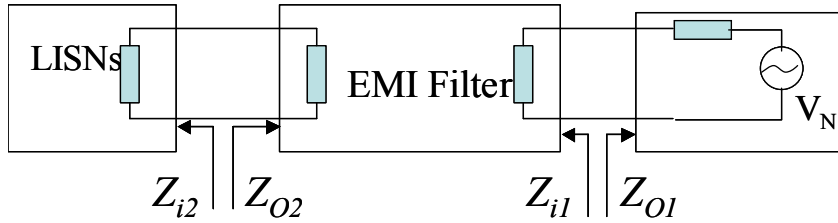


Fig. 1-28. Input and output impedances of EMI filter, noise source and LISNs.

$ Z_{O1} \backslash Z_{i2} $	High	Low
High		
Low		

Fig. 1-29. Impedance mismatch rule of EMI filter design.

For DM filter in a PFC converter, if balance capacitor is already included in the converter, for example C_x in Fig. 1-13, the output impedance of DM noise source would be low, so a series inductor (high input impedance) is preferred in the filter input to mismatch the low output impedance of the noise source. The DM input impedance of LISNs is 100Ω , so a shunt capacitor (low output impedance) is preferred at output of the DM filter to mismatch LISNs. For CM filter, the parasitic capacitance is usually small, so its impedance is high. Two shunt capacitors are therefore needed at the input of the CM

filter. The input impedance of LISNs for CM noise is only 25Ω , so a series CM inductor (high output impedance) is needed at the output of the CM filter to mismatch LISNs.

If the impedance mismatch rules are not followed, some components would be inefficient on noise attenuation. For example, if a shunt DM capacitor is still used in the input of DM filter when a balance capacitor has been used, this shunt DM capacitor would be not as efficient as a series DM inductor.

1.4. Objective of This Work

This dissertation tries to improve EMI filter's high frequency (HF) performance by canceling the effects of HF parasitics. In order to achieve that, parasitics must be first identified and quantified; cancellation methods are then proposed based on EMI filter models. Besides that, in order to accurately explain EMI filter's performance, effects of power interconnects on HF filter performance are explored and a high performance noise separator is built for EMI measurement.

References

- [1] Shuo Wang, F.C.Lee and W.G.Odendaal, "Improving the Performance of Boost PFC EMI Filters," in *Proc. IEEE Applied Power Electronics Conference and Exposition*, 2003. Eighteenth Annual, Volume 1, pp. 368 -374.
- [2] Mark J. Nave, *Power line filter design for switched-mode power supply*, Van Nostrand Reinhold, New York, 1991.
- [3] S. Qu, D. Y. Chen, "Mixed-mode EMI Noise and Its Implications to Filter Design in Offline Switching Power Supplies," *IEEE Transactions on Power Electronics*, Volume 17, Issue 4, July 2002, pp. 502 –507.

CHAPTER 2: EFFECTS OF PARASITIC PARAMETERS ON EMI FILTER

PERFORMANCE*

2.1. Introduction

It is a well-known fact that parasitic elements in the electromagnetic interference (EMI) filter can play an important role in filter performance. Most engineers are well aware of the self-resonant effects of the parasitic winding capacitance of an inductor and the parasitic inductance of a capacitor on filter performance. These effects, while annoying, are still relatively understandable and manageable because they can be measured with an impedance analyzer. The other category of parasitic effects, those related to layout and packaging, are more difficult to decipher. Although this problem is distributed in nature and can theoretically be overcome by solving field problems, this approach is impractical. In the investigation leading to this chapter, attempts were made to understand layout-related EMI filter problems. It will be shown that two filters with identical topologies and components can exhibit a significant difference in filter effectiveness when their layouts are different. The investigation will be done from the circuit standpoint so that the resultant conclusions are applicable to many practical problems. Specifically, the impacts of six coupling effects on filter performances are considered. They include the inductive couplings between the following: inductors and printed circuit board (PCB) layout, inductors and capacitors, two capacitors, ground plane and inductors, in and out trace loops and two inductors. The effects of these mutual couplings on filter attenuation are identified and quantified in this chapter.

** © 2004 IEEE. Reprinted, with permission, from IEEE Transactions on Power Electronics, Volume 19, Issue 3, May 2004, pp. 869 - 877.*

2.2. Parasitic Couplings Existing in an EMI Filter

Fig. 2-1 shows a commonly used EMI filter for AC/DC converters. The PCB layout is shown in Fig. 2-2, where C_1 and C_2 are differential-mode (DM) capacitors, C_{cm} is common-mode (CM) capacitor which is not investigated here. A CM inductor L_{cm} is used in the filter. The leakage inductance of L_{cm} , which extends to the air and couples other components, is usually used as DM inductance L_{dm} . Two BNC connectors are attached to the filter for measurement. Fig. 2-3 shows the equivalent circuit for the DM noise of the circuit in Fig. 2-1. Also indicated in Fig. 2-3 are eight mutual couplings M_1 through M_7 and C_p . The definitions of these mutual couplings are given in Fig. 2-3.

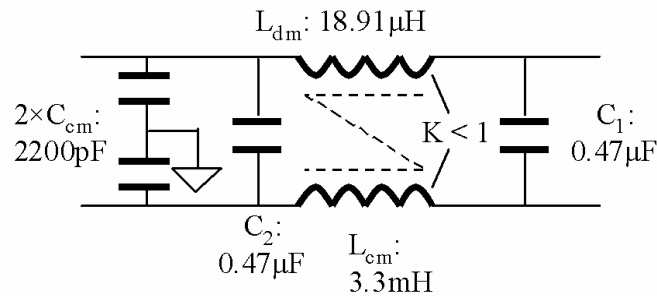


Fig. 2-1. Circuit of the investigated filter.

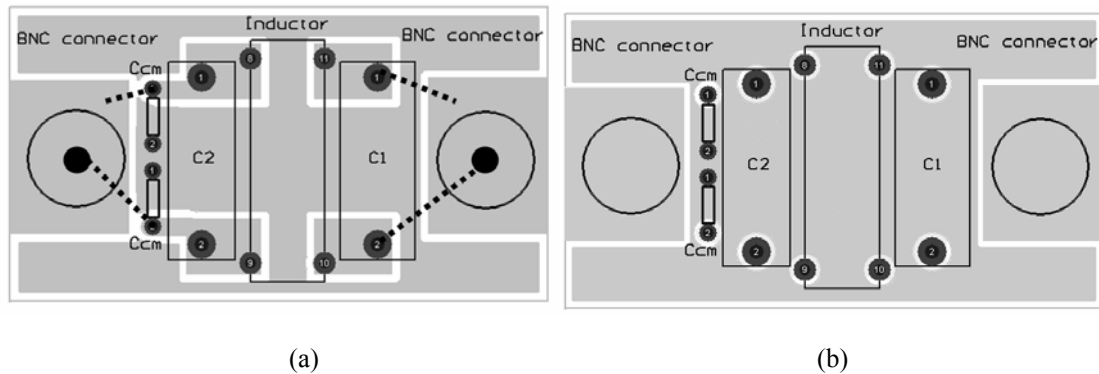
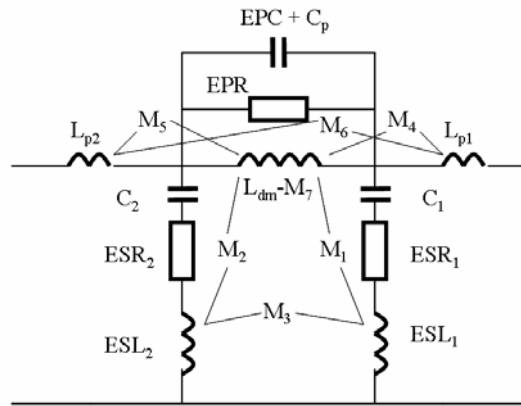


Fig. 2-2. PCB layout of the filter: (a) Bottom side and (b) Top side.



(L_{p1} , L_{p2} : trace-loop inductance; ESL, ESR, C: capacitor model parameters; L_{dm} , EPC, EPR: DM inductor model parameters; M_1 , M_2 : mutual inductance between L_{dm} and capacitor branches; M_3 : mutual inductance between two capacitor branches; M_4 , M_5 : mutual inductance between L_{dm} and trace loops; M_6 : mutual inductance between in and out trace loops; M_7 : equivalent mutual inductance between ground plane and L_{dm} ; C_p : mutual capacitance between in and out traces)

Fig. 2-3. DM filter model

Two kinds of parasitic couplings exist in the filter: inductive coupling and capacitive coupling. Inductive couplings tend to amplify their effects on the branch that has the smaller current between two branches with a large current difference. So the inductive couplings, such as those between capacitor branches and the inductor branch, between two capacitor branches, between in and out trace loops, and between inductor and in and out trace loops are the critical parasitic couplings. At the same time, the capacitive couplings tend to amplify their effects on the junction that has lower potential between two junctions with a large potential difference. So the capacitive coupling between in and out traces is a critical coupling for the performance of EMI filters.

In Fig. 2-3, M_1 - M_7 are inductive couplings. M_1 , M_2 and M_3 affect capacitor branches directly. M_4 and M_5 affect capacitor branches through branch currents. M_6 is the coupling

between in and out trace loops. M_7 is the equivalent inductance reduction that occurs due to magnetic flux cancellation between DM inductor and the eddy current in the ground plane. C_p is the capacitive coupling between in and out traces. The capacitive coupling happens both directly and through the ground plane between two traces. This capacitive coupling is equivalent to that of a capacitor C_p in parallel with the inductor.

2.3. Identifying, Analyzing and Extracting Parasitic Couplings

2.3.1. Inductive Couplings Existing between DM Inductor L_{dm} and Capacitor Branches, between DM Inductor L_{dm} and In and Out Trace Loops (M_1 , M_2 and M_4 , M_5 in Fig. 2-3)

These couplings have similar effects on the capacitor branches. The equivalent circuits for the couplings between inductor and one of the in and out trace loops are shown in Fig. 2-4. For another trace loop, the equivalent circuit is the same. The equivalent circuits for the couplings between inductor and one of the capacitor branches are shown in Fig. 2-5. For another capacitor branch, the equivalent circuit is also the same.

Based on the equivalent coupling polarities on the capacitor branch, the positive and negative couplings are defined in Figs. 2-4 and 2-5. Considering the different coupling polarities, the two circuits on the top are equivalent to the two circuits on the bottom respectively. In the circuits on the bottom, M is the equivalent inductance on the capacitor branches caused by the couplings of the inductor. If the equivalent inductance on the capacitor branch is positive, the coupling is a positive coupling; otherwise it is

negative coupling. If these two kinds of couplings exist at the same time, the total effect determines the coupling polarity.

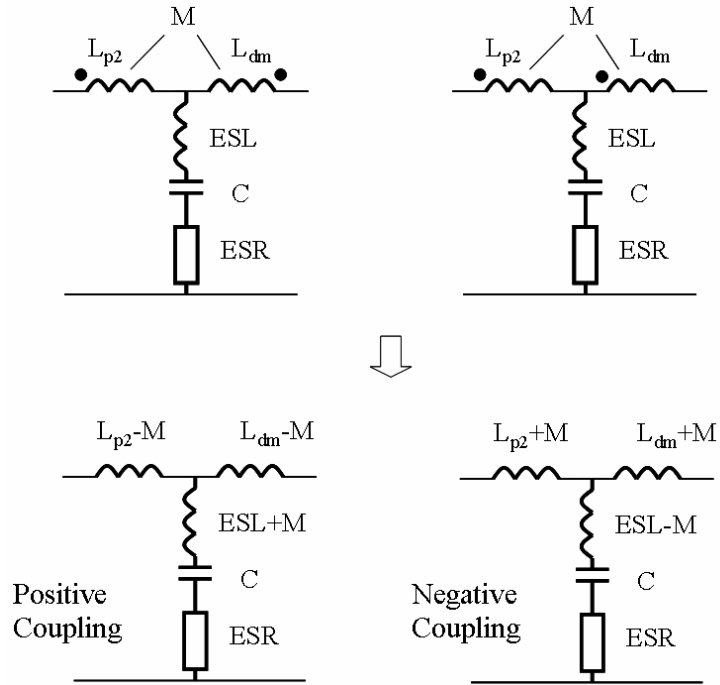


Fig. 2-4. Inductive coupling between the inductor and the trace loop.

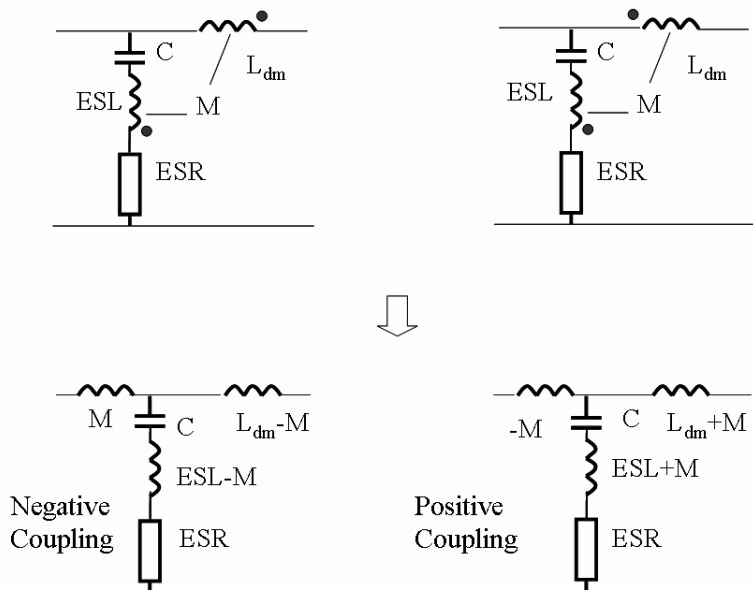


Fig. 2-5. Inductive coupling between the inductor and the capacitor branch.

The capacitor branch impedance of the positive coupling is:

$$Z_1 = ESR + j[\omega(ESL + M) - \frac{1}{\omega C}]. \quad (2-1)$$

The resonant frequency f_1 of this capacitor branch is therefore lower than that of the capacitor as follows:

$$f_1 = \frac{1}{2\pi\sqrt{(ESL + M)C}}. \quad (2-2)$$

The capacitor branch impedance of the negative coupling is:

$$Z_2 = ESR + j[\omega(ESL - M) - \frac{1}{\omega C}]. \quad (2-3)$$

If equivalent series inductance (ESL) of the capacitor is larger than mutual inductance M , then the resonant frequency f_2 of this capacitor branch is higher than that of the capacitor, such that:

$$f_2 = \frac{1}{2\pi\sqrt{(ESL - M)C}}. \quad (2-4)$$

In the case when the ESL is smaller than M , the minimum impedance instead of resonance happens at frequency f_3 ; thus:

$$f_3 = \frac{1}{2\pi\sqrt{(M - ESL)C}}. \quad (2-5)$$

The f_3 is different from f_1 and f_2 because no phase polarity change occurred at f_3 . On the contrary, f_1 and f_2 are resonant frequencies with a phase polarity change.

And for this case, (2-3) can be rewritten as:

$$Z_2 = ESR + \frac{1}{j\omega \left[\frac{C}{1 + \omega^2 C(M - ESL)} \right]} = ESR + \frac{1}{j\omega C_{eq}} \quad (2-6)$$

From (2-6), the capacitor branch can be equivalent to a capacitor C_{eq} whose capacitance is the function of frequencies. After f_3 , as the frequency increases, C_{eq} becomes smaller.

After f_1, f_2 or f_3 , the impedance of the capacitor branch becomes higher as frequency increases. Because the small impedance of the capacitor branch benefits the filter performance, the filter performance would become worse after f_1, f_2 or f_3 . Any couplings affecting the impedance of the capacitor branch would affect the performance of the filter. When the frequency is much higher than the series resonant frequency of the capacitor branch, the impedances are:

$$|Z_1| = |\omega(ESL + M)|, \quad \text{and} \quad |Z_2| = |\omega(ESL - M)| \quad (2-7)$$

From (2-7), $|Z_2|$ is smaller than $|Z_1|$. If M is equal to ESL , $|Z_2|$ is zero and the filter has the best performance in the high frequency (HF) range, while if M is much larger than ESL , $|Z_1|$ is almost equal to $|Z_2|$ and the filters have almost the same performance in the HF range.

The analysis is demonstrated in Fig. 2-6. In Fig. 2-6, four computed impedance curves for a capacitor branch are shown. These four cases are: positive coupling, zero coupling and two negative couplings. The capacitance is $0.47 \mu\text{F}$. ESL is 14 nH and equivalent series resistance (ESR) is $13 \text{ m}\Omega$. The mutual inductance is 89 nH for positive coupling, 89 nH and 10 nH for two negative couplings.

In fact, winding directions and arrangement greatly affect the couplings. The distribution of leakage magnetic flux (DM magnetic flux) of a CM inductor is described in [2]. In Fig. 2-7, winding direction 1 and winding direction 2 have opposite magnetic flux directions. Therefore, the coupling polarities between these two inductors and capacitors are opposite. So are the couplings between the inductors and the trace loops. For the proposed winding arrangement in Fig. 2-7, two windings are proposed to be rotated by 90° , and they are symmetrical to the capacitors and trace loops. Because the net magnetic flux passing through the capacitors and trace loops is greatly reduced, the couplings are much smaller than those in the previous two winding structures. In the experiments, the self-parasitic parameters of the capacitor, the inductor and the trace loops are extracted using a precision impedance analyzer Agilent 4294A. The mutual inductances are extracted through scattering parameters (S-parameters) using a network analyzer HP 4195A. The extracted mutual inductances are shown in Table 2-I.

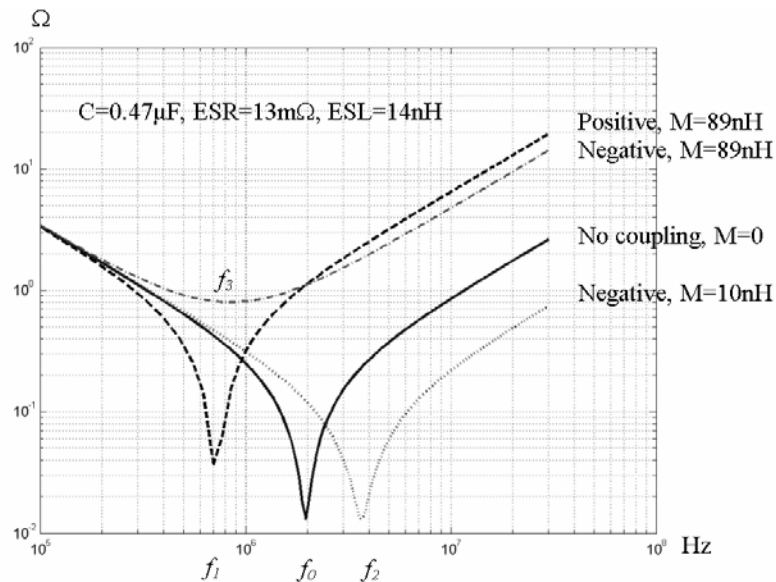


Fig. 2-6. Calculated impedances for a capacitor branch with different mutual inductances.

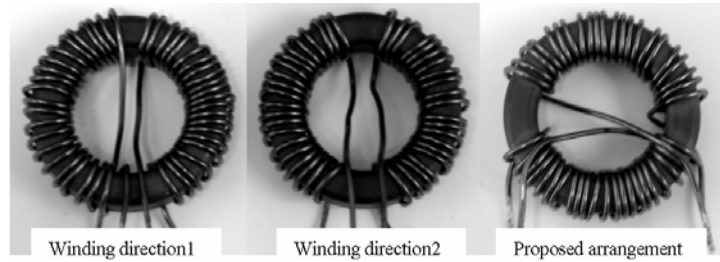


Fig. 2-7. Different winding structures have different coupling polarities.

Table 2-I. Extracted mutual inductances

Mutual inductance	Between the inductor and in/out trace loops	Between the inductor and capacitor branches
Winding direction1 (negative coupling)	18.7nH	89.3nH
Winding direction2 (positive coupling)	10.3nH	83.3nH
Proposed arrangement	1.8nH	7.5nH

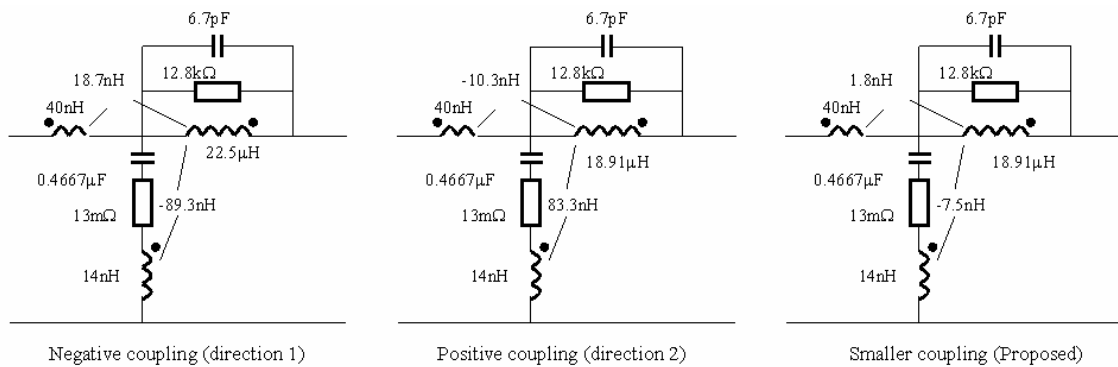


Fig. 2-8. Equivalent circuits including self and mutual inductances.

The equivalent circuits for the left half filter including the self and mutual inductances are shown in Fig. 2-8 (the filter is symmetrical so the equivalent circuits for the right half is same as that of the left half). The total effects on the capacitor branch are determined by the sum of two kinds of couplings on the capacitor branch. For the investigated EMI

filter, when winding direction 1 is used, the equivalent inductance on the capacitor branch caused by the coupling between the inductor and the capacitor branch is negative, which is opposite to that caused by the coupling between the inductor and the trace loop. Because the former is larger than the latter, the total equivalent inductance on the capacitor branch is negative. For the winding direction 2 and the proposed winding arrangement, the same principle applies.

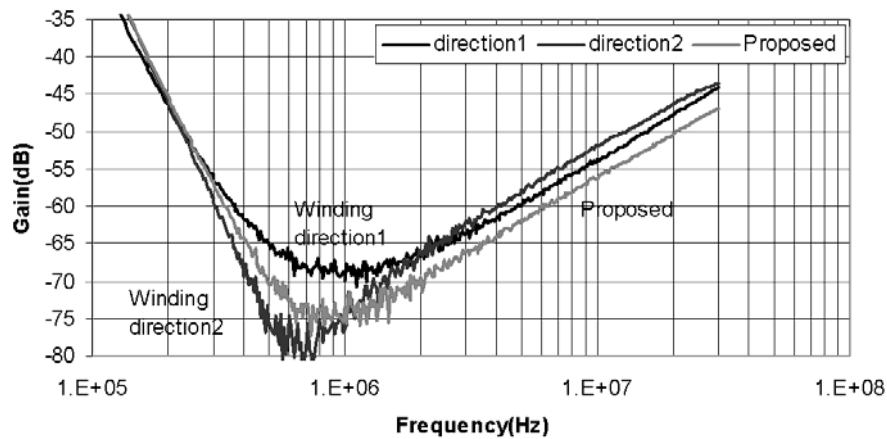


Fig. 2-9. Measured insertion voltage gains.

The measured insertion voltage gains (S_{21} of S-parameters) of the whole filter are compared in Fig. 2-9. The frequency range is from 150 kHz to 30 MHz (EMI standard: EN55022 class B for AC/DC converters). From Table 2-I and Figs. 2-8, 2-9, the insertion voltage gain with positive mutual inductance has the best performance in the low frequency (LF) range, because the series resonant frequency of the capacitor branch is reduced. The insertion voltage gain with negative mutual inductance is only slightly better than the positive case in the HF range because the mutual inductance is much larger than the ESL, just as predicted by (2-7). The proposed winding arrangement offers good performance in the entire frequency range because the couplings are reduced.

2.3.2. Inductive Couplings Existing between Capacitor Branches (M_3 in Fig. 2-3)

The inductive coupling between two capacitor branches is generally neglected; however, because there is only one inductor between them on the PCB, the two capacitors are usually close to each other. Because of the large current difference on these two branches, the inductive coupling between them plays a very important role in filter performance. The typical circuit for this effect is shown in Fig. 2-10.

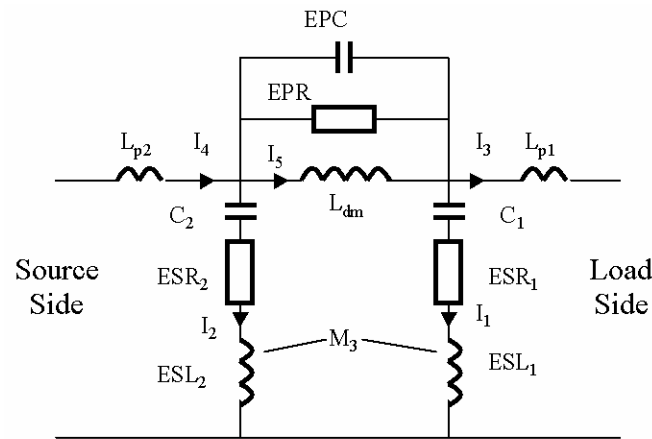


Fig. 2-10. Equivalent circuit for the coupling between two capacitor branches.

In Fig. 2-10, the voltage on ESL_1 is:

$$\dot{U}_1 = j\omega \dot{I}_1 \cdot ESL_1 + j\omega \dot{I}_2 \cdot M_3 = j\omega \dot{I}_1 \left(ESL_1 + \frac{\dot{I}_2}{\dot{I}_1} M_3 \right). \quad (2-8)$$

The I_1 is usually very small compared with I_2 because most of current is bypassed by the C_2 branch (I_2 / I_1 is 40 dB/dec after its corner frequency). When the following condition is satisfied,

$$\frac{I_2}{I_1} > \frac{ESL_1}{M_3}, \quad (2-9)$$

the mutual inductance would have a much greater effect on the capacitor branch, and thus the filter performance, than the ESL would. When I_2 / I_1 is 1,000, a coupling coefficient of 0.1% between the two capacitor branches would have obvious effects on the filter performance. In order to demonstrate this effect, experiments are carried out. In the experiment, in order to prevent the influence of other couplings, the in and out trace loops are kept very small and the inductor is mounted on the bottom side of the PCB. The longer distance and two-layer ground plane as a shield can keep the coupling between the inductor and two capacitor branches very small. Three cases are evaluated in the experiment. In the first case, the filter is measured without any actions taken; in the second case, the two capacitors are shielded with 3mil nickel ($\mu_r = 600$); and in the third case, the two capacitors are shielded with 3mil nickel and a magnetic shield is placed between them. The experiments are shown in Fig. 2-11 and the experimental results are shown in Fig. 2-12.

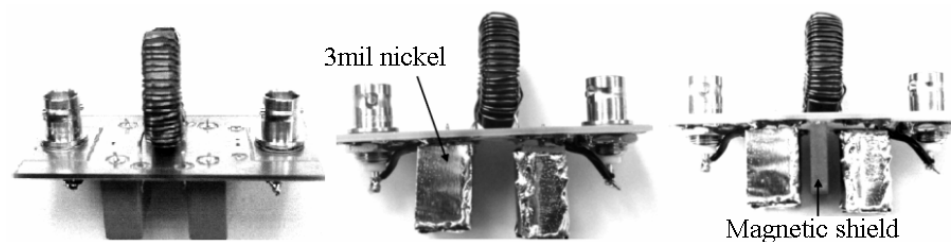


Fig. 2-11. Three cases in the experiment.

As shown in Fig. 2-12, after the capacitors are shielded with 3-mil nickel, there is a 6 dB improvement from 1 MHz to 30 MHz. After a magnetic plate was placed between the two capacitors, the improvement increased by 16 dB. It is obvious that the inductive

coupling between the two capacitor branches has a significant impact on filter performance.

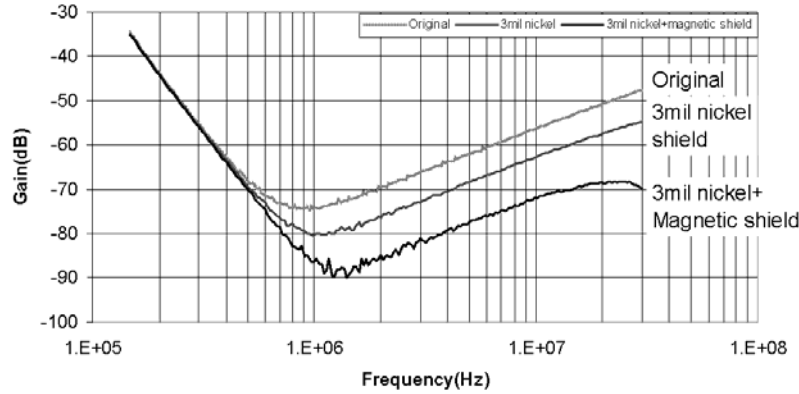


Fig. 2-12. Comparison of insertion voltage gains.

The mutual inductance between the two capacitor branches is extracted using S-parameters, and the measurement is carried out by a HP 4195A network analyzer. The extracted mutual inductance between the two capacitor branches is 0.45 nH. The corresponding coupling coefficient is 3%. That means a 30 dB difference between currents on two capacitor branches would have significant effects.

2.3.3. Capacitive Coupling and the Effects of Ground Plane (M_7 and C_p in Fig. 2-3)

In Fig. 2-13 (a), C_{p1} and C_{p2} are the parasitic capacitance between the in and out traces. They are composed of two parts. One part is the direct capacitive couplings between traces: C_3 in Fig. 2-13 (b). Another part is capacitive couplings through the ground plane: C_1 , C_2 , C_4 and C_5 in Fig. 2-13 (b). For capacitive couplings through the ground plane, each trace has parasitic capacitors with the ground plane; so the parasitic capacitors between in and out traces are effectively in series through the ground plane.

This series capacitance can be larger than that resulting from direct coupling because of the smaller distance between the ground plane and the traces. In Fig. 2-13 (b), the ground plane on the topside of the PCB actually offers a shortcut for the HF noise. The HF noise can reach the output through the parasitic capacitors between the traces and the ground planes instead of coming through the inductor. This effect is modeled by a capacitor C_p in parallel with the inductor. Another effect of the ground plane is that it reduces the inductance of the DM inductor because of the eddy current induced in the ground plane. The flux of the DM inductor would induce the eddy current in the ground plane. On the other hand, the opposite flux generated by the eddy current would cancel part of the flux of the DM inductor. As a result, the net flux is reduced, and the DM inductance is thus decreased.

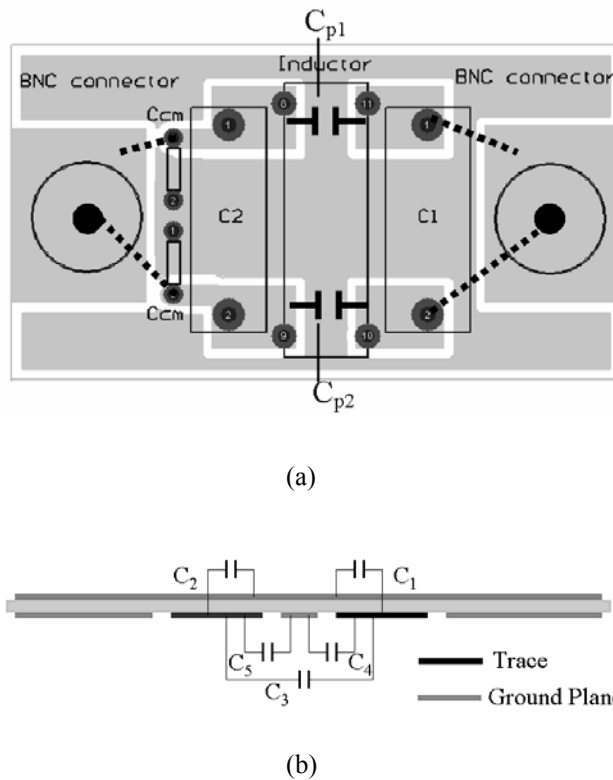


Fig. 2-13. Capacitive couplings between the in and out traces: (a) Equivalent capacitors on the bottom side. (b) Cross section view of the capacitive couplings

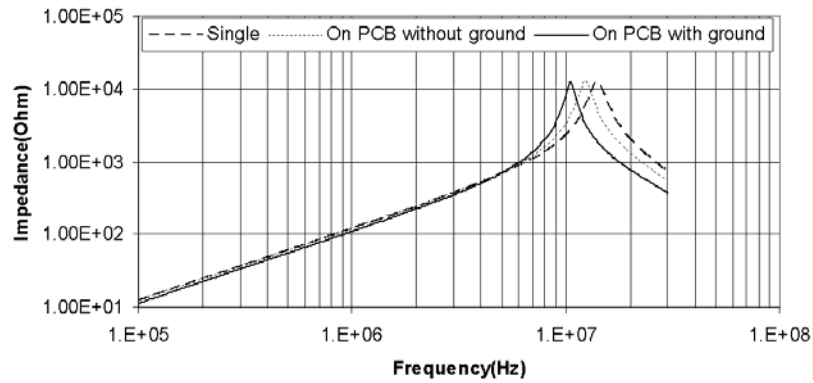


Fig. 2-14. Comparison of the measured inductor impedances.

Experiments are carried out using an Agilent 4294A precision impedance analyzer for an inductor. In the first case, the inductor is measured separately; in the second case the inductor is mounted on a PCB without the ground plane; and in the last case, the inductor is mounted on a PCB with the ground plane. The measured impedances of these three cases are shown in Fig. 2-14. In Fig. 2-14, for the single inductor case, the impedance peak due to the parallel resonance caused by the inductance and the parasitic capacitance of the inductor is at 14.14 MHz. When the inductor is mounted on the PCB without the ground plane, the resonant frequency decreases to 12.4 MHz. It further decreases to 10.5 MHz when the inductor is mounted on the PCB with the ground plane. The equivalent circuit parameters of the inductor can be easily derived from these impedance curves. The results are shown in Table 2-II. From these analysis and experiments, the capacitive coupling between in and out traces is equivalent to a capacitor C_p with a capacitance 5.8 pF paralleled with the inductor. In this 5.8 pF capacitance, 2 pF is attributed to the direct capacitive coupling between in and out traces and 3.8 pF is attributed to the capacitive

coupling through the ground plane. The inductance of the inductor is reduced by $0.81 \mu\text{H}$; so M_7 is $0.81 \mu\text{H}$.

Table 2-II. Extracted inductance and parasitic capacitance

	Single inductor	Mounted on the PCB without the ground plane	Mounted on the PCB with the ground plane
Resonant frequency	14.14 MHz	12.4 MHz	10.5 MHz
Inductance	$18.91 \mu\text{H}$	$18.91 \mu\text{H}$	$18.91 \mu\text{H}$
Parasitic capacitance	6.7 pF	8.7 pF	12.5 pF

2.3.4. Inductive Coupling between In and Out Trace Loops (M_6 in Fig. 2-3)

Due to the large current difference between the in and out trace loops, the inductive coupling M_6 is also considered and extracted using S-parameters. It is around 0.2 nH .

2.3.5. Inductive Coupling between Two Inductors in a Two-stage Filter

A $\Gamma+\Pi$ filter, shown in Fig. 2-15, is investigated last. Because of the high permeability of inductor cores, the inductive coupling between two inductors is significant. The mutual inductance between two inductors is usually much larger than other inductive couplings on the capacitor branch, therefore the C_2 branch in Fig. 2-15 would be significantly affected by this coupling. The winding directions of the two inductors also affect the mutual inductance polarities, as illustrated in Fig. 2-16.

The mutual inductance between two inductors is extracted using S-parameters. It is $1.79 \mu\text{H}$, which is much larger than the ESL (14 nH) of the capacitors and other mutual inductances. Therefore, for C_2 branch, only the effect of the inductive coupling between two inductors is considered. Experiments show this coupling greatly affects the filter performance. The equivalent circuits for C_2 and two inductors are shown in Fig. 2-17.

The resonant frequency of a 0.47 μF capacitor is around 2 MHz. In Fig. 2-17, for the positive coupling case, the resonant frequency of the capacitor branch would be 174 kHz because of the 1.79 μH mutual inductance. For the negative coupling case, from (2-5), the minimum impedance also occurs at around 174 kHz because the mutual inductance is much larger than the ESL. It is obvious that the low frequency performance of the capacitor is strongly affected by this mutual inductance.

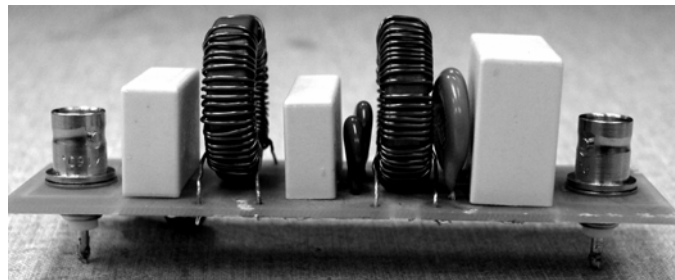
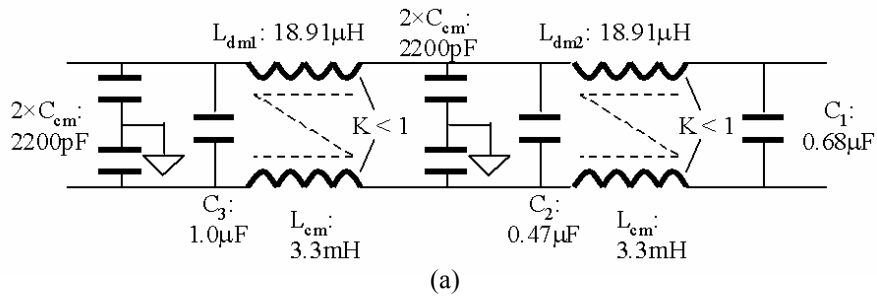


Fig. 2-15. Investigated Γ + Π filter: (a) Circuit of the filter and (b) Prototype of the filter.

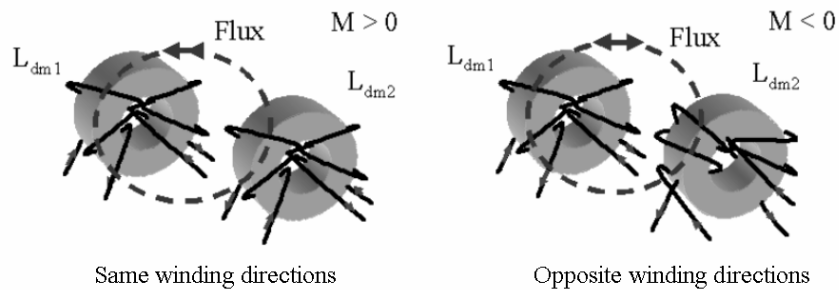


Fig. 2-16. Inductive couplings between two inductors.

Experiments are carried out for three cases. In the first case, the two inductors have the same winding direction. In the second case, the two inductors have different winding directions. In the third case, the two inductors are perpendicular. The measured insertion voltage gains are shown in Fig. 2-18. In Fig. 2-18, for the case of positive coupling, a dip shows up at 174 kHz, which is just as predicted in Fig. 2-17. As a result, it has better performance in the LF range. Negative coupling is better from 330 kHz to 1 MHz, but is almost the same as positive coupling in the HF range. The insertion voltage gain of the perpendicular inductors gives the best performance from 200 kHz to 30 MHz. The noise at the bottom of the curve is the background noise of the analyzer.

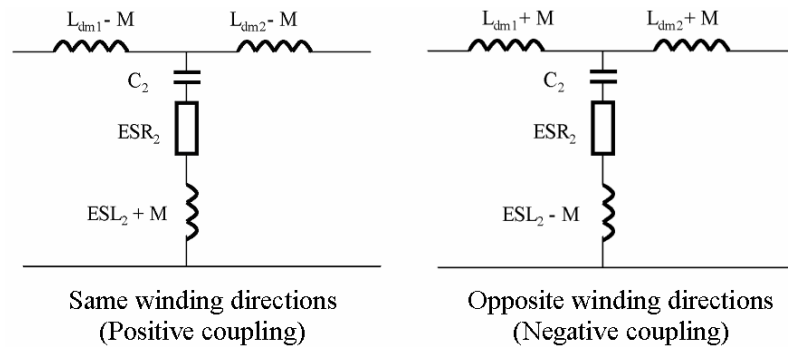


Fig. 2-17. Equivalent circuits for two inductors and C_2 .

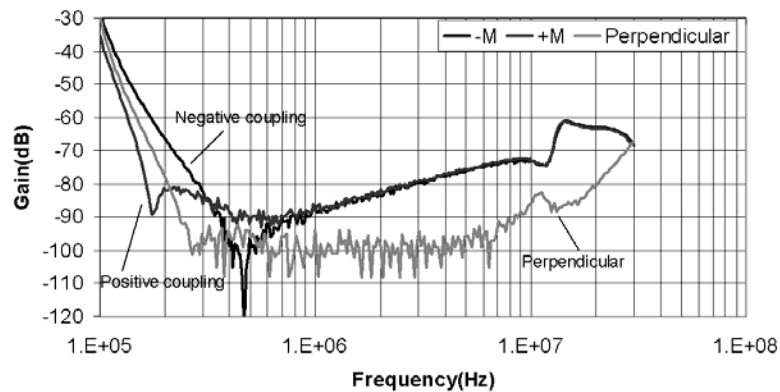


Fig. 2-18. Insertion voltage gain comparison.

2.4. Simulation Verification, Discussion and Recommendations

2.4.1. Simulation Verification on the Extracted Model

Since all the parasitic parameters in Fig. 2-3 are extracted, it is possible to simulate the insertion voltage gain of the whole filter and then compare this with the measurement result. The equivalent circuit used for the positive coupling case is shown in Fig. 2-19. The coupling is defined as positive coupling because the total equivalent inductance caused by the couplings of the inductor on the capacitor branch is positive. Fig. 2-20 illustrates simulation result in terms of both amplitude and phase. Fig. 2-21 shows the measured insertion voltage gain in terms of both amplitude and phase. Figs. 2-20 and 2-21 show that they closely match.

For the negative coupling and proposed winding structures, the simulated insertion voltage gains also match the measured insertion voltage gains very closely. From these comparisons, the parasitic couplings are successfully characterized and extracted.

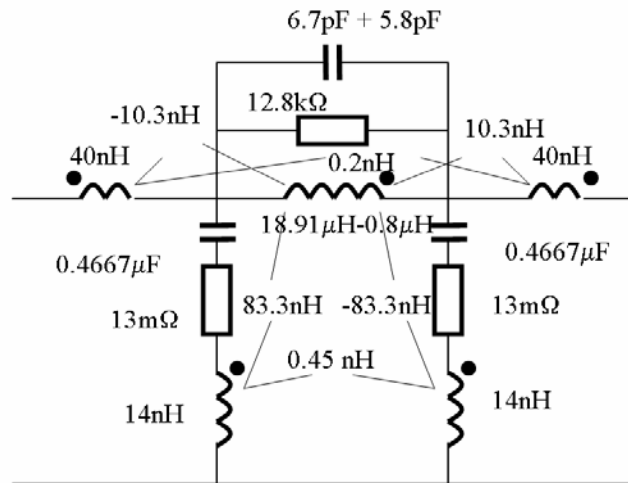


Fig. 2-19. EMI filter model for positive coupling.

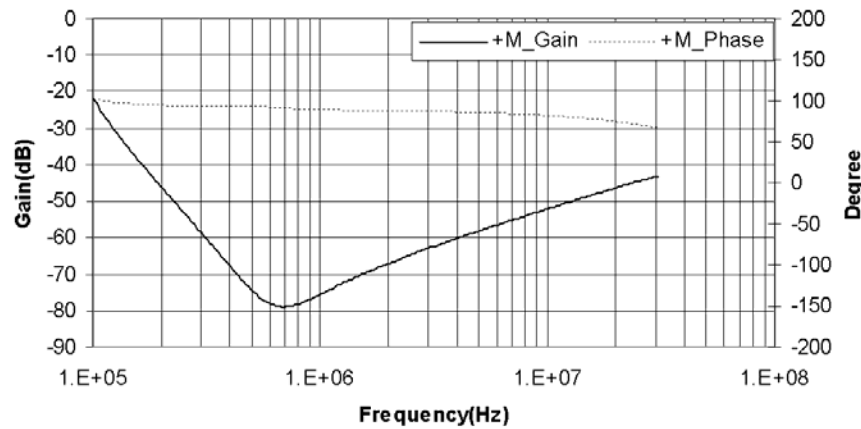


Fig. 2-20. Simulated insertion voltage gain for positive

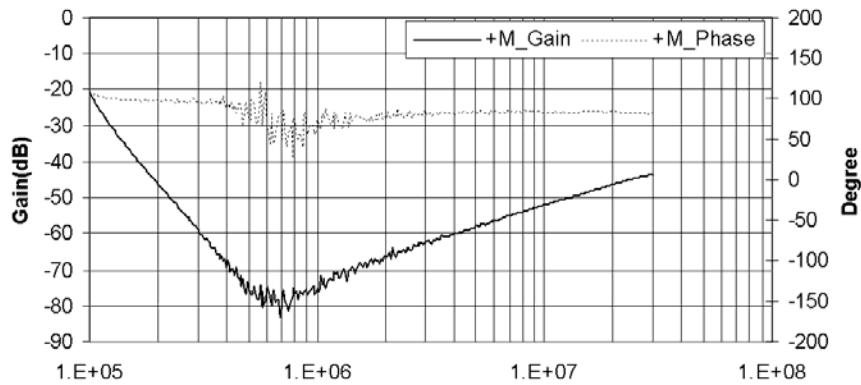


Fig. 2-21. Measured insertion voltage gain for positive

2.4.2. Discussion

From Table 2-I and Fig. 2-9, M_1 , M_2 and M_4 , M_5 are greatly reduced to improve the performance of the EMI filter if the proposed winding arrangement is used. In order to investigate the impact of other couplings on EMI filter performance when M_1 , M_2 and M_4 , M_5 are negligible, an experiment is carried out. In the experiment, the inductor is disconnected from the filter (but still kept on the PCB because the inductor affects the inductive couplings in the filter) and then the insertion voltage gain is measured. The

equivalent circuit for the measurement setup is shown in Fig. 2-22. It is obvious that the measured insertion voltage gain is determined by M_3 , M_6 and C_p because the inductor is not connected to the filter. In Fig. 2-23, the insertion voltage gain of the whole filter when the proposed winding arrangement is used is compared with this measured insertion voltage gain.

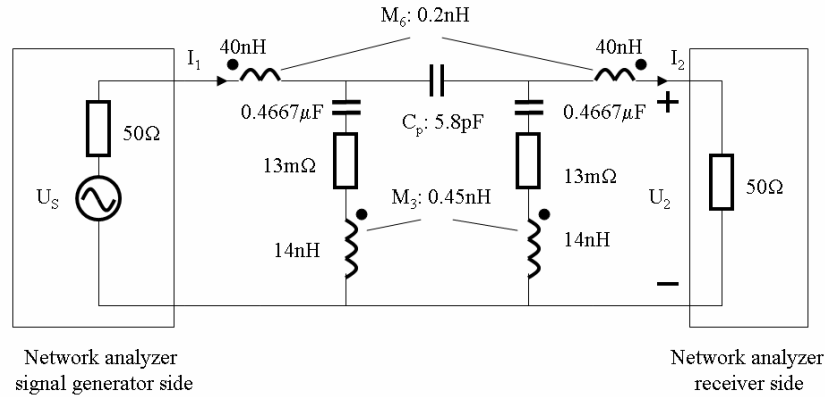


Fig. 2-22. Equivalent circuit when the inductor is disconnected.

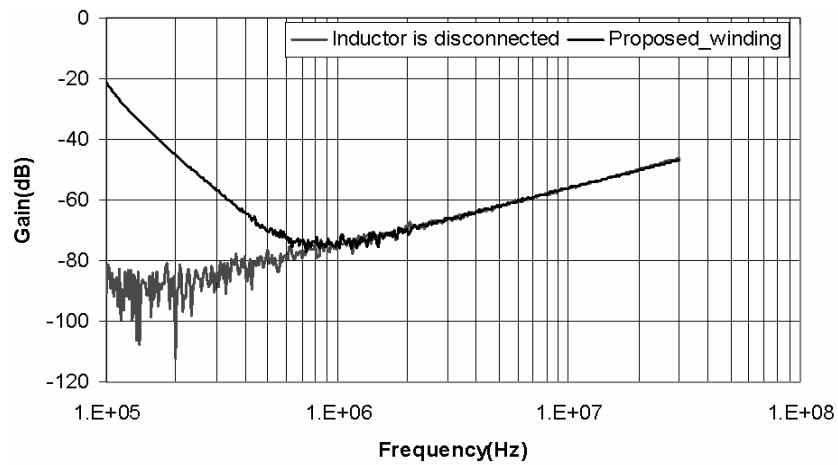
Fig. 2-23 shows that two insertion-voltage-gain curves are almost the same above 1MHz both in gain and phase. It indicates that noise does not come through the inductor in HF range. This measurement also indicates the effects of C_p (the capacitive coupling) are insignificant due to the small impedances of filter capacitors, which leads to a $+90^\circ$ phase.

In Fig. 2-22, I_1 is given as:

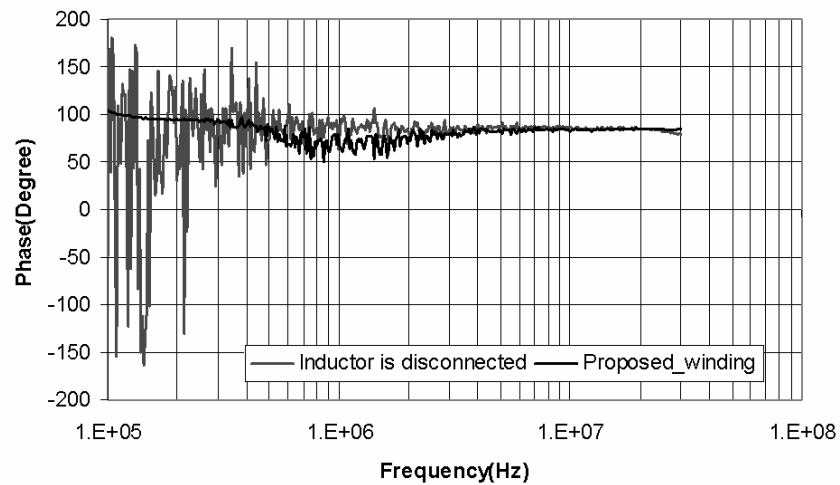
$$\dot{I}_1 \approx \frac{\dot{U}_s}{50} \quad (2-10)$$

The measured insertion voltage gain T_G in Fig. 2-22 is then described as below:

$$T_G = \frac{2\dot{U}_2}{\dot{U}_s} \approx \frac{j\omega}{25}(M_3 + M_6) \quad (2-11)$$



(a)



(b)

Fig. 2-23. Insertion voltage-gain comparison: (a) Insertion voltage gain and (b) Phase.

(The noise below 500 kHz in both diagrams is the background noise of the network)

(2-11) means because the effects of M_1 , M_2 and M_4 , M_5 are negligible, for this EMI filter the HF performance is determined by

M_3 and M_6 only. If M_3 is larger than M_6 , it would be the one dominates the insertion voltage gain in HF range. That is what Fig. 2-12 shows.

2.4.3 Measures Used to Improve Filter Performance

Based on the preceding analysis and experiments, M_1 , M_2 and M_3 are the couplings with the capacitors, so the capacitors are the components critical to the achievement of high performance. Steps can be taken to reduce these couplings.

- (1) Two capacitors should be kept far enough away to reduce the inductive coupling between them.
- (2) The capacitors and inductor should also be kept far enough away to reduce the inductive coupling between them.
- (3) The proposed winding arrangement can be used for the inductor to reduce the inductive coupling with capacitors.
- (4) Two capacitors can be shielded.
- (5) The pin of the capacitor should be kept as short as possible to reduce inductive couplings.
- (6) For a two-stage filter, two inductors can be placed in perpendicular fashion to reduce the related inductive coupling.
- (7) Purposely selecting the appropriate winding directions to get either positive or negative mutual inductance.

M_4 , M_5 and M_6 are the couplings with the in and out trace loops, so the trace loops are also important components. Steps can be taken to reduce these couplings.

- (1) The proposed winding arrangement can be used for the inductor to reduce the inductive coupling with trace loops.
- (2) The areas of in and out trace loops should be kept small to reduce the M_4 , M_5 and M_6 .

M_7 and C_p result from the ground plane. Some steps can be taken to reduce them.

- (1) Do not use a ground plane under the inductor to reduce M_7 .
- (2) Keep enough clear distance between the ground plane and traces, in and out traces to reduce the direct capacitive couplings and those through the ground plane.

2.5. Summary

In this chapter, six important inductive and capacitive couplings existing in the EMI filters are identified and quantified by both the experiments and the simulations. The theories on the parasitic couplings were developed and many measures are advised to reduce these couplings. It is found that the capacitors, the trace loops and the ground plane are critical to the achievement of high performance. The performance of a capacitor in an EMI filter is determined by the inductive couplings with other capacitors and inductors. The inductive couplings with the in and out trace loops also play an important role on the filter performance. The ground plane can reduce the inductance of inductors due to the eddy current and it also offers an easy path for the capacitive couplings between the in and out traces. For a two-stage filter, the inductive coupling between two inductors strongly affects the performance of the filter in the whole frequency range.

References

- [4] Shuo Wang, F.C.Lee and W.G.Odendaal, "Improving the Performance of Boost PFC EMI Filters," in *Proc. IEEE Applied Power Electronics Conference and Exposition*, 2003. (APEC '03). Eighteenth Annual, Volume 1, pp. 368 -374.

- [5] Mark J. Nave, *Power line filter design for switched-mode power supply*, Van Nostrand Reinhold, New York, 1991.
- [6] Henry W. Ott, *Noise Reduction Techniques in Electronic Systems*, Second edition, John Wiley & Sons, Inc, 1988.
- [7] Shuo Wang, F.C.Lee, D.Y.Chen and W.G.Odendaal, "Effects of Parasitic Parameters on EMI Filter Performance," in *Proc. CPES Seminar 2003*.
- [8] Liu, D.H. and Jiang, J.G., "High frequency characteristic analysis of emi filter in switch mode power supply (smpls)," in *Proc. IEEE Power Electronics Specialists Conference, 2002. (PESC'02)*. IEEE 33rd Annual , Volume 4 , pp. 2039 –2043.
- [9] Ozenbaugh, Richard Lee, *EMI filter design*, Marcel Dekker Inc. 1996.
- [10] Norman Balabanian and Theodore Bickart, *Linear Network Theory: Analysis, Properties, Design and Synthesis*, 1981, Matrix Publishers, Inc.
- [11] "Agilent AN154 S-Parameters Design Application Note," Agilent Technologies. 2000.
- [12] Richard Anderson, "Test and Measurement Application Note 95-1 S-Parameters Techniques," Hewlett-Packard, 1997.

CHAPTER 3: CHARACTERIZATION AND EXTRACTION OF PARASITIC PARAMETERS USING SCATTERING PARAMETERS*

3.1. Introduction

Electromagnetic interference (EMI) filters are widely used in power electronics area. Traditionally, electromagnetic interference (EMI) filters are characterized by the insertion loss that occurs when both source and load impedances are $50\ \Omega$. However, in a practical filter implementation, source and load cannot both be $50\ \Omega$; this makes it difficult to base EMI filter selection on the curves provided by manufacturers. In order to efficiently predict their performance, EMI filters should be characterized by independent network parameters.

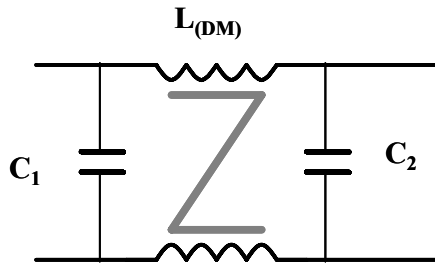


Fig. 3-1. The investigated one-stage DM EMI filter.

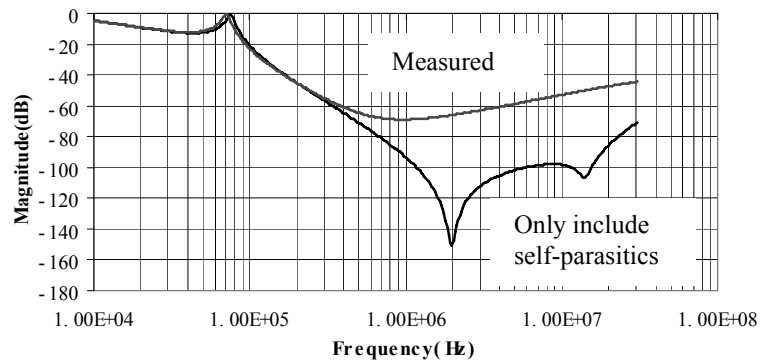


Fig. 3-2. Comparison of insertion voltage gains when both source and load are $50\ \Omega$.

* © 2005 IEEE. Reprinted, with permission, from *IEEE Transactions on Power Electronics*, Volume 20 Issue 2 March 2005 pp 502 – 510

On the other hand, an efficient network parameter is needed to extract the parasitics in EMI filters. It is shown that electromagnetic couplings among filter components and circuits layouts play very important roles in the HF performance of EMI filters [9]. Although EMI filter performance is also affected by the parasitic parameters of the components, including the equivalent series inductor (ESL) of the capacitors and the equivalent parallel capacitor (EPC) of the inductors, for many cases, especially at HF range, these factors may be less important than the couplings among components and layouts. A typical differential-mode (DM) EMI filter used for power converters is shown in Fig. 3-1, where DM inductance L is the leakage inductance of the coupled common-mode (CM) inductor. In Fig. 3-2 two insertion voltage gain curves of this filter are compared. One is the simulated curve using the model including only the component parasitic parameters [10]; and the other is the measured curve. Obviously, the measured one is much worse than the simulated one. Therefore it is necessary to carry out a detailed study of the parasitic couplings. The effects of parasitic couplings on EMI filter performance are discussed in detail in another paper [9]. Fig. 3-3 shows a model that includes all these couplings: basically, they can be divided into five categories as follows:

- 1) Coupling between inductor and capacitors: M_1 and M_2 .
- 2) Coupling between two capacitors: M_3 .
- 3) Coupling between inductor and trace loops: M_4 and M_5 .
- 4) Coupling between ground plane and inductor: M_7 and C_p .
- 5) Coupling between trace loops: M_6 .

Air is the medium for all these parasitic couplings. M_1 , M_2 , M_4 , M_5 and M_7 are much smaller than the inductance L of the inductor, so the effects of these couplings on the inductance L are negligible. The effects of parasitic couplings on the capacitors are superposed because the media of these couplings are linear. For these two reasons, these parasitic parameters can be considered independent from each other, so it is possible to extract them separately. These parasitic parameters are difficult to extract using conventional methods. It is impractical to calculate them using electromagnetic software because of the complicated structures of capacitors and inductors. It is also impossible to directly measure them using an impedance analyzer because they are mutual couplings between two components. However, these parasitic parameters can be calculated from measured network parameters based on the network theory, as will be shown in this chapter.

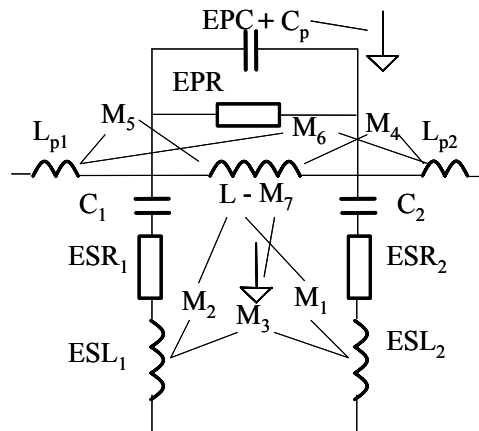


Fig. 3-3. Parasitic couplings in an EMI filter.

Scattering parameters (S-parameters) are chosen to characterize EMI filters and to extract mutual couplings because of two reasons. First, in the HF range, they are easier to accurately measure than it is to do so for the $[Z]$, $[Y]$, $[H]$ and $[ABCD]$ parameters. The

measurement of $[Z]$, $[Y]$, $[H]$ and $[ABCD]$ parameters requires either a short circuit or an open circuit at one port, which is difficult to achieve in the HF range because of parasitic parameters [1, 2, 8]; for S-parameters, no short or open circuits are needed for measurement. Second, interconnect parasitics make measurements inaccurate at high frequencies. The S-parameter method can be calibrated to the exact points of measurement, thus excluding the effects of parasitics that occur due to measurement interconnects.

3.2. Using S-parameters to Characterize EMI filters

3.2.1 Characterization of EMI Filters Using S-parameters

Strictly speaking, an EMI filter is not a linear network because it contains nonlinear components such as inductors; however, it is approximately linear for a small-signal excitation. So it is reasonable to characterize an EMI filter as a linear, passive, two-port network under small-signal excitation conditions. The nonlinear characteristics can be modeled with the current biases superposed by a small-signal excitation. The test setup for an EMI filter is shown in Fig. 3-4, where the EMI filter is characterized in terms of waves. There are four waves in Fig. 3-4, namely, incident wave a_1 and reflected wave b_1 at port1, and incident wave a_2 and reflected wave b_2 at port2. From these four variables, the voltage¹ V_1 and current I_1 at port1 and the voltage V_2 and current I_2 at port2 are found by (3-1) – (3-4) [2], where Z_0 is the reference impedance, which is usually real 50 Ω .

¹ All currents and voltages are RMS values.

$$V_1 = \sqrt{Z_0}(a_1 + b_1); \quad (3-1)$$

$$V_2 = \sqrt{Z_0}(a_2 + b_2); \quad (3-2)$$

$$I_1 = \frac{I}{\sqrt{Z_0}}(a_1 - b_1); \text{ and} \quad (3-3)$$

$$I_2 = \frac{I}{\sqrt{Z_0}}(a_2 - b_2), \quad (3-4)$$

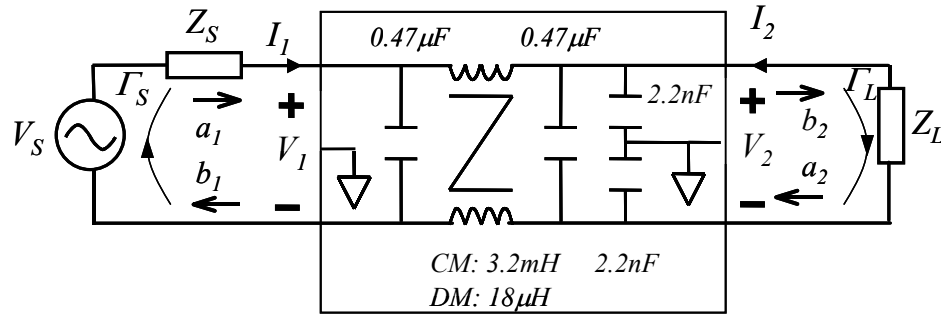


Fig. 3-4. EMI filters are treated as linear, passive, two-port networks under small-signal excitation conditions.

V_S : Voltage source

Z_S : Source impedance

Z_L : Load

a_1, a_2 : Normalized incident wave on source side and load side, respectively

b_1, b_2 : Normalized reflected wave on source side and load side, respectively

I_1, I_2 : Input current of port1 and port2, respectively

V_1, V_2 : Voltage of port1 and port2, respectively

To fully characterize a linear, passive, two-port network, two linear equations are required among the four wave variables [5]. The four S-parameters in (3-5) are therefore introduced to correlate with a_1, a_2, b_1 and b_2 [8]. S_{11} and S_{22} are called reflection coefficients. S_{12} and S_{21} are called transmission coefficients. When reflected wave b_1 or b_2 reaches the source or load side, it would be reflected because of the mismatched

impedances. The reflection coefficients, Γ_S at the source side and Γ_L at the load side, are given by (3-6, 3-7).

$$\begin{pmatrix} b_1 \\ b_2 \end{pmatrix} = \begin{pmatrix} S_{11} & S_{12} \\ S_{21} & S_{22} \end{pmatrix} \begin{pmatrix} a_1 \\ a_2 \end{pmatrix} \quad (3-5)$$

$$\Gamma_S = \frac{Z_S - Z_0}{Z_S + Z_0}, \text{ and} \quad (3-6)$$

$$\Gamma_L = \frac{Z_L - Z_0}{Z_L + Z_0}. \quad (3-7)$$

From (3-1 – 3-7), the insertion voltage gain (the reciprocal of insertion loss) of EMI filters with arbitrary levels of source and load impedances can be found by (3-8) [11].

$$A_V = \frac{S_{21}(1 - \Gamma_L \Gamma_S)}{(1 - S_{11} \Gamma_S)(1 - S_{22} \Gamma_L) - S_{21} \Gamma_L S_{12} \Gamma_S}. \quad (3-8)$$

Note that the insertion voltage gain is defined as the ratio of the port voltage at the load side without the filter to that with the filter [1], which is different from the input-to-output voltage gain. From (3-8), as long as the S-parameters of an EMI filter are measured, the insertion voltage gain (or insertion loss) for an arbitrary Z_S and Z_L can be found. Term Z_S can be found using a method described in another work [7]. It is obvious that the source and load impedances affect the insertion voltage gain through reflection coefficients Γ_S and Γ_L .

3.2.2 Experiments

Two experiments are carried out for the EMI filter in Fig. 3-4. In the first experiment, in order to investigate the effects of noise source impedance on EMI filter performance,

an inductor shown as in Fig. 3-5 is used as the DM noise source. The load is $100\ \Omega$. The predicted insertion voltage gain, the measured insertion voltage gain, and the measured 50Ω -based transfer gain (reciprocal of 50Ω -based insertion loss) of the DM filter part are all shown in Fig. 3-6. The prediction very closely matches the measurement. It is obvious that the transfer-gain curve from a 50Ω -based measurement system is quite different from the practical insertion voltage gain. So the transfer-gain curve (50Ω -based insertion loss) does not offer accurate information on filter performance. The small peak of the insertion voltage gains between 10 MHz and 20 MHz is caused by the corresponding valley of the source impedance shown in Fig. 3-5.

In the second experiment, in order to investigate the effects of CM current on the EMI filter performance, the CM, DC current bias is injected through a one-turn auxiliary winding on the CM inductor, as shown in Fig. 3-7. If the turn ratio of CM windings to the auxiliary winding is n , the equivalent CM current bias is i_{DC} / n . Because of the high turn ratio and the high impedance Z_L , the effects of the DC current loop is ignored. Both DM and CM filter parts are measured in the experiments. For the CM filter part, the final measurement results show that the S-parameters changed significantly when the equivalent CM current bias is increased from 0 A to 0.2 A. This is due to the saturation of the CM inductor. On the other hand, this experiment shows CM current bias has no significant effect on DM filter performance because the core of the DM inductor is air. Fig. 3-8 shows the predicted CM filter performance with 100pF source impedance and 25Ω load. In the HF range, saturation of the core has no effect on the insertion voltage gain because the HF noise comes through parasitic paths instead of the inductor path. The

peak on the curve of 0.2 A between 100 kHz and 200 kHz could not be estimated just from the 50Ω -based transfer-gain curve. In a practical EMI filter design, measures should be taken to prevent the saturation of the CM inductors. For example, the CM capacitors between the CM inductor and the converter should be sufficiently large that they can bypass enough CM current so as to prevent a large level of CM current from saturating the CM inductor.

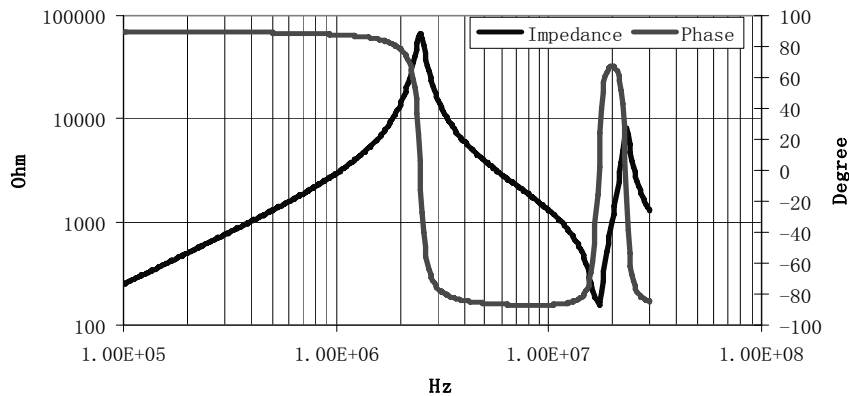


Fig. 3-5. The impedance of the inductor used as DM source.

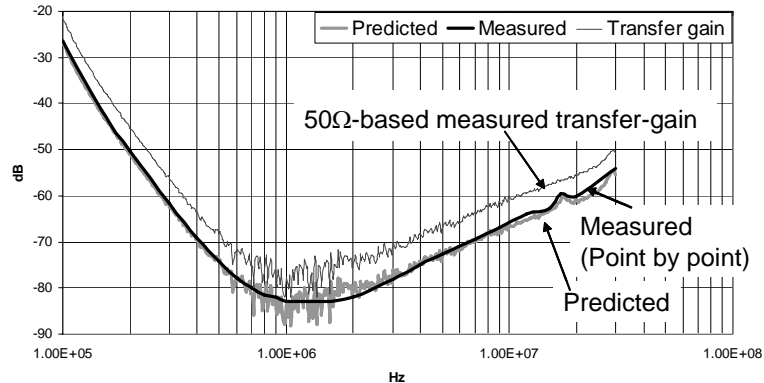


Fig. 3-6. Comparison of the predicted insertion voltage gain, the measured insertion voltage gain, and the measured 50Ω -based transfer gain.

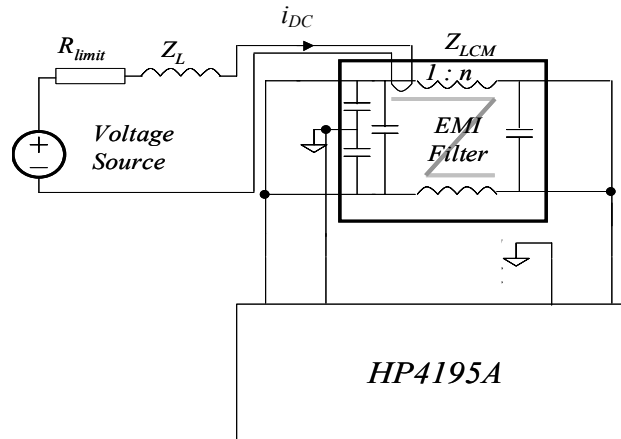
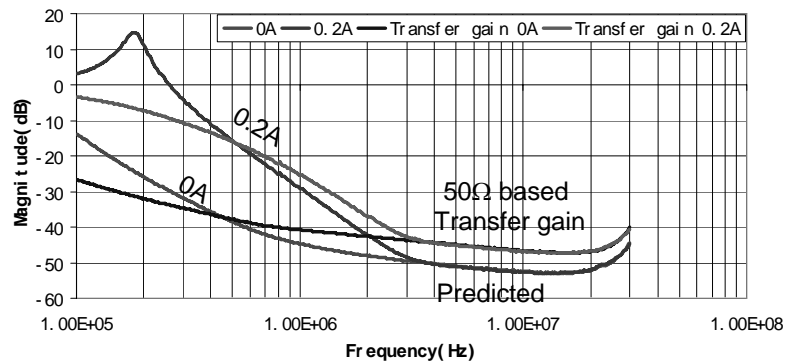


Fig. 3-7. S-parameter measurement setup for the CM filter part.

Fig. 3-8. Predicted insertion voltage gains for the CM filter part ($Z_S=100\text{pF}$, $Z_L=25\Omega$).

3.3. Using S-parameters to Extract Parasitic Parameters

3.3.1 Network Theory

In Fig. 3-3, the mutual inductances exist between two components, so it is impossible to measure them separately. Measurement can be carried out for the network that includes two components, and then the mutual inductance can be derived from the measured data. As an example, mutual inductance M_2 , which is shown in Fig. 3-9, can be calculated from the impedance of the capacitor branch.

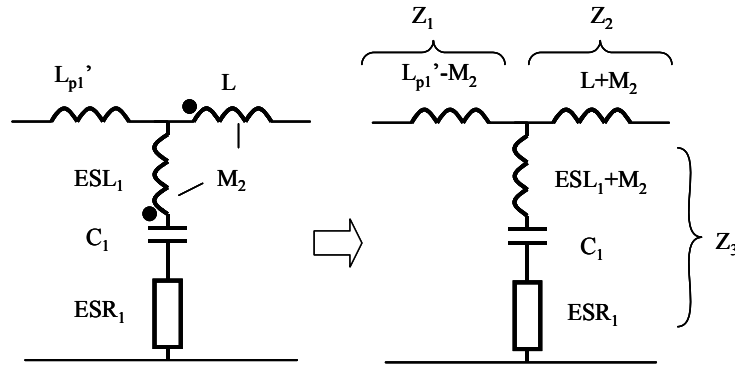


Fig. 3-9. Calculation of M_2 through the impedance of the capacitor branch.

In Fig. 3-9, the parasitic parameters of the inductor are ignored because they are insignificant in the low-frequency range. For the mutual coupling between the inductor and the capacitor, the decoupled model is shown on the right. The inductance of the capacitor branch is changed by M_2 . M_2 can therefore be calculated from the difference between the impedances of the capacitor branch with and without coupling. S-parameters are first calibrated and measured from port1 and port2, and then the impedance of the capacitor branch is calculated from measured S-parameters, and finally M_2 can be found.

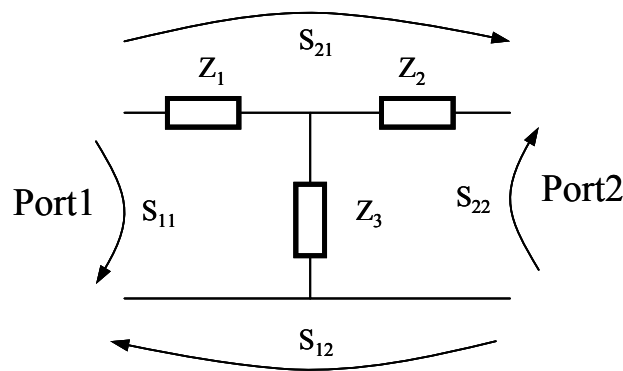


Fig. 3-10. S-parameters of a Tee network.

The decoupled model in Fig. 3-9 is in fact a Tee network as shown in Fig. 3-10. Based on the relationship between impedances and S-parameters, three impedances in the Tee network can be calculated from the measured S-parameters:

$$Z_1 = \frac{Z_0 \left(I - S_{22} - S_{22}S_{11} + S_{11} - 2S_{21} + S_{21}^2 \right)}{\left(I - S_{22} + S_{22}S_{11} - S_{11} - S_{21}^2 \right)}, \quad (3-9)$$

$$Z_2 = \frac{Z_0 \left(I + S_{22} - S_{22}S_{11} - S_{11} - 2S_{21} + S_{21}^2 \right)}{\left(I - S_{22} + S_{22}S_{11} - S_{11} - S_{21}^2 \right)}, \text{ and} \quad (3-10)$$

$$Z_3 = \frac{2Z_0 S_{21}}{\left(I - S_{22} + S_{22}S_{11} - S_{11} - S_{21}^2 \right)}. \quad (3-11)$$

From (3-11), as long as the S-parameters are measured, impedance Z_3 of the capacitor branch can be calculated, and then M_2 can be found. Most of parasitic parameters in the EMI filter can be calculated using this proposed method.

3.3.2 Extraction of Parasitic Parameters for a One-stage EMI Filter

The printed circuit board (PCB) layout of the one-stage DM filter in Fig. 3-1 is shown in Fig. 3-11. In experiments, HP 4195A is used to measure S-parameters. HP 4195A is designed for single-ended measurement; however, the DM EMI filter in Fig. 3-1 is a balanced structure. In order to solve this problem, two inductor windings are reconnected in series on one side of the filter, and the other side of the filter is grounded, which makes the filter a single-ended structure, as shown in Fig. 3-12. Because the inductor current, winding structure and inductor position on the PCB are kept the same, the extracted couplings of the filter will be the same as those of the balanced structure. The frequency is swept from 150 kHz to 30 MHz.

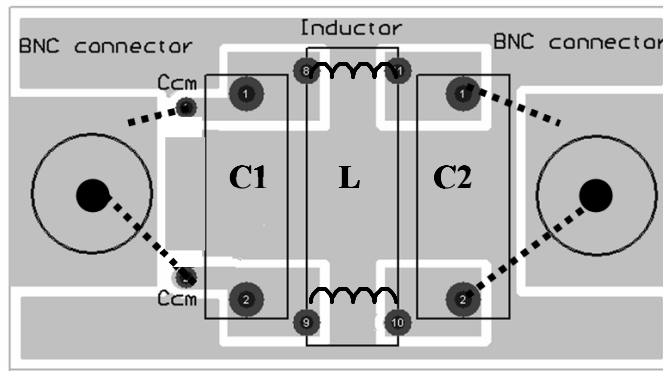


Fig. 3-11. PCB layout of the investigated one-stage DM EMI filter.

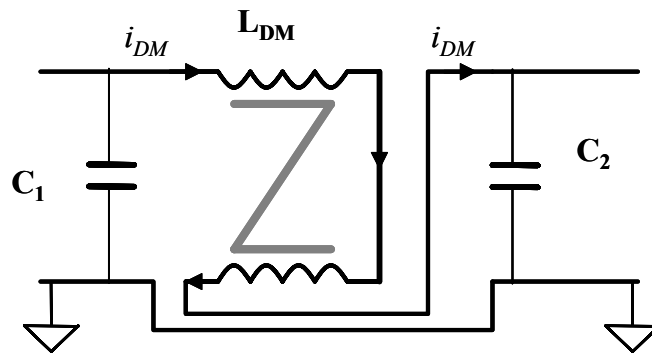


Fig. 3-12. DM EMI filter is connected to a single-ended structure.

3.3.2.1 Extraction of M_1 , M_2 , M_4 and M_5 in Fig. 3-3

In order to extract M_1 or M_2 separately, other couplings should be kept as small as possible. In the measurement, only a capacitor and the inductor are kept on the PCB, so the couplings caused by other components are excluded. In and out trace loops of the filter are kept very small so that the couplings between trace loops and other components will be negligible. In Fig. 3-9, L_{p1}' and L_{p2}' are the inductances of the modified trace loops. Because mutual inductance is to be derived from the impedance of the capacitor branch, it is necessary first to investigate the effects of these couplings on the impedance of the capacitor branch.

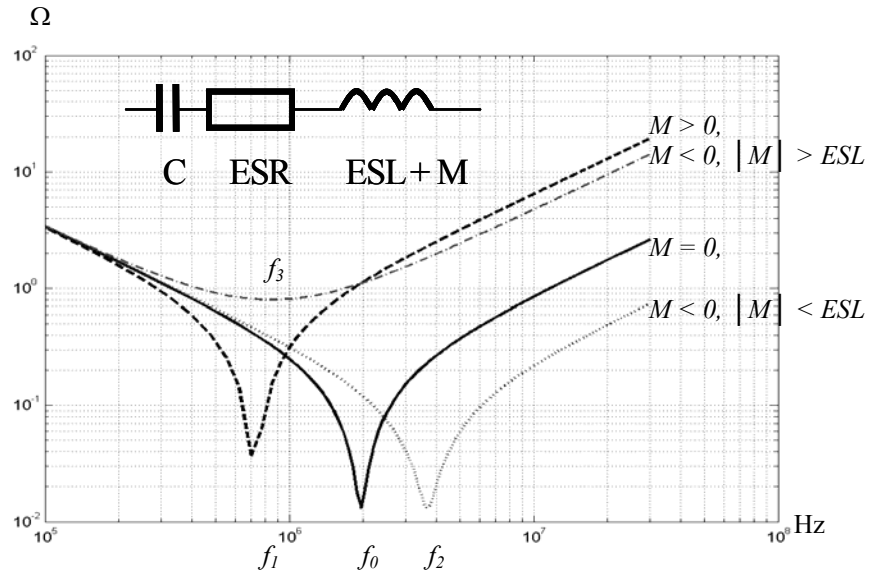


Fig. 3-13. Calculated impedances for a capacitor branch with different mutual inductances.

A general case for the capacitor branch is shown in Fig. 3-13, where mutual inductance M is added to the ESL of a capacitor. Depending on the winding directions of the inductor, M can be positive or negative [9]. f_0 is the self-resonant frequency of the capacitor; f_1 is the series resonant frequency when $M > 0$; f_2 is the series resonant frequency when $M < 0$ and $|M| < ESL$; f_3 is the minimum-impedance frequency of the capacitor branch when $M < 0$ and $|M| > ESL$; f_3 is different from the resonant frequencies because no phase polarity change occurs [9]; f_1 , f_2 and f_3 are given by (3-12 – 3-14), as follows:

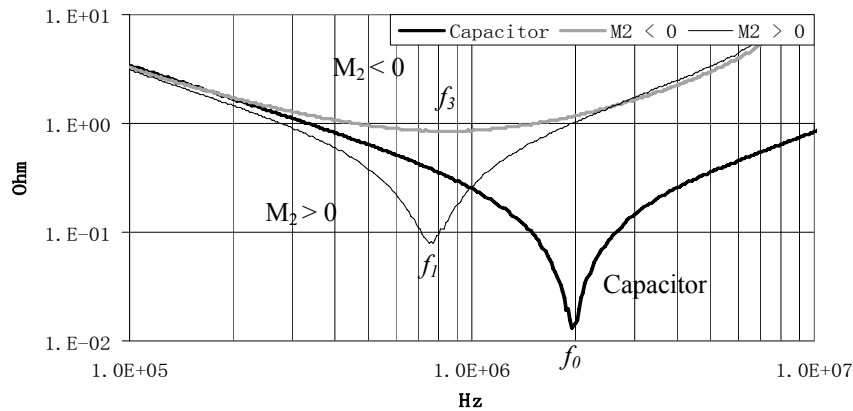
$$f_1 = \frac{1}{2\pi\sqrt{(ESL + M)C}}, \quad (3-12)$$

$$f_2 = \frac{1}{2\pi\sqrt{(ESL - M)C}}, \text{ and} \quad (3-13)$$

$$(3-14)$$

$$f_3 = \frac{1}{2\pi\sqrt{(M - ESL)C}}.$$

In the circuit shown in Fig. 3-9, in order to find M_2 , the S-parameters of the network including one capacitor and the inductor are measured, and then the impedances of the capacitor branch are derived through (3-11). The calculated impedance is shown in Fig. 3-14, where one curve is the capacitor impedance, another curve is the impedance curve when M_2 is positive (inductor winding direction1), and the last one is the impedance curve when M_2 is negative (inductor winding direction2). The self-resonant frequency f_0 of the capacitor is 1.97 MHz. From Fig. 3-14, when M_2 is positive the resonant frequency f_1 decreases to 747 kHz. When M_2 is negative, the frequency f_3 of the minimum impedance is 850 kHz. Because the capacitance is 0.4667 μF and the ESL is 14 nH, the mutual inductances are calculated using (3-12 – 3-14). For the case of $M_2 > 0$, (3-12) is used for the calculation. M_2 is found to be 83.3 nH. For f_3 , since no phase polarity change occurs, based on (3-14), the M_2 is -89.3 nH. Because of the symmetrical PCB layout, M_1 is equal to M_2 .



(a)

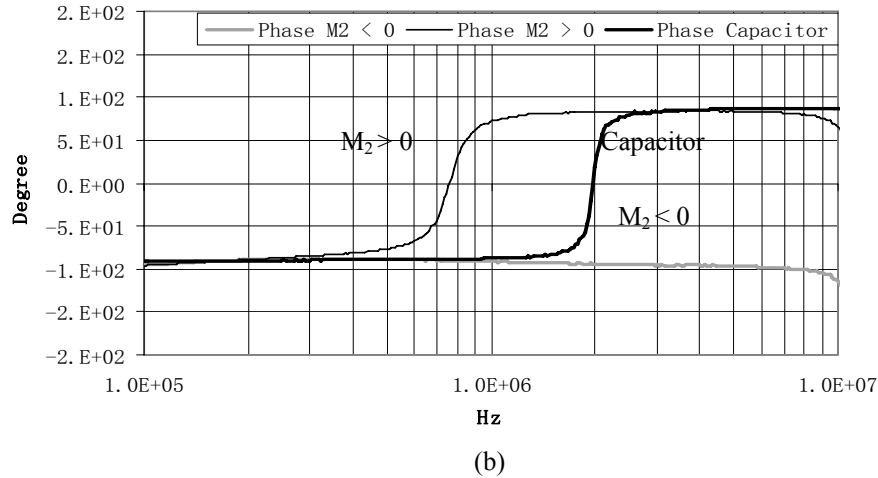


Fig. 3-14. Derived impedances for the C_1 branch from the measured S-parameters:

(a) magnitude, and (b) phase.

In order to determine M_4 and M_5 , the related in or out trace loop is changed back to their original statuses. The equivalent circuit for M_5 and M_2 is shown in Fig. 3-15. In Fig.3-15, M_2 is already known. Depending on the winding directions of the inductor, M_5 can be positive or negative. In Fig. 3-16, the derived impedance curves are compared with the previous case shown in Fig. 3-14. M_5 is then calculated using (3-12 – 3-14). In Fig.3-16, when M_2 is negative, the frequency of the minimum impedance increases from 850 kHz to 980 kHz, which means M_5 is +18.7 nH. When M_2 is positive, the resonant frequency increases from 747 kHz to 790 kHz, which means M_5 is -10.3 nH. M_4 is equal to M_5 .

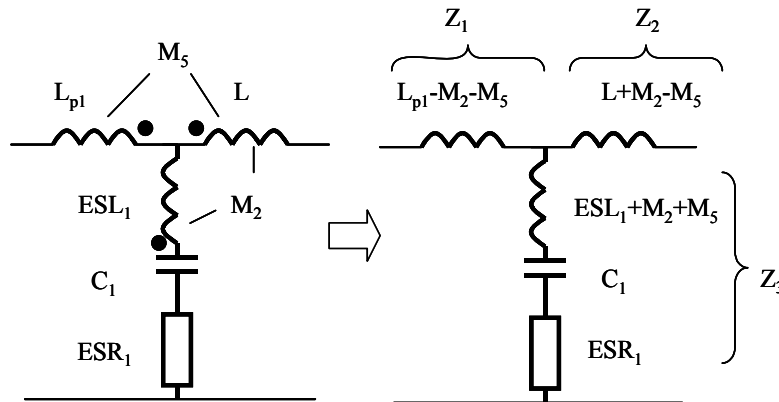


Fig. 3-15. Calculation of M_5 through the impedance of the capacitor branch.

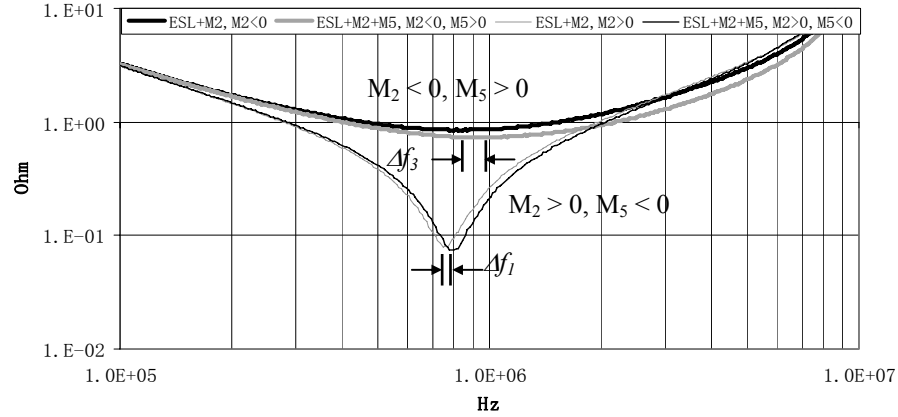


Fig. 3-16. Derived impedances of the C_1 branch from measured S-parameters.

3.3.2.2 Extraction of M_3 and M_6 in Fig. 3-3

In Fig. 3-3, in order to extract the mutual inductance M_3 between two capacitors, the inductor is disconnected from the filter, but still remains on the PCB because it affects the inductive couplings in the filter. The in and out trace loops are kept very small, so the inductive coupling M_6 between them is very small and its effect is ignored. The effect of C_p is also ignored because of the small impedances of the two capacitors. The circuit is then simplified as shown in Fig. 3-17. In Fig. 3-17, L_{p1}' and L_{p2}' are the inductances of the modified trace loops. The circuit is decoupled into a Tee network. The mutual inductance is transformed to the shunt branch, which corresponds to Z_3 in Fig. 3-10. M_3 is then determined from Z_3 . Fig. 3-18 shows the Z_3 derived from measured S-parameters. The noise before 500 kHz is the noise floor of the network analyzer. The mutual inductance is finally calculated from Fig. 3-18 as 0.45 nH. After changing the in and out trace loops back to their original statuses, M_6 can also be derived. Fig. 3-19 shows the equivalent circuit, and Fig. 3-20 shows the derived impedance. From Fig. 3-20, M_6 is 0.2 nH.

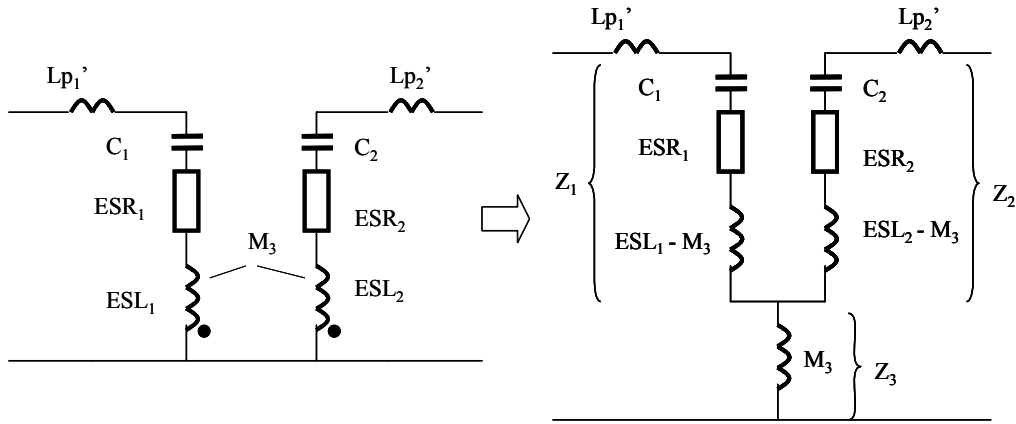


Fig. 3-17. Equivalent circuit for the inductive coupling between two capacitors.

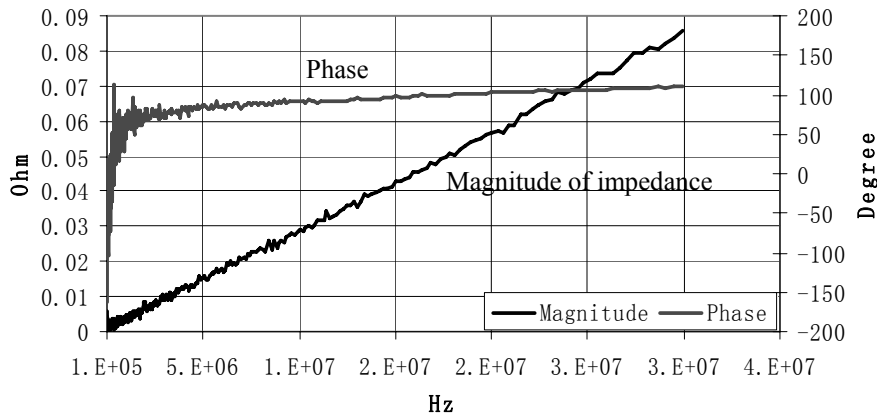


Fig. 3-18. Impedance of the Z_3 branch, derived from measured S-parameters.

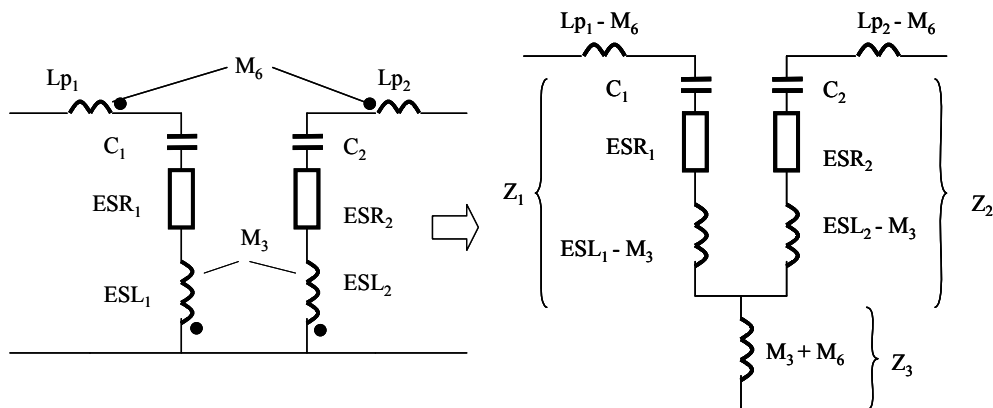


Fig. 3-19. Equivalent circuit for the inductive couplings between two capacitors and between trace loops.

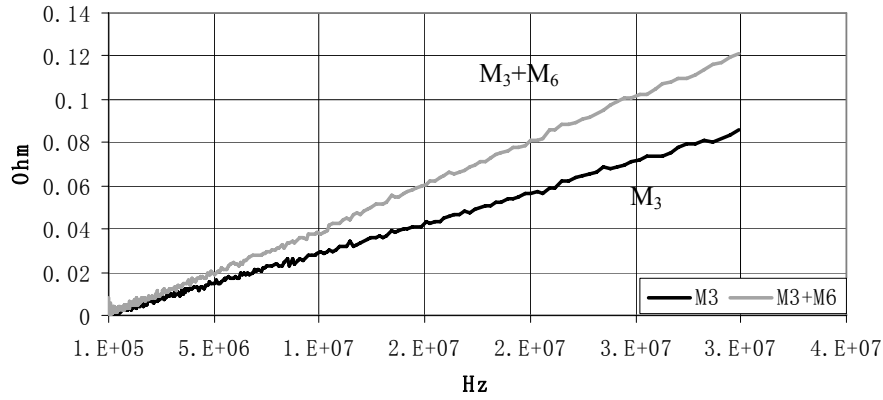


Fig. 3-20. Derived impedances of the Z_3 branch.

3.3.2.3 Extraction of M_7 and C_p in Fig. 3-3

M_7 and C_p can be derived by comparing the parallel resonant frequencies of inductor impedance with the derived impedance of the inductor branch. By leaving only the inductor on the PCB and measuring the S-parameters of the circuit, the impedance of the inductor branch can be found as follows:

$$Z_L = 2Z_0 \left(\frac{1}{S_{21}} - 1 \right). \tag{3-15}$$

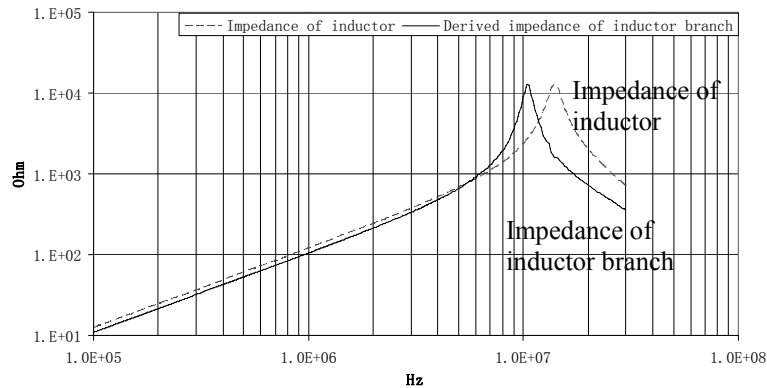


Fig. 3-21. Impedances of the inductor and the inductor branch.

The inductor impedance and the derived impedance of the inductor branch are shown in Fig. 3-21. From the impedance curves illustrated in Fig. 3-21, the resonant frequency of the inductor is 14.14 MHz, while the resonant frequency of the inductor branch is 10.5 MHz. From the impedances before 6 MHz, it is obvious that the inductance decreased from 18.91 μH to 18.1 μH . Therefore, M_7 is 0.8 μH , and C_p is found to be 5.8 pF.

3.3.3 Extraction of Parasitic Parameters for a Two-stage EMI Filter

Since two-stage EMI filters are widely used in power electronics area, it is necessary to investigate them. Fig. 3-22 shows a two-stage DM EMI filter, and its PCB layout is shown in Fig. 3-23. For this two-stage DM EMI filter, the in and out trace loops are very small, so the couplings related to them are ignored. Because the two-stage filter has five components, there are 10 mutual couplings among them. All the couplings are extracted using methods similar to those of one-stage filters except the coupling between the two inductors, which is illustrated in Fig. 3-24. In Fig. 3-24, M_1 and M_2 have been extracted by the same method as was used for one-stage EMI filters. The impedance of capacitor branch Z_3 is extracted and shown in Fig. 3-25.

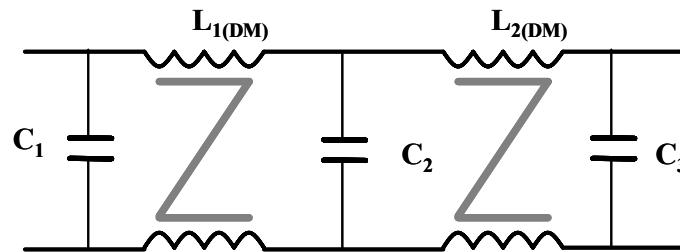


Fig. 3-22. The investigated two-stage DM EMI filter.

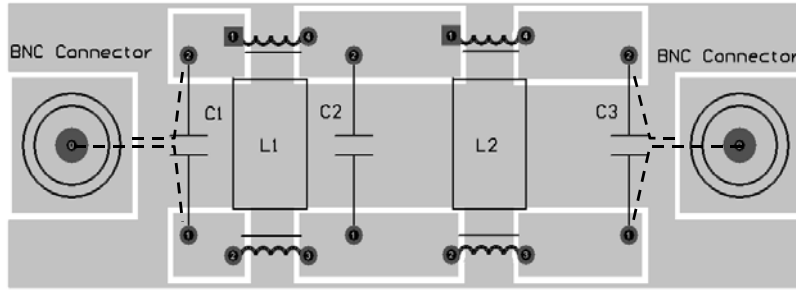


Fig. 3-23. PCB layout of the investigated two-stage EMI filter.

In Fig. 3-25, the series resonant frequency f_i of the capacitor branch is 230 kHz, which is much smaller than the 1.72 MHz of the capacitor. This difference is caused by mutual inductances M_1 , M_2 and M_3 . M_3 is then found, since M_1 and M_2 are already known. M_1 is 88.1 nH, M_2 is 44.3 nH, and M_3 is found as 0.908 μ H.

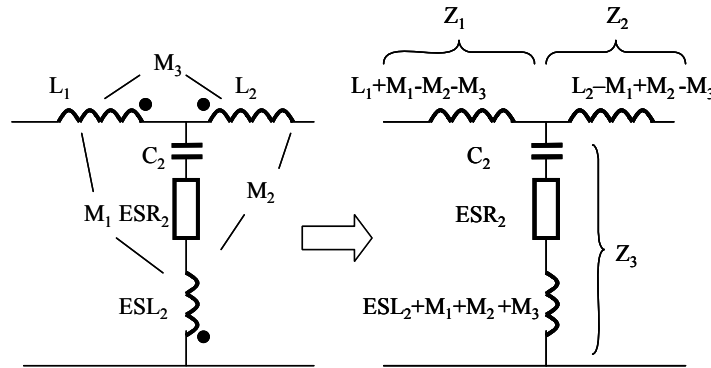


Fig. 3-24. Equivalent circuit for the inductive couplings between two inductors and between inductors and the capacitor C_2 .

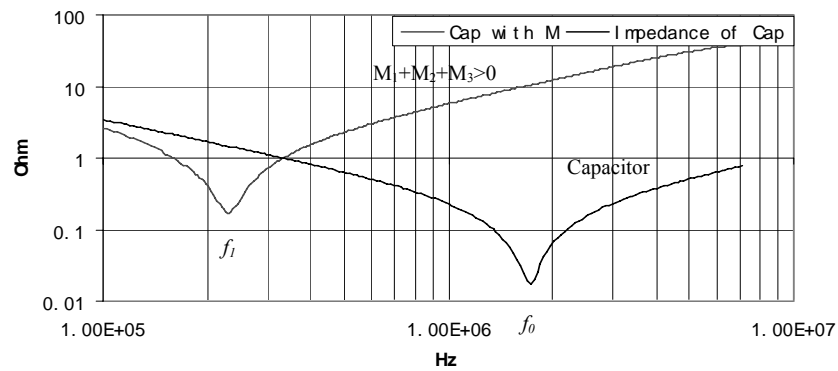


Fig. 3-25. Derived impedances of the C_2 branch from measured S-parameters.

3.4. Experimental Verification

Since all the parasitic couplings are extracted, it is possible to build and verify EMI filter models. Based on the models, parametric study can be carried out to find the critical couplings for the HF performance of EMI filters.

3.4.1 One-stage EMI Filter

The final filter models for one-stage EMI filters are shown in Figs. 3-26 and 3-27. In Figs. 3-28 and 3-29, the simulated insertion voltage gains with 50Ω source and load impedances are compared with the measured results. It is obvious that they match very closely, which verifies the extraction of mutual parasitic parameters. Further parametric study on the models shows the parasitic couplings between the two capacitors and between the inductor and capacitors are critical to the HF performance of EMI filters. This can be explained by the large current difference on two capacitor branches [9] and the large mutual inductance, which is several times larger than the ESL of capacitors, between the inductor and capacitors. The methods to control these couplings and therefore improve the filter HF performance are introduced in paper [12].

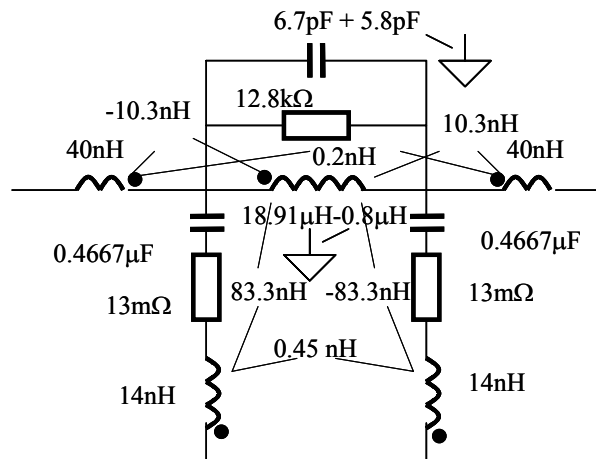


Fig. 3-26. EMI filter model for inductor winding direction1.

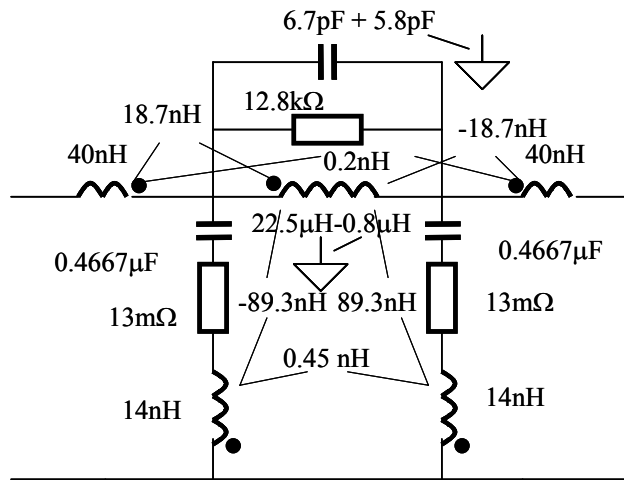


Fig. 3-27. EMI filter model for inductor winding direction2.

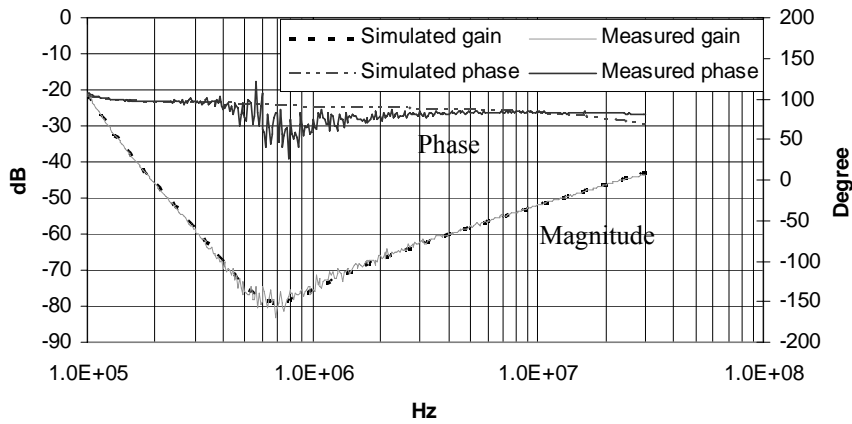


Fig. 3-28. Comparison of the measured and simulated insertion voltage gains for inductor winding direction1.

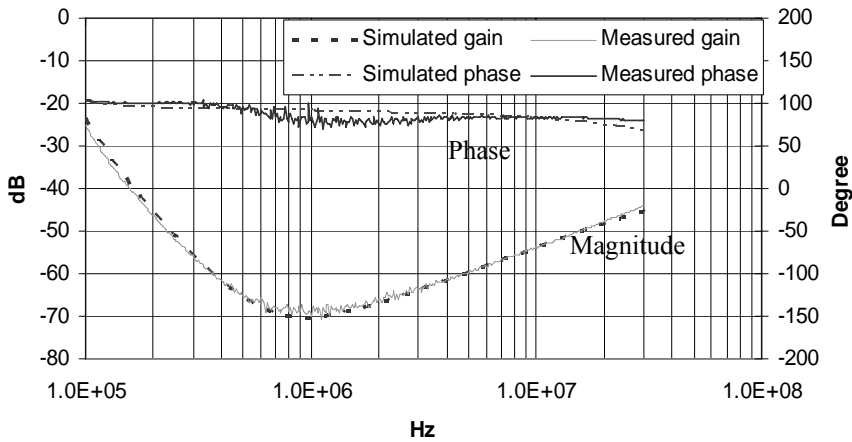


Fig. 3-29. Comparison of the measured and simulated insertion voltage gains for inductor winding direction2.

3.4.2 Two-stage EMI Filter

The final two-stage EMI filter model is shown in Fig. 3-30. The simulated insertion voltage gain when both source and load are 50Ω is compared with the measured one shown in Fig. 3-31. In Fig. 3-31, the simulated and measured curves match very closely; this verifies the extracted parasitic parameters. The noise between 200 kHz and 1 MHz in both pictures is the noise floor of the network analyzer. Further parametric study on the model shows the mutual inductance between the two inductors significantly affects the corner frequency of the insertion voltage gain at around 230 kHz. This is because the series resonant frequency of the C_2 branch is greatly lowered by the mutual inductance between two inductors. The parametric study also shows the mutual inductance between C_1 and C_3 significantly affects the insertion voltage gain above 1 MHz. Although this coupling is very small, the large current difference between two capacitor branches makes it very critical. Other couplings such as the mutual inductances between L_1 and C_1 , C_2 , and between L_2 and C_2 , C_3 also affect the HF performance of EMI filters because they affect the performance of capacitors.

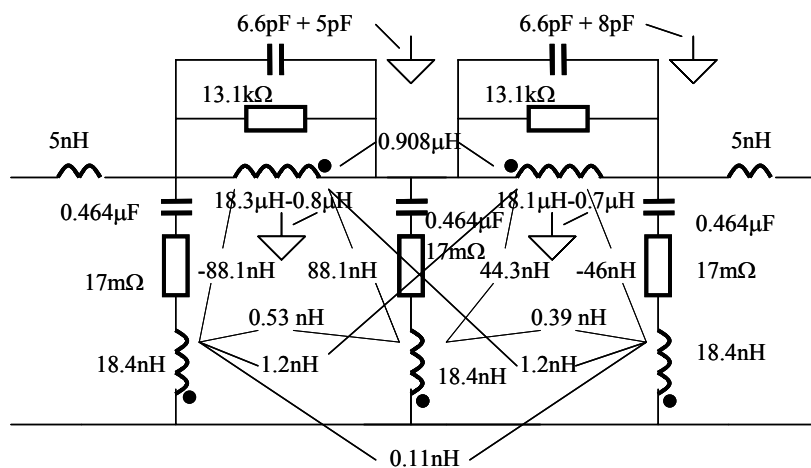
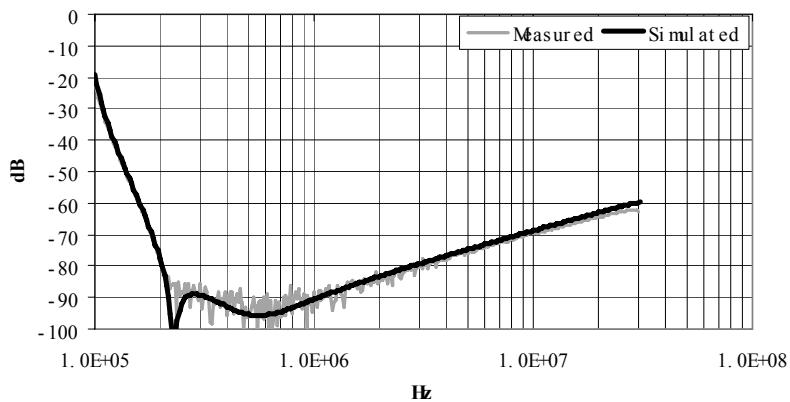
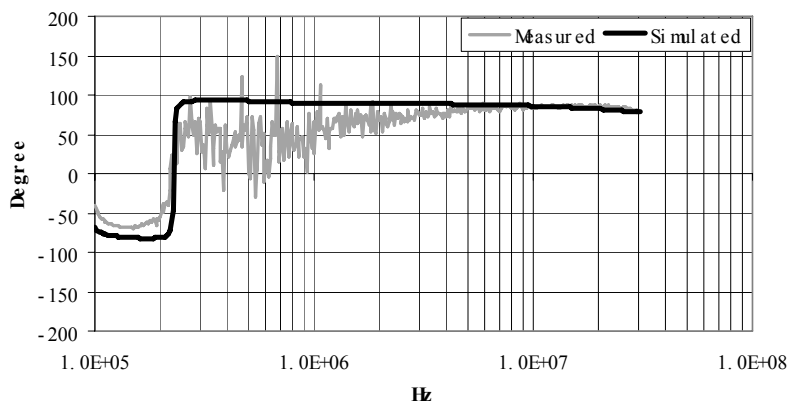


Fig. 3-30. Two-stage EMI filter model.



(a)



(b)

Fig. 3-31. Comparison of the measured and simulated insertion voltage gains:

(a) magnitude, and (b) phase.

3.5. Summary

This work firstly presented a method for using S-parameters to characterize EMI filters. An equation was developed to describe the insertion voltage gain, so it is possible to predict the EMI filter performance with arbitrary levels of source and load impedances. The approach was verified by measurements. A method that uses S-parameters to extract the parasitic parameters of EMI filters was then proposed for parasitic extraction of both

one-stage and two-stage EMI filters. The EMI filter models were built and the extracted parasitic parameters were finally verified by experiments. The constructed filter models were very useful for investigating the effects of parasitic couplings on EMI filter performance, and they therefore offer guidelines for EMI filter design.

Reference

- [1] Zhang, Dongbing, D.Y. Chen and D. Sable, "A New Method to Characterize EMI Filters," in *proc. IEEE Applied Power Electronics Conference and Exposition*, Anaheim, CA, 15-19 Feb. 1998, pp. 929-933.
- [2] Richard Anderson, "Test and Measurement Application Note 95-1 S-Parameters Techniques," Hewlett-Packard, 1997.
- [3] "Agilent AN154 S-Parameters Design Application Note," Agilent Technologies, 2000.
- [4] Shuo Wang, F.C. Lee and W.G. Odendaal, "Improving the Performance of Boost PFC EMI Filters," In *proc. IEEE Applied Power Electronics Conference and Exposition*, Miami, FL, 9-13 Feb. 2003, pp. 368-374.
- [5] Norman Balabanian and Theodore Bickart, "*Linear Network Theory: Analysis, Properties, Design and Synthesis*," Matrix Publishers, Inc., 1981.
- [6] Shuo Wang, F.C. Lee, D.Y. Chen and W.G. Odendaal, "Effects of Parasitic Parameters on the Performance of EMI Filters," In *proc. IEEE Power Electronics Specialist Conference*, Acapulco, Mexico, 15-19 Jun. 2003, pp.73-78.
- [7] Dongbing Zhang, D.Y. Chen, M.J. Nave and D. Sable, "Measurement of Noise Source Impedance of Off-Line Converters," *IEEE Transactions, Power Electronics*, Volume 15, Issue 5, Sept. 2000, pp. 820-825.
- [8] Max W.. Medley, "Microwave and RF Circuits: Analysis, Synthesis, and Design," Artech House, Inc., 1993.

- [9] Shuo Wang, F.C. Lee, D.Y. Chen and W.G. Odendaal, "Effects of Parasitic Parameters on the Performance of EMI Filters," *Power Electronics, IEEE Transactions*, Volume 19, Issue 3, May 2004, pp. 869–877.
- [10] Liu, D.H. and Jiang, J.G., "High frequency characteristic analysis of EMI filter in switch mode power supply (smes)," in *Proc. IEEE Power Electronics Specialists Conference*, 2002, Volume 4, pp. 2039 – 2043.
- [11] Shuo Wang, F.C. Lee and W.G. Odendaal, "Using Scattering Parameters to Characterize EMI Filters," in *Proc. IEEE Power Electronics Specialists Conference*, Aachen, Germany, 20-25, Jun. 2004, pp. 297 –303.
- [12] Shuo Wang, F.C. Lee and W.G. Odendaal, "Controlling the Parasitic Parameters to Improve EMI Filter Performance," in *Proc. IEEE Applied Power Electronics Conference*, Anaheim, California 22-26, Feb. 2004, Volume 1, pp. 503 –509.

CHAPTER 4: MUTUAL PARASITIC PARAMETER CANCELLATION

TECHNIQUES*

4.1. Introduction

Parasitic parameters affect electromagnetic interference (EMI) filter performance significantly in the high frequency (HF) range. Generally, there are two types of parasitic parameters: self-parasitics and mutual parasitics. The self-parasitics include the equivalent series inductance (ESL) and equivalent series resistance (ESR) of capacitors, equivalent parallel capacitance (EPC) and equivalent parallel resistance (EPR) of inductors. The mutual parasitics exist between two components, between a component and the printed circuit board (PCB) layout and between PCB traces. For the one-stage EMI filter shown in Fig. 4-1, CM and DM filter models considering self-parasitics are shown in Fig. 4-2. For convenience, CM capacitors are disconnected when the DM filter is modeled. The ESR_{1, 2} and ESL_{1, 2} are the self-parasitics of two capacitors. EPC and EPR are the self-parasitics of the inductor. Simulated and measured S₂₁ for both CM and DM filters are compared in Fig. 4-3.

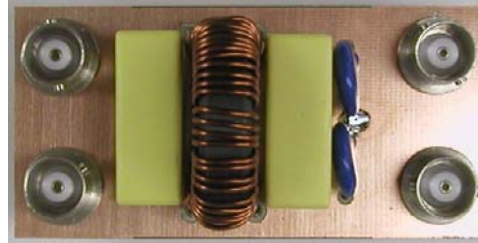
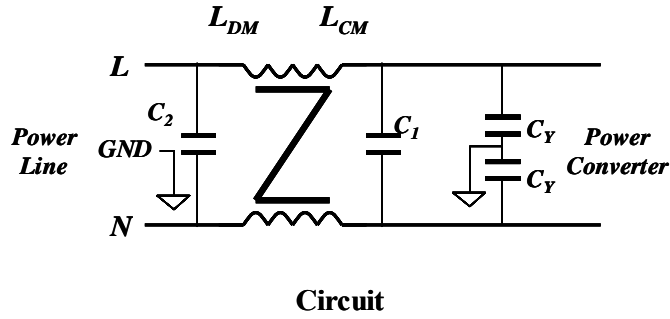
For the CM filter in Fig. 4-3, measured S₂₁ matches the simulated up to 30 MHz. The first corner frequency is generated by the parallel resonance of CM inductance L_{CM} and winding capacitance EPC_{CM} ; and the second corner frequency is generated by the series resonance of equivalent CM capacitance $2C_Y$ and equivalent series inductance $ESL_Y/2$. This indicates that self-parasitics of components determine the performance of the CM filter. In order to improve CM filter's high-frequency (HF) performance, winding

* © 2005 IEEE. Reprinted, with permission, from *IEEE Transactions on Power Electronics, Volume 20, Issue 5, Sept. 2005*. The original title is "Improvement of EMI Filter Performance with Parasitic Coupling Cancellation."

capacitance EPC_{CM} should be reduced. On the other hand, for the DM filter in Fig. 4-3, the measured S_{21} is far away from the simulated above 400 kHz, which means mutual parasitics determine the HF performance of the DM filter. In order to improve DM filter's HF performance, mutual couplings should first be reduced and then ESL should be reduced.

As stated above, mutual parasitics are important to DM filters only. Both inductive and capacitive parasitic couplings exist in DM filters. Inductive couplings tend to amplify their effects on the branch that has the smaller current between two branches with a large current difference. The inductive couplings, such as those between capacitor branches and the inductor branch, between two capacitor branches, between in and out trace loops, and between inductor and in and out trace loops, are therefore important parasitic couplings. At the same time, capacitive couplings tend to amplify their effects on the node that has the lower potential between two nodes with a large potential difference. The capacitive coupling between in and out traces is, thus an important coupling. All these parasitic couplings are shown in Fig. 4-4. They can be divided into six categories as follows:

- 1) Coupling between inductor and capacitors: M_1 and M_2 .
- 2) Coupling between two capacitors: M_3 .
- 3) Coupling between inductor and trace loops: M_4 and M_5 .
- 4) Coupling between ground plane and inductor: M_7 and C_p .
- 5) Coupling between trace loops: M_6 .



Prototype

Fig. 4-1. One-stage EMI filter under investigation.

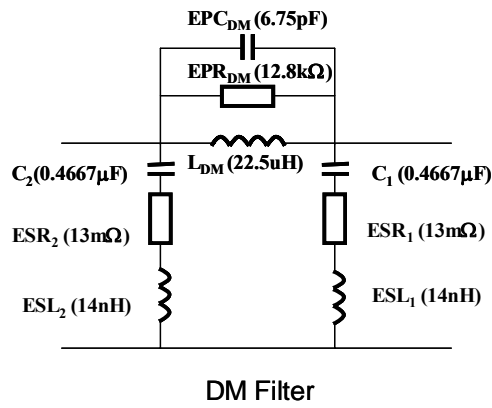
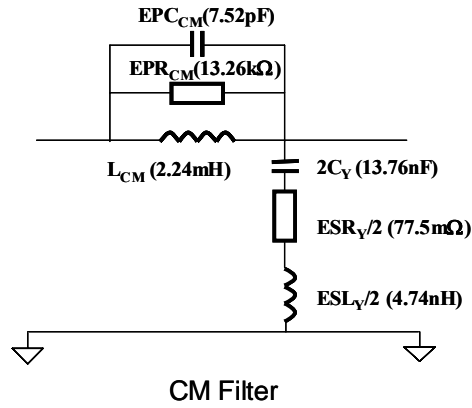
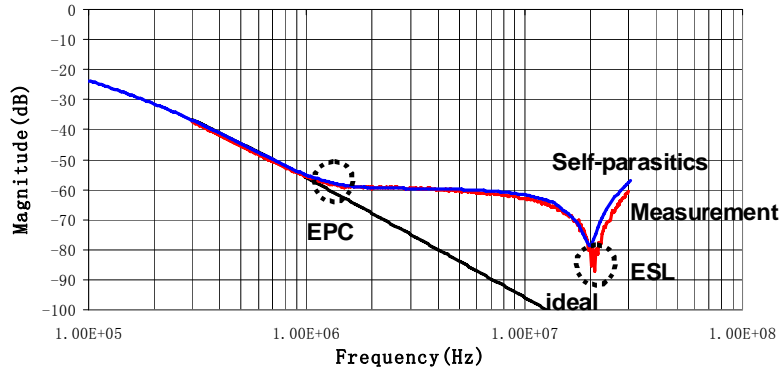
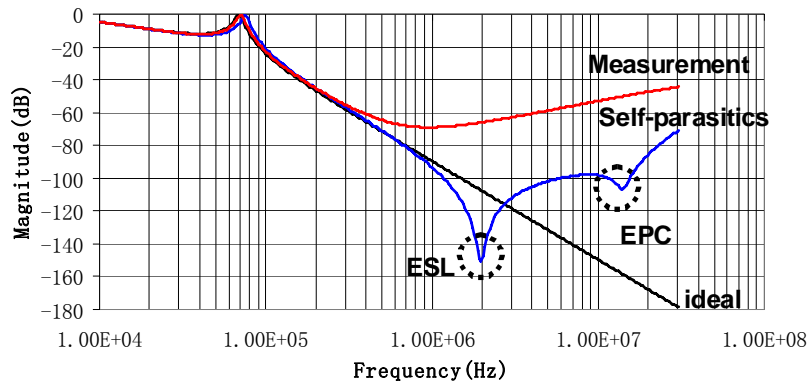


Fig. 4-2. CM and DM filter models including parasitics of components.



(a) Comparison of measured and simulated S21 for CM filter.



(b) Comparison of measured and simulated S21 for DM filter.

Fig. 4-3. Effects of parasitic parameters on EMI filter performance (Insertion voltage gain when both source and load are 50Ω).

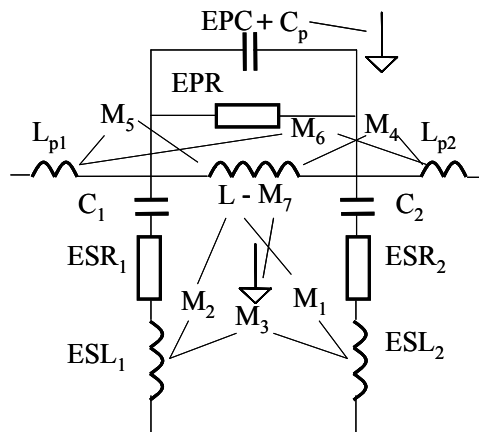
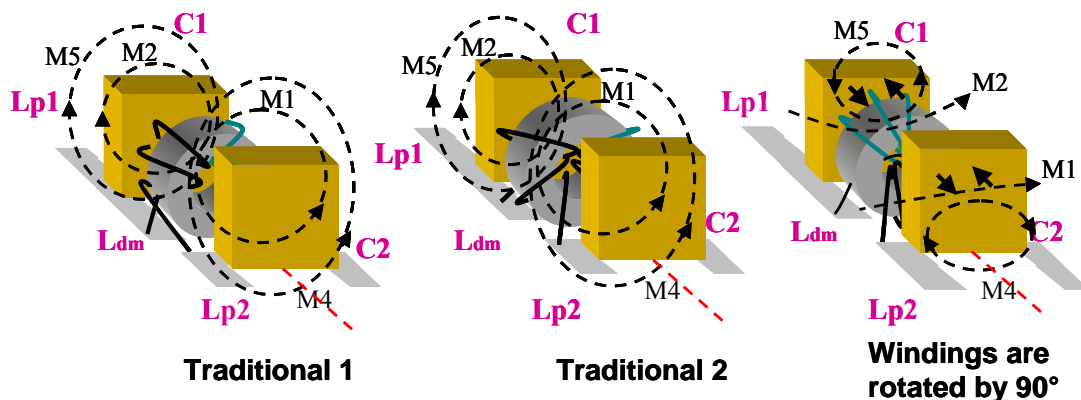
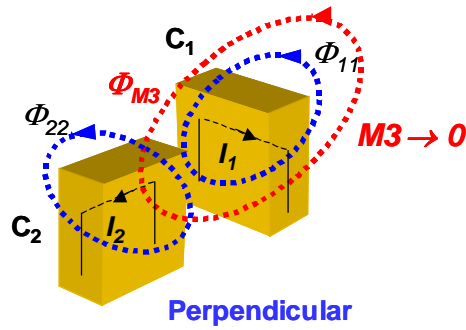


Fig. 4-4. Parasitic couplings in a DM filter.

Reference [5] introduced a network method to cancel the ESL of capacitors. Reference [7, 8] employed mutual inductance to cancel the ESL of capacitors. All of these methods are for the reduction of self-parasitics. Since EMI filter is a coupled system, reduction of mutual parasitics is even more important than the reduction of self-parasitics. In fact, experiments show that if mutual couplings are not efficiently minimized, efforts on reducing self-parasitics are in vain. Before these methods can be effectively applied to filter design, effects of mutual couplings must be minimized. Reference [2] shielded two capacitors and enlarged the distance between components to reduce the couplings, but this was at the cost of larger size and extra parasitics. In [1, 2] inductor windings were rotated by 90° to make magnetic flux symmetrical to the center line of capacitors and trace loops. As shown in Fig. 4-5 (a), after windings were rotated by 90° , the net magnetic flux linking capacitors C_1 , C_2 and trace loops L_{p1} , L_{p2} was greatly reduced so that mutual inductances M_1 , M_2 , M_4 and M_5 could be reduced by more than 90%. The improvement of these two methods on filter performance is still limited [1, 2]. Fig.4-5 (b) proposes reducing the mutual inductance M_3 between two capacitors reorientation by placing two capacitors perpendicular. This approach can reduce M_3 by $2/3$ and its improvement will be evaluated in section 4.4.



(a) Rotating inductor windings by 90° to reduce mutual inductance M_1 , M_2 , M_4 and M_5 .



(b) Using perpendicular capacitors to reduce the inductive coupling between two capacitors.

Fig. 4-5. Reducing M_1 , M_2 , M_3 , M_4 and M_5 by rotating inductor windings and a capacitor.

In order to significantly improve EMI filter performance, critical parasitic couplings must be identified and greatly reduced.

The effect of mutual inductance M_1 on capacitor C_2 is equivalent to an inductance M_1 in series with the ESL of capacitor C_2 [1]. The same rule holds true for the effect of M_2 on C_1 . Because M_1 and M_2 can be several times larger than the ESL of the capacitors [1], they are critical to the capacitor performance. The effect of M_4 or M_5 can also be equivalent to an inductance in series with the ESL of the capacitors; however they are not critical because they are much smaller than M_1 and M_2 . Due to the large magnitude difference between the HF currents on the branches C_1 and C_2 , the effect of M_3 on capacitor performance is significant [1]. The mutual inductance M_6 between input and output trace loops also plays an important role in filter performance for the same reason [1]. For M_7 and C_p , they are not critical to filter performance [1].

Experiments in [1] showed that, in HF range, after the inductor windings are rotated by 90° , effects of M_1 and M_2 on filter performance are greatly reduced. As a result, effects of M_3 and M_6 are significant so that the insertion voltage gain of the filter is given

by (4-1). This can be explained by the high impedance of the inductor actually causing noise to propagate to the load through the mutual couplings between the two capacitors and between the input and output trace loops. In order to further improve the EMI filter HF performance, M_3 and M_6 should be minimized. M_6 can be easily minimized by minimizing the input and output trace loop areas. For M_3 , this chapter introduces a new technique to effectively cancel it and consequently drastically improve filter HF performance.

$$\mathbf{T}_G = \frac{2\mathbf{U}_2}{\mathbf{U}_s} \approx \frac{j\omega}{25}(M_3 + M_6) \quad (4-1)$$

4.2. Parasitic Coupling Cancellation

In this chapter, a cancellation turn is integrated with the capacitors to cancel the parasitic coupling between the two capacitors. Two approaches are investigated. For the first approach, a cancellation turn is in series with the input or output trace loop. For the second approach, a cancellation turn is in series with either capacitor C_1 or C_2 . It can be shown that for the first approach, the integrated cancellation turn can reduce both the coupling between two capacitors and the ESL of the capacitor. Two measures are first taken before applying these two approaches to the filter.

1) Input and output trace loops are reduced as much as possible to minimize mutual inductance M_4 , M_5 and M_6 .

2) Inductor windings are rotated by 90° to reduce mutual inductance M_1 , M_2 , M_4 and M_5 .

With the help of these two measures, the effects of M_4 , M_5 and M_6 are greatly reduced. Because the current loop areas in the capacitors cannot be reduced, experiments show M_1 and M_2 are still 7.5 nH [1] and cannot be ignored in comparison with 14nH ESL. M_3 is the same as the original, because no measure has been taken to reduce the coupling loop areas of two capacitors.

4.2.1 First Approach

A cancellation inductor L_M is introduced in Fig. 4-6 (a) to be in series with the input trace loop. It has mutual inductance M_A with capacitor C_2 , M_B with capacitor C_1 and M_C with inductor L . As analyzed in section I, at HF range current does not come through the inductor L , so the corresponding HF model of the filter is simplified as in Fig. 4-6 (b). The effects of M_1 , M_2 and M_C are ignored since no current comes through the inductor at HF range. The equivalent HF model with a load Z_L and input voltage V_S is shown in Fig. 4-7.

The load voltage V_L is then given as (4-2):

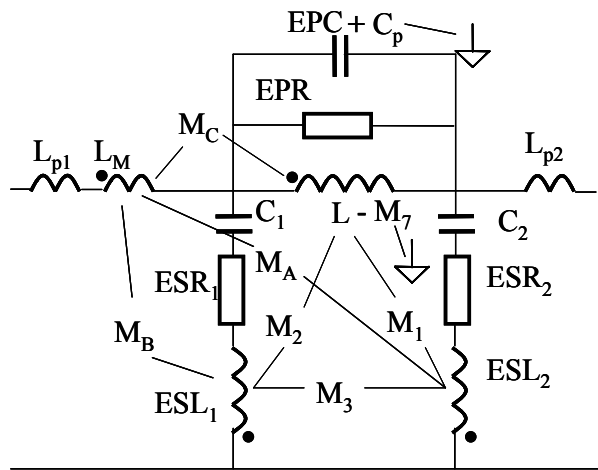
$$V_L = \frac{j\omega(M_3 - M_A)Z_L}{j\omega(M_3 - M_A)(Z_2 + Z_L) + Z_1(Z_2 + Z_L + j\omega(M_3 - M_A))} V_S \quad (4-2)$$

Obviously, the condition for zero load voltage is given by (4-3):

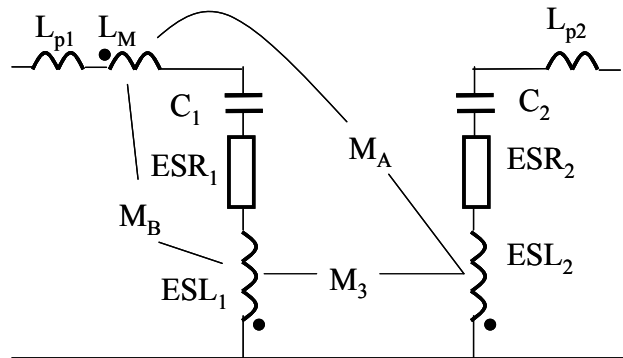
$$M_A = M_3. \quad (4-3)$$

This condition means the mutual inductance between the cancellation inductor L_M and the capacitor C_2 should be equal to that between two capacitors. Furthermore, these two mutual couplings should have opposite polarities to get the desired cancellation effect,

just as shown in Fig. 4-6 (a). The physical effect of the cancellation is that the induced voltage in C_2 due to the coupling between the cancellation inductor L_M and C_2 cancelled the induced voltage due to the coupling between two capacitors because of opposite voltage directions. It should be pointed out that if M_A is much larger than M_3 , a large equivalent negative inductance can make filter performance worse. The proposed approach differs from the existing self-parasitic cancellation methods in that the critical mutual couplings are cancelled based on the understanding of the whole filter. As a result, the HF performance of the whole filter, rather than a single component in the filter can be significantly improved.



(a) EMI filter model with a cancellation inductor L_M .



(b) HF EMI filter model with a cancellation inductor L_M .

Fig. 4-6. HF model of the filter.

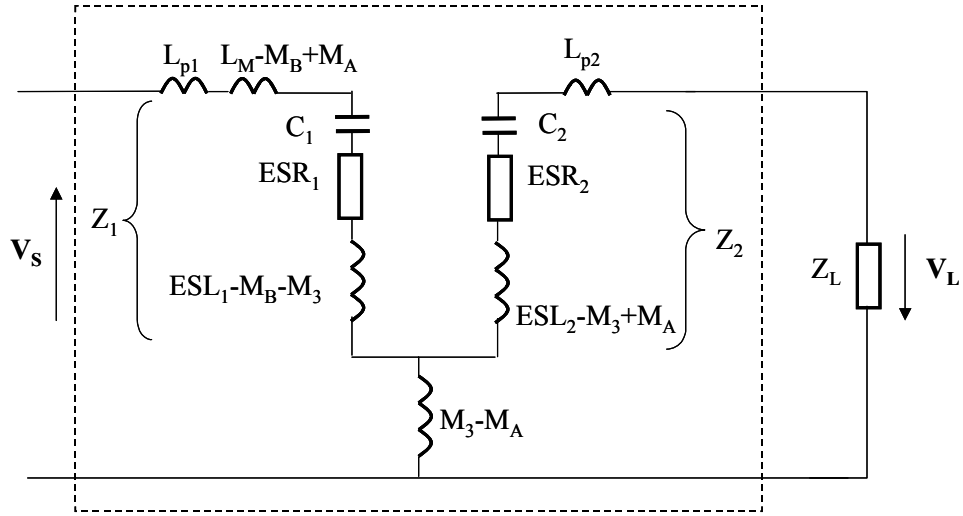


Fig. 4-7. HF equivalent circuit for the filter.

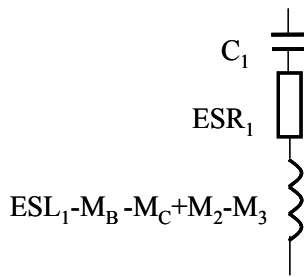


Fig. 4-8. Equivalent circuit for capacitor C_1 .

After M_3 is cancelled, HF noise will propagate through the inductor. As a result, the effects of M_1 , M_2 and ESL can become important. As stated in section I, after the inductor windings are rotated by 90° , M_1 and M_2 have been reduced by more than 90%. After introducing inductor L_M , the effects of M_2 can be further reduced because of the cancellation effects of induced voltages in C_1 . Another benefit of this approach is that the ESL of C_1 can be partly cancelled. Fig. 4-8 shows the equivalent circuit of C_1 , which illustrates these two benefits. This equivalent circuit including M_B and M_C is different from that in Fig. 4-7 because HF noise propagates through the inductor after M_3 is

cancelled. In Fig. 4-8, if M_B and M_C makes the equivalent inductance smaller than ESL_1 , the performance of capacitor C_1 is improved.

4.2.2 Second Approach

In the second approach, the capacitor C_1 is split into two identical parts. As shown in Fig. 4-9, the cancellation turn L_M is in series with the two split capacitors at the middle point. All the mutual inductances between any two components are shown in Fig. 4-9. The HF equivalent circuit is shown in Fig. 4-10. In Fig. 4-10, if $M_A + M_C = M_B$ (the mutual inductance between the split capacitors and C_2 should equal the mutual inductance between the cancellation turn and C_2), then the output of the filter is zero. However, the equivalent series inductance of the integrated structure can be enlarged, because the inductance L_M of the cancellation turn can be larger than the sum of $2M_E$ and $2M_F$. The couplings between the cancellation turn and capacitors should have the same polarities as those shown in Fig. 4-9. The advantage of this approach is that the integrated capacitor is a two-terminal component and the structure is symmetrical, which may benefit manufacturing.

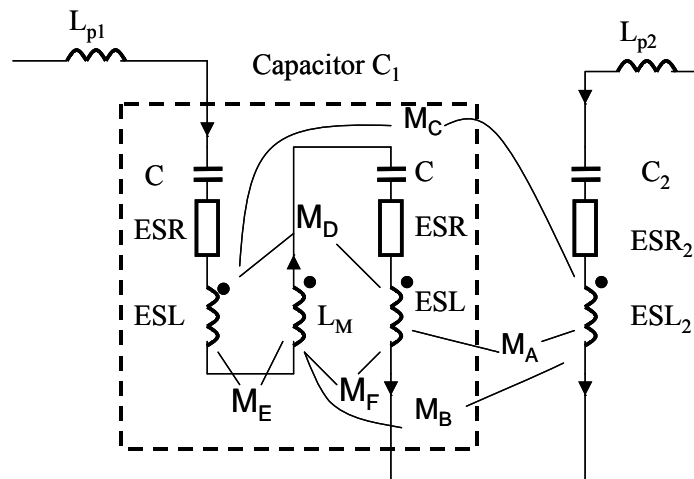


Fig. 4-9. HF model of the filter.

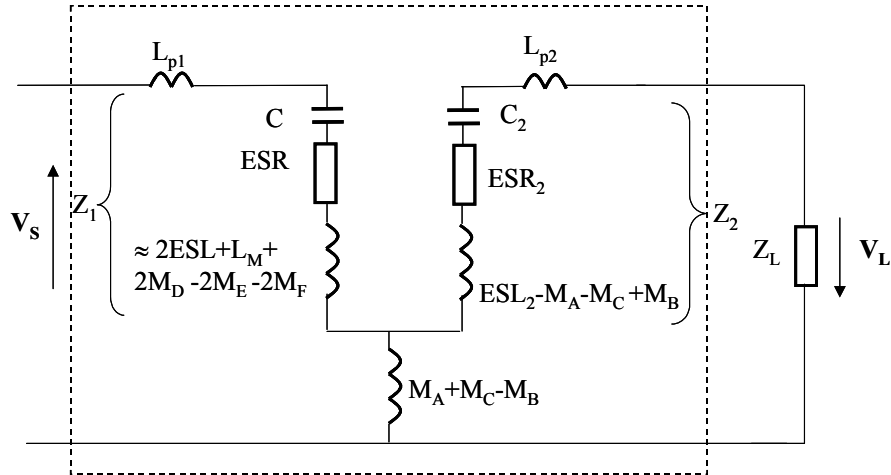


Fig. 4-10. HF equivalent circuit for the filter.

4.3. Implementation

4.3.1 Internal Structure of Film Capacitors

The commonly used dielectrics for DM EMI capacitors are metallized film and paper. The commonly used capacitor shapes are rectangular and tubular. The general internal structure of a rectangular film capacitor is shown in Fig. 4-11 [10]. Electrodes are metallized on one side of the plastic film. Two layers of films are stacked and rolled together. The roll is then embedded in resin filling and plastic coating. The ends are metal-sprayed and wire leads are soldered on the two sides of the roll to conduct the current. The film acts as the dielectric of the capacitor. The current flow in the capacitor is also illustrated in Fig. 4-11.

In Fig. 4-11, the current is first conducted through the wire lead and metal end-spray on one end of the roll. It then goes through the electrodes and film dielectric. Finally, the current reaches the wire lead and metal end-spray on the other end of the roll. The electrodes and film dielectric therefore form a capacitor. Obviously, there is a current

loop in the capacitor. It is this current loop that links the external magnetic flux so as to generate mutual inductance. This rule also holds true for capacitors in other shapes.

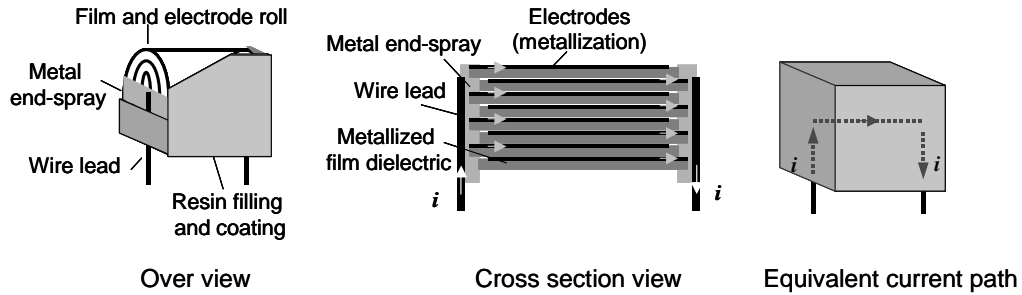


Fig. 4-11. Internal structure and current flow of film capacitors.

4.3.2 First Approach

Based on the analysis in section II, the mutual inductance M_A between the cancellation inductor L_M and capacitor C_2 should equal the mutual inductance M_3 between C_1 and C_2 .

The magnetic coupling between C_1 and C_2 is illustrated in Fig. 4-12.

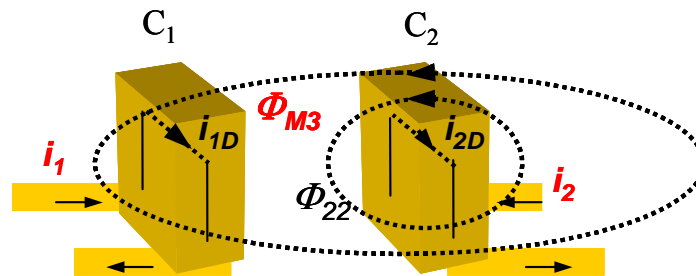


Fig. 4-12. Mutual coupling between two capacitors.

In Fig. 4-12, the magnetic flux Φ_{M3} produced by the current i_2 in capacitor C_2 links the current i_1 in capacitor C_1 . The mutual inductance M_3 is defined by (4-4). It should be pointed out that the current in the capacitor dielectric is displacement current (i_{1D} , i_{2D}).

$$M_3 = \frac{\Phi_{M3}}{i_2}. \quad (4-4)$$

In Fig. 4-13, a cancellation inductor is added beside C_1 , where the cancellation inductor is a $\frac{3}{4}$ turn, which has a similar current path as the capacitor. If Φ_{M2} is the magnetic flux produced by C_2 which links the cancellation inductor L_M , the mutual inductance M_A between L_M and C_2 is then given by (4-5):

$$M_A = \frac{\Phi_{MA}}{i_2}. \quad (4-5)$$

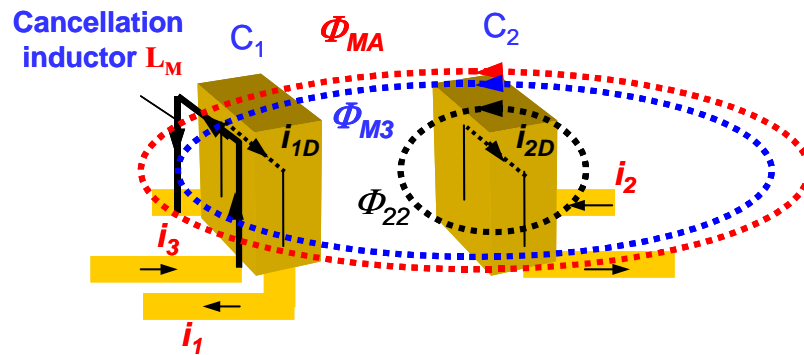


Fig. 4-13. Mutual coupling between two capacitors and between C_2 and the cancellation turn.

Comparing (4-4) and (4-5), it is obvious that only when Φ_{MA} equals Φ_{M3} will M_A equal M_3 . It is difficult to theoretically calculate the coupling area of the cancellation turn because of the complicated magnetic flux distribution. However, the optimal coupling area of the cancellation turn can be tuned by conducting experiments. In order to efficiently cancel M_3 , the cancellation turn should also be close to capacitor C_1 so as to be exposed to a similar external magnetic flux distribution to that of C_1 . A good way to do

this is to integrate the cancellation inductor with the capacitor. Fig. 4-14 is the equivalent circuit of Fig. 4-13.

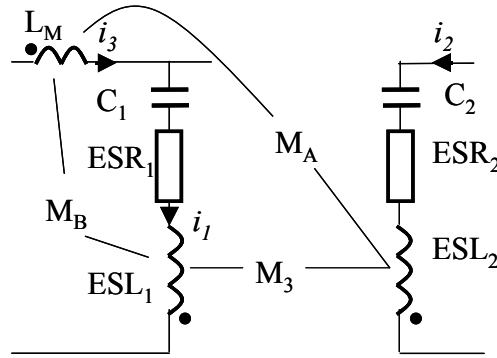


Fig. 4-14. Equivalent circuit of two capacitors when one is with a cancellation turn.

Since commonly used capacitors are rectangular and tubular, a cancellation turn will be applied to both shapes in this section. Fig. 4-15 shows the equivalent circuit of the integrated capacitor, where a cancellation inductor L_M is integrated with the capacitor. The mutual couplings between the integrated elements and external components are not shown in the figure. In this implementation, a cancellation turn, which is composed of $\frac{3}{4}$ turn of copper foil, is integrated in the film capacitor (Philips, MKP 0.47uF/400V). An isolation layer (FR4) covers the integrated cancellation turn. Fig. 4-16 shows the exploded view of the prototype. The three terminals in Fig. 4-16 correspond to those in Fig. 4-15.

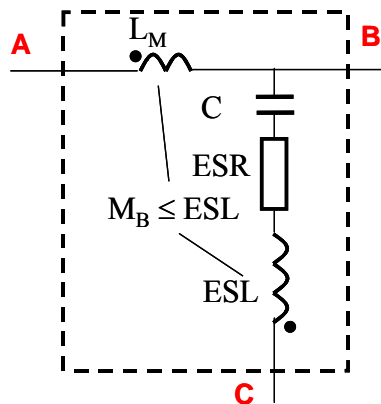


Fig. 4-15. Equivalent circuit of the integrated capacitor.

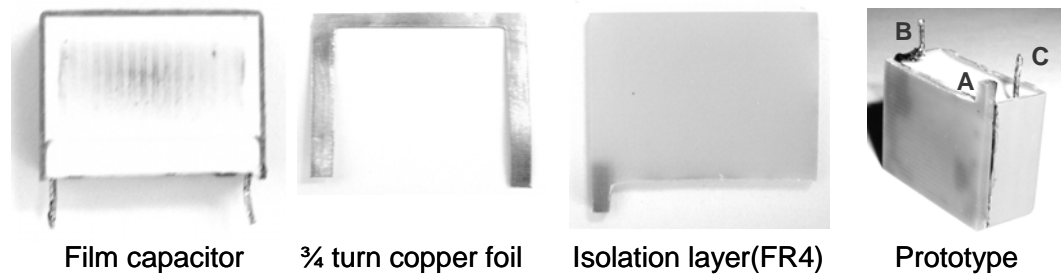


Fig. 4-16. Exploded view of the capacitor with an integrated cancellation turn.

In order to effectively cancel M_3 , three measures are taken in the design of the cancellation turn.

- 1) The plastic coating of the capacitor is removed and the cancellation turn is glued as close as possible to the film roll of the capacitor. This guarantees the cancellation turn is exposed to a similar external magnetic field distribution to the capacitor.
- 2) The cancellation turn covers the side and upper edges of the film roll, so most of the flux that links the capacitor also links the cancellation turn.
- 3) Because the HF current always flows through the inner edge of the copper foil turn, the coupling area of the cancellation turn is determined by the area enclosed by the inner edge. The optimal area is tuned by conducting experiments.

A prototype for a tubular shape film capacitor was also built and is shown in Fig. 4-17.

The cancellation turn is $\frac{3}{4}$ turn wire and the capacitance is $1\mu\text{F}$.

4.3.3 Second Approach

For the second approach, the equivalent circuit and structure of the integrated capacitor are shown in Fig. 4-18. In the experiment, two $0.39\mu\text{F}$ film capacitors (Cap1 and Cap2 in Fig. 4-18) and $\frac{3}{4}$ turn copper foil are used for integration. The design of the cancellation turn is similar to that in the first approach.

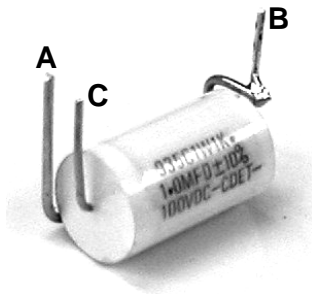


Fig. 4-17. Prototype of the integrated tubular film capacitor.

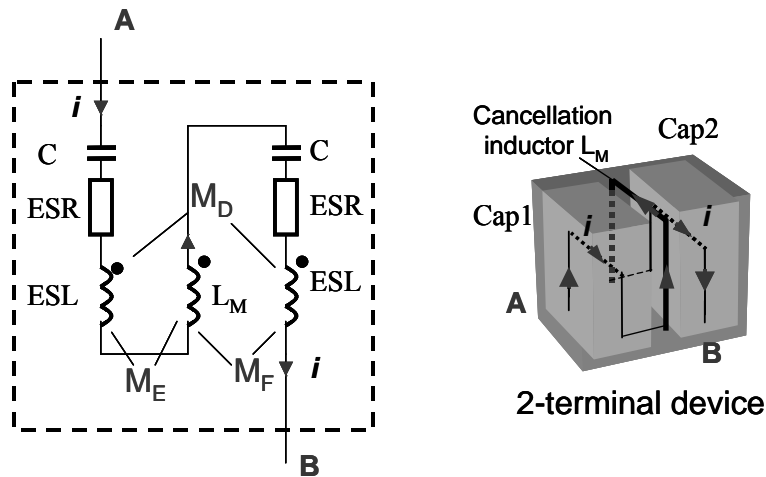


Fig. 4-18. Equivalent circuit and structure of the integrated capacitor.

4.4. Experimental Results

In this section, the prototypes are tested both in one-stage and two-stage EMI filters. For the first approach, both rectangular and tubular capacitor prototypes are measured. The two integration approaches are also compared through experiments. The cancellation

of mutual couplings and ESL are then quantified through the developed parasitic-extraction techniques [3]. Comparison of the measured results with the base line shows the drastic performance improvement on filter HF performance.

4.4.1 Applying to a One-stage EMI Filter

In the experiment, the inductance of the filter inductor is around $20\mu\text{H}$. The two measures proposed in section II to reduce M_1 , M_2 , M_4 , M_5 and M_6 are first applied to the investigated EMI filter.

For the first approach, the prototype of rectangular capacitor first replaced C_1 in the filter, which is shown in Fig. 4-19. The comparative experimental results are shown in Figs. 4-20, 4-21 and 4-22. All of the mutual inductances are extracted using developed S-parameters method [3]. Fig. 4-20 shows three impedances of M_3 , i.e. 1) with and 2) without cancellation, 3) capacitors are rotated to perpendicular fashion as proposed in section 4.1. The noise below $1\text{m}\Omega$ is the result of the noise floor of the network analyzer.

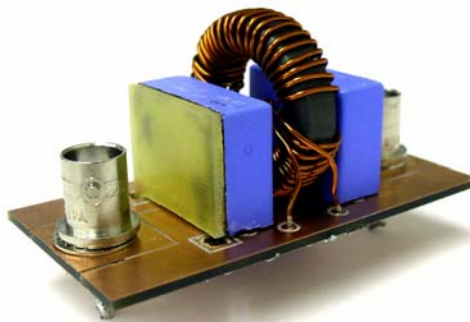


Fig. 4-19. One-stage EMI filter using the capacitor with an integrated cancellation turn.

Comparing the impedances above $1\text{m}\Omega$, inductance M_3 is reduced from 249 pH to 83 pH when capacitors are perpendicular. It is further reduced to 19 pH , a 92.4% reduction, when the cancellation turn is used. Fig. 4-21 shows the impedance of capacitor C_1 with

and without cancellation. From the change of series resonant frequency of the capacitor, it is easy to derive that ESL of integrated capacitor is reduced from 12 nH to 4 nH which is a 67% reduction because C_1 is known as 0.486 μF . The performance of the filter is shown in Fig. 4-22. Four curves are compared in Fig. 4-22. The base line case is the insertion voltage gain without using mutual coupling cancellation and 90° rotated windings. When the inductor windings are rotated by 90°, filter has about 5dB improvement, which is the second curve shows. When two capacitors are perpendicular to each other, 20dB improvement is achieved. The final case is the insertion voltage gain of the filter with 90° rotated windings and mutual coupling cancellation. The insertion voltage gain is indeed below the noise floor of the network analyzer above 1 MHz. The cancellation of M_3 and ESL of capacitor C_1 results in a factor of 100 improvement (40dB) in filtering performance at 30 MHz. The noise in Fig. 4-22 is the noise floor of the network analyzer. Perpendicular capacitors can not reduce M_3 as much as the cancellation turn can. Furthermore, 90° rotated inductor windings can not minimize M_1 and M_2 simultaneously when two capacitors are perpendicular. These make perpendicular capacitors not as good as the cancellation turn.

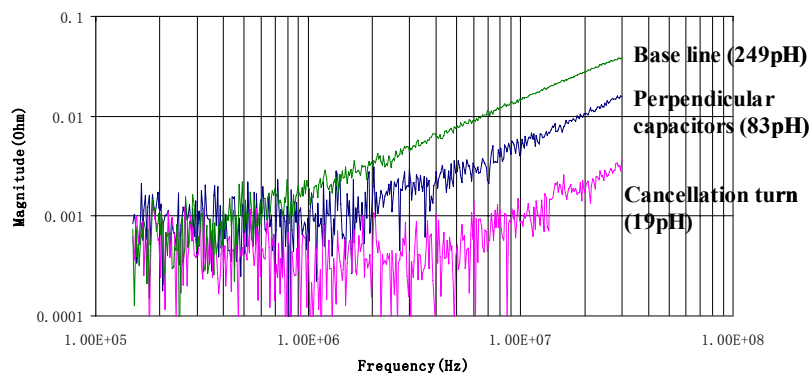


Fig. 4-20. Comparison of impedances of the mutual inductances between two capacitors.

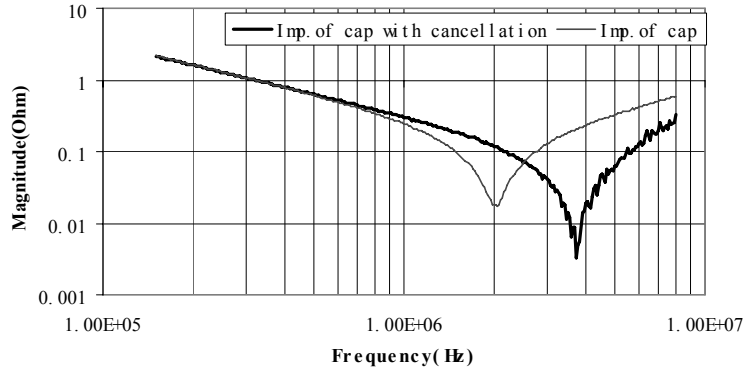


Fig. 4-21. Comparison of impedances of capacitor C_1 .

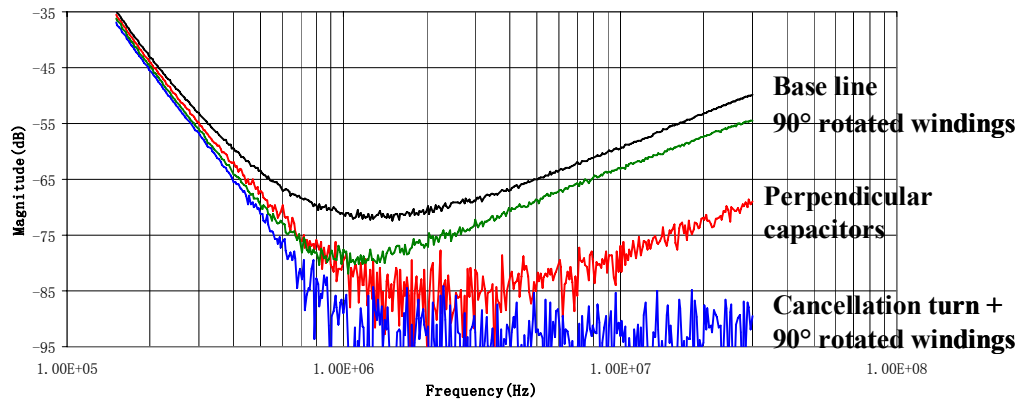


Fig. 4-22. Comparison of insertion voltage gains of a filter with and without mutual coupling cancellation for rectangular capacitors.

For the prototype of the tubular film capacitor, the measured filter has the same structure as that in Fig. 4-19 except that two capacitors are tubular shapes and the capacitance is $1\mu\text{F}$. The measured three insertion voltage gains are shown in Fig. 4-23. From Fig. 4-23, the filter with an integrated capacitor achieves 20dB improvement at 30MHz compared with the base line. Based on the results of these two experiments, it can be concluded that the proposed method can be used for both rectangular and tubular capacitors.

For the second approach, the measured filter has the same structure as that in Fig. 4-19, except that the equivalent capacitance for C_1 is $0.195\mu\text{F}$ and C_2 is $0.39\mu\text{F}$. The measured two insertion voltage gains are shown in Fig. 4-24. From Fig. 4-24, the filter with an integrated capacitor achieves $\leq -90\text{dB}$ from 1MHz to 13MHz . The improvement above 13MHz is still significant although it is not as good as the first approach due to enlarged ESL on C_1 . This also verified that the mutual inductance between two capacitors is more important than the self-parasitics. Because the first approach has the better filtering performance, it is preferred in this chapter.

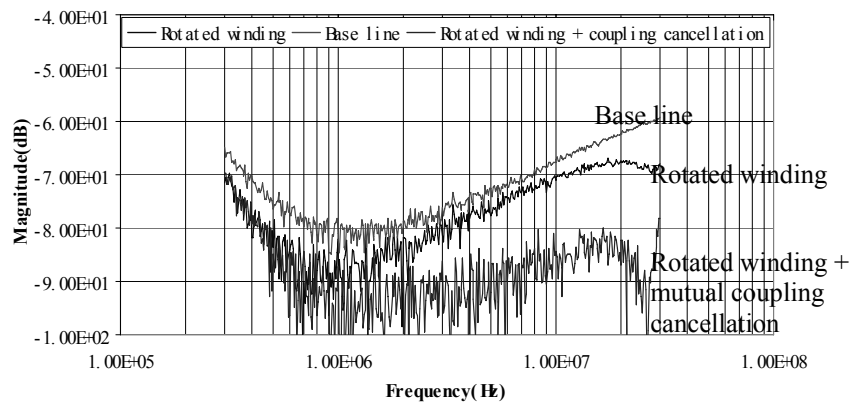


Fig. 4-23. Comparison of insertion voltage gains of a filter with and without mutual coupling cancellation for tubular capacitors.

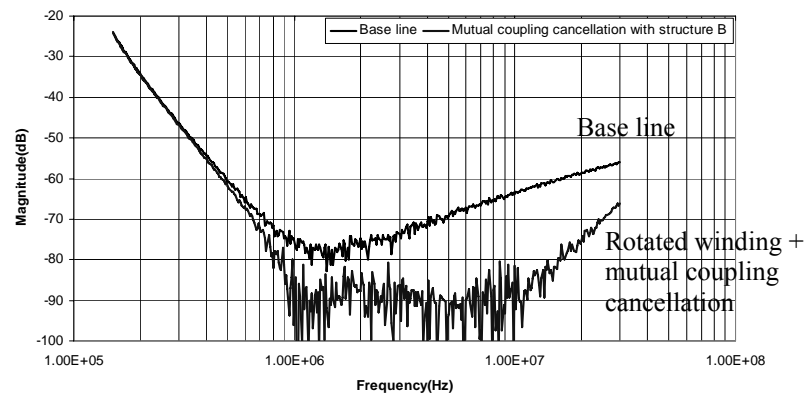


Fig. 4-24. Comparison of insertion voltage gains of a filter with and without mutual coupling cancellation for the second approach.

4.4.2 Applying to a Two-stage EMI Filter

The prototype of the rectangular capacitor in the first approach is also applied to a two-stage EMI filter. The filter circuit is shown in Fig. 4-25. The parasitic model is shown in Fig. 4-26 [3]. In the model, the mutual inductances between the input/output trace loop and other components are ignored because the trace loop area is kept very small. The mutual inductance M_9 between C_1 and C_3 are very critical to filter HF performance for the same reason they are critical in the one-stage EMI filter, which can be illustrated by the comparative experiments in Fig. 4-27. In Fig. 4-27, the base-line case is the insertion voltage gain of a two-stage EMI filter. The second curve is the insertion voltage gain of the filter when L_1 , L_2 and C_2 are disconnected from the filter. Obviously, above 400 kHz, these two cases are almost the same, so the filter performance is almost determined by the inductive coupling between C_1 and C_3 above 400 kHz. M_1 , M_2 , M_3 and M_4 are the mutual inductances between inductors and capacitors. They also affect filter performance because of their effects on capacitors. The gain dip around 200 kHz in the base-line case is strongly affected by the mutual inductance M_{10} between two inductors [3]. This mutual inductance together with M_2 , M_3 resonates with C_2 so as to cause an impedance dip and therefore a gain dip at the resonant frequency. However, this gain dip is desired because high attenuation is needed in the low frequency range to attenuate switching noise. Based on these analyses, two measures are taken to improve two-stage EMI filter performance:

- 1) Capacitor C_1 is replaced by the integrated capacitor prototype (rectangular shape) to reduce M_9 .

2) The inductor windings are rotated by 90° to reduce M_1, M_2, M_3 and M_4 .

After these two measures are taken, the results of experiments show the mutual inductance between C_1 and C_3 is reduced from 110 pH to 14 pH which is an 87.3% reduction. The ESL reduction is the same as in the one-stage filter case. Fig. 4-28 shows a comparison of the filter performance. The base-line case is the insertion voltage gain of the filter without using 90° rotated windings and mutual coupling cancellation. The second curve shows the filter performance with the 90° rotated windings and mutual coupling cancellation.

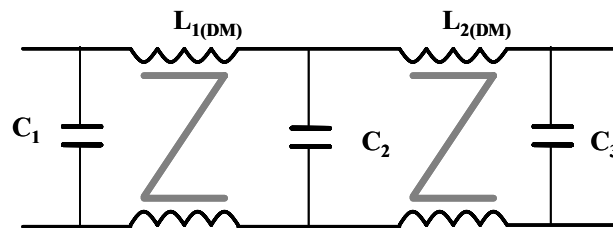


Fig. 4-25. Investigated two-stage DM EMI filter.

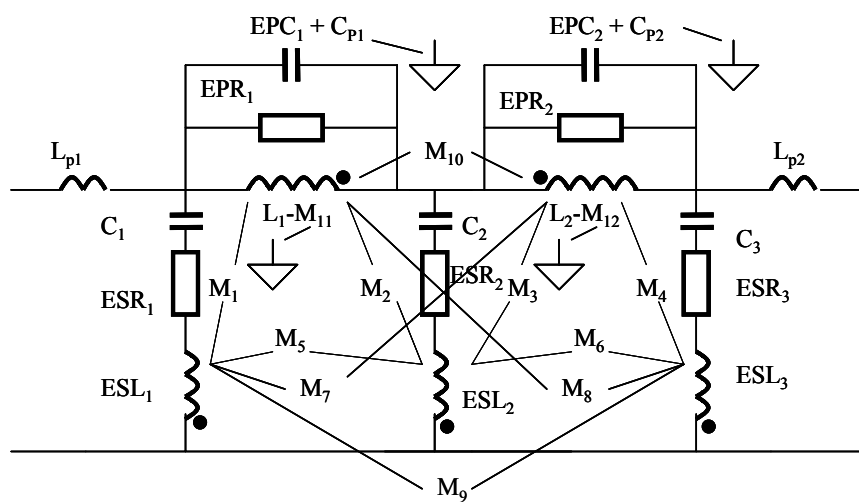


Fig. 4-26. Parasitic model for a two-stage DM EMI filter.

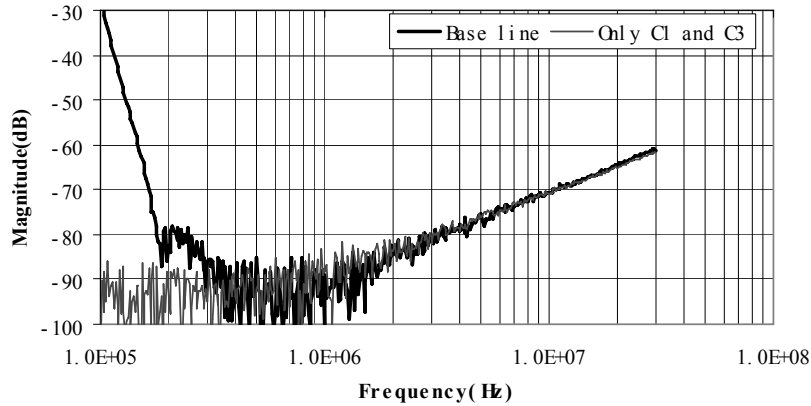


Fig. 4-27. Comparison of insertion voltage gains.

In Fig. 4-28, the measured insertion voltage gain is actually lower than the noise floor (-90 dB) of the network analyzer above 400 kHz, which implies a very good HF filtering performance. Compared with the base line, the performance after using the mutual coupling cancellation is improved from -60 dB to below -90 dB. More than 30 dB improvement is achieved at 30 MHz. Although the cancellation turn can also cancel M_1 and M_5 , it is not as important as the cancellation of M_9 .

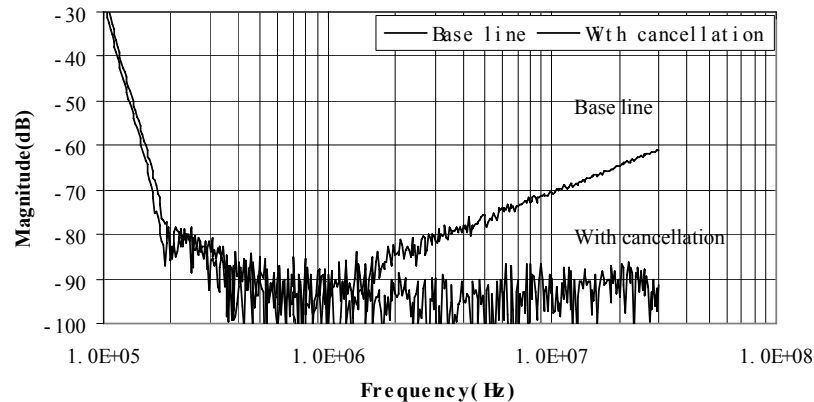


Fig. 4-28. Comparison of insertion voltage gains of a two-stage EMI filter with and without mutual coupling cancellation.

It should be pointed out that because the cancellation turn already cancels M_9 , only one of the two capacitors needs to be replaced by the integrated capacitor on the two

sides of the filter. For the electromagnetic interference from the outside of the filter, it is also expected that the cancellation turn can at least partly cancel these effects on the capacitors because of the opposite coupling polarities between the capacitor and the cancellation turn.

4.5. Summary

This work first identified the critical mutual couplings in EMI filters. These critical couplings are the mutual inductances between the input and output capacitors, between capacitors and inductors and between input and output trace loops. The latter two critical couplings can be overcome by rotating inductor windings by 90° and minimizing input/output trace loops. A cancellation inductor is proposed in this chapter to cancel the mutual inductance between the two capacitors. This cancellation inductor can also partly cancel the ESL of the capacitors. A cancellation turn working as the cancellation inductor is then integrated into a capacitor. Two different integration approaches are investigated and compared. Prototypes are finally tested in both one-stage and two-stage EMI filters. Experiments show that the proposed method works well for both rectangular and tubular film capacitors. The cancellation effects of the cancellation turn on the mutual inductance between the input and output capacitors and on the ESL of a capacitor are quantified through experiments. The measurements show the cancellation approach can achieve <-90 dB improvement in filtering performance above 1MHz for one-stage filters and the same above 400kHz for two-stage EMI filters.

References

- [1] S. Wang, F. C. Lee, D. Y. Chen and W. G. Odendaal, “Effects of Parasitic Parameters on EMI Filter Performance,” *Power Electronics, IEEE Transactions*, Volume 19, Issue 3, May 2004, pp. 869 – 877.
- [2] S. Wang, F. C. Lee and W. G. Odendaal, “Controlling the Parasitic Parameters to Improve EMI Filter Performance,” in *Proc. IEEE Applied Power Electronics Conference*, Anaheim, California 22-26, Feb. 2004, Volume 1, pp. 503 – 509.
- [3] S. Wang, W. G. Odendaal and F. C. Lee, “Extraction of Parasitic Parameters of EMI Filters Using Scattering Parameters,” in *Proc. IEEE Industry Applications Society Annual Meeting*, Seattle, WA, 3-7, Oct. 2004, Volume 4, pp. 2672 – 2678.
- [4] S. Wang, F. C. Lee and W. G. Odendaal, “Using Scattering Parameters to Characterize EMI Filters,” in *Proc. IEEE Power Electronics Specialists Conference*, Aachen, Germany, 20-25, Jun. 2004, pp. 297 – 303.
- [5] S. Wang, F. C. Lee and W. G. Odendaal, “Using a Network Method to Reduce the Parasitic Parameters of Capacitors,” in *Proc. IEEE Power Electronics Specialists Conference*, Aachen, Germany, 20-25, Jun. 2004, pp. 304 – 308.
- [6] R. Chen, J. D. van Wyk, S. Wang and W. G. Odendaal, “Application of Structural Winding Capacitance Cancellation for Integrated EMI Filters by Embedding Conductive Layers,” in *Proc. IEEE Industry Applications Society Annual Meeting*, Seattle, WA, 3-7, Oct. 2004, pp. 2679 – 2686.
- [7] T. C. Neugebauer, J. W. Phinney and D. J. Perreault, “Filters and components with inductance cancellation,” *IEEE Transactions, Industry Applications*, Volume 40, Issue 2, March/April. 2004, pp. 483 – 491.

- [8] T. C. Neugebauer and D. J. Perreault, "Filters with inductance cancellation using printed circuit board transformers," *IEEE Transactions, Power Electronics*, Volume 19, Issue 3, May. 2004, pp. 591-602.
- [9] T. C. Neugebauer, and D. J. Perreault, "Parasitic Capacitance Cancellation in Filter Inductors," in *Proc. IEEE Power Electronics Specialists Conference*, Aachen, Germany, 20-25, Jun. 2004, pp. 3102 - 3107.
- [10] EPCOS Film Capacitor Manual, EPCOS AG, Germany, 2000.
- [11] R. Anderson, "Test and Measurement Application Note 95-1 S-Parameters Techniques," Hewlett-Packard, 1997.
- [12] "Agilent AN154 S-Parameters Design Application Note," Agilent Technologies, 2000.

CHAPTER 5: SELF-PARASITIC PARAMETER CANCELLATION*

5.1. Introduction

Self-parasitic parameters in EMI filters include the equivalent series inductance (ESL) and the equivalent series resistance (ESR) of capacitors, and the equivalent parallel capacitance (EPC) and the equivalent parallel resistance (EPR) of inductors. For these parasitic parameters, ESL of DM capacitors and EPC of CM inductors play very important roles in HF performance of EMI filters. For the cancellation of EPC for CM inductors, paper [6] already proposed a method, so this chapter will concentrate on the cancellation of ESL for DM capacitors.

The equivalent series inductance (ESL) plays a very important role on capacitor high frequency (HF) performance. As important components of power converters, capacitors' HF performance significantly affects the noise peak-peak value at the converter's output and the HF conducted noise spectrum at the converter's input. It is well known that ESL and capacitance can resonate and make a capacitor perform like an inductor at HF range; therefore it is very important to reduce the ESL of capacitors. The capacitor performance is usually evaluated by the insertion voltage gain. The test setup and typical insertion voltage gain are shown in Figs. 5-1 and 5-2.

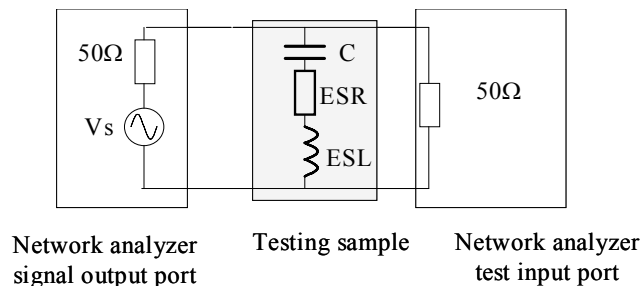


Fig. 5-1. Setup for evaluating the insertion voltage gain of a capacitor.

* © 2004 IEEE. Reprinted, with permission, from the Proc. IEEE Power Electronics Specialists Conference, Volume 1, pp. 304 -308. The original title is "Using A Network Method to Reduce the Parasitic Parameters of Capacitors."

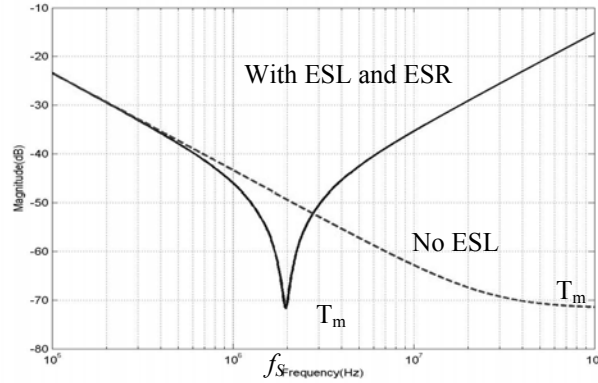


Fig.5-2. Insertion voltage gain curves of capacitors.

Two curves are shown in Fig. 5-2. One is the insertion voltage gain for a capacitor and the second one is the insertion voltage gain when ESL is zero. f_s is the series resonant frequency of the capacitor and T_m is the lowest value of the transfer-gain. They are given through (5-1, 5-2).

$$f_s = \frac{1}{2\pi\sqrt{ESL \times C}} \quad (5-1)$$

$$T_m \approx 20 \times \log\left(\frac{ESR}{25}\right) \quad (5-2)$$

If ESL is zero, the capacitor performance is significantly improved at HF range. The HF performance is determined by ESR only, and if ESR is reduced, HF performance can be further improved.

In this chapter, a method is proposed to reduce the effects of ESL and ESR, especially ESL, of capacitors. Experiments show that HF performance is greatly improved.

5.2. Network Theory of ESL and ESR Cancellation

For the network 1 shown in Fig. 5-3, it is well known that the port voltage and current satisfy the relationship defined by Z matrix, which is shown in (5-3, 5-4),

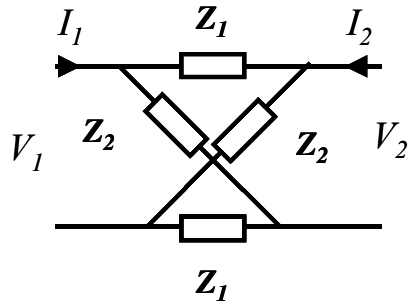


Fig.5-3. Network 1.

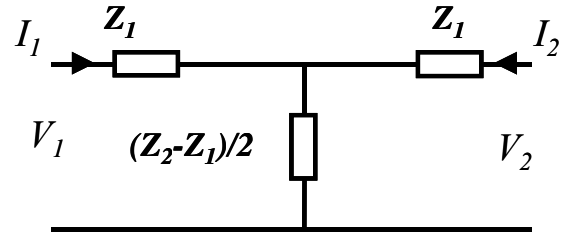


Fig. 5-4. Network 2.

$$\begin{pmatrix} V_1 \\ V_2 \end{pmatrix} = \begin{pmatrix} Z_{11} & Z_{12} \\ Z_{21} & Z_{22} \end{pmatrix} \begin{pmatrix} I_1 \\ I_2 \end{pmatrix}, \quad (5-3)$$

$$Z_{11} = \left. \frac{V_1}{I_1} \right|_{I_2=0}; Z_{12} = \left. \frac{V_1}{I_2} \right|_{I_1=0}; Z_{21} = \left. \frac{V_2}{I_1} \right|_{I_2=0}; Z_{22} = \left. \frac{V_2}{I_2} \right|_{I_1=0}. \quad (5-4)$$

The Z matrix can therefore be calculated through (5-4) as:

$$\mathbf{Z} = \begin{pmatrix} \frac{Z_2 + Z_1}{2} & \frac{Z_2 - Z_1}{2} \\ \frac{Z_2 - Z_1}{2} & \frac{Z_2 + Z_1}{2} \end{pmatrix}. \quad (5-5)$$

For the network 2, shown in Fig. 5-4, it can be proven that Z matrix is also given by (5-5). Because these two networks have the same Z matrix, they are equivalent. Two networks thus have same characteristics on two ports. Comparing these two networks, the impedances Z_1 in the network 1 are actually subtracted from Z_2 and are pushed to the two sides of the signal paths, as shown in the network 2. Based on this observation, ESL and

ESR of two capacitors can be cancelled using extra inductors and resistors. This idea is shown in Fig. 5-5.

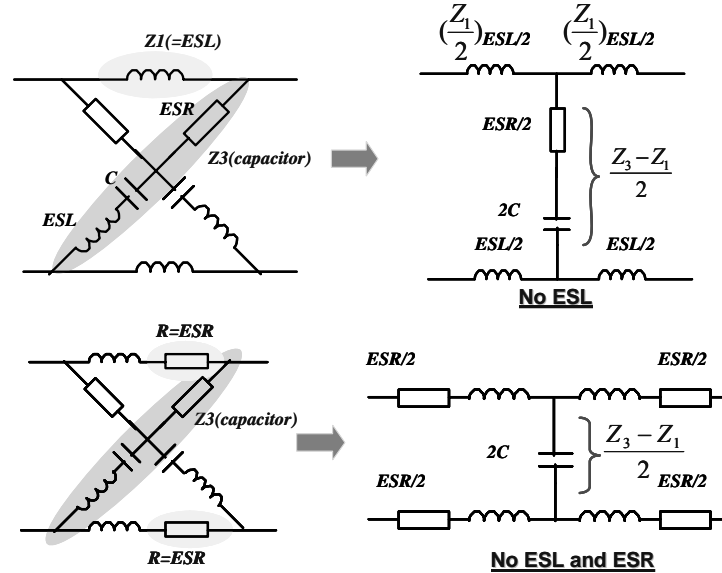


Fig. 5-5. ESL and ESR cancellation for capacitors.

In Fig. 5-5, two capacitors are diagonally connected. The cancellation inductors and resistors are connected on the top and bottom sides. It is obvious that under the ideal conditions, if the cancellation inductance is equal to ESL, then the effects of ESL on shunt path are cancelled. If cancellation resistance is equal to ESR, then the effects of ESR on shunt path are cancelled. The resultant networks are equivalent to noise filters because the ESL and ESR are on signal paths and capacitance is on a shunt path.

ESR and ESL can not be totally cancelled, because they are the functions of temperatures, frequencies and currents, however, they can be effectively reduced, thereby greatly improving the performance of the capacitors.

ESL is usually very small, so the cancellation inductors can be constructed using printed circuit board (PCB) windings or a piece of wire. The inductance for a rectangular PCB winding shown in Fig. 5-6 is given as (5-6) [1]:

$$L \approx \frac{\mu_0}{2\pi} \left[\begin{array}{l} 2l_2 \ln\left(\frac{2l_2}{w}\right) + 2l_1 \ln\left(\frac{2l_1}{w}\right) - 2l_2 \sinh^{-1}\left(\frac{l_2}{l_1}\right) - 2l_1 \sinh^{-1}\left(\frac{l_1}{l_2}\right) \\ + 4(l_1^2 + l_2^2)^{1/2} + (l_1 + l_2)\left(\frac{1}{6} - \frac{2}{3} \ln 2 - \frac{2\pi}{3}\right) \end{array} \right], \quad (5-6)$$

where, thickness of the PCB winding is ignored.

The cancellation resistors are in series with the cancellation windings. Two capacitors are not necessarily placed like the pattern shown in Fig. 5-5. They can be placed side by side making the idea easy to implement in a practical PCB layout.

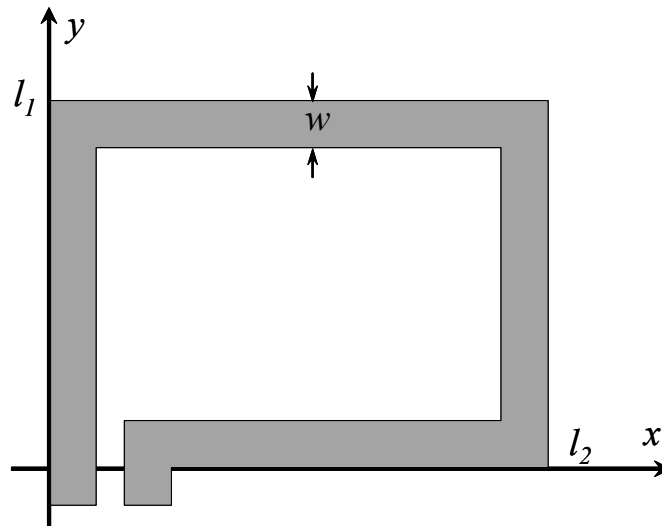


Fig. 5-6. One turn rectangular PCB winding.

5.3. Experimental Results

5.3.1 Implementation on PCB

To implement the cancellation technique on PCB is easy. In Fig. 5-7, two film capacitors are placed side by side on PCB. The cancellation windings are realized using rectangular PCB windings. Cancellation resistors are soldered in series with the PCB windings. For the design of the cancellation turn in Fig. 5-6, w is determined by operation current and thickness of copper layer; l_2 is determined by the physical distance of two capacitors and then l_1 is found through (5-6). The inductances to be cancelled include the ESL of capacitors and parasitic inductance of pins and PCB layout. The final l_1 and l_2 are tuned by conducting experiments because of the effects of parasitics on PCB.

For electrolytic capacitors, the PCB layout is almost same, while for high current application, cancellation resistors may not be anticipated because of the loss they may introduce.

The prototypes are shown in Figs. 5-8 and 5-9.

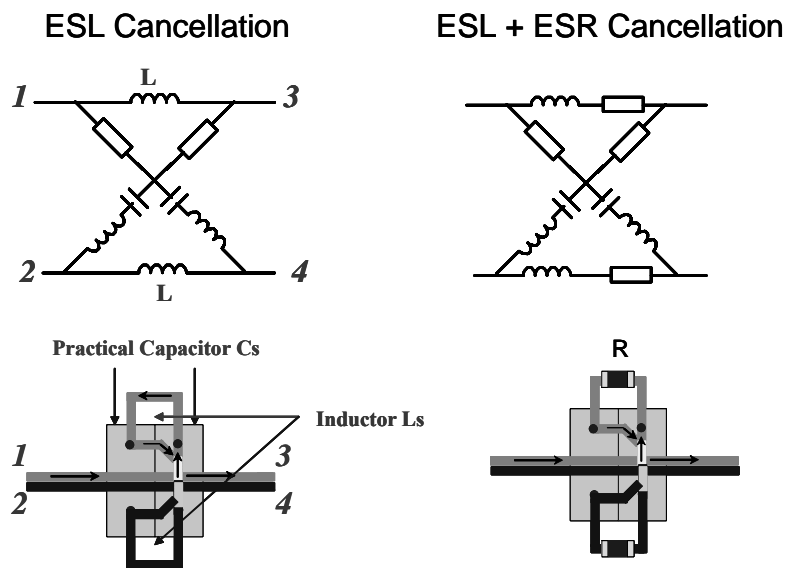


Fig. 5-7. Implementation of ESL and ESR cancellation on PCB.

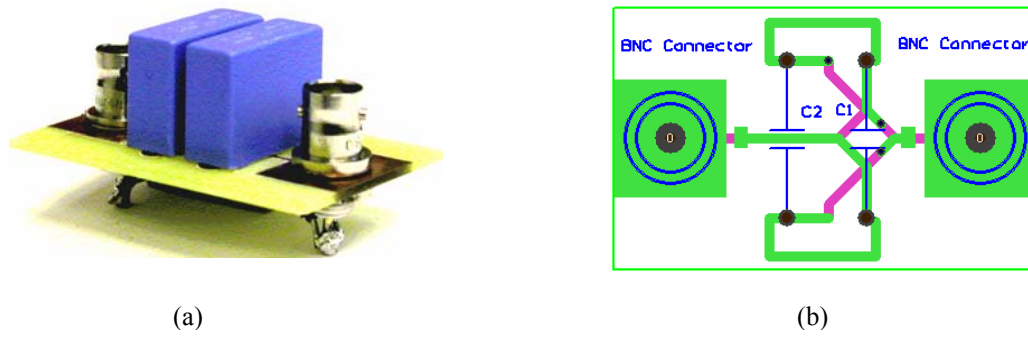


Fig. 5-8. Implementation for two 0.47uF/400V film capacitors: (a) prototype and (b) PCB layout.



Fig. 5-9. Implementation for two 220uF/250V electrolytic capacitors.

5.3.2 Measurement Results

The prototype of film capacitors is first measured. Measurements are carried out in both frequency and time domains. The equivalent measurement setup for time domain is shown in Fig. 5-10 and the measured waveforms are shown in Fig. 5-11.

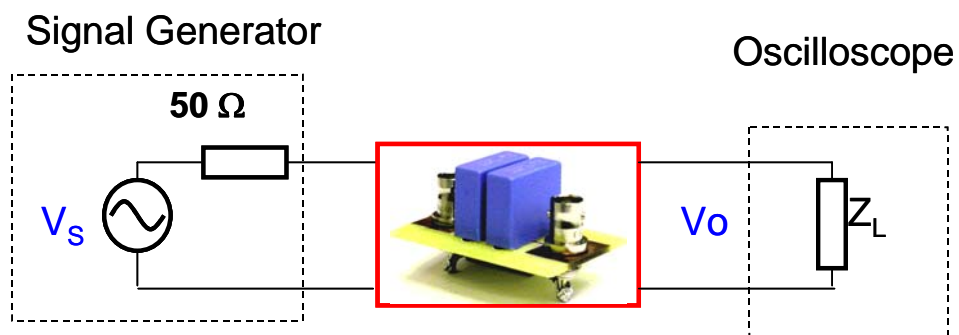
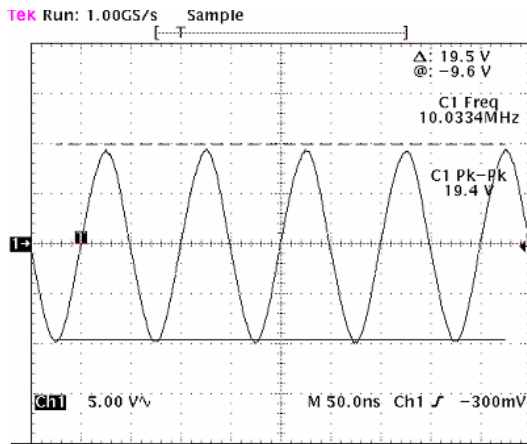
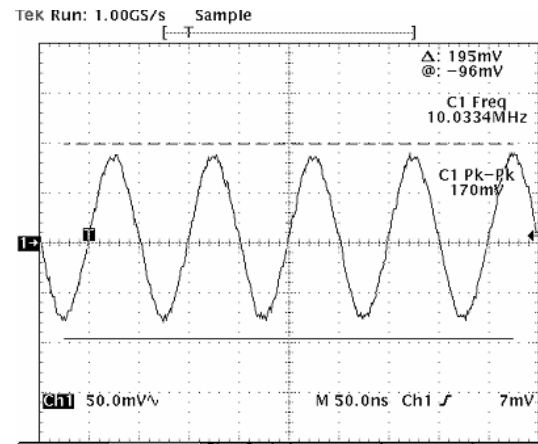


Fig. 5-10. Equivalent measurement setup in time domain.

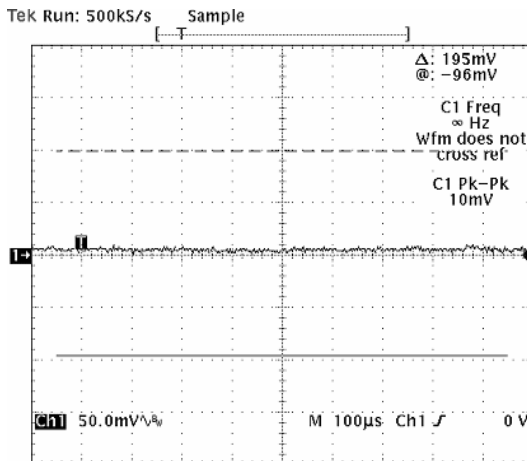
In Fig. 5-11, the signal generator's output is a 10MHz sinusoidal wave with 19.4V peak-to-peak value. Two measurements are then conducted. The first measures the output voltage of two parallel capacitors. The cancellation prototype is measured with the second measurement. From Fig. 5-11, after ESL is cancelled, the voltage ripple (10MHz) on capacitors is smaller than 10mV. This is much smaller than 170mV in the case without the cancellation because the self resonant frequency of the capacitor is around 2 MHz.



(a) Input voltage ripple.



(b) Voltage ripple of two parallel capacitors.



(c) Voltage ripple of ESL cancelled capacitors.

Fig. 5-11. Comparison of measured results.

The equivalent measurement setup for frequency domain is shown in Fig. 5-12 and measured insertion voltage gains are shown in Fig. 5-13.

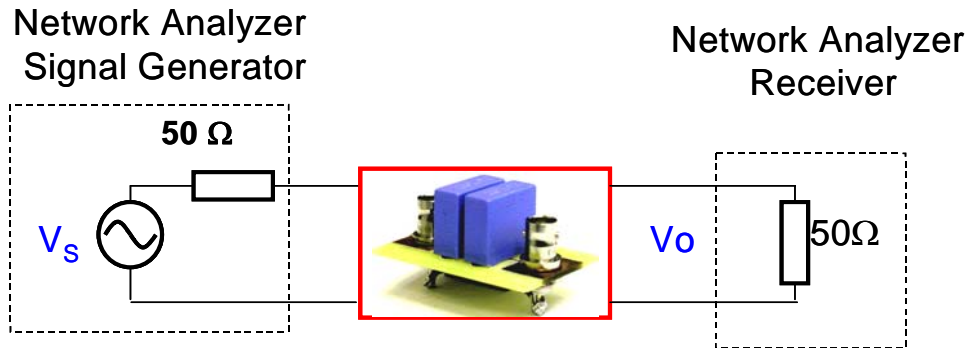


Fig. 5-12. Equivalent measurement setup in frequency domain.

Three curves are shown in Fig. 5-13. The first curve is the two parallel capacitors, the second curve is ESL cancellation and the last curve is both ESL and ESR cancellation. This shows that after ESL is cancelled, a 25dB improvement is achieved at 30MHz. Fig. 5-13 also shows that, after ESR is reduced, improvement at high frequency range is further increased to 27dB. Because ESR is just an equivalent loss of capacitors, it is the function of many parameters. As a result, ESR cancellation is not as good as we expected.

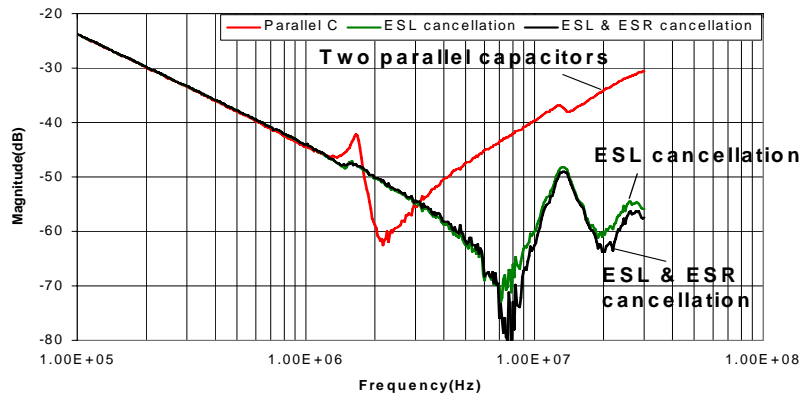


Fig. 5-13. Comparison of insertion voltage gains for film capacitors.

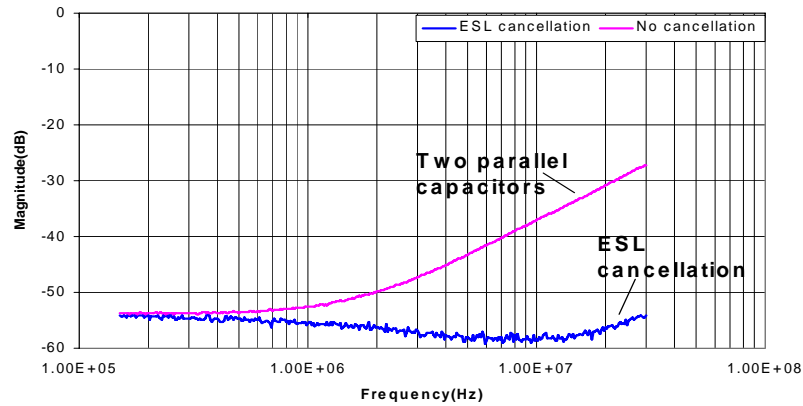


Fig. 5-14. Comparison of insertion voltage gains for electrolytic capacitors.

The bump between 10MHz and 20MHz is caused by the transmission line structure of film capacitors [3], which makes capacitor HF performance worse and ESL cancellation not as good as we expected.

Fig. 5-14 shows the measured insertion voltage gains for the prototype of electrolytic capacitors. This figure also shows that the performance of electrolytic capacitors in HF range (above 1MHz) is greatly improved. The prototype's performance at 30MHz is factually almost the same as it would be at 100 kHz, which implies no extra small HF capacitors are needed to parallel with them. The prototype achieved more than 27dB improvement at 30 MHz compared to the one without ESL cancellation. The self-resonant frequency of investigated electrolytic capacitors is lower than 100 kHz, so the curve shape is different from the cases in Fig. 5-13. Fig. 5-2 and equation (5-2) explain the flat frequency response. Because ESL is cancelled, only ESR affects capacitor performance, resulting in a frequency response that is flat. Because electrolytic capacitors are usually used for output and input filters in converters, high frequency current and voltage ripples can be significantly reduced.

5.3.3 Application for a Noise Filter

When the proposed method is used in a Γ (LC) type EMI filter, as shown in Fig. 5-15, much attention should be paid to prevent the couplings between capacitors and the inductor [4]. Measures must be taken to reduce parasitic couplings [4, 5]. For example, for a typical two-winding inductor of EMI filters, the inductor windings are proposed to rotate by 90° to greatly reduce the coupling between the inductor and capacitors [4, 5]. When the couplings are minimized, the EMI filter performance can be further improved through the reduction of capacitor parasitics.

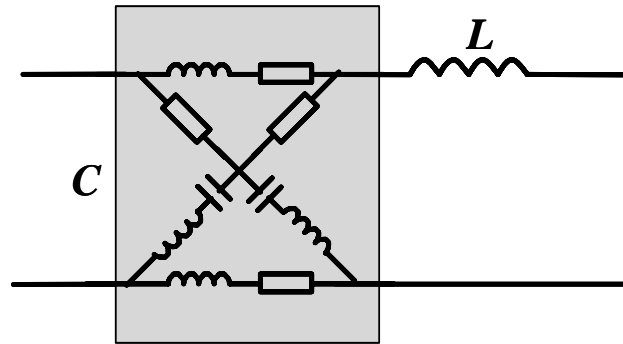


Fig. 5-15. Application for a Γ type EMI filter.

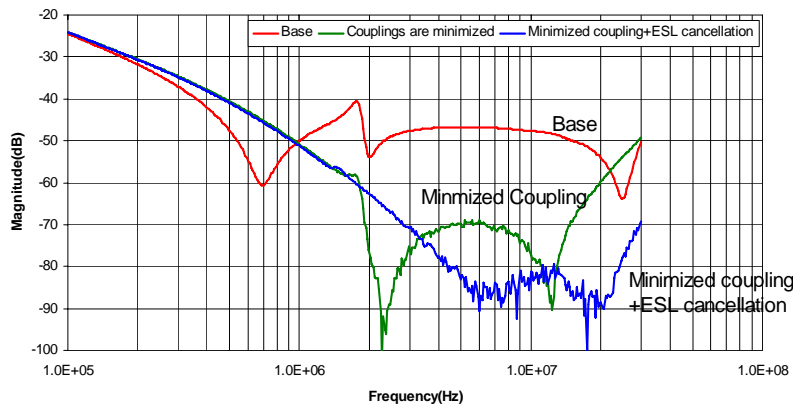


Fig. 5-16. Comparison of insertion voltage gains for a Γ type filter.

In Fig. 5-16, three Γ type filters are measured. The first one is a Γ type filter whose capacitor is composed of two parallel capacitors. The measured insertion voltage gain is the curve named base. The difference between the first and the second one is that, the couplings between inductor and capacitors are minimized for the second one. The last one is with both minimized couplings and ESL cancellation. The self-resonance frequency of capacitor is 2MHz. From Fig. 5-16, after the coupling between the inductor and capacitors are reduced, filter performance is significantly improved above 1MHz. After ESL is cancelled the filter performance is further improved. There is a 30dB at 20MHz, and a 20dB at 30MHz improvement achieved. For the filter without ESL cancellation, the effects of ESL are obvious around 2 MHz. On the contrary, for the filter with ESL cancellation, there is no resonance observed around 2 MHz and the insertion voltage gain goes down to a higher attenuation as frequency increases.

Based on these experiments, the proposed method is easily implemented in practical PCB layouts and can drastically improve the capacitor performance. It should be pointed out that the proposed cancellation method employs a balanced network structure. That means it would not cause any unbalanced problems such as the transformation between CM and DM noises.

5.4. Summary

In this chapter, a novel method is proposed to reduce the ESL and ESR of capacitors. The idea is implemented to prototypes for both film and electrolytic capacitors. The experiments are carried out in both frequency and time domains to evaluate the proposed

method. The experiments prove that the performance of capacitors is greatly enhanced. Finally, the method is used in a practical Γ type EMI filter. The filter performance is much improved in high frequency range and the effective operating frequency range is greatly broadened. The proposed method would be very useful for reduction of EMI and HF voltage ripple.

References

- [1] M. A. Bueno and A. K. T. Assis. J. Phys. D: Appl. 28, 1802 (1995).
- [2] Norman Balabanian and Theodore Bickart, “*Linear Network Theory: Analysis, Properties, Design and Synthesis*,” Matrix Publishers, Inc., 1981.
- [3] Lingyin Zhao, J. D. Van Wyk, “A Generalized Two Conductor Model for Integrated Passive Components,” *In Proc. of CPES seminar 2002*, Blacksburg, April 14-18, pp. 428-433.
- [4] Shuo Wang, F. C. Lee, D.Y. Chen and W.G. Odendaal, “Effects of Parasitic Parameters on EMI Filter Performance,” *Power Electronics, IEEE Transactions*, Volume 19, Issue 3, May 2004, pp. 869 – 877.
- [5] Shuo Wang, F. C. Lee and W.G. Odendaal, “Controlling the Parasitic Parameters to Improve EMI Filter Performance,” in *Proc. IEEE Applied Power Electronics Conference*, Anaheim, California 22-26, Feb. 2004, Volume 1, pp. 503 – 509.
- [6] R. Chen, J. D. van Wyk, S. Wang and W. G. Odendaal, “Application of Structural Winding Capacitance Cancellation for Integrated EMI Filters by Embedding Conductive Layers,” in *Proc. IEEE Industry Applications Society Annual Meeting*, Seattle, WA, 3-7, Oct. 2004, pp. 2679 – 2686.

CHAPTER 6: Mode Transformation due to the Imperfect of

Balanced Structure

6.1. Introduction

In power electronics area, in order to efficiently analyze and design EMI filters, the filters are usually decoupled to DM and CM filters. DM and CM attenuation of filters can then be analyzed respectively. This decoupling is based on the assumption that EMI filters have perfectly balanced circuit structures. As shown in Fig. 6-1, it is assumed that, L_{CM1} equals L_{CM2} , C_{Y1} equals C_{Y2} and L_{DM1} equals L_{DM2} . The PCB layout is also perfectly balanced. As a result, CM current would not flow through DM capacitors C_1 and C_2 ; and the DM voltage potential on the center line is zero for DM noise. The EMI filters can then be decoupled to a CM filter and a DM filter as shown in Fig. 6-2.

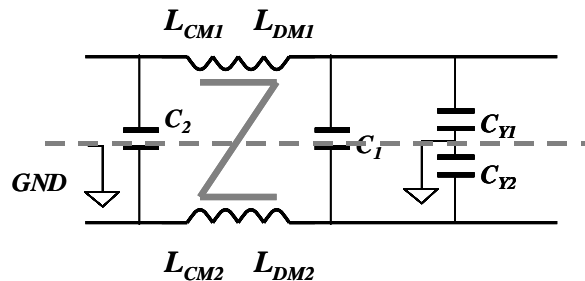


Fig. 6-1. EMI filter with balanced circuit structure.

For this decoupling approach, it is assumed that DM and CM noise is independent of each other, so the DM and CM attenuations of the filter can be evaluated separately. In a practical case, strictly speaking, component parameters such as L_{CM1} and L_{CM2} , C_{Y1} and C_{Y2} , L_{DM1} and L_{DM2} are not perfectly balanced, so DM and CM filters can not be totally decoupled as shown in Fig. 6-2. DM and CM noise can transform to each other due to the unbalances. Fig. 6-3 shows a measured transmission coefficient S_{CD21} (mixed mode S-

parameter) with DM excitation and CM response. It is compared with the measured S_{CC21} with CM excitation and CM response. The measurement is carried out using Agilent E5070B 4-port balance RF network analyzer.

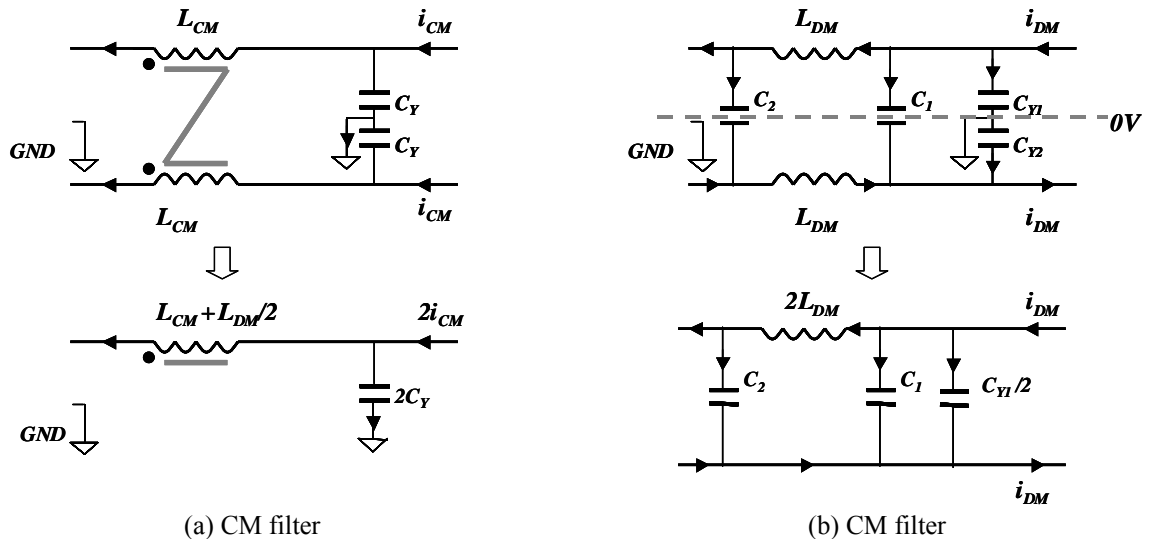


Fig. 6-2. Decoupling EMI filters to CM and DM filters.

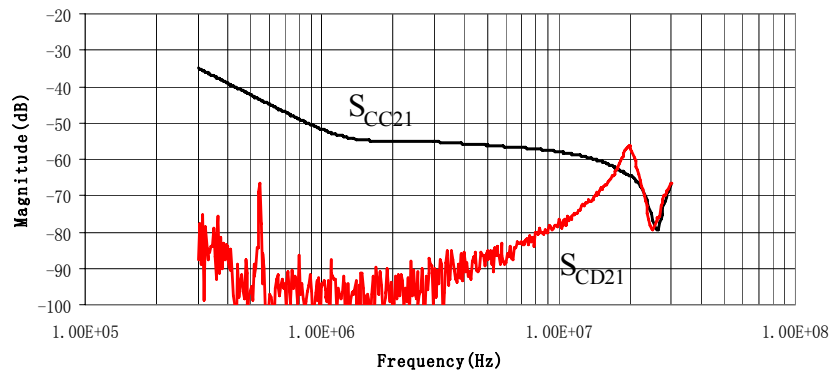


Fig. 6-3. Comparison of measured S_{CD21} and S_{CC21} .

It is shown that S_{CD21} is as high as S_{CC21} above 22MHz and even higher around 20MHz. This could be a problem on EMI filter design and noise attenuation. For example, DM noise is 120dB μ V and CM noise is 100dB μ V at 20MHz before the EMI

filter is inserted. After the filter is connected into the circuit, the CM noise is attenuated to 37dB μ V by the CM filter. At the same time, the CM noise transformed from the DM noise is 63dB μ V, which is much higher than the attenuated CM noise. This could make filter design inefficient, since it is not expected in the EMI filter design. The traditional decoupling method for CM and DM signal analysis is difficult to apply to this case because DM and CM filters are coupled together. For example, in Fig. 6-1, if C_{Y1} and C_{Y2} are not balanced, part of CM noise would transform to DM noise on these two CM capacitors. The transformed DM noise would then be attenuated by the DM inductor and DM capacitor C_2 . The noise generated by CM excitation therefore partly flows through CM filter and partly flows through DM filter. For the traditional decoupling method, CM noise is supposed to flow in CM filter only and DM noise is supposed to flow in DM filter only, so it can not give correct answers.

6.2. Analysis of Mode Transformation

Not all components in EMI filters can cause the mode transformation between CM and DM noise. In Fig. 6-4, DM capacitors C_1 and C_2 are across two lines so there are no balance issues. As a result, they would not cause mode transformation. Instead, DM inductors L_{DM1} and L_{DM2} , CM inductors L_{CM1} and L_{CM2} and CM capacitors C_{Y1} and C_{Y2} can cause mode transformation.

At high frequencies, parasitics determine the performance of components, so their unbalances determine mode transformation. The equivalent parallel winding capacitance EPC_1 and EPC_2 of inductors, equivalent series inductance ESL_{Y1} and ESL_{Y2} of capacitors

would cause mode transformation. Mutual couplings between DM inductors L_{DM1} , L_{DM2} and other components, trace loops can also generate unbalances. It is assumed in this chapter that these couplings are minimized by rotating inductor winding by 90° . The mutual coupling between two DM capacitors would not cause mode transformation; however it affects the propagation of DM noise in high frequency range, so it should be considered in the analysis of mode transformation from CM to DM. The mutual coupling between input and output trace loops can also be ignored by minimizing trace loop areas. For a general case shown in Fig. 6-4, the load of EMI filters are power lines terminated by two balanced LISNs and unbalanced converter source.

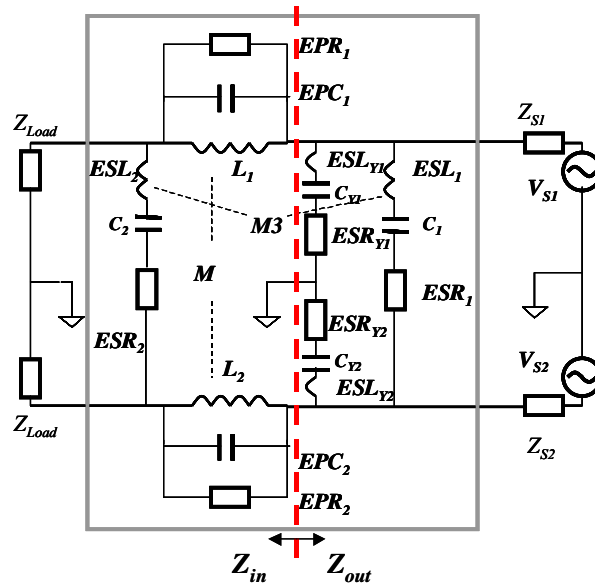


Fig. 6-4. EMI Filter including parasitic parameters.

6.2.1 Partition of the Filter

At the interface, which is defined by the dash line in Fig. 6-4, the output impedance Z_{out} of right part is much smaller than the input impedance Z_{in} of the left part. It is

resulted from the mismatch rule in EMI filter design. The EMI filter can be split into two mismatched networks. For the right part, the circuit is represented by Fig. 6-5 using impedances. In the left part, DM inductors L_{DM1} and L_{DM2} are not coupled since they are the leakage of CM inductors L_{CM1} and L_{CM2} . CM inductors L_{CM1} and L_{CM2} are coupled at frequencies before the parallel resonant frequency of L_{CM} and EPC and not coupled after that. The coupled inductor can be decoupled as shown in Fig. 6-6. After the inductors are decoupled, all components in the left part are no longer coupled. The left part in Fig. 6-4 can then be replaced by Fig. 6-7 using impedances.

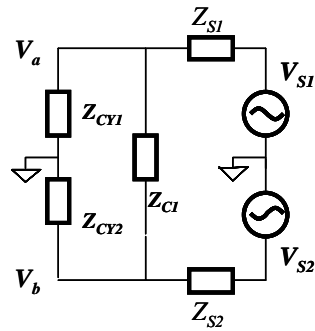


Fig. 6-5. Representing the right part using impedances.

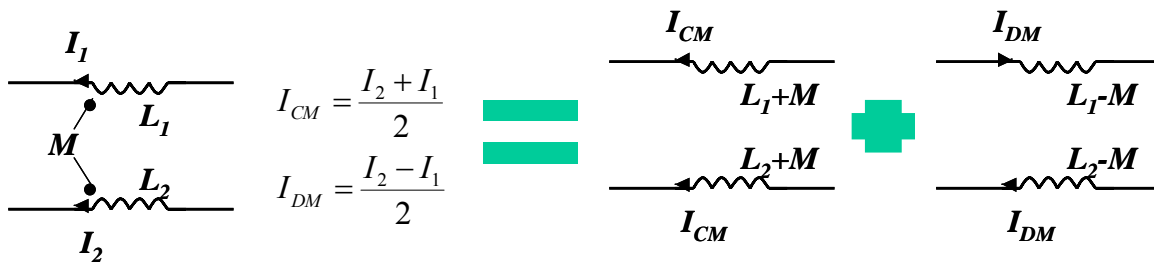


Fig. 6-6. Decoupling DM and CM inductors.

Because noise sources are unbalanced, the excitations in Fig. 6-5 are composed of both DM excitation V_D and CM excitation V_C . They are given by (6-1, 6-2). The outputs of the right part are V_a and V_b . V_a and V_b can be represented using a DM response V_{DM}

and CM response V_{CM} . They are given by (6-3, 6-4). The V_{DM} and V_{CM} then work as the excitations of the left part shown in Fig. 6-7. The output impedances of the right part are ignored in Fig. 6-7 since they are much smaller than the input impedances of the left part.

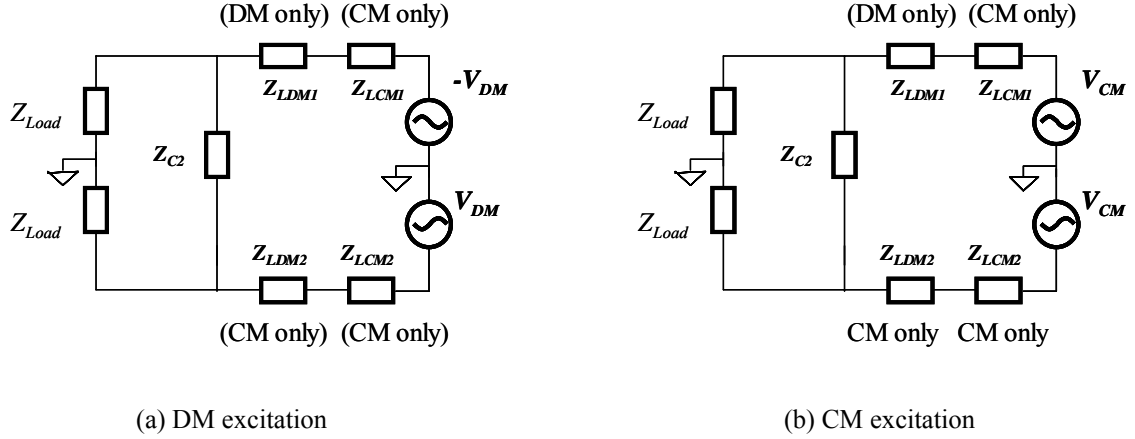


Fig. 6-7. Representing the left part using impedances.

$$V_D = \frac{V_{S2} - V_{S1}}{2} \quad (6-1)$$

$$V_C = \frac{V_{S2} + V_{S1}}{2} \quad (6-2)$$

$$V_{DM} = \frac{V_b - V_a}{2} \quad (6-3)$$

$$V_{CM} = \frac{V_b + V_a}{2} \quad (6-4)$$

6.2.2 Analysis of DM Excitation

The unbalances and the average values of the noise source impedances, CM capacitors, DM and CM inductor are defined in (6-5, 6-7, 6-9 and 6-11). The noise source impedances, the impedances of CM capacitors, the impedances of CM and DM inductors can then be expressed using these two parameters in (6-6, 6-8, 6-10 and 6-12).

$$\Delta Z_S = \frac{Z_{S2} - Z_{S1}}{2}, Z_S = \frac{Z_{S2} + Z_{S1}}{2}, \quad (6-5)$$

$$Z_{S1} = Z_S - \Delta Z_S, Z_{S2} = Z_S + \Delta Z_S, \quad (6-6)$$

$$\Delta Z_{CY} = \frac{Z_{CY2} - Z_{CY1}}{2}, Z_{CY} = \frac{Z_{CY2} + Z_{CY1}}{2}, \quad (6-7)$$

$$Z_{CY1} = Z_{CY} - \Delta Z_{CY}, Z_{CY2} = Z_{CY} + \Delta Z_{CY}. \quad (6-8)$$

$$\Delta Z_{LDM} = \frac{Z_{LDM2} - Z_{LDM1}}{2}, Z_{LDM} = \frac{Z_{LDM2} + Z_{LDM1}}{2}, \quad (6-9)$$

$$Z_{LDM1} = Z_{LDM} - \Delta Z_{LDM}, Z_{LDM2} = Z_{LDM} + \Delta Z_{LDM}. \quad (6-10)$$

$$\Delta Z_{LCM} = \frac{Z_{LCM2} - Z_{LCM1}}{2}, Z_{LCM} = \frac{Z_{LCM2} + Z_{LCM1}}{2}, \quad (6-11)$$

$$Z_{LCM1} = Z_{LCM} - \Delta Z_{LCM}, Z_{LCM2} = Z_{LCM} + \Delta Z_{LCM}. \quad (6-12)$$

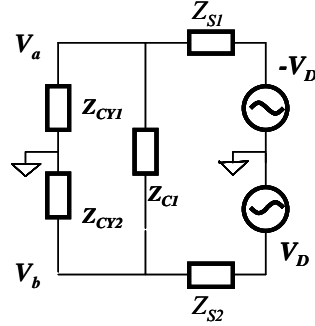


Fig. 6-8. DM excitation on the right part.

The noise excitations are decoupled to DM and CM in (6-1) and (6-2). For the DM excitation in Fig. 6-8, the DM and CM responses defined in (6-3) and (6-4) are calculated by solving network equations. Ignoring all second order terms, the final results are shown in (6-13, 6-14). (6-13)

$$\dot{V}_{DM} \approx \frac{\dot{V}_D}{Z_S} \frac{1}{1/(Z_{CI}/2) + 1/Z_S + 1/Z_{CY}} \quad (6-14)$$

$$\dot{V}_{CM} \approx \frac{\dot{V}_D}{(Z_S + Z_{CY})} \left\{ \frac{\Delta Z_{CY}}{Z_{CY}} \frac{1}{[1/(Z_{CI}/2) + 1/Z_S + 1/Z_{CY}]} - \frac{\Delta Z_S}{Z_S} Z_{CY} \left[1 - \frac{1}{Z_S [1/(Z_{CI}/2) + 1/Z_S + 1/Z_{CY}]} \right] \right\} \quad (6-15)$$

$$Z_{CI} \rightarrow 0 \Rightarrow \dot{V}_{CM} \rightarrow -\frac{Z_{CY} \dot{V}_D}{(Z_S + Z_{CY})} \frac{\Delta Z_S}{Z_S}$$

The attenuation on DM noise is given by (6-13). The transformation from DM to CM noise is given by (6-14). It is shown that the transformation has a linear relationship with the unbalance. ΔZ_{CY} and ΔZ_S can be positive and negative, so the total effects of the unbalances would be the sum or difference of the effects of two unbalances. From (6-15), even if Z_{C1} is zero, the transformation still can not be eliminated. The effects of the unbalanced DM noise source can not therefore be eliminated using a balance capacitor.

The DM and CM responses of the right part act as the DM and CM excitations of the left part, which is shown in Fig. 6-7. The final CM and DM responses on loads due to these two excitations are given by (6-16, 6-17).

$$\dot{V}_{LoadCM} = \frac{Z_{Load}}{(Z_{LCM} + Z_{Load})} \left(\dot{V}_{CM} - \frac{\Delta Z_{LDM}}{Z_{LDM}} \dot{V}_{DM} \right) \quad (6-16)$$

$$\dot{V}_{LoadDM} = \frac{Z_{C2}}{2Z_{LDM}} \left(\dot{V}_{DM} - \frac{\Delta Z_{LCM}}{(Z_{LCM} + Z_{Load})} \dot{V}_{CM} \right) \quad (6-17)$$

Substituting (6-13, 6-14) into (6-16, 6-17) and ignoring all second order terms, final expressions for DM and CM responses are given by (6-18 - 6-23).

$$\dot{V}_{LoadDM} \approx k_D \dot{V}_D \quad (6-18)$$

$$\dot{V}_{LoadCM} \approx \left[-k_1 \frac{\Delta Z_S}{Z_S} + k_2 \frac{\Delta Z_{CY}}{Z_{CY}} - k_3 \frac{\Delta Z_{LDM}}{Z_{LDM}} \right] \dot{V}_D \quad (6-19)$$

$$k_D = \frac{Z_{C2}}{2Z_{LDM}Z_S} \frac{1}{1/(Z_{C1}/2) + 1/Z_S + 1/Z_{CY}} \quad (6-20)$$

$$k_3 = \frac{Z_{Load}}{(Z_{LCM} + Z_{Load})Z_S} \frac{1}{[1/(Z_{C1}/2) + 1/Z_S + 1/Z_{CY}]} \quad (6-21)$$

$$k_2 = \frac{1}{(1 + Z_{CY}/Z_S)} k_3 \quad (6-22)$$

$$k_1 = \frac{1/(Z_{C1}/2) + 1/Z_{CY}}{(1/Z_{CY} + 1/Z_S)} k_3 = \left(1 + \frac{2Z_{CY}}{Z_{C1}} \right) k_2 \quad (6-23)$$

It is shown that the CM response due to the unbalanced parameters is composed of three parts. The first part is due to the unbalanced noise source impedances and the second part is due to the unbalanced CM capacitors. The last part is due to the unbalanced DM inductors. The mode transformation has linear relationship with these unbalances. The unbalances on the signal paths lead to positive coefficients and those on shunt paths lead to negative coefficients in the mode transformation equation.

6.2.3 Analysis of CM Excitation

The right part when the excitation is CM is shown in Fig. 6-9. Using the same definitions as (6-5 – 6-12), the DM and CM responses defined in (6-3) and (6-4) are calculated by solving network equations. Ignoring all second order terms, the final results are given by (6-24, 6-25).

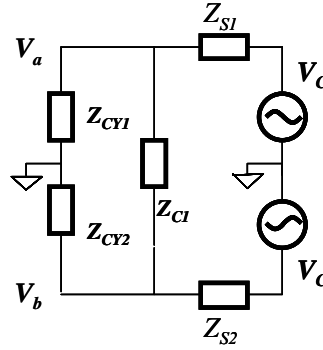


Fig. 6-9. CM excitation on right part.

$$\dot{V}_{CM} \approx \frac{Z_{CY}}{Z_{CY} + Z_S} \dot{V}_C \quad (6-24)$$

$$\dot{V}_{DM} \approx \frac{\dot{V}_C}{(Z_S + Z_{CY})[1/(Z_{C1}/2) + 1/Z_S + 1/Z_{CY}]} \left(\frac{\Delta Z_{CY}}{Z_{CY}} - \frac{\Delta Z_S}{Z_S} \right) \quad (6-25)$$

$$Z_{C1} \rightarrow 0 \Rightarrow \dot{V}_{DM} \rightarrow 0 \quad (6-26)$$

The transformation from CM to DM is composed of two parts. The first part is due to the unbalanced CM capacitors and the second part is due to the unbalanced noise source impedances. ΔZ_{CY} and ΔZ_S can be positive and negative, so the total effects of the unbalances would be the sum or difference of the effects of two unbalances. Unlike the transformation from DM to CM, for the transformation from CM to DM, if Z_{C1} is zero, an ideal capacitor, the mode transformation can be eliminated.

The DM and CM responses of the right part act as the excitations of the left parts shown in Fig. 6-7. The final responses are still given by (6-16, 6-17). Substituting (6-24, 6-25) into (6-16, 6-17) and ignoring all second order terms, the final expressions for DM and CM responses are given by (6-27 - 6-32).

$$\dot{V}_{LoadCM} \approx k_C \dot{V}_C \quad (6-27)$$

$$\dot{V}_{LoadDM} = \left[-k_5 \frac{\Delta Z_S}{Z_S + Z_{CY}} + k_6 \frac{\Delta Z_{CY}}{Z_S + Z_{CY}} - k_7 \frac{\Delta Z_{LCM}}{Z_{LCM} + Z_{Load}} \right] \dot{V}_C \quad (6-28)$$

$$k_C = \frac{Z_{Load} Z_{CY}}{(Z_{LCM} + Z_{Load})(Z_S + Z_{CY})} \quad (6-29)$$

$$k_5 = \frac{Z_{C2}}{2Z_{LDM} Z_S} \frac{1}{[1/(Z_{C1}/2) + 1/Z_S + 1/Z_{CY}]} = \frac{Z_{CY}}{Z_S} k_6 \quad (6-30)$$

$$k_6 = \frac{Z_{C2}}{2Z_{LDM} Z_{CY}} \frac{1}{[1/(Z_{C1}/2) + 1/Z_S + 1/Z_{CY}]} \quad (6-31)$$

$$k_7 = \frac{Z_{C2} Z_{CY}}{2Z_{LDM} (Z_S + Z_{CY})} \quad (6-32)$$

It is shown that the DM response due to unbalances is composed of three parts. The first part is due to the unbalanced noise source impedances and the second part is due to the unbalanced CM capacitors. The last part is due to the unbalanced impedances of inductors. The mode transformation has linear relationship with these unbalances. The

unbalances on the signal paths lead to positive coefficients and those on shunt paths lead to negative coefficients in the mode transformation equation.

If the mutual coupling between two DM capacitors is considered, (6-28) is rewritten as (6-33). Z_{M3} is the impedance of mutual inductance M_3 between two DM capacitors. M_3 do not affect the propagation of CM noise.

$$\dot{V}_{LoadDM} = \left[-k_5 \frac{\Delta Z_S}{Z_S + Z_{CY}} + k_6 \frac{\Delta Z_{CY}}{Z_S + Z_{CY}} - k_7 \frac{\Delta Z_{LCM}}{Z_{LCM} + Z_{Load}} + (-k_9 \frac{\Delta Z_S}{Z_S + Z_{CY}} + k_{10} \frac{\Delta Z_{CY}}{Z_S + Z_{CY}}) Z_{M3} \right] \dot{V}_C \quad (6-33)$$

$$Z_{M3} = j\omega M_3 \quad (6-34)$$

$$k_9 = \frac{2}{Z_S Z_{C1}} \frac{1}{[1/(Z_{C1}/2) + 1/Z_S + 1/Z_{CY}]} \quad (6-35)$$

$$k_{10} = \frac{2}{Z_{CY} Z_{C1}} \frac{1}{[1/(Z_{C1}/2) + 1/Z_S + 1/Z_{CY}]} \quad (6-36)$$

6.2.4 Summary of the Effects of Unbalances

For a general case shown in Fig. 6-10, the general expressions for mode transformation due to unbalances are shown (6-37, 6-38). If the mutual coupling between two DM capacitors is considered, two more terms as in (6-33) should be included in (6-37, 6-38).

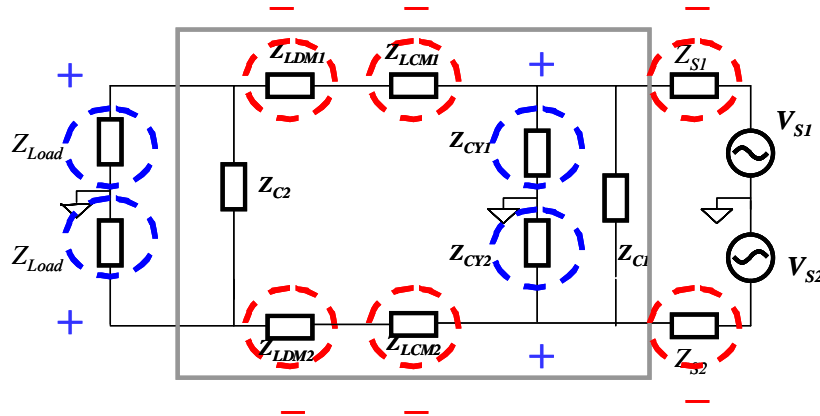


Fig. 6-10. Effects of unbalance on EMI filter Performance.

Fig. 6-10 includes the unbalance of loads. (6-37, 6-38) hold true when the second and above orders are ignored. This means the unbalance should not be too large. One example is if the noise source Z_{S2} is three times of Z_{S1} , the unbalance of Z_S for DM to CM mode transformation is then 50%. The calculation error can be up to 12%. For components, the unbalances are usually very small, for example, smaller than 10%, so the calculation result is accurate enough.

In Fig. 6-10, the unbalances on signal paths have negative coefficients in (6-37, 6-38). On the other hand, the unbalances on shunt paths have positive coefficients in (6-37, 6-38). The total effect of all unbalances on mode transformation is the sum of all unbalances multiplied by their coefficients and the excitation.

$$\dot{V}_{LoadCM} \approx [-k_1 \frac{\Delta Z_S}{Z_S} + k_2 \frac{\Delta Z_{CY}}{Z_{CY}} - k_3 \frac{\Delta Z_{LDM}}{Z_{LDM}} + k_4 \frac{\Delta Z_{Load}}{Z_{Load}}] \dot{V}_D \quad (6-37)$$

$$\dot{V}_{LoadDM} \approx [-k_5 \frac{\Delta Z_S}{(Z_S + Z_{CY})} + k_6 \frac{\Delta Z_{CY}}{(Z_S + Z_{CY})} - k_7 \frac{\Delta Z_{LCM}}{(Z_{LCM} + Z_{Load})} + k_8 \frac{\Delta Z_{Load}}{(Z_{LCM} + Z_{Load})}] \dot{V}_C \quad (6-38)$$

If more stages are cascaded, the general expression for mode transformations can be given by (6-39, 6-40).

$$\dot{V}_{LoadCM} \approx [\sum_{n=1}^m k_n \frac{\Delta Z_n}{Z_n} - \sum_{p=1}^q k_p \frac{\Delta Z_p}{Z_p}] \dot{V}_D \quad (6-39)$$

$$\dot{V}_{LoadDM} \approx [\sum_{n=1}^{m,q} \frac{k_n \Delta Z_n - k_p \Delta Z_p}{Z_n + Z_p}] \dot{V}_C \quad (6-40)$$

In (6-39, 6-40), Z_n is the impedance on signal path and ΔZ_n is its unbalance. k_n is its coefficient. Z_p is the impedance on shunt path and ΔZ_p is its unbalance. k_p is its coefficient. $Z_n + Z_p$ is actually the impedance of CM path. Effects of these unbalances on mode transformation depend on both the unbalances and their coefficients.

6.3. Experiments

In the experiment, a one-stage EMI filter is investigated. Both source and load impedances are balanced, which is achieved by network analyzer Agilent E5070B. The practical CM capacitors and filter inductors, which cannot be perfectly balanced, are measured using precision impedance analyzer HP4294A.

The measurement results of CM capacitors are shown in Fig. 6-11. The R-L-C series equivalent circuits are also derived from the figure. For C_{Y1} , they are $74\text{m}\Omega$, 9.96nH and 6.9nF . For C_{Y2} , they are $66.8\text{m}\Omega$, 9.8nH and 7.54nF . The unbalance $\Delta Z_{CY}/Z_{CY}$ is shown in Fig. 6-12. It is as high as 0.46 at resonant frequencies of CM capacitors.

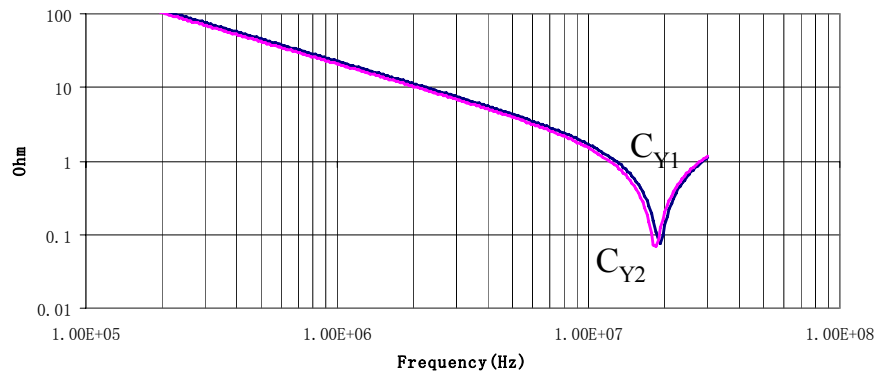


Fig. 6-11. Impedances of two CM capacitors.

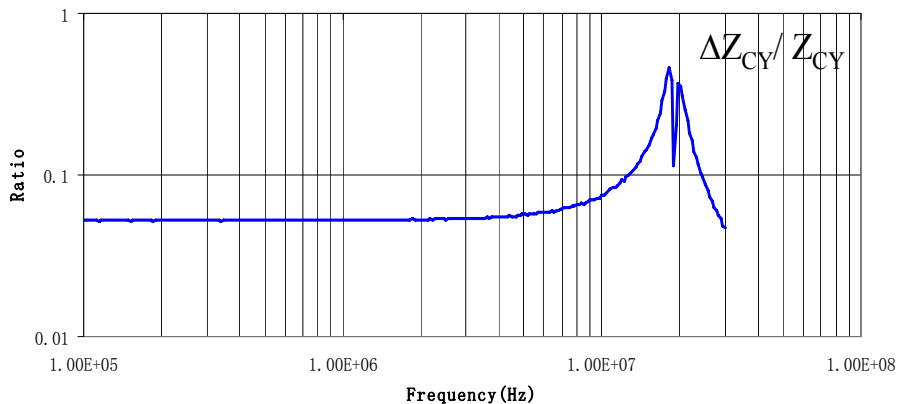


Fig. 6-12. Unbalance of two CM capacitors.

Two DM capacitors are also measured and R-L-C series equivalent circuits are derived.

C1: ESR is 35.3m Ω , ESL is 17.4nH and C1 is 475nF.

C2: ESR is 34.9m Ω , ESL is 16.2nH and C2 is 492nF.

For the inductor, a toroidal core OJ42908TC (Magnetics) is used. Two windings (each one is a 21 turn AWG20) are wound on each side respectively. Two windings are very symmetrical so that the parameters are very close. The parameters are measured on the printed circuit board. With the help of the relationship in Fig. 6-6, the parameters for R-L-C parallel equivalent circuit are easily found as:

Parameters for one CM inductor: L_{CM} 3.1mH, EPC 7.16pF, EPR 9.34k Ω

Parameters for one DM inductor: L_{DM} 8.76 μ H, EPC 14.15pF, EPR 7.45k Ω

The PCB layout of the investigated EMI filter is shown in Fig. 6-13. Mixed mode S-parameters in Fig. 6-14 are used to characterize the mode transformation of the investigated EMI filter.

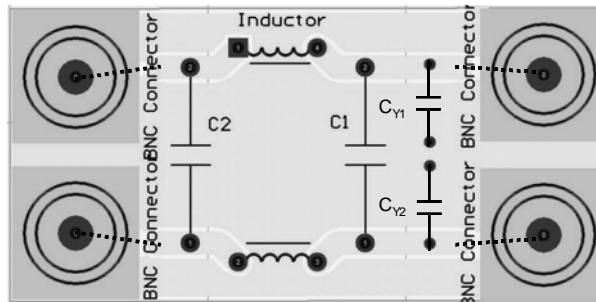


Fig. 6-13. PCB layout of the investigated EMI filter.

Four parameters, S_{DD21} , S_{CC21} , S_{DC21} and S_{CD21} are measured. They characterize the attenuations of DM filter, CM filter, and the transformations from CM to DM and from DM to CM.

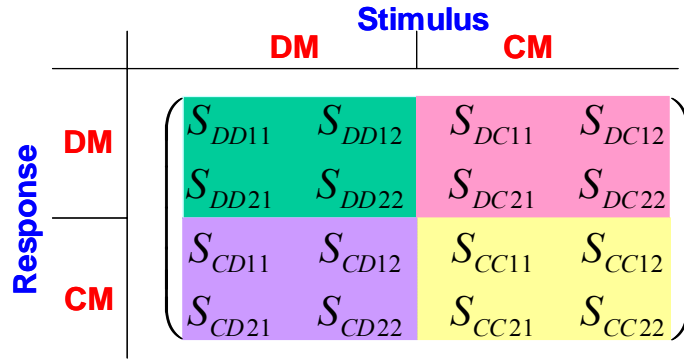


Fig. 6-14. Mixed mode S-parameters.

6.3.1 Effects of the Unbalance of CM Capacitors

Measured S_{DD21} , S_{CC21} , S_{DC21} and S_{CD21} for the filter in Fig. 6-13 are shown in Figs. 6-15 and 6-16.

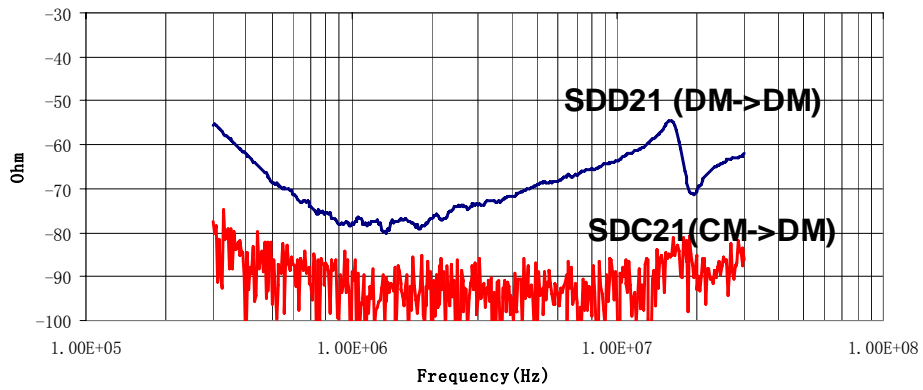


Fig. 6-15. Measured S-parameters.

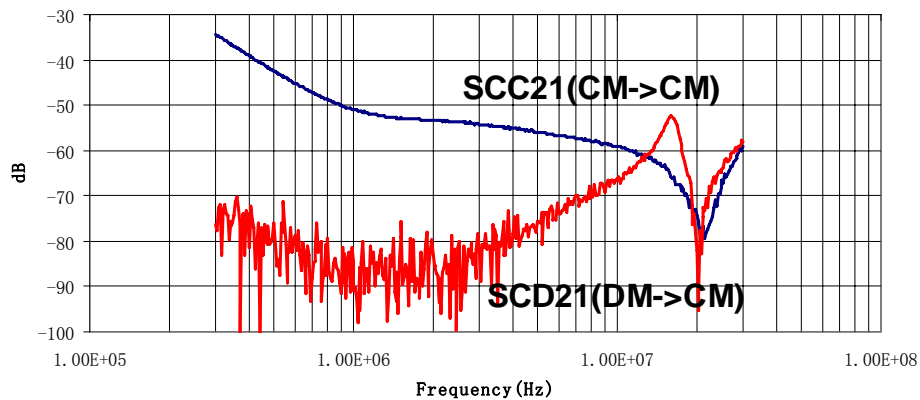


Fig. 6-16. Measured S-parameters.

In Fig. 6-15, the transformation from CM to DM is not an issue since the transformation is even smaller than the background noise of the network analyzer, a very small value. On the other hand, the transformation from DM to CM is significant above 4MHz. It is even higher than the attenuation of S_{CC21} above 13MHz, which means that when the DM and CM noise excitations are same, the transformed CM noise from the DM noise is even higher than the attenuated CM noise. Fig. 6-12 shows the unbalance of CM capacitors is significant in the corresponding frequency range. The unbalance of the CM capacitor is therefore an important reason.

The second experiment is carried out by changing the lead length of the two CM capacitors. The measured impedances of these two capacitors are shown in Fig. 6-17. The unbalance is as high as 0.73 at resonant frequency of CM capacitors. It is compared with the first experiment in Fig. 6-18. Other components and layouts are kept intact.

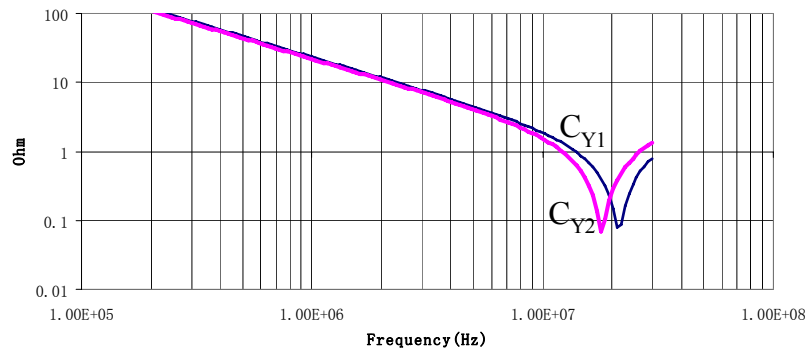


Fig. 6-17. Impedances of two CM capacitors.

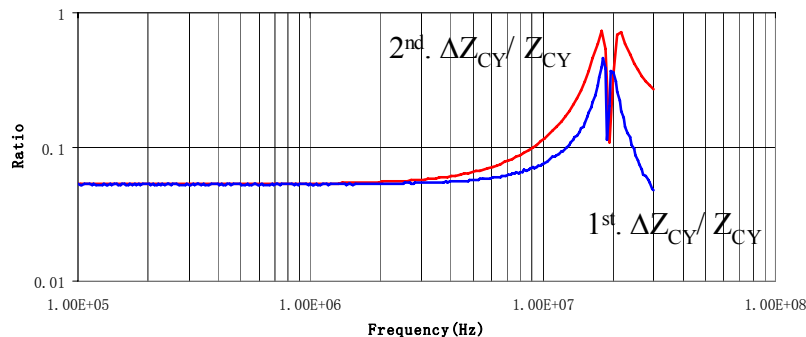


Fig. 6-18. Comparison of unbalance of two CM capacitors.

Measured S_{DD21} , S_{CC21} , S_{DC21} and S_{CD21} for the second experiment are shown in Figs. 6-19 and 6-20. The comparison of S_{CD21} is shown in Fig. 6-21.

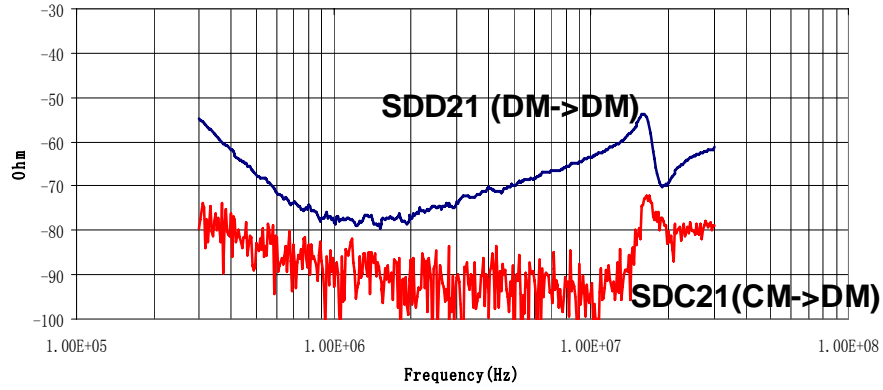


Fig. 6-19. Measured S-parameters.

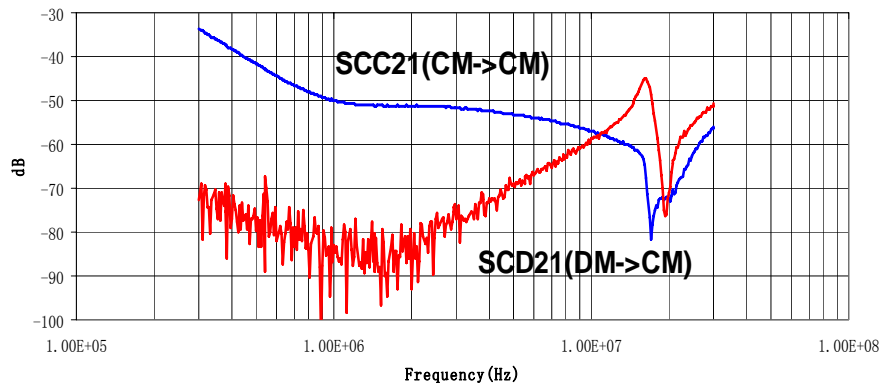


Fig. 6-20. Measured S-parameters.

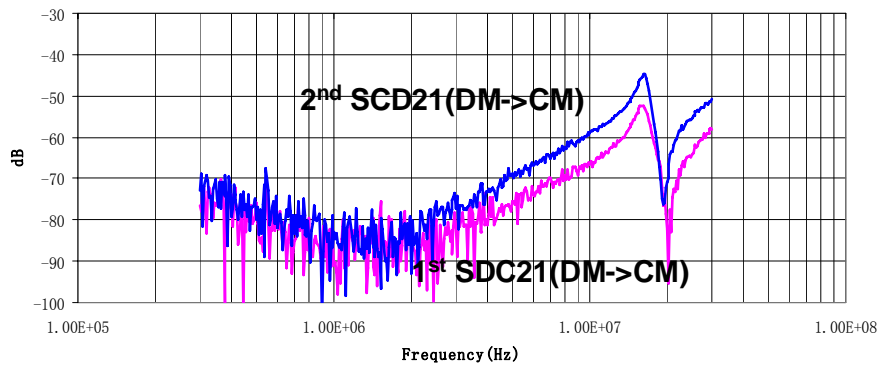


Fig. 6-21. Comparison of transformation from DM to CM.

In Fig. 6-19, the transformation from CM to DM is still ignorable because the unbalance of the transformation from CM to DM, which is given by $\Delta Z_{CY} / (Z_S + Z_{CY})$, is much smaller than the unbalance of the transformation from DM to CM, which is given by $\Delta Z_{CY} / Z_{CY}$. Despite that, it is still larger than that in the first experiment due to the more unbalance between the two CM capacitors. The transformation from DM to CM becomes more significant than that in the first experiment. It is significant from 2MHz and exceeds the attenuated CM noise above 9MHz. The comparisons in Figs. 6-18 and 6-21 show that the unbalance of two CM capacitors significantly affects the mode transformation. When the maximum unbalance increased from 0.46 to 0.73, as a result, the maximum transformation increased from -53dB vs. -44dB. As analyzed in 6.1 Introduction, -43dB is very unacceptable since the transformed CM noise can be easily higher than the attenuated CM noise.

6.3.2 Effects of the Unbalance of Inductors

In order to investigate the effects of the unbalance of the inductors, one winding is kept on 21 turns and the other is changed to 22turn. The CM capacitors are kept at their original status as in Fig. 6-11. The parameters for two windings are:

Winding 1: L_{CM1} 3.1mH, EPC 7.16pF, EPR 9.34k Ω

Winding 2: L_{CM2} 3.22mH, EPC 9.03pF, EPR 10.3k Ω .

Total parameters of two DM inductors: 20.1 μ H, EPC 12.3pF, EPR 4.78k Ω

Based on the analysis in Fig. 6-6, the relationship between ΔL_{DM} and ΔL_{CM} is shown in (6-41):

$$\left. \begin{array}{l} L_{DM1} = L_1 - M \\ L_{DM2} = L_2 - M \end{array} \right\} \Delta L_{DM} = \frac{L_{DM2} - L_{DM1}}{2} \left. \begin{array}{l} L_{CM1} = L_1 + M \\ L_{CM2} = L_2 + M \end{array} \right\} \Delta L_{CM} = \frac{L_{CM2} - L_{CM1}}{2} \left. \begin{array}{l} \Delta L_{DM} = \Delta L_{CM} = \Delta L = \frac{L_2 - L_1}{2} \end{array} \right\} \quad (6-41)$$

Some conclusions can be drawn from (6-41):

- 1) Unbalances of CM and DM inductances are same
- 2) Unbalances have nothing to do with M
- 3) L_{DM} can be minus
- 4) ΔL_{DM} can be larger than $L_{DM1} + L_{DM2}$

The unbalance of DM inductors before the resonant frequency f_r of the DM inductors can therefore be expressed as:

$$\frac{\Delta Z_{LDM}}{Z_{LDM}} = \frac{\Delta L}{L_{DM}} = \frac{60\mu H}{10.5\mu H} = 5.7, f < f_r \quad (6-42)$$

And the unbalance of CM inductors before the resonant frequency f_r of the CM inductors can therefore be expressed as:

$$\frac{\Delta Z_{LCM}}{Z_{LCM} + Z_{Load}} = \frac{\Delta L}{L_{CM} + Z_L / (2\pi f)} = \frac{60\mu H}{3160\mu H + 50 / (2\pi f)} \approx 0.019, 150\text{kHz} < f < f_r \quad (6-43)$$

Although the unbalance of CM inductors is much smaller than that of DM inductors, coefficients of unbalances are different, so they are not comparable. Experiments show, for CM unbalance, even 0.019 is a significant value. For DM unbalance, 5.7 is also a significant value. So the mode transformations in low frequency range are caused by the unbalances of DM and CM inductances. Near the resonant frequency of the DM or CM inductor, the EPR and the quality coefficient Q determine the unbalance and mode

transformation. Above the resonant frequencies, EPC determines the unbalance and mode transformation.

When one winding is increased to 22 turn and the other is kept to 21 turn, not only the CM inductors are unbalanced but also the DM inductors are unbalanced. Beside DM and CM inductances, the unbalanced parameters include EPC and EPR of CM and DM inductors. As a result, the measured mode transformations are produced from both the unbalances of CM and DM inductors.

The measurement results are shown in Figs. 6-22 and 6-23.

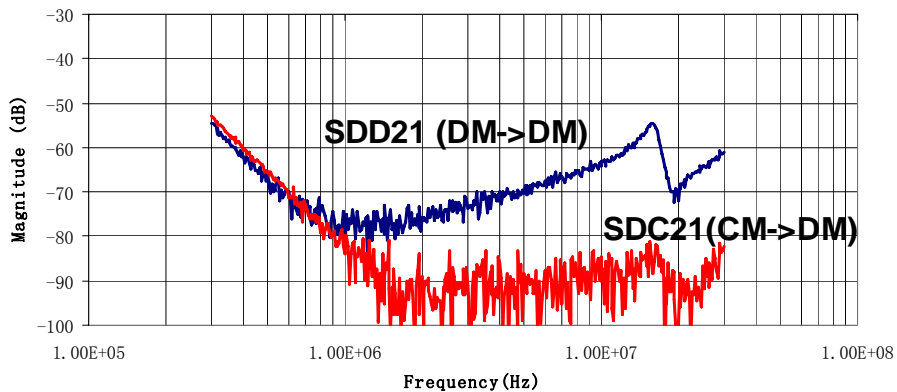


Fig. 6-22. Measured S-parameters.

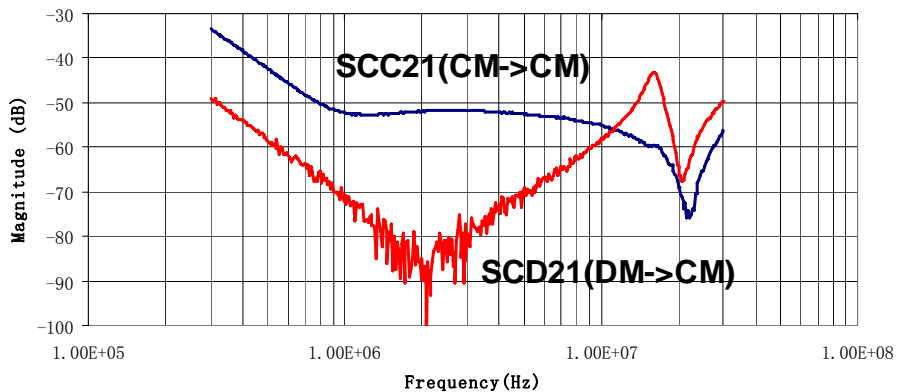


Fig. 6-23. Measured S-parameters.

Fig. 6-22 shows the mode transformation from CM to DM. In low frequency range, the unbalance of the CM inductance causes significant transformation from CM to DM, which is even higher than the attenuated DM noise. In high frequency range, the mode transformation is caused by the EPC_{CM} , whose effects are insignificant. In Fig. 6-23, the mode transformation from DM to CM is significant in almost the whole frequency range. This is caused by the unbalances of the DM inductances and EPC_{DM} .

In a practical EMI filter, two windings would not have different number of turns, so that the mode transformation would not be as significant as shown in Figs. 6-22 and 6-23.

6.4. Discussion

6.4.1 Mode Transformation on Different Directions

According to network theory, for a linear, passive network, the matrix in Fig. 6-14 is diagonally symmetric, so the following equivalences are satisfied:

$$S_{DC21} = S_{CD12} \quad (6-44)$$

$$S_{CD21} = S_{DC12} \quad (6-45)$$

$$S_{DD21} = S_{DD12} \quad (6-46)$$

$$S_{CC21} = S_{CC12} \quad (6-47)$$

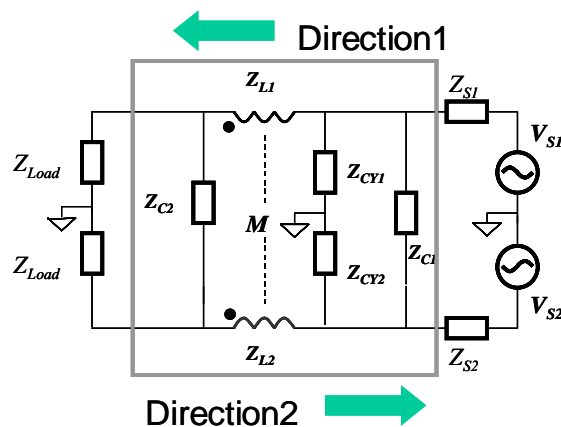


Fig. 6-24. Mode transformations on different directions.

(6-44) and (6-45) mean the transformation from DM to CM or from CM to DM in direction1 in Fig. 6-24 are equal to the transformation from CM to DM or from DM to CM in direction2 in Fig. 6-24. (6-46) and (6-47) mean the attenuation to DM or CM in direction1 is equal to the attenuation to DM or CM in direction2.

6.4.2 Effects of Cancellation Turn on Unbalance

Chapter 4 proposed to use the cancellation turn to cancel the mutual inductance between two capacitors. The question is whether the cancellation turn causes significant mode transformation. The answer is no. There are several reasons. First, the noise is already attenuated to a very small level before the cancellation turn, so mode transformation due to cancellation turn is very limited. Second, the net unbalanced inductance is the difference between inductance of cancellation turn, and the mutual inductance of cancellation turn and the capacitor. So the net unbalance is smaller. Third, impedance of unbalance is typically much smaller than the load. Measurement in Figs 6-25 and 6-26 proved this. In Fig. 6-25, the cancellation turn has little effects on the transformation from CM to DM except that several dB difference above 13MHz. In Fig. 6-26, the cancellation turn has no noticeable effects on the transformation from DM to CM.

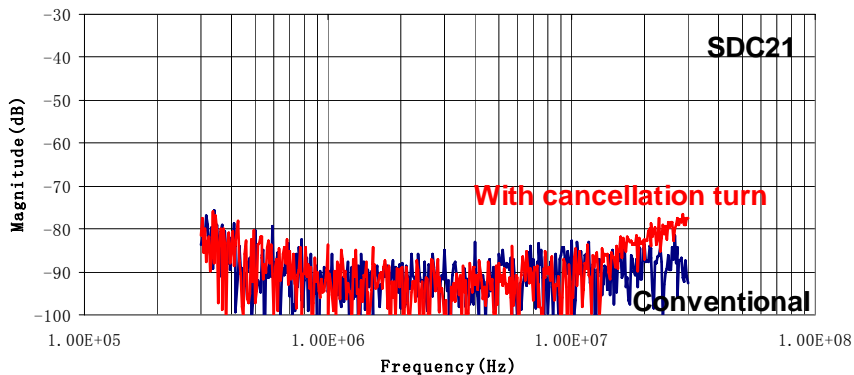


Fig. 6-25. Measured S-parameters.

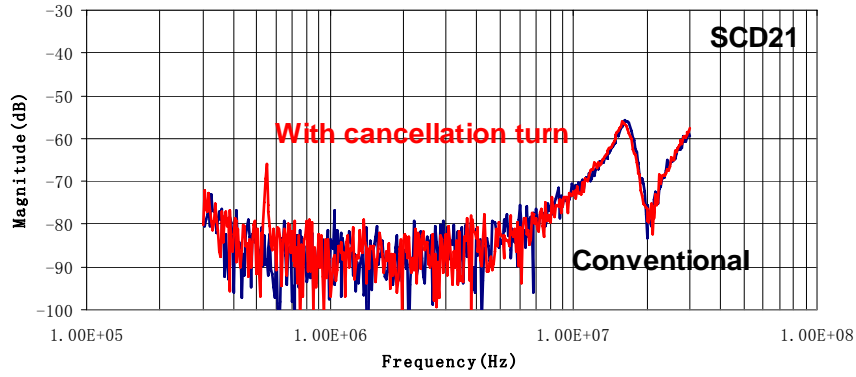


Fig. 6-26. Measured S-parameters.

6.4.3 The Bump on S_{CD21} and S_{DD21}

In previous diagrams, there is always a bump on S_{CD21} and S_{DD21} . This is resulted from the interaction between CM capacitors and DM capacitor C_1 . Fig. 6-27 shows this concept.

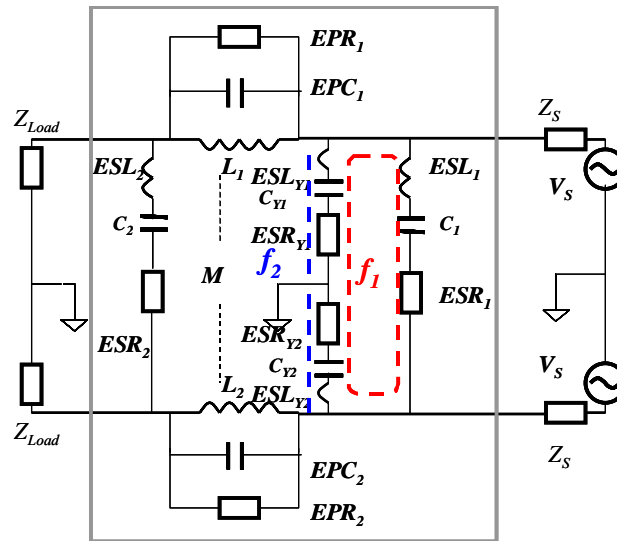


Fig. 6-27. Resonances in the EMI filter.

There are one series resonance between DM capacitor C_1 and two CM capacitors. The resonant frequency is given by (6-48). This resonance causes a bump at f_1 .

$$f_1 \approx \frac{1}{2\pi\sqrt{(ESL_1 + 2ESL_Y)\left(\frac{C_Y}{2}\right)}} \quad (6-48)$$

The series resonant frequency of CM capacitors is given by (6-49). This resonance causes a dip at f_2 .

$$f_2 \approx \frac{1}{2\pi\sqrt{ESL_Y C_Y}} \quad (6-49)$$

f_1 is smaller than f_2 because of ESL_1 . They are shown in Fig. 6-28.

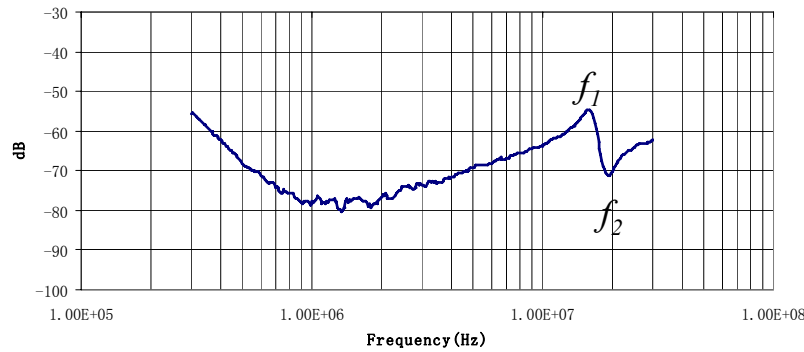


Fig. 6-28. Effects of resonances in the EMI filter.

The bump and dip in S_{DD21} show up in S_{CD21} , because of the unbalance of the circuit parameters, for example, the unbalance of CM capacitors.

6.4.4 Effects of Unbalanced Mutual Couplings

Effects of unbalanced mutual couplings are not analyzed in this chapter. If the unbalances are analyzed, for example, the unbalanced of mutual inductances between the inductor and capacitors, they would also contribute to the mode transformation.

6.5. Summary

This chapter first analyzed the effects of unbalanced parameters in EMI filters on the mode transformation. Experiments are then carried out to prove the analytical results. It is found that, the mode transformations have a linear relationship with the unbalances of parameters. The transformed noise due to the unbalances of CM capacitors and CM/DM inductors can be higher than the attenuated noise, which make filter design inefficient. In order to design EMI filter efficiently, filter parameters should be kept as balanced as possible to prevent the harmful mode transformation.

References

- [1] *Agilent E5070B/E5071B ENA Series RF Network Analyzers User's Guide*, Fifth Edition, Agilent Technologies, 2004.
- [2] W. Fan, Albert Lu, L. L. Wai, B. K. Lok, "Mixed-Mode S-parameters Characterization of Differential Structures," in *IEEE 2003 Electronics Packaging Technology Conference*, Dec. 2003, pp. 533 - 537.
- [3] Shuo Wang, J. D. van Wyk, Fred C. Lee and W. G. Odendaal, "Transformation between Common Mode and Differential Mode due to Imperfect Balance of EMI Filters," in *proc. 2005 CPES Power Electronics Conference*, Blacksburg, VA, 17-20 April, 2005, pp. 551 -555.
- [4] R. E. Collin, *Foundations for Microwave Engineering*, Second Edition, McGraw-Hill, N.Y., 1992.

CHAPTER 7: Transmission Line Effects of Power Interconnects on EMI Filter High-Frequency Performance*

7.1. Introduction

A typical conducted EMI measurement setup for a power converter is shown in Fig. 7-1. CM noise first flows through the parasitic capacitors between the converter and the ground plane. Most of the CM noise is then bypassed by the EMI filter through the ground point of the CM filter. At last, the remaining CM noise flows through the ground plane, the LISNs, the power interconnects and back to the EMI filter and the converter. In order to efficiently bypass CM noise, the grounding impedance of the CM filter should be as small as possible. On the other hand, the DM noise in Fig. 7-1 is first attenuated by the DM filter and then flows between two power interconnects through LISNs. The noise is measured from the voltage drops of the noise current on the 50Ω input impedances of the noise separator. In EMI measurements, it is sometimes found that there are unexpected noise peaks in the high frequency (HF) range. For different cases, these noise peaks can be attributed to different mechanisms, such as the resonance of the ground loop [3]. This chapter tries to analyze one of these mechanisms in relation to the measurement done, including realistic power line interconnects as encountered in practical measurement setup.

In Fig. 7-1, the distance between the equipment under test (EUT) (A PFC converter and an EMI filter) and LISNs, which is usually 0.8m-1.5m, is specified by EMI standards. The input impedance of a LISN is supposed to be 50Ω , which is usually

* © 2005 IEEE. Reprinted, with permission, from the Proc. IEEE Power Electronics Specialists Conference, 12-16, Jun. 2005.

treated as the load of the EMI filter. However because the distance between the LISNs and the EMI filter is comparable with $\lambda/20$ for high frequency noise, the transmission line effects of the power interconnects between the EMI filter and the LISNs should be considered in the analysis. The load of the EMI filter is no longer 50Ω , but a capacitive or inductive load. Its magnitude can also be much higher or lower than 50Ω . This load can interact with the EMI filter's parasitics so as to worsen EMI filter performance above 10MHz. The phenomenon is attributed to the impedance transformation of the power interconnects. Since the high frequency noise can be very difficult to handle, it is important to investigate the mechanism of this interaction.

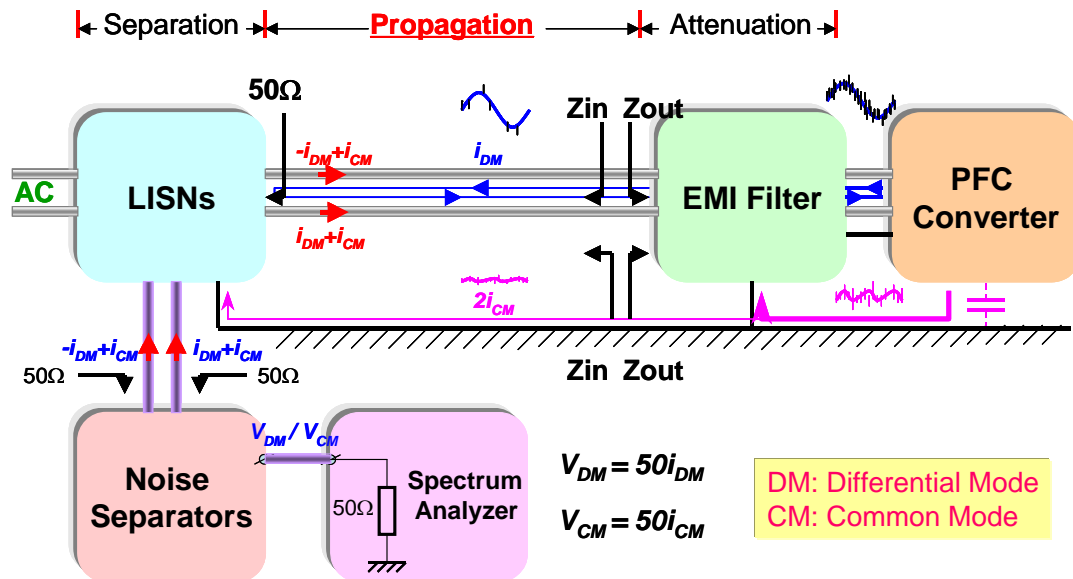


Fig. 7-1. Conducted EMI measurement setup for a PFC converter.

7.2. Electrical Parameters for Noise Propagation Path

In Fig. 7-1, just as analyzed in section I, CM and DM noise propagates through different paths. Because of these different propagation paths, the electrical parameters for CM and DM noise propagation are different. Fig. 7-2 shows a cross section view of power lines and a ground plane. For DM mode noise, voltages on the two lines have the same absolute value, but with different polarities. For CM noise, voltages on the two lines have the same absolute value, with the same polarity. It is assumed that the permittivity of the cable's insulation layers is the same as that of air, that the two conductors perfectly conduct surface current, and that only TEM mode waves propagate and no higher order mode waves are triggered. The static theory is therefore applied to electrical parameter calculation. Fig. 7-3 shows the distribution of magnetic field.

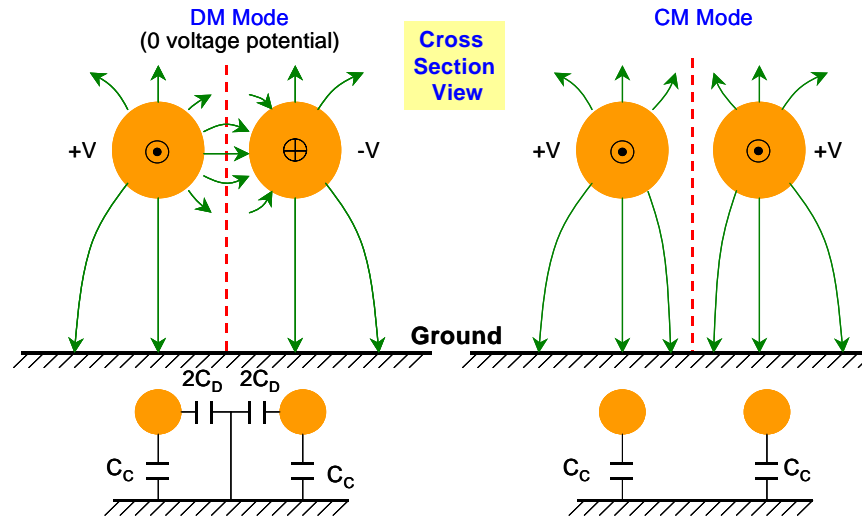


Fig. 7-2. Distribution of electrical field.

In Fig. 7-2, for DM noise, due to the zero voltage potential of the center line, the capacitance between the power interconnects and the ground plane is composed of two parts, the capacitance C_C directly to the ground and the capacitance C_D between power

interconnects and center line (zero voltage potential) [5]. For CM noise, since no electrical flux crosses the center line, the capacitance C_D between two lines is zero; and then only the capacitance C_C between the ground and the power line exists [5]. Then the capacitances for DM and CM noise propagation are given by (7-1) and (7-2).

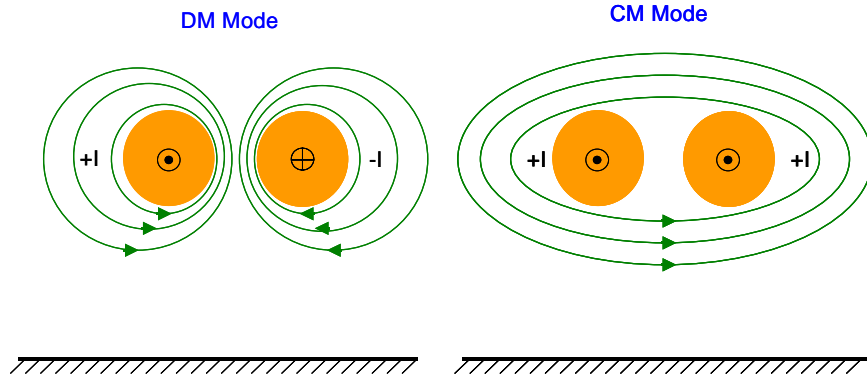


Fig. 7-3. Distribution of magnetic field.

$$C_{DM} = C_C + 2C_D \tag{7-1}$$

$$C_{CM} = C_C \tag{7-2}$$

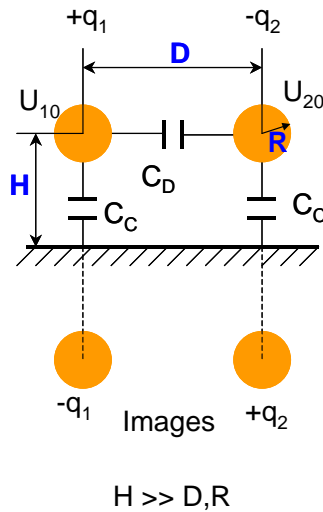


Fig. 7-4. Calculation of capacitance.

The capacitances C_D and C_C per meter in Fig. 7-4 can be calculated using electromagnetic theory shown in (7-3) to (7-9). U_{10} and U_{20} are the voltages on two wires. The inductances for both CM and DM propagation are calculated from C_D and C_C using the 2D relationship of capacitance and inductance, which is given by (7-10) and (7-11).

$$B = \sqrt{(D/2)^2 - R^2} \quad (7-3)$$

$$\alpha_{11} = \frac{1}{2\pi\epsilon_0} \ln \frac{2H}{R}, \alpha_{12} = \frac{1}{2\pi\epsilon_0} \left[\ln \frac{2H}{R} + \ln \frac{B - (D/2 - R)}{B + (D/2 - R)} \right] \quad (7-4)$$

$$\alpha_{21} = \frac{1}{2\pi\epsilon_0} \left[\ln \frac{2H}{R} + \ln \frac{B - (D/2 - R)}{B + (D/2 - R)} \right], \alpha_{22} = \frac{1}{2\pi\epsilon_0} \ln \frac{2H}{R} \quad (7-5)$$

$$C_D = \alpha_{21} / (\alpha_{11}^2 - \alpha_{21}^2) \quad (7-6)$$

$$C_C = 1 / (\alpha_{11} + \alpha_{21}) \quad (7-7)$$

$$C_C \approx 2\pi\epsilon_0 / \ln \left[\left(\frac{2H}{R} \right)^2 \frac{B - (D/2 - R)}{B + (D/2 - R)} \right] \quad (7-8)$$

$$C_D \approx \left[\frac{2\pi\epsilon_0 \ln \left[\frac{2H}{R} \frac{B - (D/2 - R)}{B + (D/2 - R)} \right]}{\ln \left[\left(\frac{2H}{R} \right)^2 \frac{B - (D/2 - R)}{B + (D/2 - R)} \right] \bullet \ln \left[\frac{B + (D/2 - R)}{B - (D/2 - R)} \right]} \right] \quad (7-9)$$

$$L_{DM} = \frac{1}{C_{DM} \bullet c^2} \quad (7-10)$$

$$L_{CM} = \frac{1}{C_{CM} \bullet c^2} \quad (7-11)$$

The characteristic impedances for DM and CM noise propagation are therefore given by (7-12) to (7-15). These characteristic impedance equations can be used to analyze the high frequency influences of the power interconnects.

$$\text{DM between one power interconnect and the ground: } Z_{0DM} = \sqrt{\frac{L_{DM}}{C_{DM}}} = \frac{1}{C_{DM} \cdot c} \quad (7-12)$$

$$\text{DM between two power interconnects: } Z_{0DM}' = 2Z_{0DM} \quad (7-13)$$

$$\text{CM between one power interconnect and the ground: } Z_{0CM} = \sqrt{\frac{L_{CM}}{C_{CM}}} = \frac{1}{C_{CM} \cdot c} \quad (7-14)$$

$$\text{CM between two power interconnects and the ground: } Z_{0CM}' = \frac{Z_{0CM}}{2} \quad (7-15)$$

7.3. Impedance Transformation

It is assumed that two power interconnects are perfectly balanced, so no mode transformation is considered in this chapter. Both CM and DM propagation paths can be decoupled into two pairs of transmission lines as Fig. 7-5, where both CM and DM transmission lines are considered as the combination of one power interconnect and the ground plane. The characteristic impedance for DM and CM transmission lines are therefore given by (7-12) and (7-14).

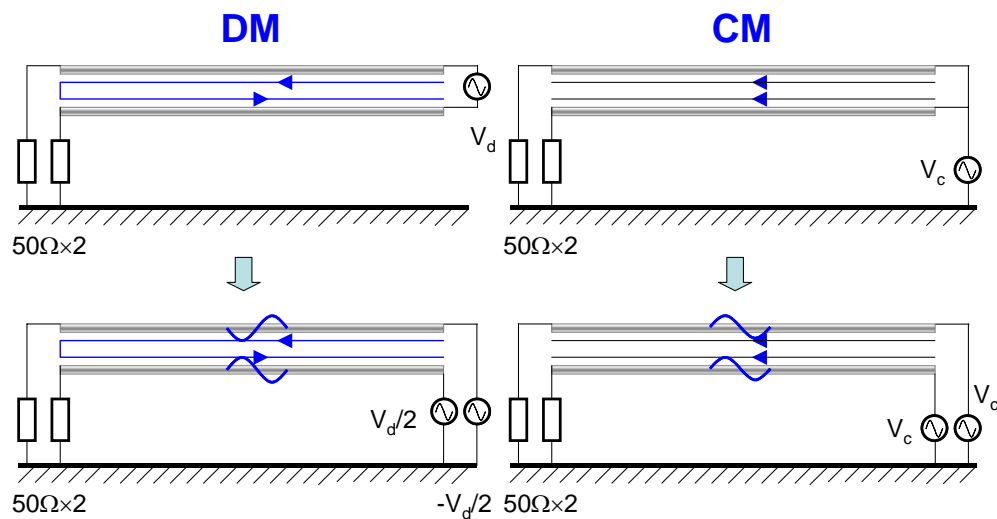


Fig. 7-5. Decoupling the noise propagation paths.

Since the noise propagation paths are decoupled, the noise propagation can be analyzed in Fig. 7-6. In Fig. 7-6, for the transmission line on the lower side, V^+ is incident wave and V^- is reflected wave; β is propagation constant. The boundary conditions are given by the source and load on two sides of the transmission line. V^+ , V^- , load voltage V_L and input impedance $Z_{in}(x)$ are therefore given by (7-16) to (7-19).

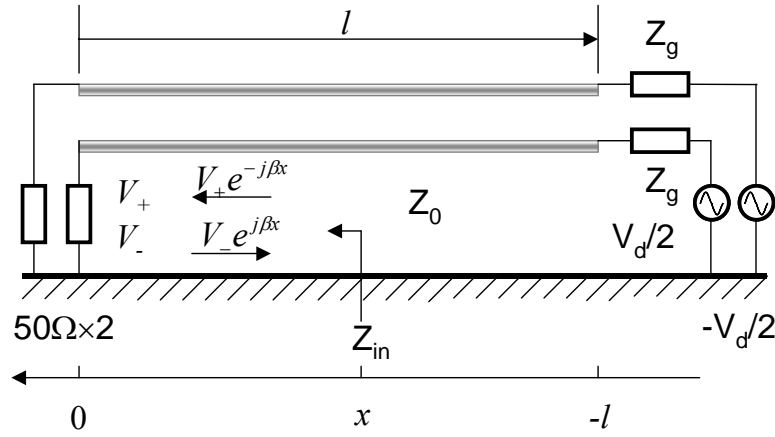


Fig. 7-6. Propagation of noise waves.

$$V_+ = \frac{Z_0 V_d}{2(Z_0 + Z_g)} \left(\frac{e^{-j\beta l}}{1 - \Gamma_g \Gamma_L e^{-j2\beta l}} \right) \quad (7-16)$$

$$V_- = \frac{Z_0 V_d}{2(Z_0 + Z_g)} \left(\frac{e^{-j\beta l}}{1 - \Gamma_g \Gamma_L e^{-j2\beta l}} \right) \Gamma_L \quad (7-17)$$

$$V_L = \frac{Z_0 V_d}{2(Z_0 + Z_g)} \left(\frac{(1 + \Gamma_L) e^{-j\beta l}}{1 - \Gamma_g \Gamma_L e^{-j2\beta l}} \right) \quad (7-18)$$

$$\begin{aligned} Z_{in}(x) &= \frac{V(x)}{I(x)} = Z_0 \frac{1 + \Gamma_L e^{j2\beta x}}{1 - \Gamma_L e^{j2\beta x}} \\ &= Z_0 \frac{Z_L + jZ_0 \tan \beta x}{Z_0 + jZ_L \tan \beta x} \end{aligned} \quad (7-19)$$

Relation (7-19) results from the standing waves due to the impedance mismatch. In (7-19), Z_0 is the characteristic impedance of the transmission line, for DM noise it is Z_{0DM}

and for CM noise it is Z_{0CM} . $Z_{in}(x)$ is the input impedance at any place on the power interconnects. From (7-19), the input impedance at the source side ($x = -l$) depends on the noise frequency, length of power interconnects, the load and the characteristic impedance of the transmission line. The input impedance of the power interconnects is no longer the LISN's input impedance of 50Ω . The impedance transformation of the power interconnects can be easily analyzed using the Smith chart shown in Fig. 7-7. The impedance as a function of the power interconnect length can be illustrated in Fig. 7-8. Under ideal conditions, the noise source impedance is almost balanced due to the EMI filter.

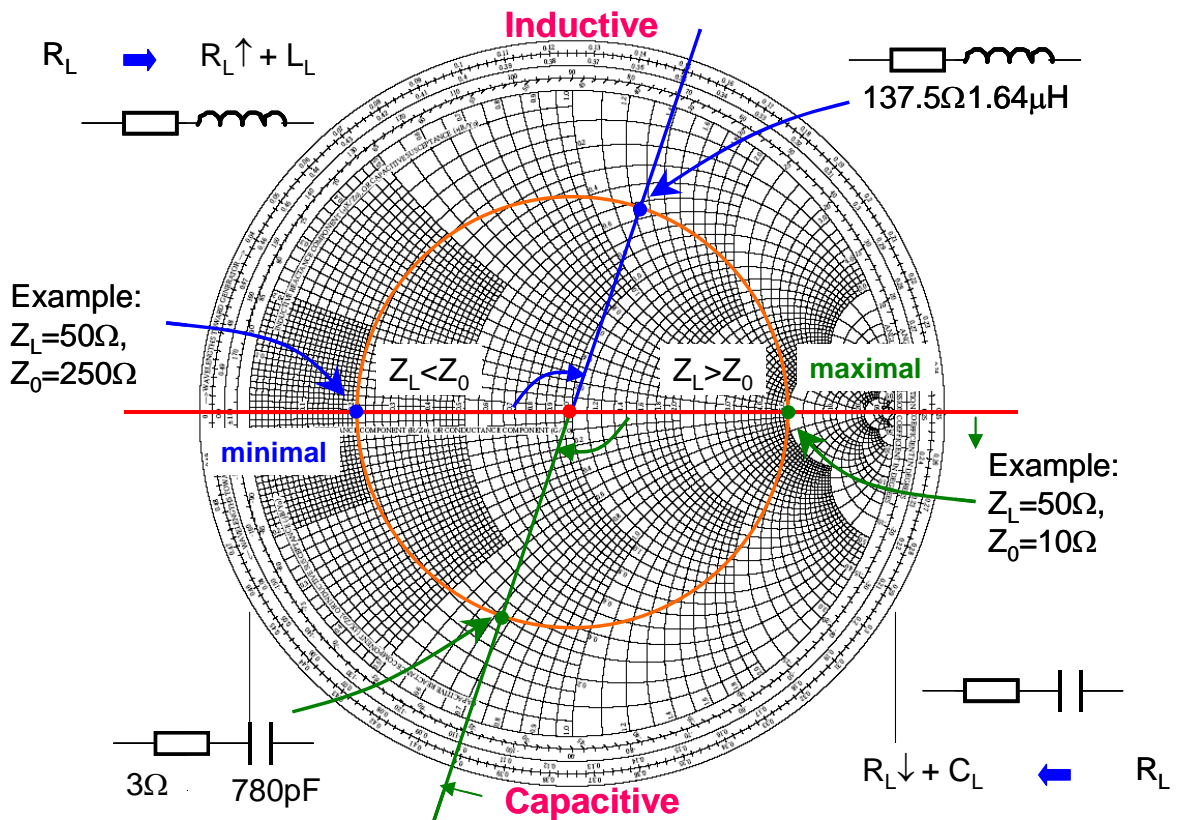


Fig. 7-7. Impedance transformation analysis using smith chart.

In Fig. 7-7, the power interconnect length is 1.5m and the noise frequency is 30MHz . For the case that Z_0 is 250Ω , the input impedance is found by rotating clockwise from the original impedance as start point by 0.15λ . The input impedance is therefore a 137Ω resistance in series with a $1.64\mu\text{H}$ inductance. For the case that Z_0 is 10Ω , the input impedance is found by rotating clockwise from the original impedance as start point by 0.15λ . The input impedance is therefore a 3Ω resistance in series with a 780pF capacitance. Obviously, the input impedance is far removed from 50Ω in both cases.

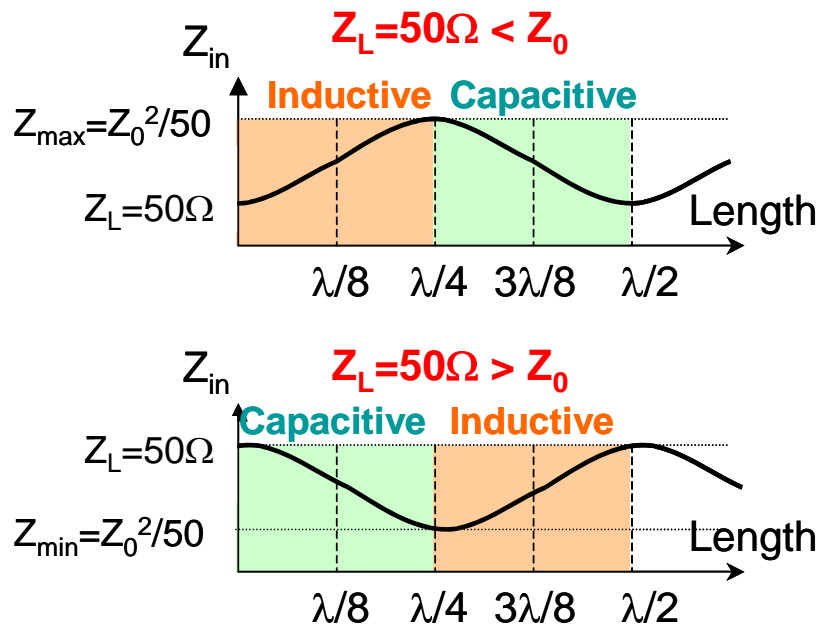


Fig. 7-8. Input impedance as a function of the length of power interconnects.

In Fig. 7-8, when the characteristic impedance of the power interconnect is larger than the LISN's input impedance of 50Ω , the magnitude of the input impedance of the power interconnect is always larger than 50Ω . In the first quarter wave length, the load of the EMI filter, i.e. the input impedance of the power interconnect is inductive. At the first

quarter wavelength, the maximal impedance is $Z_0^2/50$. In the second quarter wavelength, the load of the EMI filter is capacitive. The quarter wavelength at 30MHz is 2.5m.

In Fig. 7-8, when the characteristic impedance of the power interconnect is smaller than the LISN's input impedance of 50Ω , the magnitude of the input impedance of the power interconnect is always smaller than 50Ω . In the first quarter wave length, the load of the EMI filter, i.e. the input impedance of the power interconnect is capacitive. At quarter wavelength, the minimal impedance is $Z_0^2/50$. In the second quarter wavelength, the load of the EMI filter is inductive. If the power interconnect between EMI filter and the LISNs is not short enough ($< \lambda/20$) and the characteristic impedance of the power interconnect is much different from 50Ω , the impedance transformation is significant.

7.4. Interaction with EMI Filters

EMI filters have output impedances, which are determined by the parasitic parameters in the EMI filters at high frequencies. A typical one-stage EMI filter circuit is shown in Fig. 7-9. The DM filter model including parasitics is shown in Fig. 7-10. Because the impedances of the DM inductors are much higher than the impedance of C_2 , the output impedance of the DM EMI filter is determined by the output trace-loop impedance and the impedances of C_2 . The measured output impedance is shown in Fig. 7-11. For the CM filter, because the impedances of the CM capacitors are much lower than the impedances of the CM inductors as shown by the parasitic model in Fig. 7-12, the output impedance is determined by the CM inductors. The measured output impedance is shown in Fig. 7-13.

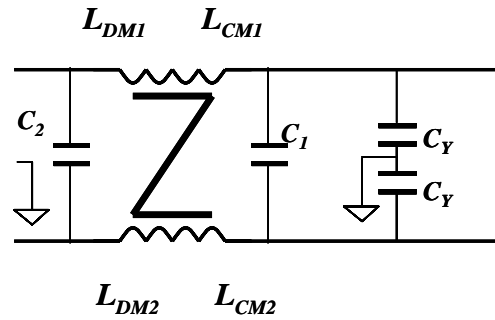


Fig. 7-9. Investigated one-stage EMI filter.

From Figs. 7-10 to 7-13, in the high frequency range, for the investigated EMI filter, the output impedance Z_{out} of the DM filter is determined by ESL_2 of the DM capacitor C_2 and the trace inductance L_{p2} . For the CM filter, Z_{out} is determined by the winding capacitance (EPC_{CM}) of the CM inductors. Since the DM and CM input impedances of the power interconnects are the load of the EMI filter, they can interact with the output impedances of the DM and CM filters respectively. The system being considered is shown in Fig. 7-14.

Table 7-I illustrates the possible interaction between the EMI filter and power interconnects. From Table 7-I, the output impedances can resonate with the input impedances of the power interconnects. The resonances can cause noise voltage peaks on

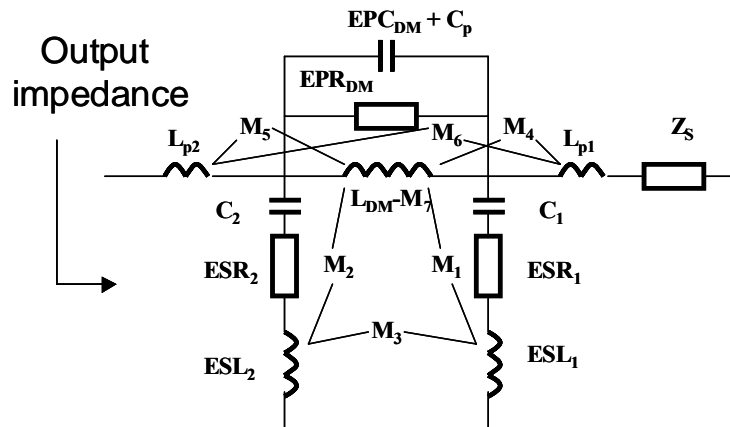


Fig. 7-10. Output impedance of the DM filter.

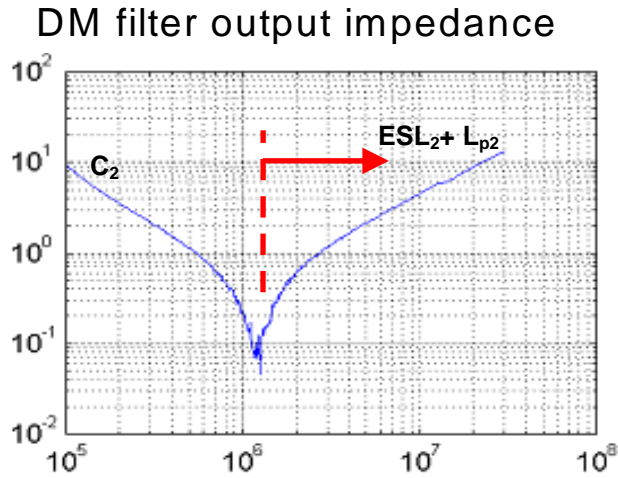


Fig. 7-11. Measured output impedance of the DM filter.

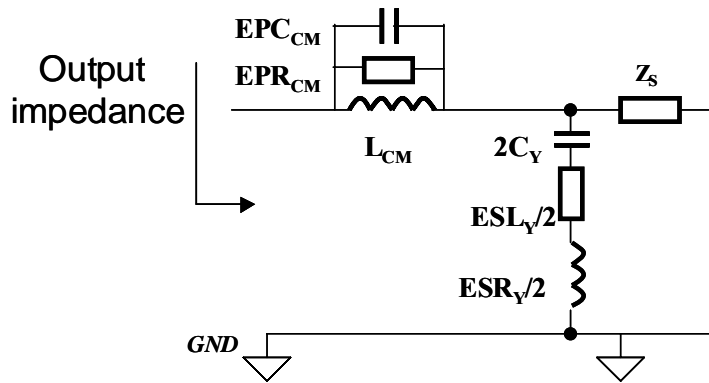


Fig. 7-12. Output impedance of the CM filter.

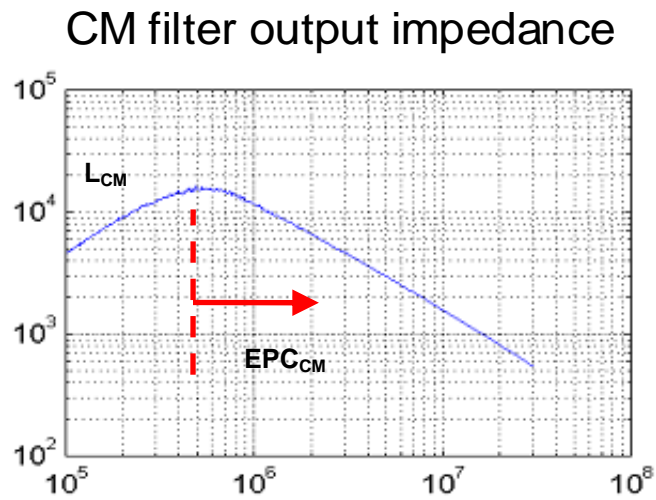


Fig. 7-13. Measured output impedance of the CM filter.

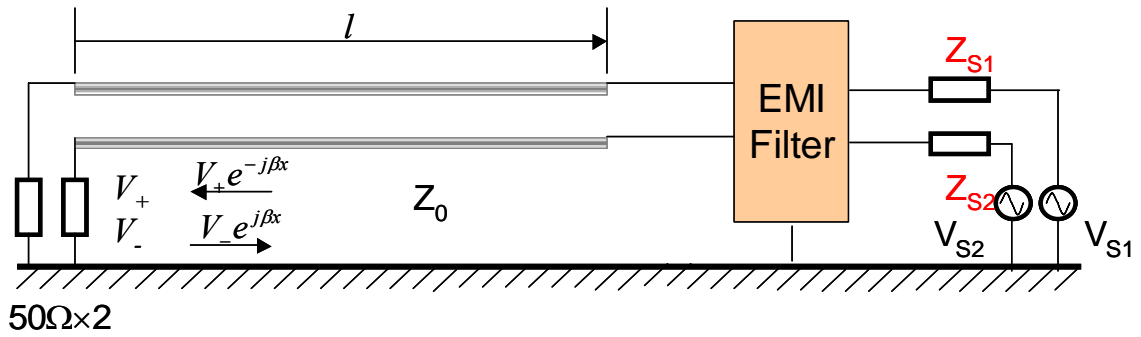


Fig. 7-14. EMI filter with noise source, power interconnect and load.

the real part of the input impedances. These noise peaks finally propagates to the LISN side without attenuation, as shown in Fig. 7-15, because the power interconnects are assumed lossless. (7-20) to (7-23) explain this.

Table 7-I. Interaction between the filter and power interconnects

Conditions	Zin	Zout + Source	Possible Effects
$Z_L = 50\Omega$ $Z_0 = 250\Omega$ $f = 30MHz$ $l = 1.5m$ $Z_L = 50\Omega$ $Z_0 > Z_L$	$l = 3\lambda / 20$ $Z_{in} = 137.5 + j310\Omega$ Z_{in} 137.5Ω $1.64\mu H$ Series resonance		Higher noise level or Lower noise level (for different time constants)
$Z_L = 50\Omega$ $Z_0 = 10\Omega$ $f = 30MHz$ $l = 1.5m$ $Z_L = 50\Omega$ $Z_0 < Z_L$	Series resonance Z_{in} 3Ω $780pF$ $l = 3\lambda / 20$ $Z_{in} = 3 - j6.8\Omega$		Noise peak
			Noise peak
			Higher noise level or Lower noise level (for different time constants)

Table 7-I illustrates the possible interaction between the EMI filter and power interconnects. From Table 7-I, the output impedances can resonate with the input impedances of the power interconnects. The resonances can cause noise voltage peaks on

the real part of the input impedances. These noise peaks finally propagate to the LISN side without attenuation, as shown in Fig. 7-15, because the power interconnects are assumed lossless. (7-20) to (7-23) explain this.

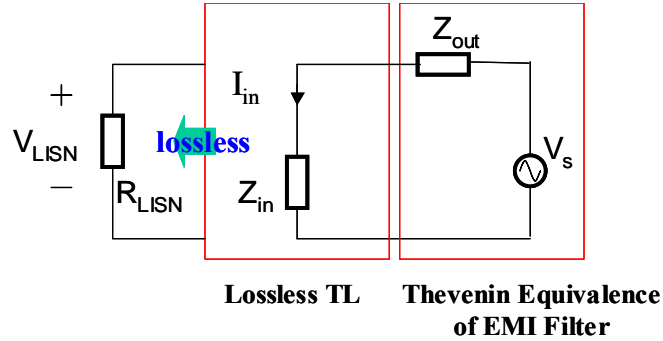


Fig. 7-15. Noise peaks caused by the resonances propagate to LISNs.

$$I_{in} = \frac{V_s}{(Z_{out} + Z_{in})}; \quad (7-20)$$

$$P_{in} = I_{in}^2 \operatorname{Re}(Z_{in}); \quad (7-21)$$

$$V_{LISN} = \sqrt{R_{LISN} P_{in}} \quad (7-22)$$

$$V_{LISN} = \frac{V_s}{(Z_{out} + Z_{in})} \sqrt{R_{LISN} \times \operatorname{Re}(Z_{in})} \quad (7-23)$$

7.5. Effects on EMI Filter Performance

The process of the theoretical analysis for Fig. 7-14 is shown in Fig. 7-16. In Fig. 7-16, both the EMI filter and the power interconnects are first characterized by S-parameters. They are then transformed to T parameters for cascade calculation. The calculated T parameters are finally transformed back to S-parameters for the insertion voltage gain calculations.

The calculations are carried out for four cases in Figs. 7-17 to 7-24. In Figs. 7-17 and 7-18, for the DM filter shown in Figs. 7-9 to 7-11, two cases are considered. For the first

case, the characteristic impedance of the power interconnect is 5Ω , which is much smaller than the LISN's impedance of 50Ω . The small characteristic impedance could occur in some cases, for example, a power bus bar, which has a large capacitance and a small inductance between the two bars. For the second case, the characteristic impedance of the power interconnect is 500Ω , which is much larger than the LISN's impedance 50Ω . The large characteristic impedance could happen when the distance between two power interconnects is much larger than the conductor's dimensions, which has a large inductance and a small capacitance between two power interconnects. For both cases, the noise source impedance used for calculation is a $330\mu\text{H}$ PFC inductor.

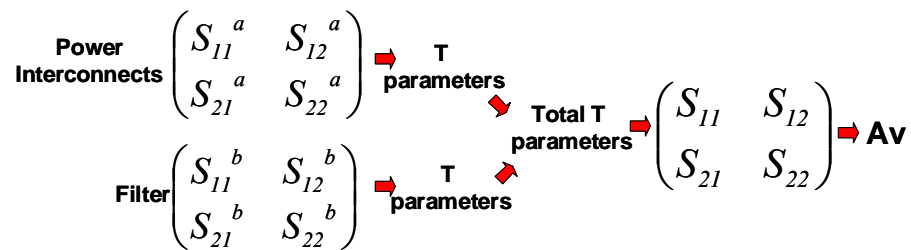


Fig. 7-16. Calculation process.

In Fig. 7-17, when Z_0 is 5Ω , the input impedance of the power interconnects is capacitive if the length of the power interconnects between LISNs and EMI filter is smaller than a quarter wave length of noise frequency. An $R(f)$ - $C(f)$ equivalent circuit is derived for power interconnects. Because the output impedance of the investigated DM EMI filter is inductive at high frequencies, series resonance could happen at high frequencies. The resonant frequency varies with the length of the power interconnects. The longer the power interconnects, the lower the series resonant frequency. For the case in Fig. 7-18 when Z_0 is 500Ω , an $R(f)$ - $L(f)$ equivalent circuit is derived for the power

interconnects. If the noise frequency is higher than the corner frequency $R(f)/(2\pi(L(f)+ESL+L_{p2}))$ the noise is attenuated. The calculated 3D (power interconnect length – noise frequency – noise amplitude on LISNs in dB) results are shown in Figs. 7-19 and 7-20 for 5Ω and 500Ω characteristic impedances respectively.

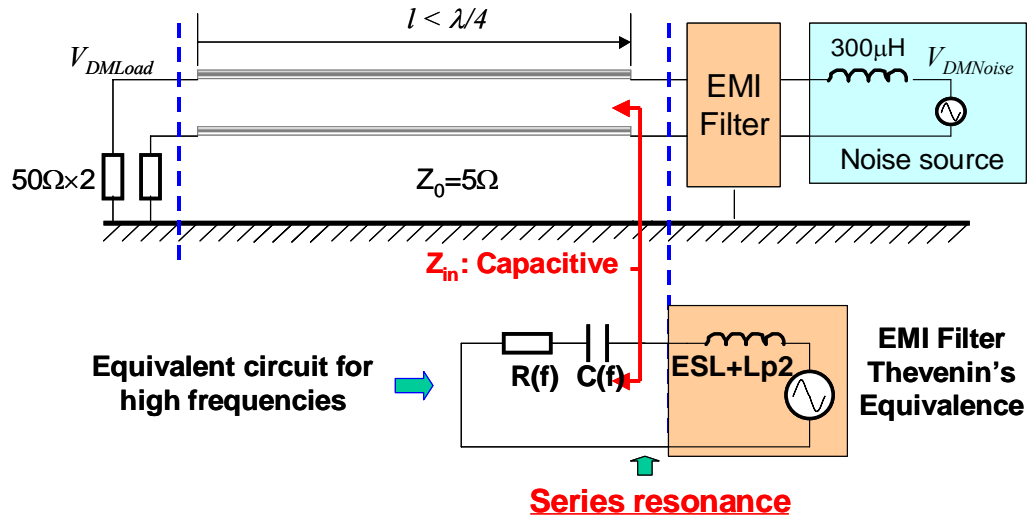


Fig. 7-17. Effects of power interconnect on DM EMI filter performance: $Z_0 < 50\Omega$.

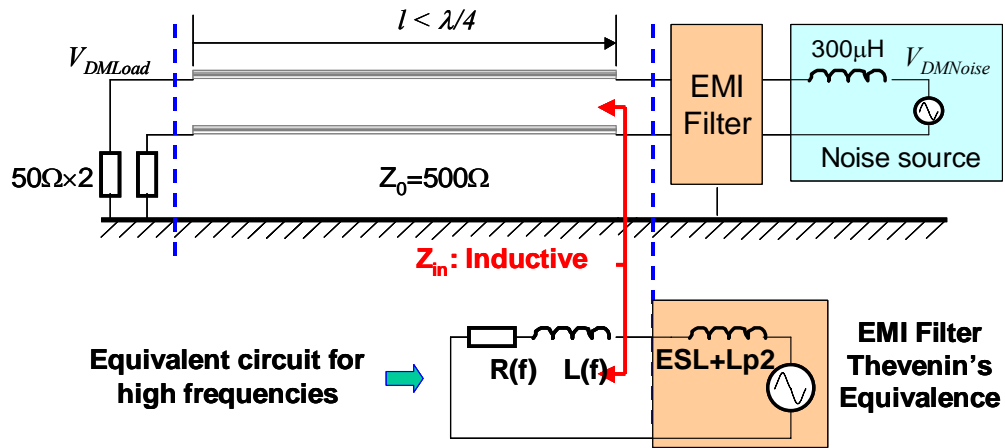


Fig. 7-18. DM noise analysis when $Z_0 > 50\Omega$.

In Fig. 7-19, the noise peak shows up at 30MHz when the interconnect length is 1m. It moves down to 18MHz when interconnect length increases to 2.5m. Compared with the

case without the power interconnects, the noise is amplified by 10-17dB when the noise peak shows up. This verifies the previous analysis. Since longer power interconnect causes larger input capacitance, resonant frequency will become lower.

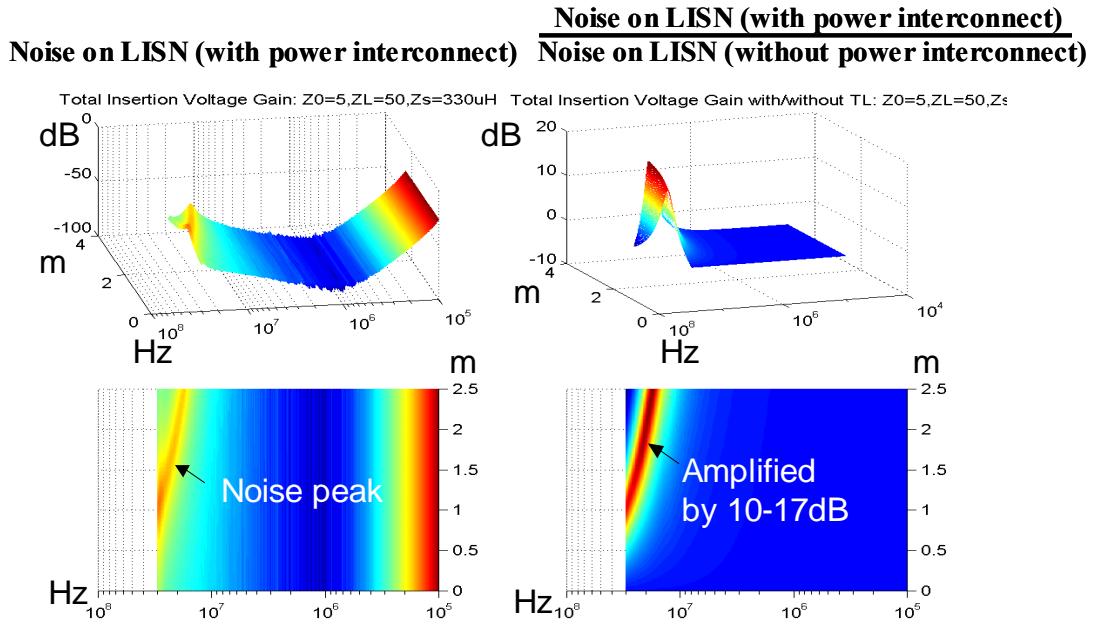


Fig. 7-19. Effects of power interconnect on DM EMI filter performance: $Z_0=5\Omega$.

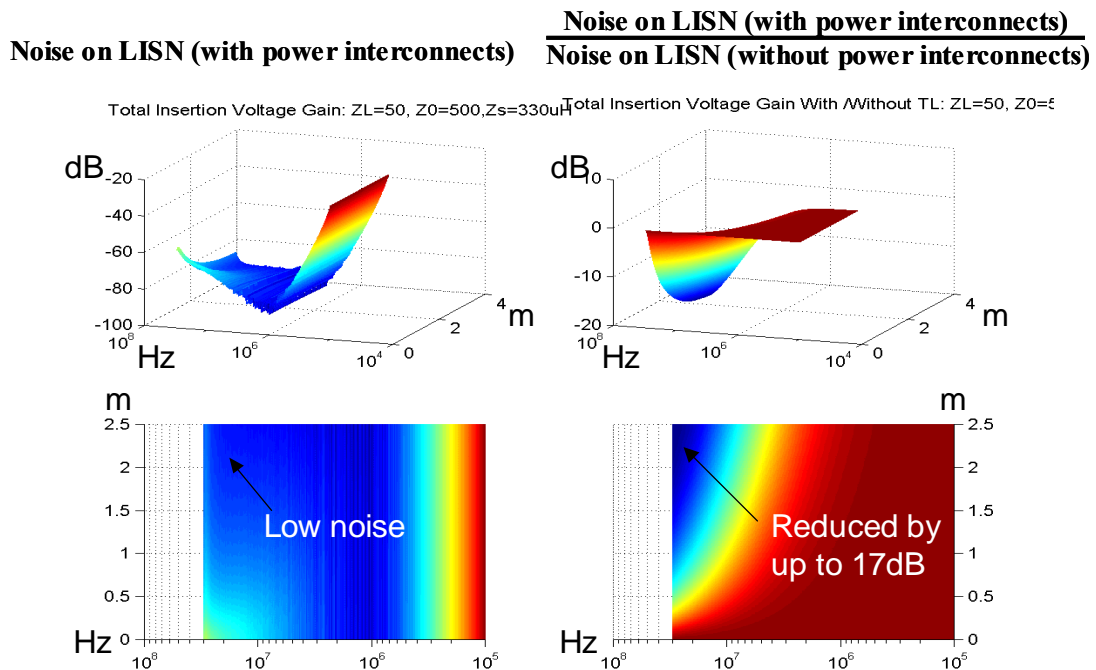


Fig. 7-20. DM noise analysis when $Z_0 = 500\Omega$.

In Fig. 7-20, the noise is significantly reduced at 30MHz when the power interconnect length is 1m. It moves down to 18MHz when the length increases to 2.5m. Compared with the case without the power interconnect, the noise is reduced by up to 17dB at high frequencies since the frequency of HF noise becomes higher than the corner frequency of the equivalent circuit. This verifies the previous analysis. Longer power interconnects cause larger input inductance, the corner frequency of the equivalent circuit in Fig. 7-18 becomes lower. As a result, the noise is attenuated to lower levels at high frequencies.

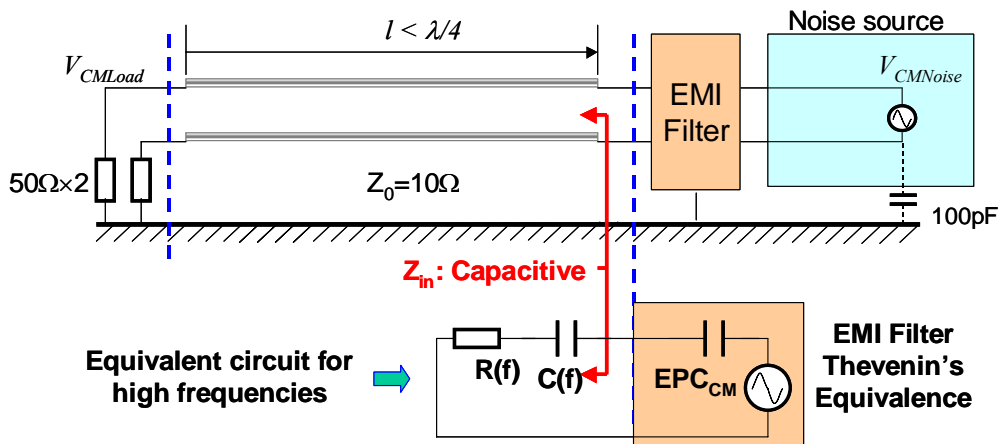


Fig. 7-21. Effects of power interconnect on CM EMI filter performance: $Z_0 < 50\Omega$.

In Fig. 7-21 and 7-22, for the CM filter shown in Figs. 7-9, 7-12 and 7-13, two cases are considered. For the first case, the characteristic impedance of the power interconnects is 10Ω , which is much smaller than the LISN's impedance of 50Ω . This small characteristic impedance could occur when a power bus-bar pair is located very close to the ground plane, which has a large capacitance and a small inductance. For the second case in Fig. 7-22, the characteristic impedance of the power interconnects is 500Ω , which is much larger than the LISN's impedance of 50Ω . This large characteristic impedance

could occur when the distance between the two power interconnects and the ground plane is much larger than the power-interconnect conductor's dimensions, which has a large inductance and a small capacitance. For both cases, a 100pF capacitor is used to represent the noise source impedances of the CM noise. The calculated 3D (power interconnect length – noise frequency – noise amplitude on LISNs in dB) results are shown in Figs. 7-23 and 7-24 for 10 Ω and 500 Ω characteristic impedances respectively. In Fig. 7-21, an $R(f)$ - $C(f)$ equivalent circuit is derived for power interconnects. If the frequency of noise is lower than the corner frequency of $(C(f)+EPC_{CM})/(2\pi R(f)\times EPC_{CM}\times C(f))$, the noise is attenuated. In Fig. 7-22, an $R(f)$ - $L(f)$ equivalent circuit is derived for power interconnects because the characteristic impedance is higher than 50 Ω . There is a resonance in the output loop of the CM filter since the output impedance is the winding capacitor EPC_{CM} .

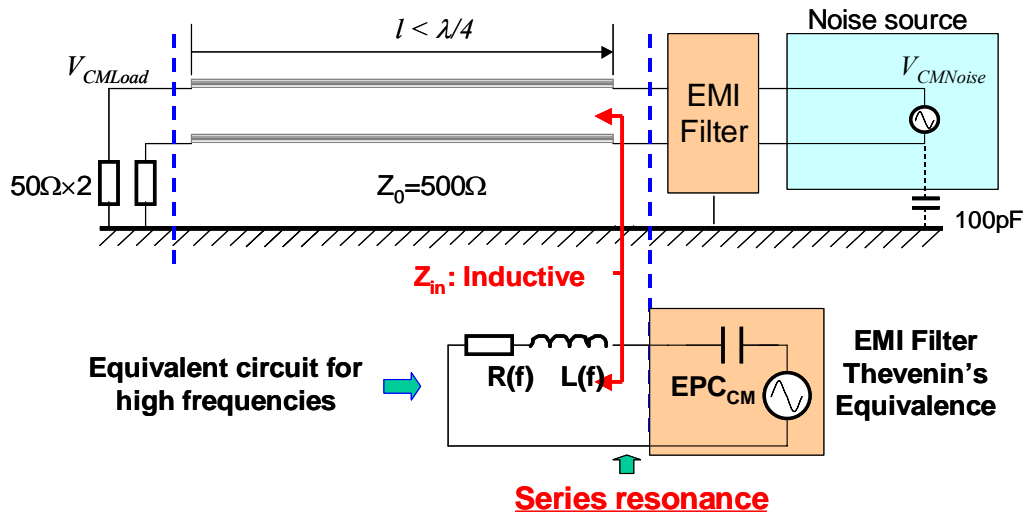


Fig. 7-22. Effects of power interconnect on CM EMI filter performance: $Z_0 > 50\Omega$.

In Fig. 7-23, the noise at high frequencies is lower than the case without power interconnects, since the frequency of the HF noise becomes lower than the corner

frequency of the equivalent circuit. In Fig. 7-24, the noise peak shows up at 30MHz when the interconnect length is 1m. It moves down to 18MHz when the interconnect length increases to 2.5m, since a longer interconnect causes larger input inductance. Compared with the case without the power interconnect, the noise is amplified by 6-14dB when noise peak shows up. This verifies the previous analysis.

Noise on LISN (with power interconnects) **Noise on LISN (with power interconnects)**
Noise on LISN (without power interconnects) **Noise on LISN (without power interconnects)**

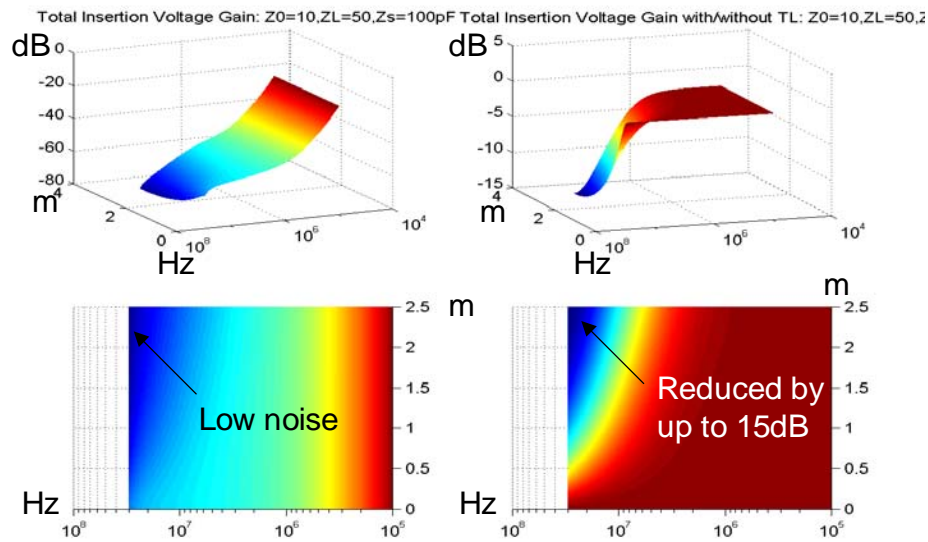


Fig. 7-23. CM noise analysis when $Z_0 = 10\Omega$.

Noise on LISN (with power interconnect) **Noise on LISN (with power interconnect)**
Noise on LISN (without power interconnect) **Noise on LISN (without power interconnect)**

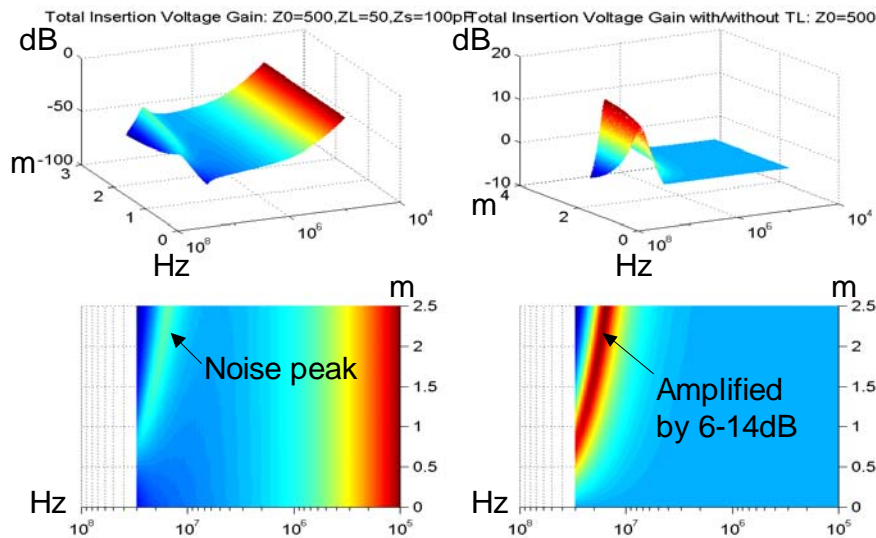


Fig. 7-24. CM noise analysis when $Z_0 = 500\Omega$.

Based on these calculations and analysis, it is found that the DM noise peaks at high frequencies can result from the interactions between power interconnects and the filter trace inductance plus the ESL of the DM capacitor in the filter. CM noise peaks at high frequencies can result from the interactions between power interconnects and the winding capacitor of the CM inductors in the filter.

In order to prevent possible DM noise peaks, the output loop inductances of the DM filter and the ESL of the DM capacitor should be as small as possible, which can push the resonance to frequencies beyond 30MHz. In order to prevent possible CM noise peaks, the winding capacitance of the CM inductor should be as small as possible, which can push the resonance to the frequencies beyond 30MHz. The measurement setup is also an important contributor to noise peaks at high frequencies. If the characteristic impedance between one power interconnect and the ground plane is near 50Ω , noise peak values would be much lower. If the length of power interconnects between the EMI filter and the LISNs is short, for example, shorter than 0.5m, the possibilities for noise peaks would be much lower. In a practical EMI measurement setup, the distance between the power interconnects and the ground plane are not constant, so the characteristic impedance varies along the interconnects. As a result, the magnitude of reflection coefficients also varies along the power interconnects. The reflection coefficient of the interconnects at the EMI filter side can be estimated using reflection theory [1]. The power interconnects and LISNs can be simply characterized using S-parameters for DM and CM respectively as shown in Fig. 7-25.

In Fig. 7-25, power interconnects - LISNs is characterized by a DM S matrix and a CM S matrix. The effects of parasitics of the LISNs and ground wires are included in the S matrices. The impedance transformation effects of the power interconnects and LISNs can then analyzed from the DM reflection coefficients Γ_{DM} and the CM reflection coefficients Γ_{CM} . Γ_{DM} and Γ_{CM} are first calculated from the measured DM and CM S matrices. The interaction between the input impedances Z_{inDM} and Z_{inCM} of the power interconnect - LISNs network and the output impedances of DM and CM filters can then be analyzed.

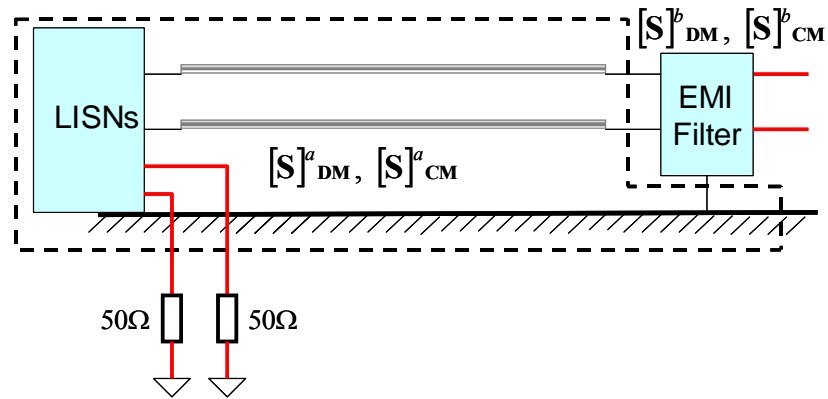


Fig. 7-25. Characterizing power interconnects and LISNs as a network.

$$Z_{inDM} = Z_{0D} \frac{1 + \Gamma_{DM}}{1 - \Gamma_{DM}} \quad (7-24)$$

$$Z_{inCM} = Z_{0C} \frac{1 + \Gamma_{CM}}{1 - \Gamma_{CM}} \quad (7-25)$$

7.6. Experiments

The experiments are carried out in an EMI chamber and the setup is shown in Fig. 7-26. An Agilent four-port, ENA, RF network analyzer, E5070B is used in the experiment.

In the experiment, DM and CM S matrices of power interconnects-LISNs are first measured. The input impedances are then calculated. Second, the DM and CM S matrixes of the EMI filter are measured and the output impedances are calculated. By analyzing these input and output impedances, the possible resonant frequencies are identified. At last, the DM and CM S matrices of the whole system (EMI filter-power interconnects-LISNs) are measured. The measured results are explained by the results from the first two experiments.

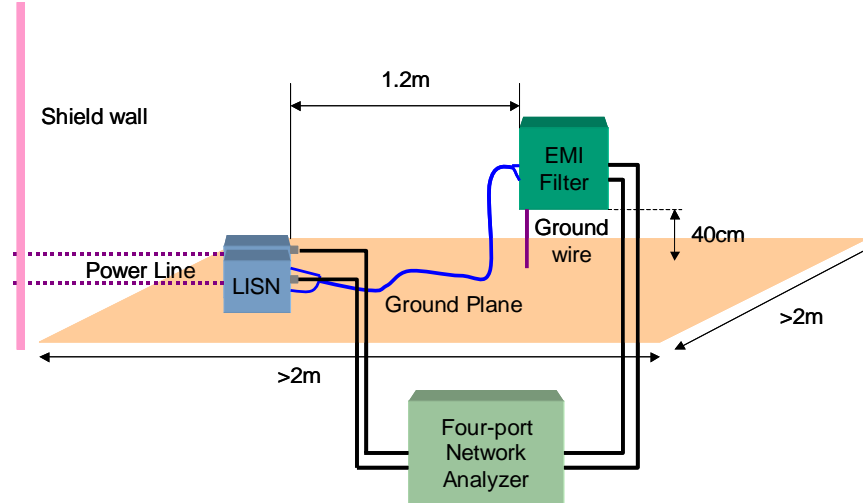


Fig. 7-26. Experiment setup.

For the DM part, the transmission line effects are not significant. The measured reflection coefficient is actually smaller than -20dB up to 50MHz, so the characteristic impedance of the power interconnect is near the load impedance. DM performance of the EMI filter-power interconnects-LISNs is almost the same as the EMI filter as shown in Fig. 7-27. The peak and dip around 20MHz on both curves are due to the resonances between the CM and DM capacitors in the EMI filter [2]. For the CM part, the imaginary part of the input impedance of power interconnects-LISNs and the imaginary part of the output impedance of the CM EMI filter are calculated from the measured S matrices and

compared in Fig. 7-28. The resonance occurs when the imaginary parts cancel each other. Fig. 7-29 shows the comparison of the measured S21 between the filter and the whole system (EMI filter-power interconnects-LISNs).

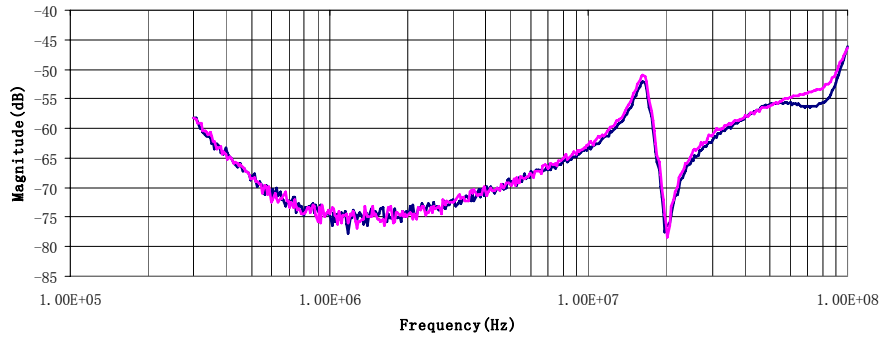


Fig. 7-27. Comparison of S21 on DM propagation.

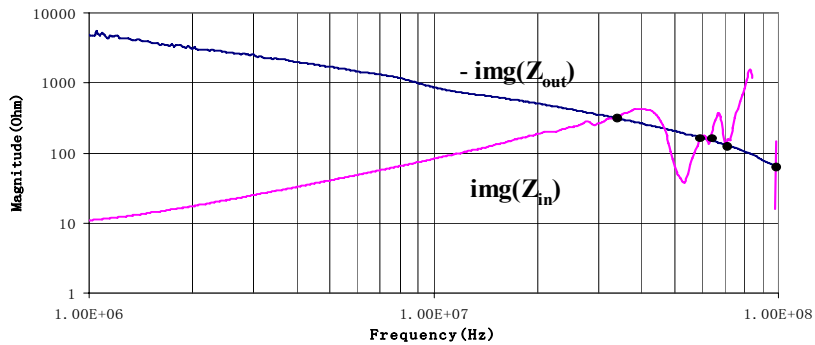


Fig. 7-28. Imaginary parts of the input and output impedances.

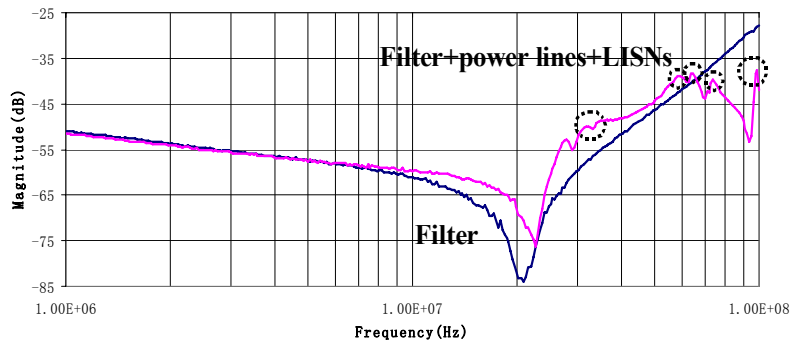


Fig. 7-29. Comparison of S21 on CM propagation.

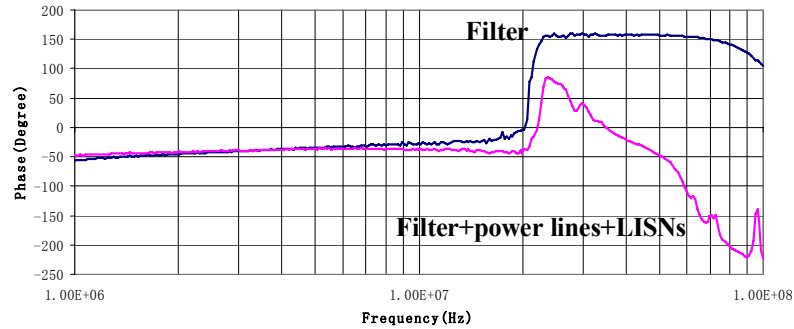


Fig. 7-30. Phases of S21.

In Fig. 7-28, the output impedance of the filter is the winding capacitance of the CM inductor. The input impedance of the power interconnects is inductive below 40MHz since the characteristic impedance of the power interconnects is larger than the load impedance 25Ω. At the frequencies above 40MHz, the input impedance is somewhat complicated because of the varying characteristic impedance along the interconnects and mismatched load at the ends of the interconnects. The imaginary curve of input impedance is not shown from 83MHz to 97MHz in Fig. 7-28 since it is negative in that frequency range. From Fig. 7-28, two curves cross at 34MHz, 59MHz, 63MHz, 71MHz and 98MHz. The imaginary parts cancelled each other at these frequencies. Based on the previous analysis, series resonances would happen at these frequencies and peaks would show on the S21 curve. In Fig. 7-29, at corresponding frequencies, peaks show up on the curve of filter-power interconnects-LISNs, which proves the interaction between the parasitics of the EMI filters and the impedance transformed by power interconnects. The cross point between 40MHz and 53MHz in Fig. 7-28 does not cause a peak in Fig. 7-29 because of the capacitive behavior of input impedance in that frequency range. Fig. 7-30 shows the corresponding phases of S21. Comparing the two curves in Fig. 7-29, the resonance at 34MHz degrades the filter performance by up to 13dB from 8MHz to

30MHz. The actual filter performance is kept degraded until 65MHz due to other resonances. The interaction between the winding capacitor of the CM inductors in the filter and the impedance transformed by the power interconnects could therefore be an important issue for high frequency analysis.

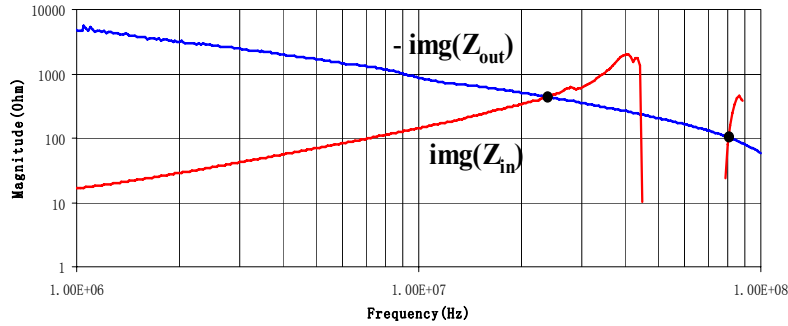


Fig. 7-31. Imaginary parts of input and output impedances.

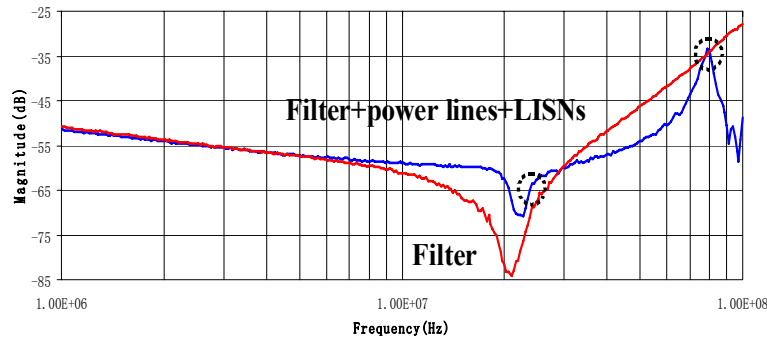


Fig. 7-32. Comparison of S21 on CM propagation.

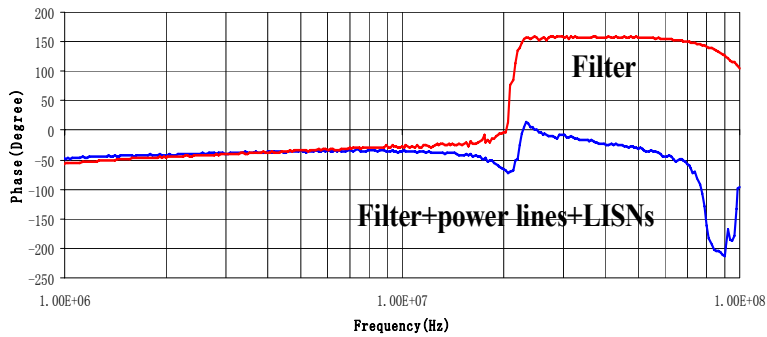


Fig. 7-33. Phases of S21.

The second experiment is carried out by increasing the distance between the power interconnects and the ground plane. From (7-2), (7-8) and (7-14), it is expected that the characteristic impedance is higher than the previous case. As a result the input impedance would be more inductive than the previous case. The first resonance frequency should be lower than that in the first experiment. Figs. 7-31, 7-32 and 7-33 show the results.

In Fig. 7-31, the first resonance shows up at 24MHz, which is very close to the series resonant frequency (21MHz) of the CM capacitors (due to ESL). As a result, the two resonances partly cancel each other. This is clearly shown on the phase curves in Fig. 7-33. The cross point around 80MHz in Fig. 7-31 causes a resonance on the S21 curve in Fig. 7-32. The imaginary curve of the input impedance is not shown in Fig. 7-31 from 45MHz to 79MHz, since it is negative in that frequency range. The performance of the filter is degraded by up to 20dB in the frequency range of 6MHz to 30MHz, due to the resonance between the winding capacitor of the CM inductors in the filter and the impedance transformed by the power interconnects.

7.7. Summary

This chapter first analyzed the electrical parameters for both DM and CM propagation on power interconnects. Power interconnects are then considered as transmission lines with an impedance transformation function. As a result, the input impedances of power interconnects, i.e. the loads of DM and CM EMI filters, are no longer the LISN's real 50Ω impedances, but capacitive or inductive impedances. These impedances can interact with the parasitic parameters of EMI filters and degrade the filters' performance at high

frequencies. Finally, both simulations and experiments are carried out to prove the analysis. Solutions are proposed to avoid these interactions.

Reference

- [1] R. E. Collin, *Foundations for Microwave Engineering*, Second Edition, McGraw-Hill, N.Y., 1992.
- [2] Shuo Wang, J. D. van Wyk, Fred C. Lee and W. G. Odendaal, "Transformation between Common Mode and Differential Mode due to Imperfect Balance of EMI Filters," in *proc. 2005 CPES Power Electronics Conference*, Blacksburg, VA, 17-20 April. 2005, pp. 551 -555.
- [3] Shuo Wang, F.C. Lee, D.Y. Chen and W.G. Odendaal, "Effects of Parasitic Parameters on the Performance of EMI Filters," In *proc. IEEE Power Electronics Specialist Conference*, Acapulco, Mexico, 15-19 Jun. 2003, pp.73-78.
- [4] Chizhang Feng, *Electromagnetic Field*, 2nd ed, Advanced Education Publishing House. 1992.
- [5] David M. Pozar, *Microwave Engineering*, John Wiley & Sons, Inc., 1998.
- [6] Mark J. Nave, *Power line filter design for switched-mode power supply*, Van Nostrand Reinhold, New York, 1991.
- [7] L. Ran, J. C. Clare, K. J. Bradley and C. Christopoulos, "Measurement of Conducted Electromagnetic Emissions in PWM Motor Drive Systems Without the Need for an LISN," *Electromagnetic Compatibility, IEEE Transactions*, Volume 41, No. 1 February 1999, pp. 50 -55.
- [8] *Agilent E5070B/E5071B ENA Series RF Network Analyzers User's Guide*, Fifth Edition, Agilent Technologies, 2004.
- [9] Reinhold Ludwig and Pavel Bretchko, *RF Circuit Design: Theory and Applications*, Second Edition, Prentice Hall, 2000.

50Ω terminations due to the high impedance of the two 50μH inductors in the LISNs. Here, 50Ω terminations can also be the input impedances of a spectrum analyzer. The DM or CM noise voltage drop on a 50Ω resistance is defined as DM or CM noise voltage.

In Fig. 8-1, the noise voltage drop V_1 or V_2 on one of the 50Ω terminations is defined as the total noise, and it is the vector sum or vector difference of CM and DM noise voltages. The DM and CM noise voltages can then be calculated from (8-1, 8-2). In order to separate DM and CM noise, the noise separator should satisfy three requirements:

- Input impedances are always real 50 Ω and are independent from noise source impedances.
- Output is $|(V_1 - V_2)/2|$ for DM noise measurement and $|(V_1 + V_2)/2|$ for CM noise measurement.
- Leakage between the CM and the DM at the output should be small.

$$|V_{DM}| = \left| \frac{V_2 - V_1}{2} \right| = 50|i_{DM}| \quad (8-1)$$

$$|V_{CM}| = \left| \frac{V_2 + V_1}{2} \right| = 50|i_{CM}| \quad (8-2)$$

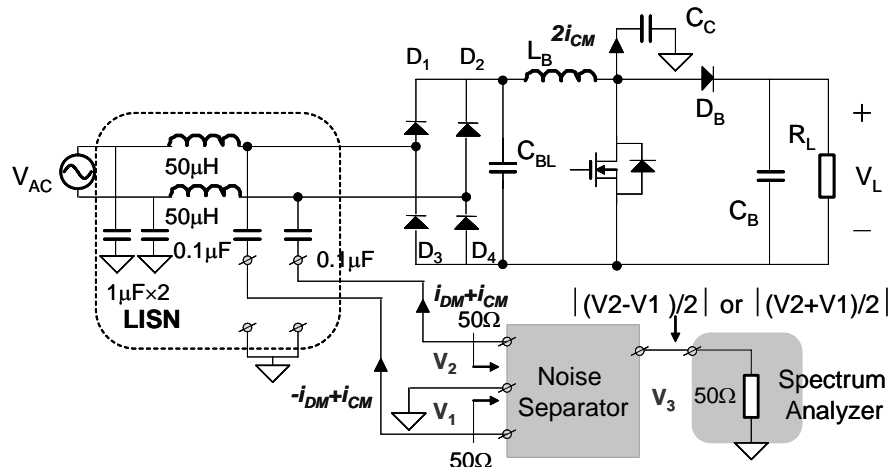


Fig. 8-2. Using noise separator to separate DM and CM noise.

The requirement a) guarantees consistent measurement conditions and accurate sampling of noise voltage; b) guarantees correct noise separation; and c) guarantees small interference between the CM and DM noise measurements. Most of the noise separators [1-9, 16] cannot satisfy all these three requirements, and therefore measurement results are questionable. For example, input impedances of many separators are noise source dependent. These noise separators do not yield correct measurement results because their input impedances are functions of input voltages or source impedances. Other separators fail to satisfy requirement b); therefore they lack an accurate output. In order to evaluate a noise separator, the above three requirements should be checked one by one. The first is input impedance. Papers [3, 4] designed and measured input impedance for one input port, assuming the input of another port was zero with a 50Ω source impedance; this method is not correct, because another input can affect the input impedance of the designed port and the practical source impedance is not 50Ω . The second requirement is the transmission coefficient of noise separators. The DM transmission ratio (DMTR) for the DM noise separator and the CM transmission ratio (CMTR) for the CM noise separator are two parameters that need to be evaluated, as follows:

$$\text{For DM noise separator: } DMTR = \left| \frac{V_{OD}}{V_{DM}} \right|, \text{ and} \quad (8-3)$$

$$\text{For CM noise separator: } CMTR = \left| \frac{V_{OC}}{V_{CM}} \right|, \quad (8-4)$$

where V_{DM} is the DM voltage fed to the inputs of a DM noise separator, V_{OD} is the output voltage of this DM noise separator due to V_{DM} , V_{CM} is the CM voltage fed to the inputs of a CM noise separator, and V_{OC} is the output voltage of this CM noise separator

due to V_{CM} . From (8-3, 8-4), the ideal DMTR and CMTR should be 0 dB. Papers [2, 3, 6] used power splitters to generate CM and DM sources and then evaluated the transmission coefficients of the noise separators using a network analyzer, as shown in Fig. 8-3. This method has three potential problems. First, in point of network analysis, the measured result is only valid when the noise source is a power splitter. In fact, nine network parameters are needed to fully characterize a three-port noise separator. The measured transmission coefficient is only one parameter, which does not guarantee the noise separator has the similar performance when the noise source is not a power splitter. Second, the power splitter is imperfect, and its negative effects cannot be excluded through calibration of the network analyzer. For example, the phase difference of its two outputs is not exactly 0° or 180° , and this may cause significant measurement errors [5, 9]. The magnitude difference of the two outputs can cause similar problems [5, 9]. Third, for a two-way power splitter, the amplitude of the outputs is 3 dB lower than its input and the network analyzer's reference, so the measured DMTR, CMTR, DMRR and CMRR are 3dB lower than they should be. The third requirement can be characterized by two parameters: the CM rejection ratio (CMRR) and the DM rejection ratio (DMRR), which are defined as follows in this chapter:

$$\text{For DM noise separator : } CMRR = \left| \frac{V_{OD}}{V_{CM}} \right|, \text{ and} \quad (8-5)$$

$$\text{For CM noise separator : } DMRR = \left| \frac{V_{OC}}{V_{DM}} \right|, \quad (8-6)$$

where V_{CM} is the CM voltage fed to the inputs of a DM noise separator, V_{OD} is the output voltage of this DM noise separator due to V_{CM} , V_{DM} is the DM voltage fed to the inputs

of a CM noise separator, and V_{OC} is the output voltage of this CM noise separator due to V_{DM} . CMRR and DMRR should be as small as possible.

For the same reason as the second requirement, if a power splitter is used to evaluate CMRR and DMRR, the measurement does not guarantee the noise separator has the similar performance in practical applications; thus the method is not adequate.

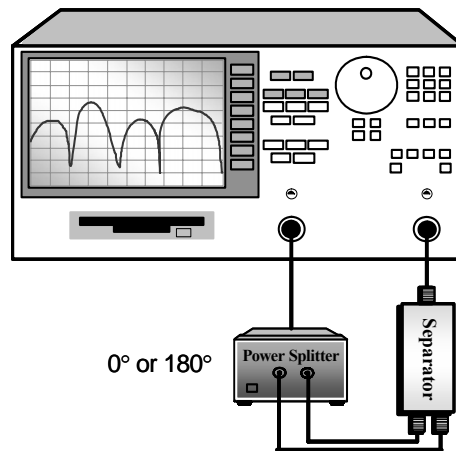


Fig. 8-3. Using a power splitter and a network analyzer to measure the noise separator may not yield accurate results.

Appropriate network parameters must be introduced in order to characterize and evaluate noise separators using the three requirements. Scattering parameters (S-parameters) are selected in this chapter because of three reasons. First, frequency domain characterization of network employing $[Z]$, $[Y]$, $[H]$ and $[ABCD]$ parameters often requires either a short circuit or an open circuit at one port, which is difficult to achieve in the high frequency (HF) range because of parasitic parameters [14, 15]. On the other hand, for S-parameters, no short or open circuit is needed. Second, S-parameter method can be calibrated to the exact points of measurement, so that the effects of parasitics due to measurement interconnects are excluded. For $[Z]$, $[Y]$, $[H]$ and $[ABCD]$ parameters

measurement, expensive special probes may be needed for calibration. Third, S-parameters are analytically convenient, and capable of providing a great insight into a measurement or design problem [15]. Thanks to S-parameters, the powerful signal flow graph can be used for network analysis with clear physical concepts.

8.2. Characterization of Noise Separator

For a DM or CM noise separator, there are two input ports, port1 and port2 and one output port, port3 so it is a three-port network. This three-port linear passive network can be characterized in terms of waves, as shown in Fig. 8-4. In Fig. 8-4, a_n is the normalized incident wave, and b_n is the normalized reflected wave. Port voltage V_n can be expressed by (8-7) [10, 11]:

$$V_n = \sqrt{Z_0}(a_n + b_n) \quad (8-7)$$

where Z_0 is the reference impedance, which is usually 50Ω , and n is the port number.

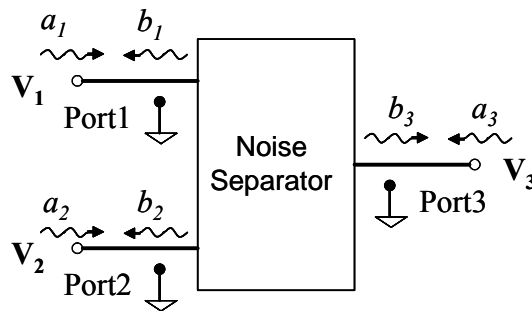


Fig. 8-4. Characterizing noise separator in terms of waves.

To fully characterize a three-port linear passive network, three linear equations are required among the six wave variables [11]. The nine S-parameters in (8-8) are therefore introduced to correlate a_n and b_n [10, 12]. S_{nn} refers to the reflection coefficients, and S_{mn}

represents the transmission coefficients. According to the transmission-line theory [10, 13], when reflected wave b_n reaches the source or load side, it will also be reflected because of the mismatched impedances. The reflection coefficients Γ_{sn} at source side and Γ_L at load side are given through (8-9, 8-10). It is known that for passive networks, $|\Gamma_{sn}| \leq 1$ and $|\Gamma_L| \leq 1$.

$$\begin{pmatrix} b_1 \\ b_2 \\ b_3 \end{pmatrix} = \begin{pmatrix} S_{11} & S_{12} & S_{13} \\ S_{21} & S_{22} & S_{23} \\ S_{31} & S_{32} & S_{33} \end{pmatrix} \begin{pmatrix} a_1 \\ a_2 \\ a_3 \end{pmatrix} \Rightarrow \mathbf{b} = \mathbf{S}\mathbf{a} \quad (8-8)$$

$$\Gamma_{sn} = \frac{Z_{sn} - Z_0}{Z_{sn} + Z_0}, \text{ and} \quad (8-9)$$

$$\Gamma_L = \frac{Z_L - Z_0}{Z_L + Z_0}. \quad (8-10)$$

Fig. 8-4 is then characterized by the signal flow graph in Fig. 8-5. In Fig. 8-5, b_{sn} is the normalized wave emanating from the source. For a given voltage source V_{sn} with source impedance Z_{sn} , b_{sn} is given by (8-11) [13]:

$$b_{sn} = \frac{\sqrt{Z_0} V_{sn}}{Z_{sn} + Z_0}. \quad (8-11)$$

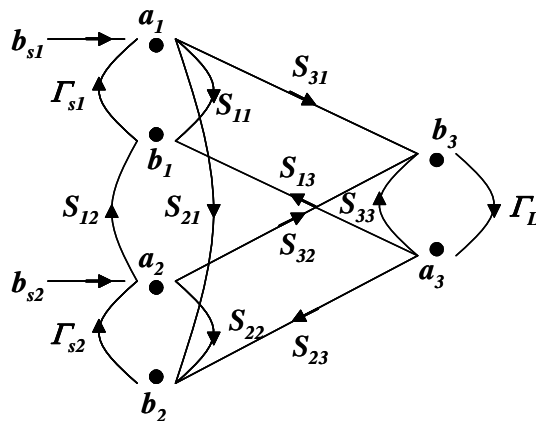


Fig. 8-5. Characterizing the noise separator using a signal flow graph.

Because the output of the noise separator is terminated by the 50Ω input impedance of the spectrum analyzer, which is shown in Fig. 8-2, reflection coefficient Γ_L is zero. As a result, a_3 is zero, and the signal-flow graph is equivalent to Fig. 8-6. Fig. 8-6 characterizes a practical noise separator matched by a spectrum analyzer at port3. It is now important to determine the appropriate S matrix for an ideal noise separator.

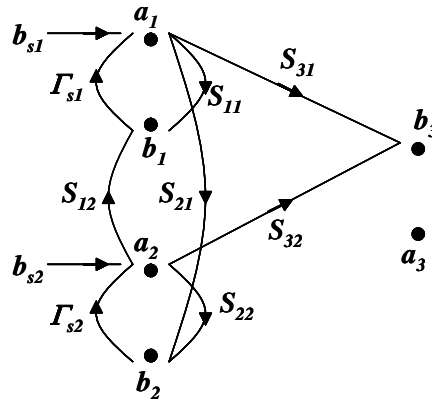


Fig. 8-6. Signal-flow graph for a practical noise separator with a matched load at port3.

In order to achieve 50Ω input impedance independent from noise source impedance, the reflection coefficients at port1 and port2 must be zero. The reflection coefficients Γ_1 and Γ_2 for port1 and port2 in Fig. 8-6 are described as (8-12, 8-13):

$$\Gamma_1 = \frac{Z_{in1} - Z_0}{Z_{in1} + Z_0} = S_{11} + \frac{S_{21}\Gamma_{s2}S_{12}}{1 - S_{22}\Gamma_{s2}}, \text{ and} \quad (8-12)$$

$$\Gamma_2 = \frac{Z_{in2} - Z_0}{Z_{in2} + Z_0} = S_{22} + \frac{S_{21}\Gamma_{s1}S_{12}}{1 - S_{11}\Gamma_{s1}}, \quad (8-13)$$

where Z_{in1} and Z_{in2} are the input impedances of port1 and port2. From (8-12, 8-13), in order to guarantee a 50Ω input impedance independent from noise source impedance, S_{11} , S_{22} and S_{12} , S_{21} must be zero; therefore b_1 and b_2 are zero. So the signal-flow graph is thus equivalent to Fig. 8-7. In Fig. 8-7, based on (7), the voltage at port3 is given by (8-14):

$$\mathbf{V}_3 = \mathbf{V}_1 S_{31} + \mathbf{V}_2 S_{32}. \quad (8-14)$$

Based on (8-1, 8-2, 8-14), for a DM noise separator:

$$S_{31} = -S_{32} = \frac{1}{2}, \text{ or } -S_{31} = S_{32} = \frac{1}{2}. \quad (8-15)$$

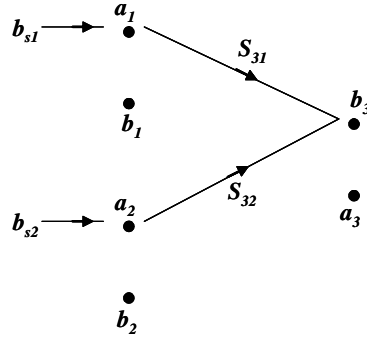


Fig. 8-7. Signal-flow graph for an ideal noise separator with a matched load at port3.

For a CM noise separator:

$$S_{31} = S_{32} = \frac{1}{2}, \text{ or } -S_{31} = -S_{32} = \frac{1}{2}. \quad (8-16)$$

The final \mathbf{S} matrix for an ideal DM noise separator is therefore:

$$[\mathbf{S}] = \begin{pmatrix} 0 & 0 & S_{13} \\ 0 & 0 & S_{23} \\ \pm \frac{1}{2} & \mp \frac{1}{2} & S_{33} \end{pmatrix}. \quad (8-17)$$

And for an ideal CM noise separator:

$$[\mathbf{S}] = \begin{pmatrix} 0 & 0 & S_{13} \\ 0 & 0 & S_{23} \\ \pm \frac{1}{2} & \pm \frac{1}{2} & S_{33} \end{pmatrix}. \quad (8-18)$$

In (8-17, 8-18), the third column in the \mathbf{S} matrix has nothing to do with the performance of a noise separator because port3 is matched. Therefore, there is no need to match output impedance although paper [3] tries to get 50Ω output impedance. For a noise separator, S_{11} , S_{22} and S_{12} , S_{21} should be as small as possible. S_{31} and S_{32} should be 0.5, and should be out of phase for a DM noise separator, and in phase for a CM noise separator.

For a practical noise separator, S_{11} , S_{22} and S_{12} , S_{21} are not zero; and S_{31} and S_{32} are not exactly 0.5, so Fig. 8-6 should be used for evaluation. The input impedance of a noise separator can be evaluated through (8-12, 8-13). In (8-12, 8-13) the second term can be ignored if it is much smaller than the first term, which means input impedances are independent from Γ_{s1} and Γ_{s2} , which represent the source impedances. Then the input impedances can be characterized solely by S_{11} and S_{22} , and are free of noise source impedances (8-19, 8-20), as follows:

$$Z_{in1} \approx Z_0 \frac{1+S_{11}}{1-S_{11}}, \text{ and} \quad (8-19)$$

$$Z_{in2} \approx Z_0 \frac{1+S_{22}}{1-S_{22}}. \quad (8-20)$$

Based on (8-3, 8-4, 8-7) and Fig. 8-6, the DMTR for the DM noise separator and the CMTR for the CM noise separator can also be derived using Mason's rule (8-21, 8-22), in which the approximately equal values hold if the third term is much smaller than the second term in the denominators. This is also the condition for independent real 50Ω in (8-19, 8-20).

$$\text{For DM noise separator : } DMTR = \frac{S_{31}}{(1 + S_{11} + \frac{S_{21}\Gamma_{s2}S_{12}}{1 - S_{22}\Gamma_{s2}})} - \frac{S_{32}}{(1 + S_{22} + \frac{S_{21}\Gamma_{s1}S_{12}}{1 - S_{11}\Gamma_{s1}})} \approx \frac{S_{31}}{1 + S_{11}} - \frac{S_{32}}{1 + S_{22}} \quad (8-21)$$

$$\text{For CM noise separator : } CMTR = \frac{S_{31}}{(1 + S_{11} + \frac{S_{21}\Gamma_{s2}S_{12}}{1 - S_{22}\Gamma_{s2}})} + \frac{S_{32}}{(1 + S_{22} + \frac{S_{21}\Gamma_{s1}S_{12}}{1 - S_{11}\Gamma_{s1}})} \approx \frac{S_{31}}{1 + S_{11}} + \frac{S_{32}}{1 + S_{22}} \quad (8-22)$$

Based on (8-5, 8-6, 8-7) and Fig. 8-6, the CMRR for the DM noise separator and the DMRR for the CM noise separator can be derived similarly as follows:

$$\text{For DM noise separator : } CMRR = \frac{S_{31}}{(1 + S_{11} + \frac{S_{21}\Gamma_{s2}S_{12}}{1 - S_{22}\Gamma_{s2}})} + \frac{S_{32}}{(1 + S_{22} + \frac{S_{21}\Gamma_{s1}S_{12}}{1 - S_{11}\Gamma_{s1}})} \approx \frac{S_{31}}{1 + S_{11}} + \frac{S_{32}}{1 + S_{22}} \quad (8-23)$$

$$\text{For CM noise separator : } DMRR = \frac{S_{31}}{(1 + S_{11} + \frac{S_{21}\Gamma_{s2}S_{12}}{1 - S_{22}\Gamma_{s2}})} - \frac{S_{32}}{(1 + S_{22} + \frac{S_{21}\Gamma_{s1}S_{12}}{1 - S_{11}\Gamma_{s1}})} \approx \frac{S_{31}}{1 + S_{11}} - \frac{S_{32}}{1 + S_{22}} \quad (8-24)$$

Equations (8-19 – 8-24) are critical for noise-separator evaluation. For a noise separator, as long as the S-parameters are measured using a network analyzer, its performance can be evaluated through (8-19 – 8-24). No extra power splitter is needed; therefore the results can be applied to any application. In (8-12, 8-13), if $S_{21}S_{12}$ is small enough to make the second term approach zero or much smaller than the first term, the input impedances are independent from noise source impedances.

8.3. Evaluation of Existing Noise Separators

Just as stated in chapter I, a qualified noise separator should meet three requirements. The first requirement is independent real 50Ω input impedances. Some existing noise separators assume the noise impedances are infinite [1, 2, 5, 9], real 50Ω [3, 4] or 0Ω [7]. This is not correct because the noise source impedances can be any value. As an

example, the noise separator in paper [1] is shown in Fig. 8-8. The input impedances for this separator are given as:

$$Z_{in1} = 82 \parallel (50 + 82 \parallel Z_{S2}), \text{ and} \quad (8-25)$$

$$Z_{in2} = 82 \parallel (50 + 82 \parallel Z_{S1}). \quad (8-26)$$

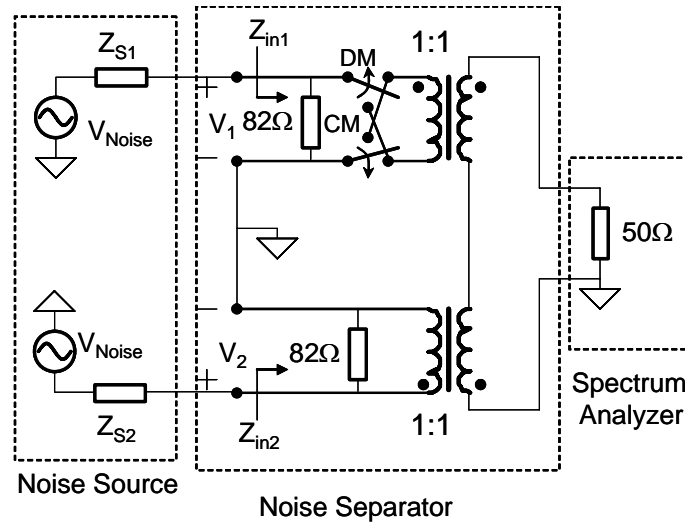


Fig. 8-8. Noise separator proposed by paper [1].

Obviously, if $Z_{S1} = Z_{S2} = \infty$, $Z_{in1} = Z_{in2} \approx 50 \Omega$; however for practical cases, $Z_{S1} \neq \infty$ and $Z_{S2} \neq \infty$, so $Z_{in1} \neq 50 \Omega$ and $Z_{in2} \neq 50 \Omega$. This also means the input impedances are functions of the input voltages. As a result, this noise separator cannot correctly separate noise. Theoretically, only the noise separators in papers [6, 16] can offer 50Ω input impedances.

Under the condition of real 50Ω input impedances, CMTR and DMTR should be 0 dB, which is the second requirement. Because the noise separators in paper [1-5, 7, 9] cannot meet the first requirement, they certainly cannot meet the second one. The input impedances of the noise separator (power combiner) in paper [6] are real 50Ω ; however

both CMTR and DMTR are 3 dB higher. Furthermore, two sets of circuits are needed to measure CM and DM noise respectively. The noise separator in paper [16], which is shown in Fig. 9, meets 0dB CMTR but its DMTR is 6 dB higher.

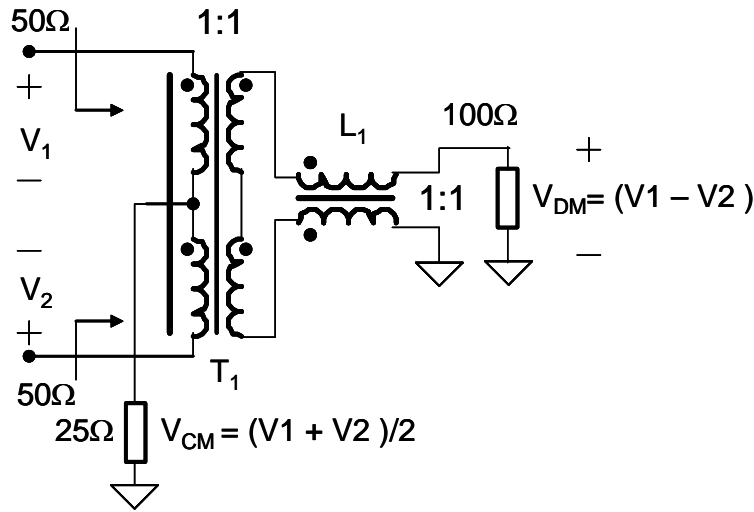


Fig. 8-9. Noise separator proposed by paper [16].

The third requirement is very small CMRR and DMRR. The noise separator works at frequencies as high as 30 MHz, so parasitic parameters play very important roles on separator performance. Because both CMRR and DMRR are usually very small, parasitic parameters can significantly affect them at high frequencies. Some designs are theoretically applicable; however due to parasitics, may not be good in practical designs.

For HF design, the conventional transformer T_1 and the conventional common choke L_1 shown in Fig. 8-9 should be avoided. The parasitic parameters in this noise separator are shown in Fig. 8-10. In Fig. 8-10, L_{K1} , L_{K2} , L_{K3} and L_{K4} are the leakage inductance between primary and secondary sides of the transformer. C_{W1} and C_{W2} are the winding capacitance between primary and secondary sides of the transformer. L_{K5} and L_{K6} are

leakage inductance between two windings of the CM choke. Obviously the DM input impedance Z_{in} of the CM choke shown in Fig. 8-10 would no longer be real $100\ \Omega$ due to leakage inductance L_{K5} and L_{K6} at high frequencies. L_{K1} , L_{K2} , L_{K3} and L_{K4} also introduce extra impedances at high frequencies. As a result of these parasitics, the input impedances of the separator would deviate from real $50\ \Omega$ at high frequencies. The transformer would also no longer block CM noise at high frequencies due to winding capacitance C_{W1} and C_{W2} . The CMRR is therefore compromised. The transformer could be unbalanced at high frequencies due to parasitic parameters, which also degrades the CMRR and DMRR. In order to reduce leakage inductance, two windings of the transformer are twisted in paper [4]; however this increases winding capacitance so that CMRR is degraded.

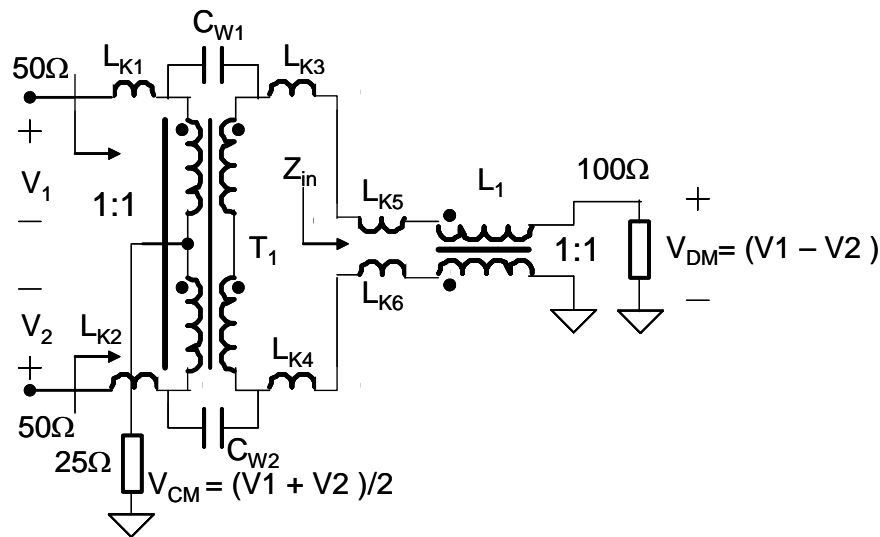


Fig. 8-10. Parasitic parameters in a noise separator.

For the noise separators in [6, 18], conventional transformers are used at outputs for impedance transformation [18]: $50\ \Omega - 100\ \Omega$ and $50\ \Omega - 25\ \Omega$. These transformers have

two disadvantages: first, the parasitics degrade separator HF performance and second, the output is 3dB higher. Output should be redesigned to get rid of conventional transformers. The transmission line transformers [17], which have much better performance at high frequencies, should be used in noise separator design.

8.4. Developing a High Performance Noise Separator

In order to build a high performance noise separator, transmission line transformers [17] are employed in this chapter. A transmission line transformer is constructed by winding a transmission line on a magnetic core such as a ferrite toroid. Fig. 8-11 shows the schematic and the typical structure of a transmission line transformer. In Fig. 8-11, two wires form a transmission line and are wound on a ferrite toroid. L is the CM inductance of transmission line, which is attributed to the high permeability of the ferrite toroid. The DM inductance L_K of the transmission line is factually the distributed leakage inductance of two CM inductance. C_w is the distributed winding capacitance between two wires. Ignoring the losses, it is well-known that the characteristic impedance Z_0 of the transmission line is given by (8-27).

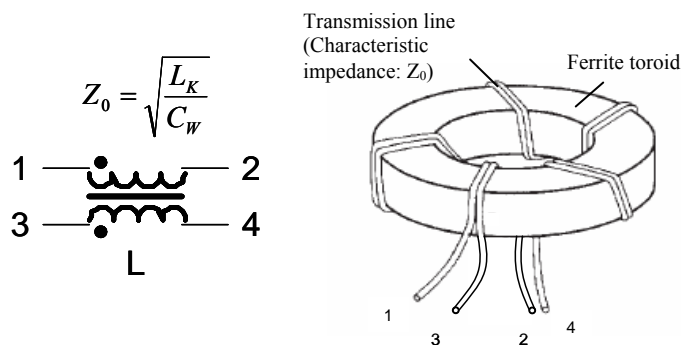


Fig. 8-11. Transmission line transformer.

$$Z_0 = \sqrt{\frac{L_K}{C_w}} \quad (8-27)$$

Z_0 can be determined through measurements using equation (28):

$$Z_0 = \sqrt{Z_S Z_P}, \quad (8-28)$$

where Z_S is the short-circuit impedance (with the other end of the transmission line short-circuited) and Z_P is the open-circuit impedance (with the other end of the transmission line open).

According to transmission line theory, if the characteristic impedance is equal to load impedance, the input impedance is equal to load impedance. The DM input impedances Z_{in1} and Z_{in2} of transmission line transformer shown in Fig. 8-12 are therefore equal to half of the load impedance. The output DM voltage is also equal to input DM voltage. The CM input impedance is very high because of CM inductance and HF losses. As a result the output CM voltage is very small.

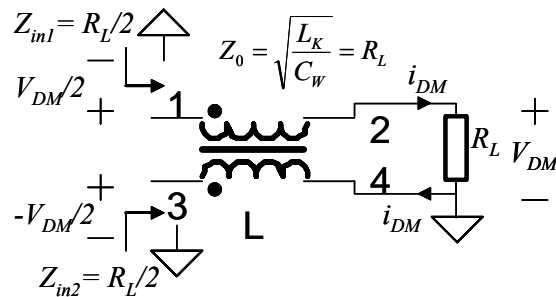


Fig. 8-12. Utilizing winding capacitance and leakage inductance to match DM load.

These properties are important because the effects of the winding capacitance and the leakage inductance are cancelled so that DM input is transferred to the load without

change. The negative effects of parasitics are factually excluded. It is a significant difference from the conventional CM choke shown in Fig. 8-10.

The transmission line transformer can also be connected to the style as shown in Fig. 8-13. In Fig. 8-13, the terminals 2 and 3 and load R_L are connected together. It can be proven that if the characteristic impedance of the transmission line is equal to $2R_L$, CM input impedances Z_{in1} and Z_{in2} are $2R_L$. The CM input is then added to the load without change. Because effects of the winding capacitance and the leakage inductance are cancelled, the negative effects of parasitics are excluded so that the design is better than the design in Fig. 8-10. Because two windings are in series for DM noise, the DM input impedance is very high. Because load is connected to the mid-point of two windings, the output due to DM inputs is zero.

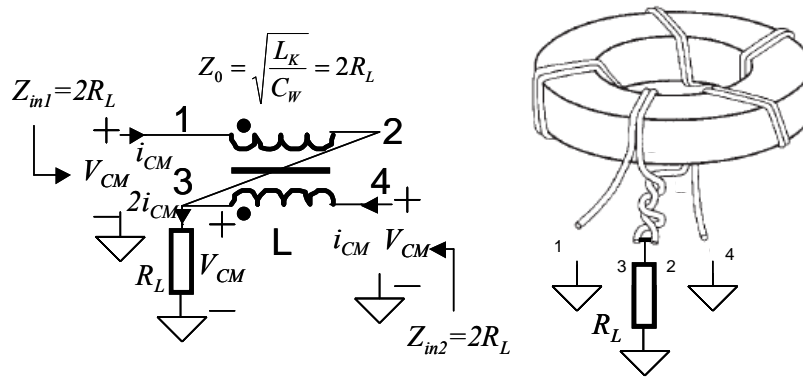


Fig. 8-13. Utilizing winding capacitance and leakage inductance to match CM load.

A performance-improved noise separator shown in Fig. 14 is finally proposed based on the circuits in Figs. 8-12 and 8-13. In Fig. 8-14, transmission line transformer T1 is connected as in Fig. 8-13. It conducts CM noise, while blocking DM noise. T2 is connected, as in Fig. 8-12. It conducts DM noise, while blocking CM noise. A 50Ω

resistor is in parallel with the input impedance of the spectrum analyzer at CM output port, and another 50Ω resistor is in series with the input impedance of the spectrum analyzer at DM output port. Based on previous analysis, this simple design for outputs results in two benefits: 1) Real 50Ω DM and CM input impedances occur without using conventional transformers at output to transform impedance. 2) Outputs are exact DM and CM noise voltages: no extra adjustment needed.

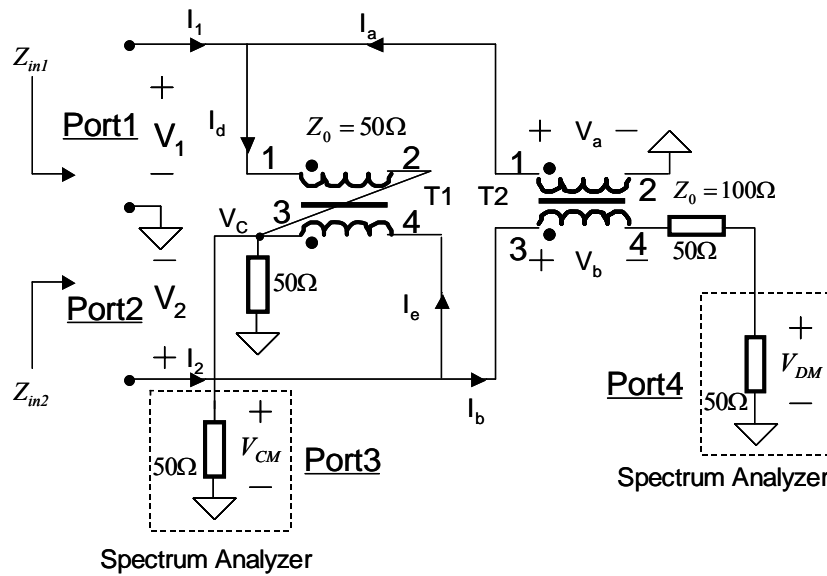


Fig. 8-14. Proposed noise separator.

The following is the circuit analysis for Fig. 8-14 on output voltages and input impedances,

$$\mathbf{V}_b = \mathbf{V}_a = \mathbf{V}_1, \quad (8-29)$$

$$\mathbf{V}_{DM} = \frac{\mathbf{V}_2 - \mathbf{V}_1}{2}, \text{ and} \quad (8-30)$$

$$\mathbf{V}_{CM} = \mathbf{V}_c = \frac{\mathbf{V}_2 + \mathbf{V}_1}{2}. \quad (8-31)$$

From (8-30, 8-31), the separator outputs the exact DM and CM noise voltages. The input impedances are real 50Ω , because:

$$\mathbf{I}_a = \mathbf{I}_b = \frac{\mathbf{V}_2 - \mathbf{V}_1}{100}, \quad (8-32)$$

$$\mathbf{I}_d = \mathbf{I}_e = \frac{\mathbf{V}_2 + \mathbf{V}_1}{100}, \quad (8-33)$$

$$Z_{in1} = \frac{\mathbf{V}_1}{\mathbf{I}_1} = \frac{\mathbf{V}_1}{\mathbf{I}_d - \mathbf{I}_a} = 50\Omega, \text{ and} \quad (8-34)$$

$$Z_{in2} = \frac{\mathbf{V}_2}{\mathbf{I}_2} = \frac{\mathbf{V}_2}{\mathbf{I}_b + \mathbf{I}_e} = 50\Omega. \quad (8-35)$$

In the design, the characteristic impedance should be 50 Ω for T1 and 100 Ω for T2. For convenience, commercial products (Coilcraft WB1010, inductance: 780 μ H, 250 mA, ferrite toroid, Z_0 : 100 Ω) are used in the design. The magnetizing inductance of the transformer should be large enough to cover low end frequency. The length of winding wires should be as short as possible to reduce the effects of possible standing waves in the windings. The characteristic impedance of PCB traces is designed to 50 Ω because their parasitic inductance and capacitance may affect noise separator HF performance.

The prototype is shown in Fig. 8-15. Port1 and 2 are for inputs, port3 is for CM output and port4 is for DM output. In the design, in order to keep four ports an equal ground potential at high frequencies, four BNC connectors are mounted on one PCB and kept as close as possible.

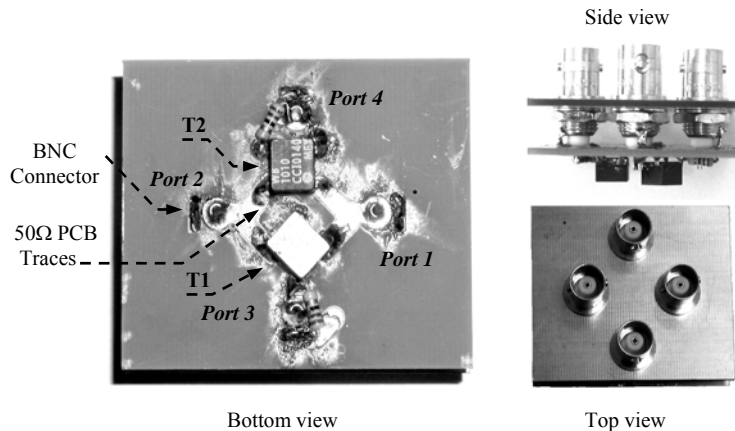


Fig. 8-15. Prototype of the proposed noise separator.

The S-parameters of the prototype are measured using an HP 4195A network/spectrum analyzer. The oscillator level is set at 122 dB μ V (Maximum level HP4195A can offer). For higher noise power measurement, two precision 50 Ω attenuators can be used before the noise separator. For EMI standard EN55022, the sweep range is from 150 kHz to 30 MHz (other EMI standards may specify different frequency ranges). When the DM noise separator is measured, the CM port is terminated by a 50 Ω termination and vice versa. Measurement results are shown in Figs. 8-16 and 8-17.

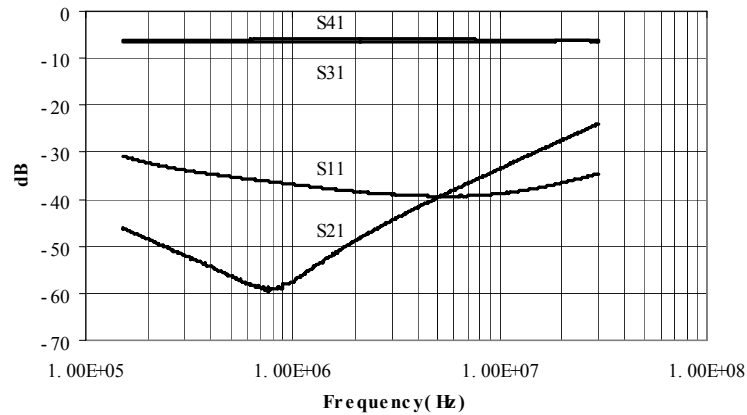


Fig. 8-16. Measured S-parameters of the prototype.

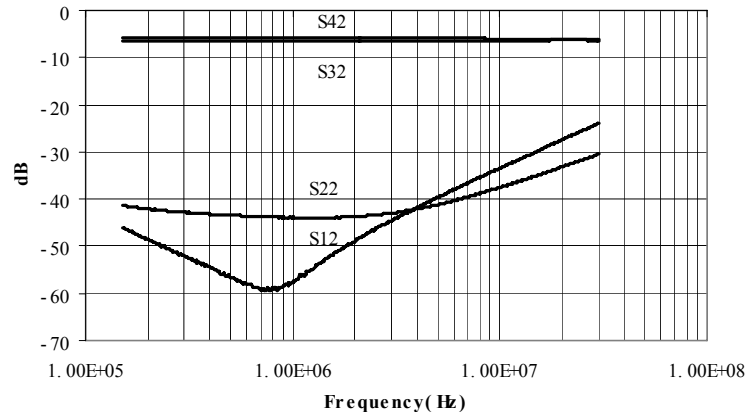


Fig. 8-17. Measured S-parameters of the prototype.

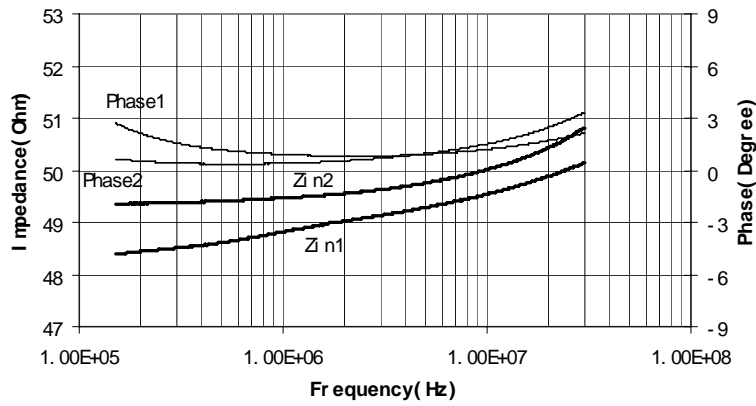


Fig. 8-18. Input impedances of the prototype.

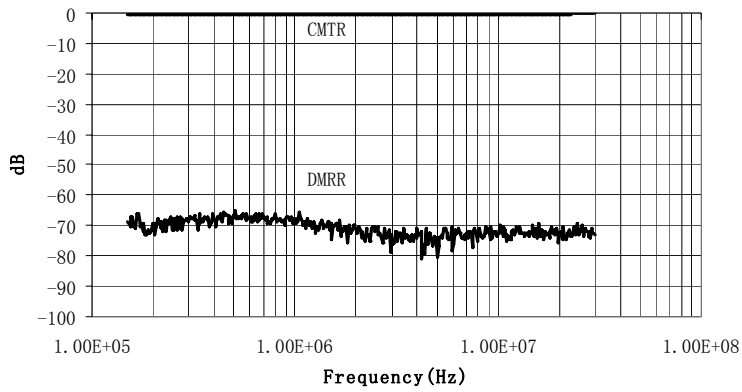


Fig. 8-19. DMRR and CMTR of the prototype.

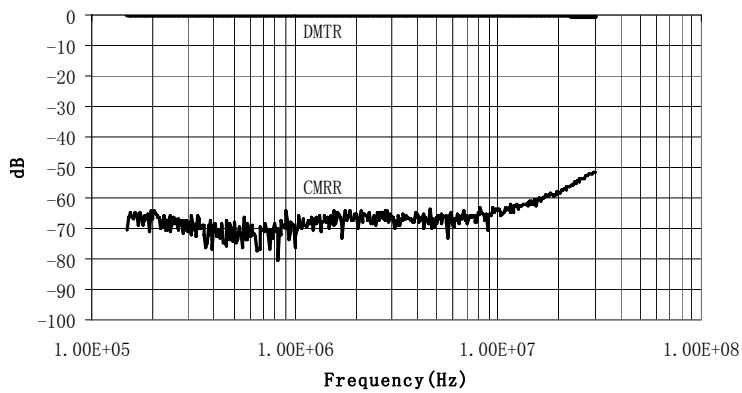


Fig. 8-20. CMRR and DMTR of the prototype.

From Figs. 8-16 and 8-17, because the approximation conditions for (19-24) are satisfied, the input impedances are therefore independent from noise source impedances and are calculated using (8-19, 8-20). CMTR and DMTR, CMRR and DMRR are calculated using (8-21 – 8-24). All of them are shown from Figs. 8-18 to 8-20. Fig. 8-18 shows that the input impedances are between 48.4Ω and 50.8Ω ; the phases are between 0.3° and 3.3° . They are very near a real 50Ω . From Figs. 8-19 and 8-20, the DMRR < -65 dB and the CMRR < -51 dB, so the leakage between DM and CM is very small. Transmission ratios DMTR and CMTR range from 0.1 dB to -0.5 dB. The prototype satisfies all the requirements and achieves DM and CM noise separators in one circuit.

Based on all these analyses and measurements, the proposed noise separator has the following advantages.

- 1) Input impedances are always real 50Ω and are independent from source impedances.
- 2) Outputs are exact DM and CM noise voltages.
- 3) DM and CM are simultaneously measured using the same circuit.
- 4) DMRR and CMRR are very good.

8.5. Noise Measurement Result

The prototype was finally used for the noise measurement of a 1.1kW PFC converter. The PFC converter has a circuit topology similar to that shown in Fig. 8-2 and a switching frequency of 67 kHz. The measurement setup is shown in Fig. 8-21. An HP 4195A network/spectrum analyzer is used in the measurement. Because the HP 4195A

has four input ports for spectrum measurement, port3 and port4 of the prototype were connected to input ports R1 and R2 of the HP 4195A, respectively, through 50Ω coaxial cables. In the measurement, DM and CM noise can be measured separately just by selecting the input port between R1 and R2 through the panel of HP 4195A or the connected computer. There is no need to replace the noise separator or shut off the converter, which is very convenient.

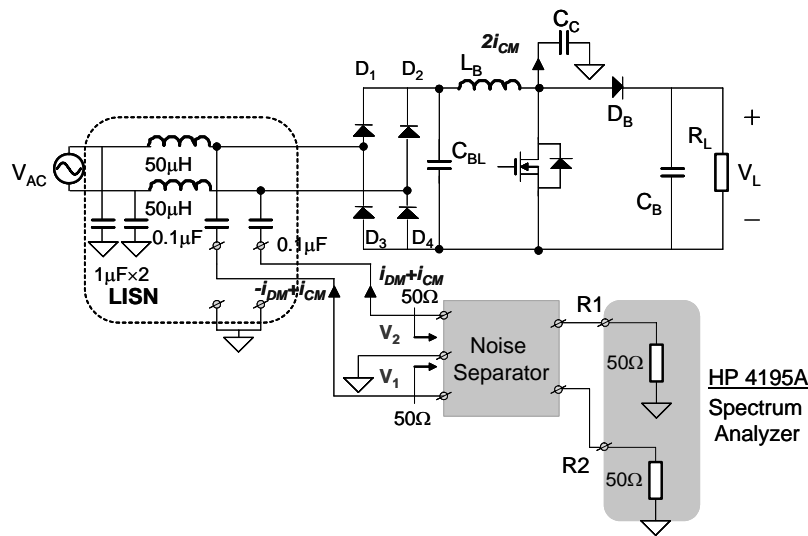


Fig. 8-21. Conducted EMI measurement setup for a 1.1kW PFC converter.

For this PFC converter, diode D_B and the MOSFET are mounted on one heat-sink. Experiments are carried out for two cases. In the first case, the heat-sink of the converter is not grounded; therefore the parasitic capacitance C_C in Fig. 8-21 is small. In the second case, the heat-sink is grounded, so C_C is larger. It is expected that the CM noise in the second case will be much larger, and DM noise will be almost same due to balance capacitor C_{BL} . Figs. 8-22 and 8-23 show measured CM, DM and total noise when the heat-sink is ungrounded. It shows that for this case, total noise is determined by DM

noise when the frequency is below 1 MHz and above 20 MHz; meanwhile CM noise is dominant from 1 MHz to 20 MHz.

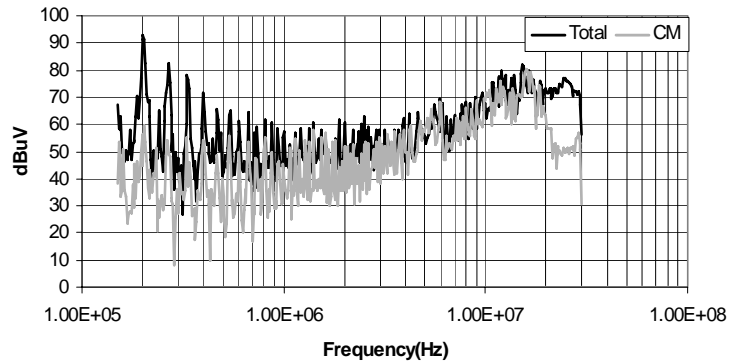


Fig. 8-22. Total noise and CM noise when the heat-sink is ungrounded.

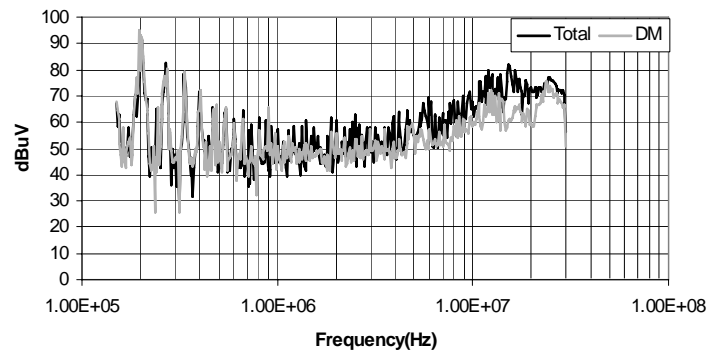


Fig. 8-23. Total noise and DM noise when heat-sink is ungrounded.

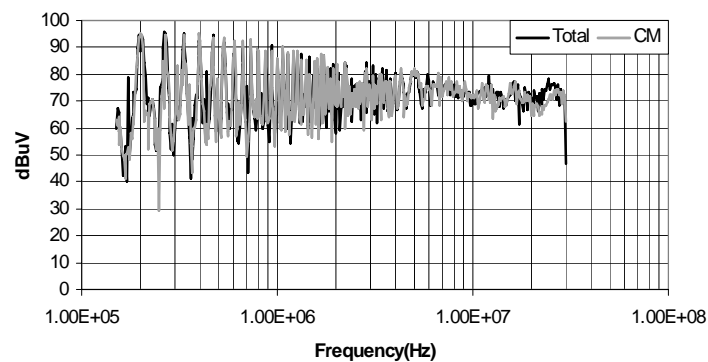


Fig. 8-24. Total noise and CM noise after heat-sink is grounded.

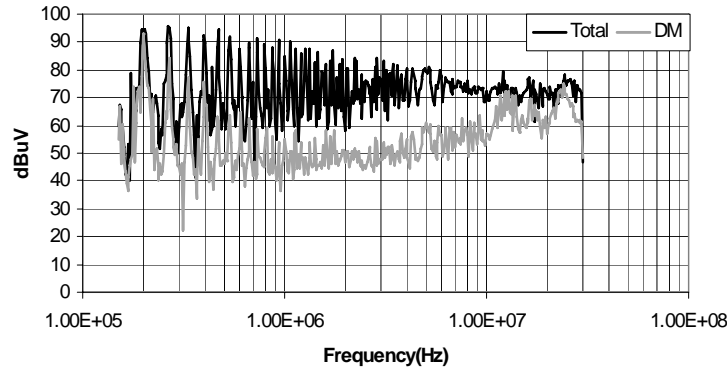


Fig. 8-25. Total noise and DM noise after heat-sink is grounded.

Figs. 8-24 and 8-25 show results after the heat-sink is connected to the ground. Once the heat-sink is grounded, CM noise is dominant in almost the entire frequency range (150 kHz – 30 MHz) because of the larger C_C . DM noise is almost unchanged. This proves the good performance of the prototype.

Based on the preceding S-parameters and noise measurements, the prototype can correctly and accurately separate DM and CM noise; thus it is a powerful tool for EMI noise diagnosis.

8.6. Summary

In this chapter, both ideal and practical noise separators are initially characterized using S-parameters. Based on these models, the methods and equations used to correctly and accurately evaluate noise separators are specified and developed. Existing noise separators are investigated one by one according to developed methods and equations. It is found that most existing noise separators offer neither real 50Ω input impedance nor exact noise separation. A performance-improved noise separator is then proposed with parasitic cancellation. The prototype is evaluated using the developed methods.

Experiments verify that the proposed noise separator satisfies all requirements and that it shows very good performance.

References

- [1] C. R. Paul and K. B. Hardin, "Diagnosis and reduction of conducted Noise Emissions," *IEEE Transactions, Electromagnetic Compatibility*, Volume 30, Issue 4, Nov. 1988, pp. 553 – 560.
- [2] Hsin-Lung Su and Ken-Huang Lin, "Computer-aided design of power line filters with a low cost common and differential-mode noise diagnostic circuit," In *proc. IEEE Electromagnetic Compatibility International Symposium*, Montreal, Canada, 13-17 Aug. 2001, pp. 511 – 516.
- [3] M. C. Caponet, F. Profumo, L. Ferraris, A. Bertoz and D. Marzella, "Common and differential mode noise separation: comparison of two different approaches," In *proc. IEEE Power Electronics Specialist Conference*, Vancouver, Canada, 17-21 June 2001, pp. 1383 – 1388.
- [4] M.C. Caponet and F. Profumo, "Devices for the separation of the common and differential mode noise: design and realization," In *proc. IEEE Applied Power Electronics Conference and Exposition*, Dallas, TX, 10-14 March 2002, pp. 100 –105.
- [5] M. J. Nave, "A novel differential mode rejection network for conducted emissions diagnostics," In *proc. IEEE Electromagnetic Compatibility National Symposium*, Denver, CO, 23-25 May 1989, pp. 223 – 227.
- [6] Guo Ting, D. Y. Chen and F. C. Lee, "Separation of the common-mode and differential-mode conducted EMI noise," *IEEE Transactions, Power Electronics*, Volume 11, Issue 3, May 1996, pp. 480 – 488.

- [7] See Kye Yak and Ng Chee Sum, "Diagnosis of conducted interference with discrimination network," In *proc. IEEE Power Electronics and Drive Systems International Conference*, Singapore, 21-24 Feb. 1995, pp. 433 – 437.
- [8] Yu-Kang Lo, Huang-Jen Chiu and Tzu-Herng Song, "A software-based CM and DM measurement system for the conducted EMI," *IEEE Transactions, Industrial Electronics*, Volume 47, Issue 4, Aug. 2000, pp. 977 – 978.
- [9] Mark J. Nave, *Power line filter design for switched-mode power supply*, Van Nostrand Reinhold, New York, 1991.
- [10] David M. Pozar, *Microwave Engineering*, John Wiley & Sons, Inc., 1998.
- [11] Norman Balabanian and Theodore Bickart, *Linear Network Theory: Analysis, Properties, Design and Synthesis*, Matrix Publishers, Inc., 1981.
- [12] W. Medley, *Microwave and RF Circuits: Analysis, Synthesis, and Design*, Artech House, Inc., 1993.
- [13] Agilent AN154 S-Parameters Design Application Note, Agilent Technologies, 2000.
- [14] Zhang, Dongbing, D.Y. Chen and D. Sable, "A New Method to Characterize EMI Filters," in *proc. IEEE Applied Power Electronics Conference and Exposition*, Anaheim, CA, 15-19 Feb. 1998, pp. 929 -933.
- [15] Richard Anderson, "Test and Measurement Application Note 95-1 S-Parameters Techniques," Hewlett-Packard, 1997.
- [16] A. Nagel, R. W. De Donker, "Separating Common Mode and Differential Mode Noise in EMI Measurements," In *EPE conf proc.*, Lusanne, 1999, pp.1-8.
- [17] Jerry Sevick, *Transmission Line Transformers*, American Radio Relay League, 1987.
- [18] Guo Ting, *Separation of the common-mode and the differential-mode conducted electromagnetic interference noise*, Master thesis, Virginia Tech, 1994.

CHAPTER 9: Conclusions and Future Work

9.1. Conclusions

EMI filters play a very important role in power electronics and other electronics areas. In power electronics area, EMI standards specify the frequency ranges and amplitude limits for conducted noise spectrums. In order to meet the EMI standard, EMI filters are needed between the converter and the power interconnects. Lots of work has been done on the topologies and design for ideal EMI filters. For practical EMI filters, existing works try to resolve the parasitic issues based on experience without quantified analysis.

This dissertation focuses on EMI filters and tries to explore several important issues. The author's wish is to find some helpful approaches to benefit the understanding and design of EMI filters. The contributions of the dissertation can be summarized below:

- 1) Identification of mutual couplings and their effects on EMI filter performance
- 2) Extraction of mutual couplings using scattering parameters
- 3) Cancellation of mutual couplings to improve EMI filter performance
- 4) Cancellation of equivalent series inductance to improve capacitor performance
- 5) Analysis of mode transformations due to the imperfectly balanced parameters in EMI filters
- 6) Analysis of interaction between power interconnects and EMI filters on filter high-frequency performance
- 7) Modeling and design of high-performance noise separator for EMI diagnosis
- 8) Identification of the effects of parasitics in boost PFC inductor on DM noise

The dissertation first identifies the mutual couplings in EMI filters. It is found that for CM filters, self-parasitics determine filter's performance. However for DM filters, magnetic couplings in EMI filters determine filters' high frequency performance. All of the identified mutual couplings are extracted using scattering parameters. The parasitic models are built and verified by measurements. Based on the models, it is easy to identify that inductive couplings between two capacitors, between the inductor and capacitors are most important. The inductor windings are then proposed to be rotated by 90° to reduce the couplings between the inductor and the capacitors. A cancellation turn is integrated with one capacitor to cancel the coupling between two capacitors. This cancellation turn can also partly cancel the ESL of the capacitor. Experiments show these two methods can greatly improve EMI filter performance. For the self-parasitics, a cancellation method employing a network is proposed to cancel the ESL of capacitors. By simply making the inductance of two PCB windings equal to ESL, the ESL of capacitors are cancelled. The experiments are carried out to verify this approach.

The ideal EMI filter has the exact balanced component and layout parameters, so the transformation between the CM and DM noise is usually ignored; however the practical one may have a different story. The very small difference on CM capacitor impedances or on inductor impedances can lead to significant mode transformation, which could make EMI filter design inefficient. The dissertation analyzes the relationship between the mode transformation and the unbalances.

In standard EMI noise measurement, the load of EMI filters is a piece of power interconnects and two LISNs. Effects of the power interconnects are usually ignored. In

the dissertation, the power interconnects are characterized by a transmission line with impedance transformation function. The transformed impedances would not be the LISNs' impedance 50Ω , but capacitive and inductive impedances. It is found that the transformed impedances can resonate with the parasitics in the EMI filter and worsen filter's high-frequency performance.

In order to efficiently diagnose DM and CM noise and figure out which one is dominant, the noise separator is a very useful tool in the EMI measurement. Most of the existing noise separators cannot correctly and accurately separate DM from CM noise. The existing evaluation method is also not good. The dissertation proposed a high performance noise separator with parasitic cancellation. It is used for EMI measurement and proved to be with high performance. A method employing S-parameters is also proposed to correctly and accurately evaluate noise separator.

The effects of the inductor in boost PFC converters are investigated in the dissertation. It is found that the resonances between the inductance and winding capacitance can lead to DM noise peaks in high frequency range. Experiment and theoretical analysis are carried out to support this claim.

9.2. Future Work

Future work will focus on the application of the developed techniques. The EMI filter would work with the current bias in converters. The large signal behavior of the EMI filter would be studied. The near field coupling between the EMI filter components and other components in converters is also an important topic to investigate.

APPENDIX A:

A.1. Characterization of EMI Filters Using S-parameters*

A.1.1 Introduction

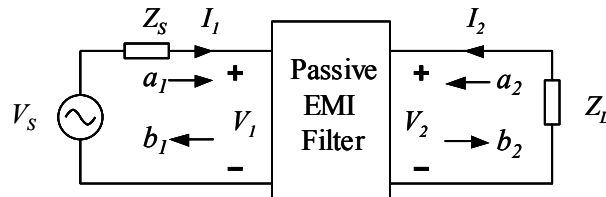
Modern telecommunications systems need power supplies with low electromagnetic interference (EMI). EMI filters are therefore used to reduce the EMI of power supplies. Traditionally, EMI filters are characterized by the insertion loss when both source and load impedances are 50Ω . However, in a practical filter implementation, both source and load cannot be 50Ω , which makes it difficult to base EMI filter selection on the curves given by manufacturers. In order to efficiently predict the performance of EMI filters and select EMI filters for the power supply of telecommunications equipment, EMI filters should be characterized by independent network parameters instead of the insertion loss, which is dependent on source and load impedances.

Scattering parameters (S-parameters) are chosen to characterize EMI filters because they are easy to measure accurately as compared with the $[Z]$, $[Y]$, $[H]$ and $[ABCD]$ parameters in the high frequency (HF) range. The measurement of $[Z]$, $[Y]$, $[H]$ and $[ABCD]$ parameters requires either a short circuit or an open circuit at one port, which is difficult to achieve in the HF range because of parasitic parameters [1]. If the filter size is large and irregular, the long connections between the filter and the measurement equipment fixture also introduce parasitic parameters affecting the measurement results. Sometimes, expensive special probes are needed to get accurate network parameters. For S-parameters, they are calibrated to the two ports of the filters so the effects of the long

* © 2004 IEEE. Reprinted, with permission, from the Proc. IEEE Power Electronics Specialists Conference. 20-25, Jun. 2004, Volume 1, pp. 297 -303.

connections can be excluded without using expensive probes. Furthermore, no short or open circuits are needed for measurement. The measurement results should therefore be expected to be more accurate in the HF range than are other measured parameters. By employing S-parameters, the concept of power waves can be used to analyze EMI filter performance and EMI noise transmission. S-parameters can also be transformed to a chain scattering matrix. With the chain scattering matrix, the cascade networks can be easily analyzed using the concept of power waves. By measuring the S-parameters of an EMI filter and all of the connections, the performance of the whole filter system can be evaluated.

A.1.2 Using Scattering Parameters to Characterize EMI Filters



V_S : Voltage source

Z_S : Source impedance

Z_L : Load

a_1, a_2 : Normalized incident wave on source side and load side, respectively

b_1, b_2 : Normalized reflected wave on source side and load side, respectively

I_1, I_2 : Input current of port1 and port2, respectively

V_1, V_2 : Voltage of port1 and port2, respectively

Fig. A-1. EMI filters are treated as linear passive two-port networks under small-signal excitation conditions.

Strictly speaking, an EMI filter is not a linear network because it contains the nonlinear components such as inductors; however it is approximately linear for a small-

signal excitation. So it is reasonable to characterize an EMI filter as a linear passive two-port network under small-signal excitation conditions. The nonlinear characteristics can be modeled with the current biases superposed by a small-signal excitation. The test setup for an EMI filter is shown in Fig. A-1, where the EMI filter is characterized in terms of waves.

There are four waves in Fig. A-1, namely, incident wave a_1 and reflected wave b_1 at port1, and incident wave a_2 and reflected wave b_2 at port2. From these four variables, the voltage² V_1 and current I_1 at port1, the voltage V_2 and current I_2 at port2 are found by Equations A-1 – A-4 [2]:

$$V_1 = \sqrt{Z_0}(a_1 + b_1); \quad (\text{A-1})$$

$$V_2 = \sqrt{Z_0}(a_2 + b_2); \quad (\text{A-2})$$

$$I_1 = \frac{I}{\sqrt{Z_0}}(a_1 - b_1); \text{ and} \quad (\text{A-3})$$

$$I_2 = \frac{I}{\sqrt{Z_0}}(a_2 - b_2), \quad (\text{A-4})$$

where Z_0 is the reference impedance and is usually 50Ω .

To fully characterize a two-port linear passive network, two linear equations are required among the four wave variables. The four S-parameters in Equation A-5 are therefore introduced to correlate a_1 , a_2 , b_1 and b_2 . S_{11} and S_{22} are called reflection coefficients. S_{12} and S_{21} are called transmission coefficients.

$$\begin{pmatrix} b_1 \\ b_2 \end{pmatrix} = \begin{pmatrix} S_{11} & S_{12} \\ S_{21} & S_{22} \end{pmatrix} \begin{pmatrix} a_1 \\ a_2 \end{pmatrix} \quad (\text{A-5})$$

² All currents and voltages are RMS values.

According to the transmission line theory [2, 3], when reflected wave b_1 or b_2 reaches the source or load side, it would also be reflected respectively because of the mismatched impedances. The reflection coefficients Γ_S at source side and Γ_L at load side are:

$$\Gamma_S = \frac{Z_S - Z_0}{Z_S + Z_0}, \text{ and} \quad (\text{A-6})$$

$$\Gamma_L = \frac{Z_L - Z_0}{Z_L + Z_0}. \quad (\text{A-7})$$

The circuit in Fig. A-1 is then characterized by the signal flow graph in Fig. A-2 [2, 3].

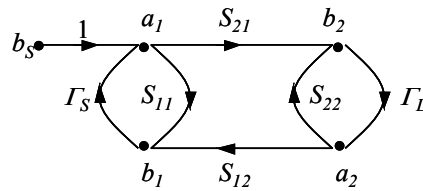


Fig. A-2. Characterizing the filter circuit using a signal flow graph.

In Fig. A-2, b_s is the normalized wave emanating from the source. For a given noise voltage source V_S with impedance Z_S , b_s is given by:

$$b_s = \frac{\sqrt{Z_0} V_S}{Z_S + Z_0}. \quad (\text{A-8})$$

For a network characterized by S-parameters, by using Mason's rule for the signal flow graph in Fig. A-2, a_1 , b_1 and a_2 , b_2 are found. The port voltages and currents are thus obtained using Equations A-1 to A-4. According to the S-parameters theory [2, 3], if V_S and Z_S are the noise source and source impedance, respectively, the noise power (dB) on Z_L (LISN impedance) is given by:

$$\begin{aligned}
10\log P_L &= 10\log(|b_2|^2 - |a_2|^2) \\
&= 10\log\left(\left|\frac{S_{21}}{\Delta} b_s\right|^2 (1 - |\Gamma_L|^2)\right),
\end{aligned} \tag{A-9}$$

where

$$\Delta = 1 - (S_{11}\Gamma_S + S_{21}\Gamma_L S_{12}\Gamma_S + S_{22}\Gamma_L) + S_{11}\Gamma_S S_{22}\Gamma_L \tag{A-10}$$

For differential mode (DM) noise, Z_L is 100Ω ; therefore, the DM spectrum (peak value in dB μ V) on an equivalent 50Ω load is:

$$20\log\left(\frac{\sqrt{2}V_{DM}}{1\mu V}\right) = 137 + 10\log P_L, \tag{A-11}$$

where V_{DM} is the RMS voltage on an equivalent 50Ω load.

For common mode (CM) noise, Z_L is 25Ω ; therefore, the CM spectrum (peak value in dB μ V) on an equivalent 50Ω load is:

$$20\log\left(\frac{\sqrt{2}V_{CM}}{1\mu V}\right) = 143 + 10\log P_L, \tag{A-12}$$

where V_{CM} is the RMS voltage on an equivalent 50Ω load.

Similarly, the power (dB) delivered to the EMI filter from the noise source can be obtained by:

$$\begin{aligned}
10\log P_s &= 10\log(|a_1|^2 - |b_1|^2) \\
&= 10\log\left(\left|\frac{b_s(1 - S_{22}\Gamma_L)}{\Delta}\right|^2 \left[1 - \left|S_{11} + \frac{S_{21}\Gamma_L S_{12}}{1 - S_{22}\Gamma_L}\right|^2\right]\right).
\end{aligned} \tag{A-13}$$

The power consumed by the EMI filter is therefore:

$$P_{loss} = P_S - P_L. \quad (\text{A-14})$$

A.1.3 Insertion Voltage Gain with Arbitrary Source and Load Impedances

A.1.3.1 Insertion Voltage Gain under Small-signal Excitation Conditions

In order to find the insertion voltage gain [8] of EMI filters with arbitrary source and load impedances, it is necessary to first check the radio frequency (RF) theory. In the RF area, the input-to-output voltage gain, which is given as Equation A-15, is defined as the ratio of the port voltage V_2 at the load side to V_1 at the source side [2, 3]:

$$A_V = \frac{S_{21}(1 + \Gamma_L)}{(1 + S_{11})(1 - S_{22}\Gamma_L) + S_{21}\Gamma_L S_{12}} \quad (\text{A-15})$$

For EMI filters, insertion voltage gain is defined as the ratio of the port voltage at load side without the filter to that with the filter [1]. The insertion voltage gain is the ratio of V_2 in Fig. A-1 to V_O in Fig. A-3.

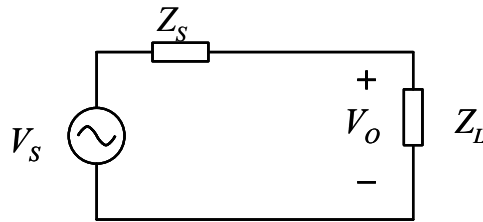


Fig. A-3. The dual circuit for the measurement and calculation of insertion voltage gain.

So Equation A-15 from the RF area cannot be directly used. The insertion voltage gain equation should be further developed.

From Figs. A-1 and A-3, the insertion voltage gain of an EMI filter is given as:

$$\begin{aligned}
A_V &= \frac{V_2}{V_O} = \frac{V_2}{V_S} \left(I + \frac{Z_S}{Z_L} \right), \text{ and} \\
&= \frac{V_2}{(V_I + I_I Z_S)} \left(I + \frac{Z_S}{Z_L} \right).
\end{aligned} \tag{A-16}$$

Substituting Equations A-1, A-2 and A-3 into A-16 yields:

$$A_V = \frac{\frac{a_2}{b_S} + \frac{b_2}{b_S}}{\frac{a_1}{b_S} \left(I + \frac{Z_S}{Z_0} \right) + \frac{b_1}{b_S} \left(I - \frac{Z_S}{Z_0} \right)} \left(I + \frac{Z_S}{Z_L} \right). \tag{A-17}$$

In Fig. A-2, according to Mason's rule:

$$\frac{a_2}{b_S} = \frac{S_{21} \Gamma_L}{\Delta}; \tag{A-18}$$

$$\frac{b_2}{b_S} = \frac{S_{21}}{\Delta}; \tag{A-19}$$

$$\frac{a_1}{b_S} = \frac{(I - S_{22} \Gamma_L)}{\Delta}; \text{ and} \tag{A-20}$$

$$\frac{b_1}{b_S} = \frac{S_{11}(I - S_{22} \Gamma_L) + S_{21} \Gamma_L S_{12}}{\Delta}. \tag{A-21}$$

Substituting Equations A-6, A-7 and A-18 – A-21 to Equation A-17, Δ is cancelled, and the insertion voltage gain is:

$$A_V = \frac{S_{21}(I - \Gamma_L \Gamma_S)}{(I - S_{11} \Gamma_S)(I - S_{22} \Gamma_L) - S_{21} \Gamma_L S_{12} \Gamma_S} \tag{A-22}$$

S_{21} , S_{22} , S_{12} and S_{11} of the EMI filters are obtained by the measurement of the S-parameters. Term Z_S is known through the method given in other work [7]. Z_L is the impedance of LISN. For a DM filter, Z_L is 100 Ω . For a CM filter, Z_L is 25 Ω . Z_0 is the reference impedance of 50 Ω . Γ_L and Γ_S are determined through Equations A-6 and A-7.

Therefore, A_V is finally found using Equation A-22. From Equation A-22, it is obvious that source and load impedances affect the insertion voltage gain of a filter through reflection coefficients Γ_S and Γ_L .

Because S-parameters are independent of Z_L and Z_S , they are parameters of the networks themselves. For any two-port network with its S-parameters, the insertion voltage gain or insertion loss with arbitrary source and load impedances can be found using Equation A-22. All S-parameters are measured directly by HP network analyzers, such as the HP4195A network analyzer. The calibration is done on the two ports of the EMI filters. Because no open or short circuit is used in the measurement, the model is expected to be more accurate, especially at HF, than are the $[Z]$, $[Y]$, $[H]$ and $[ABCD]$ parameter measurement-based models. S_{21} is also the so-called transfer gain when Z_S and Z_L both are 50Ω .

A.1.3.2 Experimental Verification

The investigated filter is shown in Fig. A-4. The measurement is carried out by HP4195A both on the DM and the CM filter parts. The measured S-parameters for the DM filter part are shown in Fig. A-5.

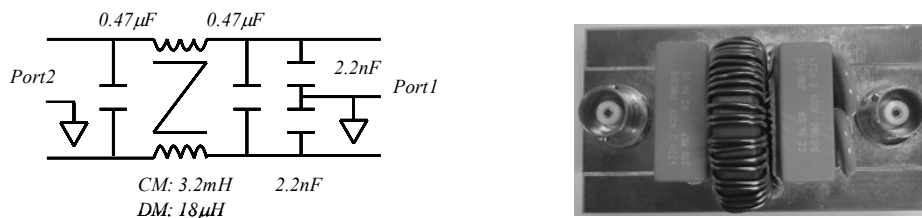


Fig. A-4. The schematic and the photo of an investigated

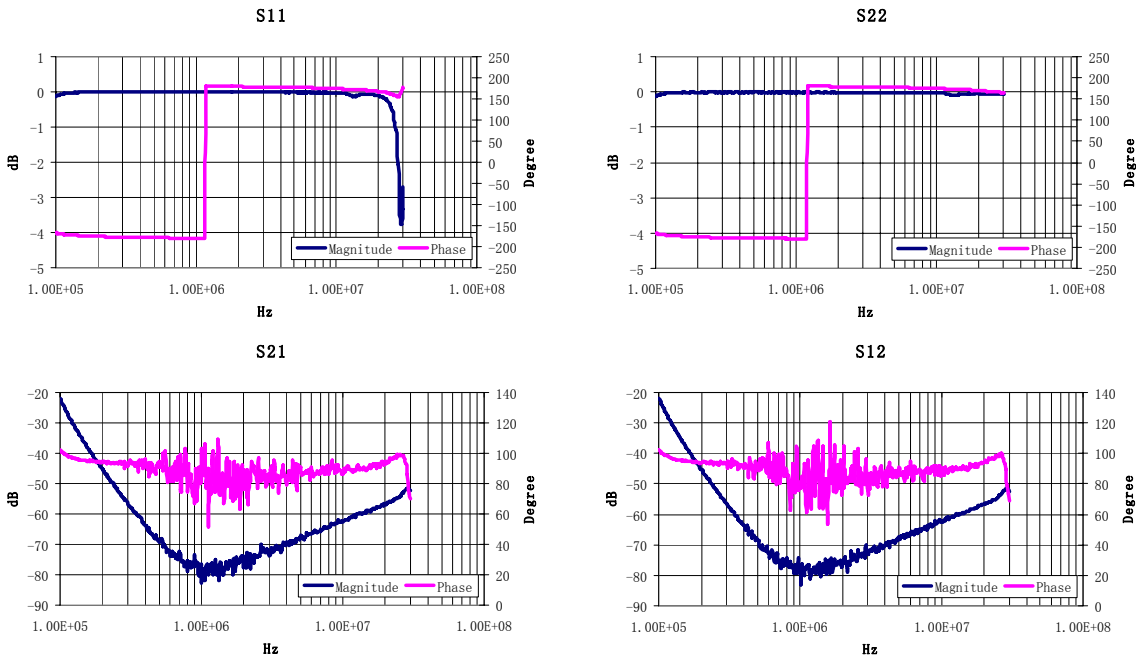


Fig. A-5. The measured S-parameters of the DM filter part.

In Fig. A-5, just as stated at the end of Section A, S_{21} is also the transfer gain when both Z_S and Z_L are 50Ω . The predicted insertion voltage gain is calculated by Matlab using Equation A-22. The measured (by HP4194A) and predicted insertion voltage gains when Z_S is 50Ω and Z_L is $1\text{meg}\Omega$ are compared in Fig. A-6.

$Z_S=500\Omega$, $Z_L=1\text{meg}$

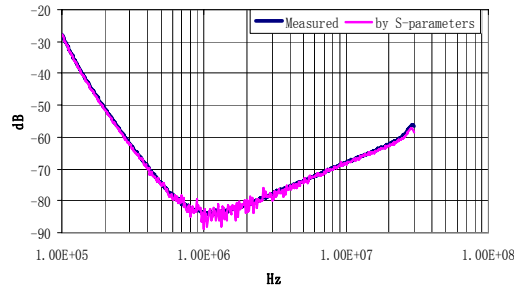


Fig. A-6. The comparison of calculated and measured DM insertion voltage gains when load is $1\text{meg}\Omega$ and source is 50Ω .

As shown in Fig. A-6, the calculated and measured insertion voltage gains match very closely. For the CM filter part, the measured and predicted insertion voltage gains when

Z_S is $1\text{meg}\Omega$ and Z_L is 50Ω are compared in Fig. A-7. As shown, they also match very closely.

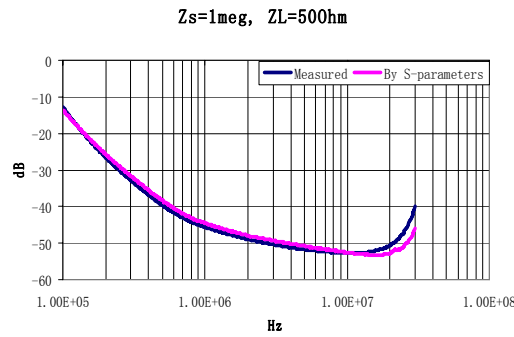
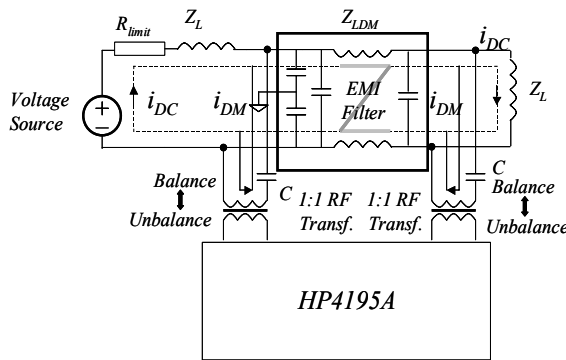


Fig. A-7. The comparison of calculated and measured CM insertion voltage gains when source is $1\text{meg}\Omega$ and load is 50Ω .

A.1.3.3 Insertion Voltage Gain with Current Bias

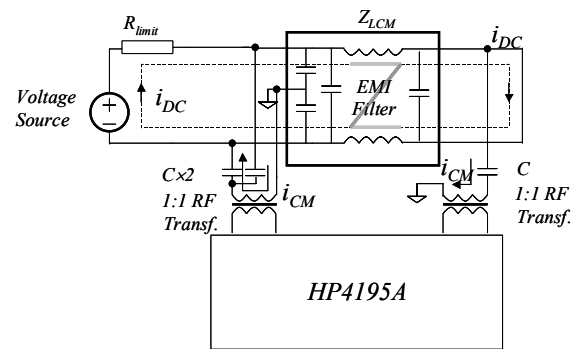
A.1.3.3.1 DM Current Bias

The S-parameters are then measured with DM DC current bias to find out if the core is saturated under the current bias conditions. The measurement setups for the DM and CM filter parts are shown in Figs. A-8 and A-9, respectively.



Z_{LDM} : The impedance of the DM inductor ($Z_L \gg Z_{LDM}$)

Fig. A-8. S-parameters measurement setup for the DM filter part.



Z_{LCM} : The impedance of the CM inductor

Fig. A-9. S-parameters measurement setup for the CM filter part.

In Fig. A-8, R_{limit} is used to limit the bias current. The testing signals between HP4195A and the investigated filter are coupled through the RF transformers and the capacitors. Two air-core inductors Z_{LS} are used to block the testing signal from being short-circuited by the DC loop. They have no effects on DC current bias. In order to achieve this, Z_L should be much larger than Z_{LDM} . The DC current bias i_{DC} can be changed by regulating the output of voltage source, and it can freely pass through the EMI filter inductor.

In Fig. A-9, testing signals are added between the two lines of the filter and the ground. The testing signals are coupled through the RF transformers and three capacitors.

In the experiments, the DC current bias is increased by 1A from 0A to 5A. Four S-parameters are measured for every current step. In total, six groups of data are measured. The measurement results show that, for both DM and CM filters, the four S-parameters don't change significantly when the current is increased from 0A to 5A. That means, for this case, 5A of current bias doesn't have obvious effects on the EMI filter performance. The small-signal model can be directly used to evaluate the filter performance.

A.1.3.3.2 CM Current Bias

In order to investigate the effects of CM current on the EMI filter performance, the CM DC current bias is added through a one-turn auxiliary winding on the CM inductor shown in Figs. A-10 and A-11. If the turn ratio of CM windings to the auxiliary winding is n , then the equivalent CM current bias is i_{DC}/n . Because of the high turn ratio and the

high impedance of Z_L , the effects of the DC current loop can be ignored. Both the DM and CM filter parts are measured in the experiments.

For the CM filter part, the final measurement results show that the S-parameters changed when the equivalent CM current bias is increased from 0A to 0.2A. This is due

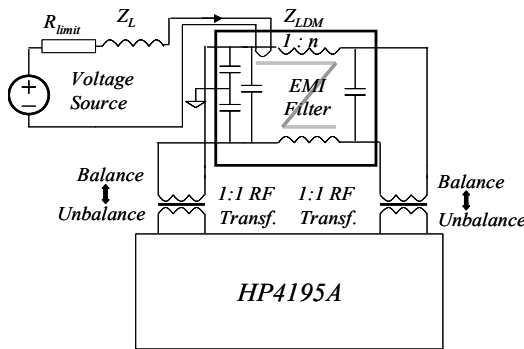


Fig. A-10. S-parameter measurement setup for the DM filter part.

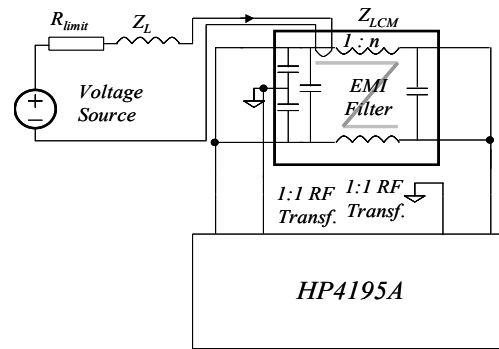
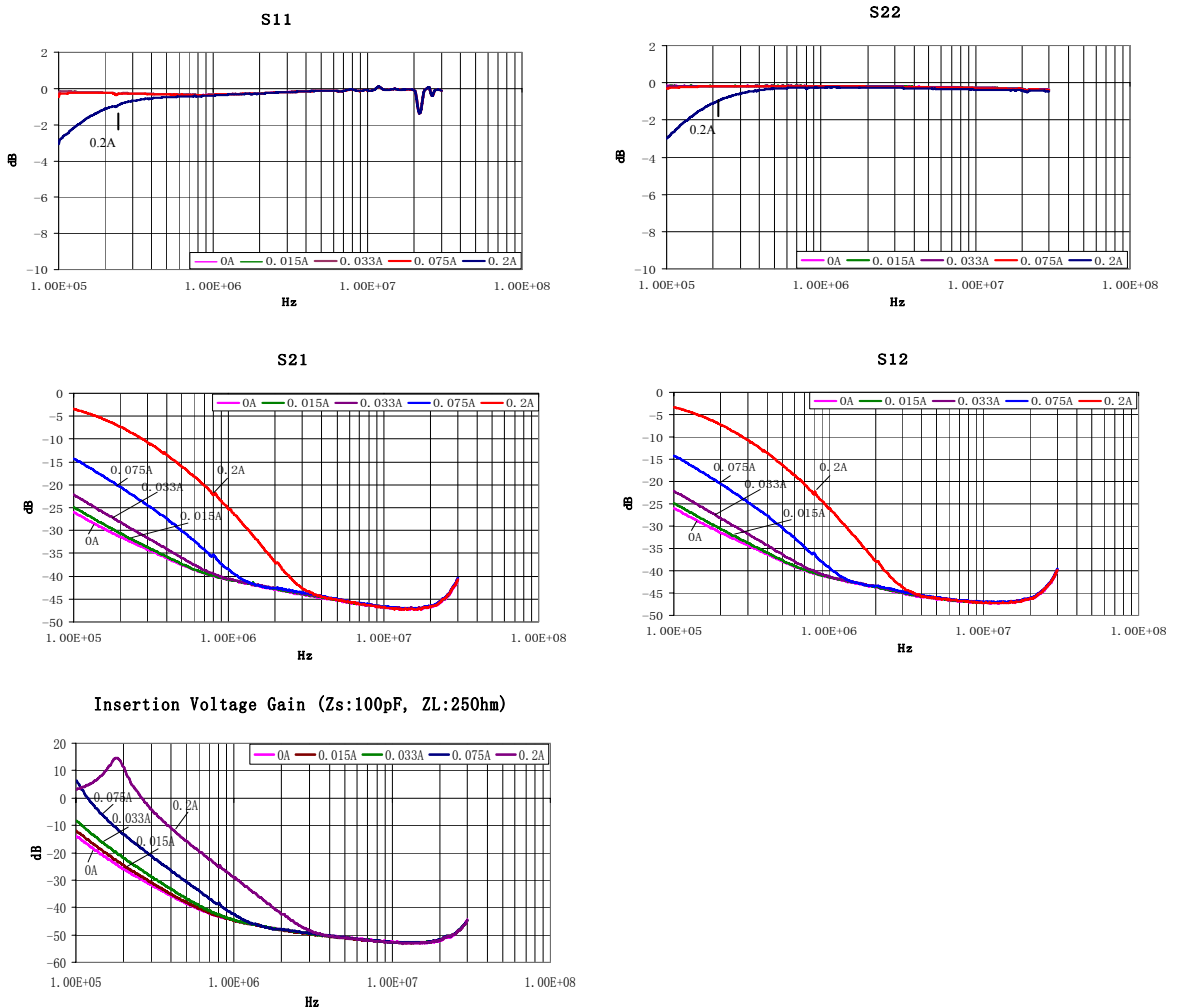


Fig. A-11. S-parameter measurement setup for the CM filter part.

to the saturation of the CM inductor. On the other hand, CM current bias has no significant effects on DM filter performance because the DM inductor core is air. So the measured S-parameters are almost the same when the current bias is increased. The measured S-parameters for the CM filter part are shown in Fig. A-12. In Fig. A-12, in the HF range, the saturation of the core has no effects on the S-parameters because the HF noise goes through parasitic paths instead of the inductor path. The insertion voltage gain with arbitrary source and load impedances under CM current bias conditions can be calculated through Equation A-22 from the measured data and is shown in Fig. A-12. The peak on the curve of 0.2A between 100kHz and 200kHz could not be estimated just from the transfer-gain curve. The physical meaning of this peak is that the corner frequency of

the CM filter part increases when the CM inductance is reduced due to the saturation of the core.

In a practical EMI filter design, measures should be taken to prevent the saturation of the CM inductors. For example, the two CM capacitors before the CM inductor should be large enough to bypass enough CM current so as to prevent large level of CM current from passing through the CM inductor.



The predicted insertion voltage gains ($Z_s=100\text{pF}, Z_L=25\Omega$)

Fig. A-12. The magnitude of the measured S-parameters and the predicted insertion voltage gains for the CM filter part.

A.1.4 Filter Input and Output Impedance Requirement from the Standpoint of Waves

Using the concept of waves, it is easy to find the impedance requirement in a filter design. In Fig. A-2, the reflected wave b_1 is:

$$b_1 = a_1 \left(S_{11} + \frac{S_{21} S_{12} \Gamma_L}{1 - S_{22} \Gamma_L} \right) \quad (\text{A-23})$$

For the EMI filter, the DM load is 100Ω and the CM load is 25Ω . So the reflection coefficients are:

$$DM : \Gamma_L = \frac{1}{3} \text{ and } CM : \Gamma_L = -\frac{1}{3}. \quad (\text{A-24})$$

It is known that:

$$0 \leq |S_{22}| \leq 1. \quad (\text{A-25})$$

For an EMI filter, the transmission coefficients S_{21} and S_{12} are much smaller, so the second term in Equation A-23 is ignored; thus Equation A-23 is simplified as:

$$b_1 \approx a_1 S_{11}. \quad (\text{A-26})$$

So the signal flow graph in Fig. A-2 is simplified, as shown in Fig. A-13.

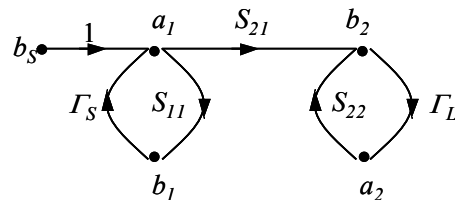


Fig. A-13. The simplified signal flow graph for an EMI filter.

Equation A-22 can then be simplified as follows:

$$|A_V| \approx \frac{|S_{21}| |I - \Gamma_L \Gamma_S|}{|I - S_{11} \Gamma_S| |I - S_{22} \Gamma_L|}, \quad (\text{A-27})$$

where

$$0 \leq |I - S_{11} \Gamma_S| \leq 2, \text{ and} \quad (\text{A-28})$$

$$0 \leq |I - S_{22} \Gamma_L| \leq 2. \quad (\text{A-29})$$

From Equation A-27, in order to improve the performance of EMI filters, besides reducing S_{21} , $|I - S_{11} \Gamma_S|$ and $|I - S_{22} \Gamma_L|$ should be kept as large as possible. Because Γ_S and Γ_L are determined by source and load impedances, a filter designer can control S_{11} and S_{22} .

DM Filter Impedance Requirement

For an AC/DC converter with a large input capacitor, Γ_S approaches -1 because of the small impedance of the input capacitor; in order to get large $|I - S_{11} \Gamma_S|$, S_{11} should approach 1, which means a high filter input impedance. For a boost power factor correction (PFC) converter with a large boost inductor at the input, Γ_S approaches 1. In order to obtain a large $|I - S_{11} \Gamma_S|$, S_{11} should approach -1 , which means a low input impedance of the filter. This is just the impedance requirement for a filter design.

At load (LISN) side, Γ_L is $1/3$; in order to obtain a large $|I - S_{22} \Gamma_L|$, S_{22} should approach -1 , which means a low filter input impedance at the output port.

CM Filter Impedance Requirement

For the CM filter part, the source impedance is the impedance of a small parasitic capacitor, which has high impedance, so Γ_S approaches 1. In order to obtain a large $|1 - S_{11}\Gamma_S|$, S_{11} should approach -1, which means a low input impedance of the filter.

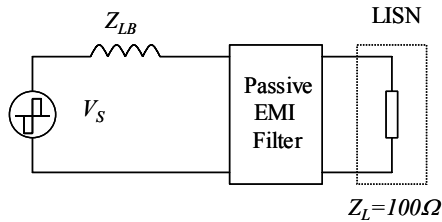
At load side, Γ_L is -1/3; in order to obtain a large $|1 - S_{22}\Gamma_L|$, S_{22} should approach 1, which means a high filter input impedance at the output port.

In order to achieve low input impedance, shunt capacitors can be used on the filter ports. In order to achieve high input impedance, series inductors can be used on the filter ports.

A.1.5 Analyzing the EMI Filter Performance with Practical Noise Source Impedances

The practical noise source impedances are not purely capacitive, inductive or resistive. For example, for a boost PFC converter, the source impedance of DM noise is the impedance of the boost inductor if other parasitic parameters are ignored [4]. For a forward converter, the source impedance of DM noise is the impedance of the input bulk capacitor if other parasitic parameters are ignored. The simplified DM noise loop for a boost PFC is shown in Fig. A-14. In order to find the insertion voltage gain of the EMI filter in this boost PFC converter, the impedance of the boost inductor is first measured, and then the insertion voltage gain is calculated from Equation A-22. The impedance of the boost inductor is shown in Fig. A-15. Another experiment shown in Fig. A-16 was carried out to verify this prediction.

The predicted insertion voltage gain, the measured insertion voltage gain and the measured transfer gain are all shown in Fig. A-17.



Z_{LB} : The impedance of the boost inductor

V_S : The equivalent voltage source on the main switch of a boost PFC converter

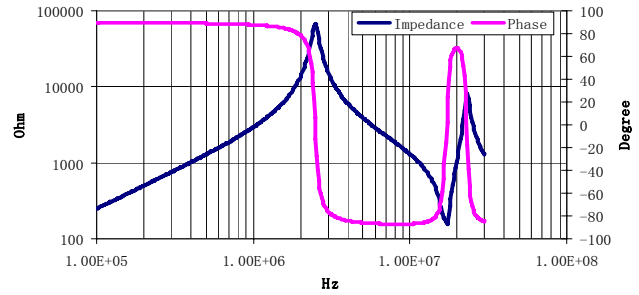


Fig. A-14. Simplified boost PFC DM noise loop. Fig. A-15. The impedance of the boost inductor Z_{LB} .

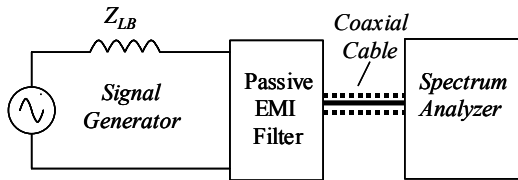


Fig. A-16. The measurement setup for the insertion voltage gains when the source impedance is the boost inductor Z_{LB} .

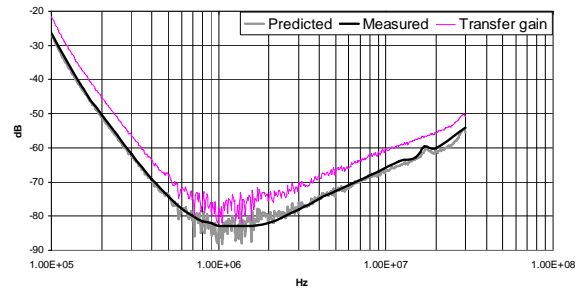


Fig. A-17. The comparison of the predicted and the measured insertion voltage gains.

In Fig. A-17, the predicted one matches the measured one very closely. From the graph, it is obvious that the transfer gain curve is quite different from the insertion voltage gain. So the transfer-gain curve from a 50Ω-based measurement system doesn't offer accurate information at this time. The small peak of the predicted curve between 10MHz and 20MHz is caused by the impedance valley of the source impedance in Fig. A-15.

In order to evaluate the effects of the impedance resonance of the boost inductor on the filter performance, insertion voltage gains with a practical inductor and with an ideal inductor are compared in Fig. A-18. In Fig. A-18, the two insertion voltage gain curves aren't obviously different except for a small peak that occurs in the practical inductor case. The reason for such a small difference is that the reflection coefficient Γ_s doesn't change too much, and from Equation A-22, the insertion voltage gain doesn't change too much either. Therefore, in this case, the HF resonance of the boost inductor does not have significant effects on the filter performance.

In a more general case, in order to predict the EMI filter performance, noise source impedances should first be found by the method given in other work [7]. With the S-parameters of a filter, the insertion voltage gain or insertion loss of the filter can then be obtained.

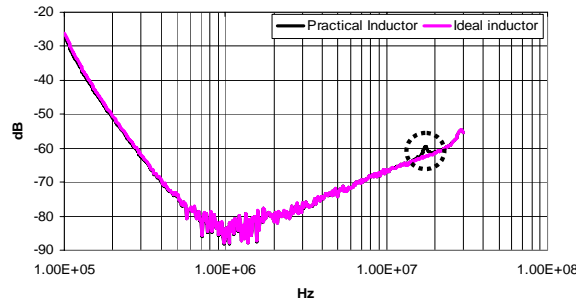


Fig. A-18. The comparison of predicted insertion voltage gains with practical and ideal inductors.

A.1.6 Summary

A method for using S-parameters to characterize EMI filters was presented in this work. The equation for insertion voltage gain with arbitrary source and load impedances was developed. The approach was verified with the measurements under the small-signal excitation conditions and further demonstrated under the current bias conditions. It is shown that the proposed approach is efficient in predicting and analyzing the performance of EMI filters; therefore it also benefits the EMI filter selection and design.

References

- [1] Zhang, Dongbing, D.Y. Chen and D. Sable, "A New Method to Characterize EMI Filters," in *proc. IEEE Applied Power Electronics Conference and Exposition*, Anaheim, CA, 15-19 Feb. 1998, pp. 929 -933.
- [2] Richard Anderson, "Test and Measurement Application Note 95-1 S-Parameters Techniques," Hewlett-Packard, 1997.
- [3] "Agilent AN154 S-Parameters Design Application Note," Agilent Technologies, 2000.
- [4] Shuo Wang, F.C. Lee and W.G. Odendaal, "Improving the Performance of Boost PFC EMI Filters," In *proc. IEEE Applied Power Electronics Conference and Exposition*, Miami, FL, 9-13 Feb. 2003, pp. 368 - 374.
- [5] Norman Balabanian and Theodore Bickart, "*Linear Network Theory: Analysis, Properties, Design and Synthesis*," Matrix Publishers, Inc., 1981.
- [6] Shuo Wang, F.C. Lee, D.Y. Chen and W.G. Odendaal, "Effects of Parasitic Parameters on the Performance of EMI Filters," In *proc. IEEE Power Electronics Specialist Conference*, Acapulco, Mexico, 15-19 Jun. 2003, pp.73-78.
- [7] Zhang, Dongbing, D.Y. Chen, M.J. Nave and D. Sable, "Measurement of Noise Source Impedance of Off-line Converters," *IEEE Transactions, Power Electronics*, Volume 15, Issue 5, Sept. 2000, pp. 820 -825.
- [8] Max W.Medley, "*Microwave and RF Circuits: Analysis, Synthesis, and Design*," Artech House, Inc., 1993.

A.2. Procedures of Extracting Parasitic Parameters for EMI Filters

Objective

1. Extracting the parasitic parameters, including M1, M2, M3, M4, M5, M6 and Cp, from a one stage DM filter, as shown in Figure A-19.

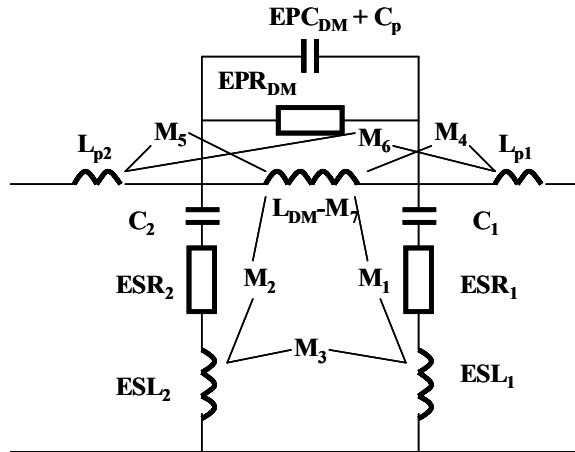


Fig. A-19. One-stage EMI filter model including parasitics.

2. Extracting the parasitic parameters, including M1 to M12, Cp1 and Cp2, from a two stage DM filter, as shown in Figure A-20.

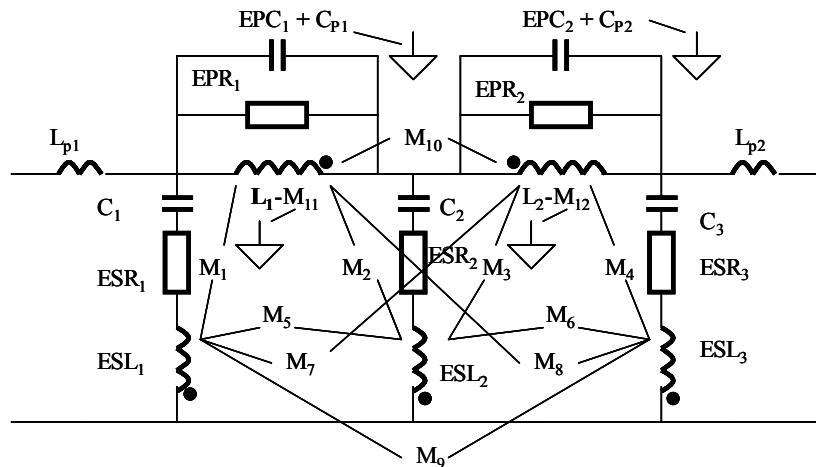


Fig. A-20. Two-stage EMI filter model including parasitics.

Prototype for Experiments

A one stage DM filter and a two stage DM filter, the layout of which shown in Figs. A-21 and A-22.

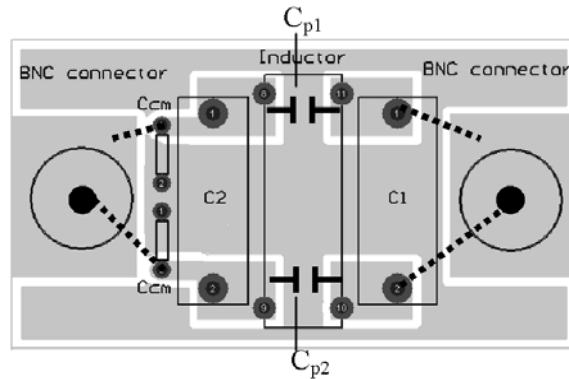


Fig. A-21. Two-stage EMI filter model including parasitics.

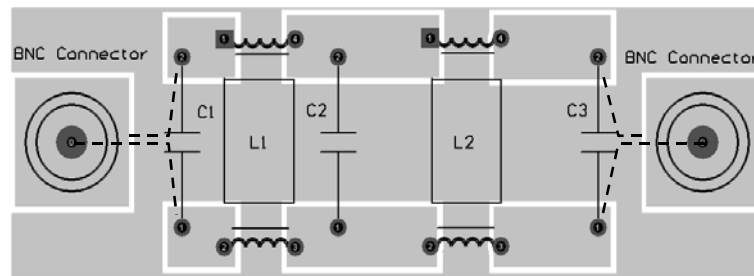


Fig. A-22. Two-stage EMI filter model including parasitics.

Equipments:

Impedance analyzer 4194A or Precision Impedance Analyzer 4294A

Network analyzer E5070B or 4195A

Experiment Steps

1. One Stage Filter

Preparation works:

- Build a PCB according to Fig. A-21, a 3.3uH CM inductor connected as a DM

inductor, two coaxial connectors and two 0.47 μ F capacitors

- b) Measure the DM impedance of a CM inductor to get its equivalent circuit parameters including L, EPR, EPC
- c) Measure the impedance of the two capacitors to get C1, ESR1, ESL1, C2, ESR2, ESL2
- d) Mount C1 and coaxial connector 1 onto PCB, measure the input impedance, compare to ESL1 to get Lp1
- e) Mount C2 and coaxial connector 2 onto PCB, measure the input impedance, compare to ESL2 to get Lp2

Measurements:

- a) Two capacitors are kept on PCB. Place a core to the location where the DM inductor is supposed to be, measure the S-parameters and save the data (s2c1)
- b) Minimize the trace loop, measure the S-parameters and save the data (s2cm)
- c) Change the trace loop back to normal, mount the DM inductor onto PCB, and then measure the S-parameters and save the data (swh)
- d) Dismount the right capacitor, measure the S-parameters and save the data (slcl)
- e) Minimize the left trace loop, measure the S-parameters and save the data (slcm)
- f) Dismount the left capacitor with only the inductor left and minimize the trace loops, measure the S-parameters and save the data (sind)
- g) Mount the right capacitor, measure the S-parameters and save the data (srcm)

h) Change the trace loop back to normal, measure the S-parameters and save the data (srcl)

Data processing:

a) Use S-parameters in sind to calculate Z_L , the impedance of the DM inductor mounted on PCB, with the equation below

$$Z_L = 2Z_0 \left(\frac{1}{S_{21}} - 1 \right), \quad Z_0 = 50\Omega, \quad (\text{A-30})$$

Compare Z_L with L, EPR and EPC, get M7 and Cp.

b) Use S-parameters in s2cm to calculate the impedance of M3, with the equation below

$$Z_3 = \frac{2Z_0 S_{21}}{(1 - S_{22} + S_{22} S_{11} - S_{11} - S_{21}^2)} \quad (\text{A-31})$$

c) Use S-parameters in s2cl to calculate the sum impedance of M3 and M6, with Equation 1.2 and calculate M6 with the result of procedure (b)

d) Use S-parameters in slcm to calculate the impedance of Capacitor 1 branch (Z_{slcm}) affected by M2, compare it with the impedance of Capacitor 1 to get M2

e) Use S-parameters in slcl to calculate the impedance of Capacitor 1 branch affected by M2 and M5, compare it with Z_{slcm} to get M5

f) Use S-parameters in srcm to calculate the impedance of Capacitor 2 branch affected by M1, compare it with the impedance of Capacitor 2 to get M1

g) Use S-parameters in srcl to calculate the impedance of Capacitor 2 branch affected by M1 and M4, compare it with Z_{srcm} to get M4

h) Simulate the filter model with M1 to M7, C_p and the self parasitic, and then compare the result with the magnitude and phase of S21 measured in step (c), the two results should match.

2. Two Stage Filter

Preparation works:

a) Build a PCB according to Fig. A-22, two 3.3uH CM inductors connected as DM inductors, two coaxial connectors and three 0.47uF capacitors. In the PCB design the input and output trace loop should be minimized so that their mutual effects with other components are ignored.

b) Connect two hard wires to a coaxial as two legs to form measurement kit, it will be used to touch two different points on the PCB in measurement

c) Measure the DM impedance of the CM inductors to get their equivalent circuit parameters including L1, EPR1, EPC1, L2, EPR2, EPC2.

d) Measure the impedance of the three capacitors to get C1, ESR1, ESL1, C2, ESR2, ESL2, C3, ESR3, ESL3.

e) Mount C1 and coaxial connector 1 onto PCB, measure the input impedance, compare to ESL1 to get Lp1

f) Mount C3 and coaxial connector 2 onto PCB, measure the input impedance, compare to ESL2 to get Lp2

Measurements:

This part of experiment should be done on 4195A.

a) Two capacitors C1 and C3 are kept on a PCB. Place two core to the location where the DM inductors is supposed to be, also place C2 on the PCB without electrical connection, measure the S-parameters and save the data for calculating M1 (sc1c3),

b) Dismount C3, mount L2 onto PCB and Short-circuiting L1, place a core to the location where L1 is supposed to be, measure the S-parameters and save the data for calculating M4 (sC1L2),

c) Dismount C1, remove the wire, mount L1 and C2 on the PCB. Measure the S-parameters and save the data for calculating M10 (sL1L2C2),

d) Mount C1 and C3 on the PCB, Measure the S-parameters and save the data (sWhole)

e) Dismount C1, L2 and C2, short-circuit L2 and place a core where L2 is supposed to be, measure the S-parameters and save the data for calculating M5 (sL1C3),

f) Calibrate the measurement kit made in the preparation step with 4195A.

g) Dismount C3, remove the short-circuit wire and place a core where L2 is supposed to be, use Coaxial 1 as one end, the measurement kit touching the PCB as the other end with its two legs making the trace loop smallest, measure the S-parameters and save the data for calculating M11 and Cp1 (sL1),

h) Mount C1 and place a core where L2 is supposed to be, use Coaxial 1 as one end, the measurement kit touching the PCB as the other end with its two legs making the trace loop smallest, measure the S-parameters and save the data for calculating M6 (sC1 L1),

i) Dismount C1, mount C2 and place a core where L2 is supposed to be, use Coaxial 1 as one end, the measurement kit touching the PCB as the other end with its two legs making the trace loop smallest, measure the S-parameters and save the data for calculating M7 (sL1C2),

j) Dismount L1 and mount L2, place a core where L2 is supposed to be, use Coaxial 2 as one end, the measurement kit touching the PCB as the other end with its two legs making the trace loop smallest, measure the S-parameters and save the data for calculating M8 (sL2C2),

k) Dismount C2, place a core to the location where L1 is supposed to be, use Coaxial 2 as one end, the measurement kit touching the PCB as the other end with its two legs making the trace loop smallest, measure the S-parameters and save the data for calculating M12 and Cp2 (sL2),

l) Mount C3, place a core to the location where L1 is supposed to be, use Coaxial 2 as one end, the measurement kit touching the PCB as the other end with its two legs making the trace loop smallest, measure the S-parameters and save the data for calculating M9 (sL2C3),

m) Dismount L2 and mount C2, place two core where the DM inductors should be, use Coaxial 2 as one end, the measurement kit touching the PCB as the other end with its two legs making the trace loop smallest, measure the S-parameters and save the data for calculating M3 (sC2C3),

n) Dismount C3 and mount C1, place two core where the DM inductors should be, use Coaxial 1 as one end, the measurement kit touching the PCB as the other end with its

two legs making the trace loop smallest, measure the S-parameters and save the data for calculating M2 (sC1C2).

Data processing:

- a) Use S-parameters in sL1 to calculate Z_{L1} , the impedance of L1 mounted on PCB, with Equation 1.1. Compare Z_{L1} with L1, EPR1 and EPC1 to get M11 and Cp1.
- b) Use S-parameters in sL2 to calculate Z_{L2} , the impedance of L2 mounted on PCB, with Equation 1.1. Compare Z_{L2} with L2, EPR2 and EPC2 to get M12 and Cp2.
- c) Use S-parameters in sC1C3 and Equation 1.2 to calculate the impedance M1.
- d) Use S-parameters in sC2C3 and Equation 1.2 to calculate the impedance M3.
- e) Use S-parameters in sC1C2 and Equation 1.2 to calculate the impedance M2.
- f) Use S-parameters in sC1L2 and Equation 1.2 to calculate the impedance, compare the impedance with the impedance of C1 to get M4.
- g) Use S-parameters in sL1C3 and Equation 1.2 to calculate the impedance, compare the impedance with the impedance of C3 to get M5.
- h) Use S-parameters in sC1L1 and Equation 1.2 to calculate the impedance, compare the impedance with the impedance of C1 to get M6.
- i) Use S-parameters in sL1C2 and Equation 1.2 to calculate the impedance, compare the impedance with the impedance of C2 to get M7.
- j) Use S-parameters in sL2C2 and Equation 1.2 to calculate the impedance, compare the impedance with the impedance of C2 to get M8.
- k) Use S-parameters in sL2C3 and Equation 1.2 to calculate the impedance,

compare the impedance with the impedance of C3 to get M9.

l) Use S-parameters in sL1L2C2 and Equation 1.2 to calculate the impedance, compare the impedance with the impedance of C2, M1 and M2 to get M10.

m) Simulate the filter model with M1 to M12, Cp1, Cp2 and the self parasitic, and then compare the result with the magnitude and phase of S21 measured in step (d), the two results should match.

In order to guarantee the match between the model and the prototype, the coupling polarities between different components should be carefully identified before the simulation.

APPENDIX B:

B.1. Evaluation of Existing Noise Separators

Many noise separators have been proposed and discussed in past papers; however most of them do not satisfy all three requirements:

a) Input impedances are always real 50Ω and are independent from noise source impedances.

b) Output is $|(V_1 - V_2)/2|$ for DM noise measurement and $|(V_1 + V_2)/2|$ for CM noise measurement.

c) Leakage between the CM and the DM at the output should be small.

The first one is Clayton R. Paul's separator [1], which is shown in Fig. B-1.

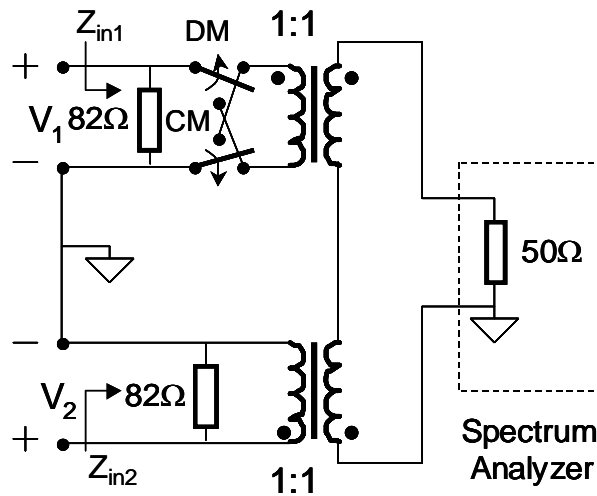


Fig. B-1. Noise separator proposed by Clayton R. Paul.

The input impedances for this separator are given as:

$$Z_{in1} = \frac{50V_1}{V_1 \mp V_2} // 82 \quad (\text{B-1})$$

$$Z_{in2} = \frac{50V_2}{V_2 \mp V_1} // 82 \quad (\text{B-2})$$

The input impedances are functions of the input voltages. This also means that input impedances are dependent on noise source impedances. Moreover, it does not satisfy conditions (a, b).

The second one is Hsin-Lung Su's separator [2]. This CM noise separator is shown in Fig. B-2. Its input impedances are given as (B-3, B-4). Obviously, they are functions of the input voltages and are therefore wrong. The same is true for his DM noise separator [2].

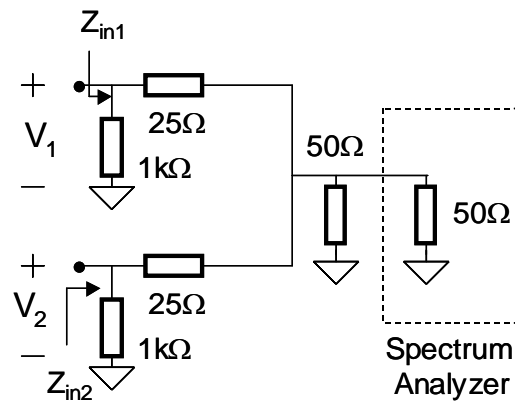


Fig. B-2. Noise separator proposed by Hsin-Lung Su.

$$Z_{in1} = \frac{75V_1}{2V_1 - V_2} \quad (\text{B-3})$$

$$Z_{in2} = \frac{75V_2}{2V_2 - V_1} \quad (\text{B-4})$$

The third one is M. Chiado Caponet's separator [3, 4]. It is shown in Fig. B-3. Its input impedances are given as (B-5, B-6).

For the same reason as the first two, its input impedances are functions of input voltages, and so it is also incorrect. The same problem exists in another proposed noise separator in his papers [3, 4].

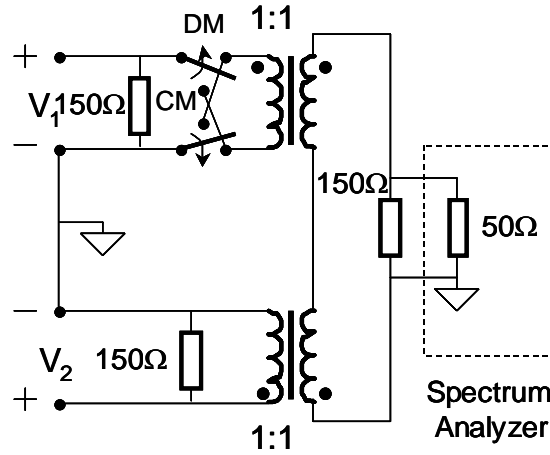


Fig. B-3. Noise separator proposed by M. Chiado Caponet.

$$Z_{in1} = \frac{37.5V_1}{V_1 \mp V_2} // 150 \quad (\text{B-5})$$

$$Z_{in2} = \frac{37.5V_2}{V_2 \mp V_1} // 150 \quad (\text{B-6})$$

The fourth one is Mark J. Nave's separator [5, 9], as shown in Fig. B-4. The CM noise separator is shown in Fig. B-4. This separator has problems similar to the first three; i.e. input impedances are functions of the input voltages. His DM noise separator also has the same problems.

$$Z_{in1} = \frac{150V_1}{5V_1 - 4V_2} // 50 \quad (\text{B-7})$$

$$Z_{in2} = \frac{150V_2}{5V_2 - 4V_1} // 50 \quad (\text{B-8})$$

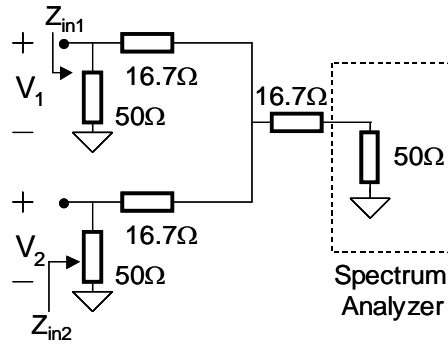


Fig. B-4. Noise separator proposed by Mark J. Nave.

The fifth is Ting Guo's separator [6, 18]. Because he used 0° and 180° power combiners, the input-impedance requirement is naturally satisfied. The disadvantage is the output does not satisfy conditions (a, b). In fact the output is 3 dB higher. 0° and 180° power combiners are needed to measure CM and DM, respectively, which may complicate the measurement. The traditional transformers are used at outputs, which degrade the high frequency performance.

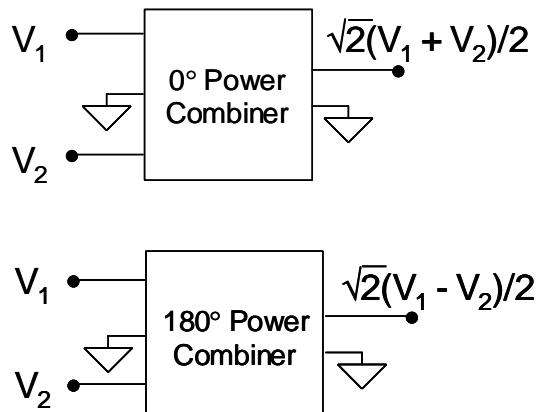


Fig. B-5. Noise separator proposed by Ting Guo.

The sixth is See Kye Yak's separator [7], which is shown in Fig. B-6. These input impedances are also functions of input voltages (B-9, B-10), so it does not correctly separate noise. It does not satisfy conditions (a, b) too.

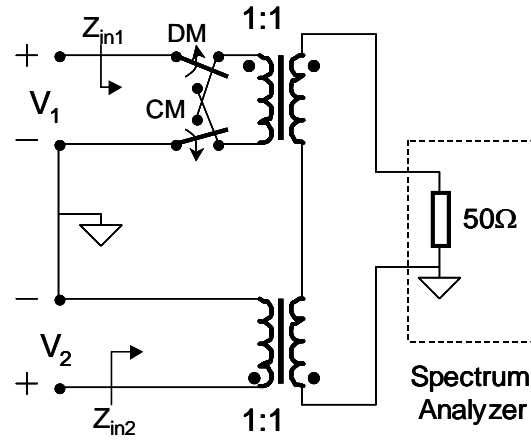


Fig. B-6. Noise separator proposed by K. Y. See.

$$Z_{in1} = \frac{50V_1}{V_1 \mp V_2} \tag{B-9}$$

$$Z_{in2} = \frac{50V_2}{V_2 \mp V_1} \tag{B-10}$$

From the preceding analysis, most of the existing noise separators' input impedances are functions of input voltages, although some papers claim that the input impedances are matched. In fact, however, they cannot correctly separate noise because the two input ports are not isolated.

An alternative approach to measure DM and CM noise is using current probes as shown in Fig. B-7 [9].

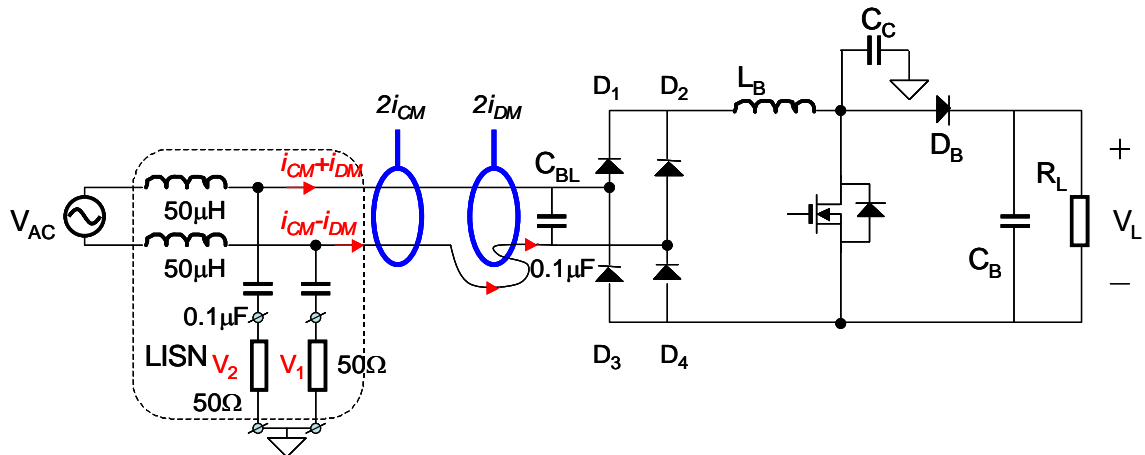


Fig. B-7. Noise measurement using current probes.

The current probes are connected to spectrum analyzer in Fig. B-8.

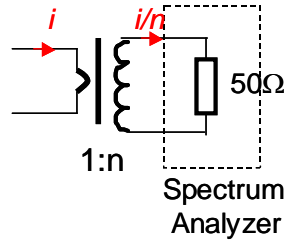


Fig. B-8. Noise measurement using current probes and a spectrum analyzer.

The measured DM and CM noise through spectrum analyzer are given by (B-11) and (B-12).

$$V_{DM}^m = \frac{2i_{DM} \times 50}{n} = \frac{2V_{DM}}{n}; \quad (\text{B-11})$$

$$V_{CM}^m = \frac{2i_{CM} \times 50}{n} = \frac{2V_{CM}}{n}. \quad (\text{B-12})$$

(B-11) and (B-12) show that the measured noise is reduced by $n/2$ times, which has three disadvantages:

- 1) Lower dynamic range (Higher noise floor): $20\log(n/2)$ dB lower than network separator ($n=1000, 54\text{dB}$).
- 2) Outputs are not exact V_{DM} or V_{CM} .
- 3) Complicated post processing.

The turn ratios of current probes should be high enough to minimize the effects of the input impedance of the spectrum analyzer on noise current.

The noise separator in [16] is discussed in Chapter 8. Its DMTR is 6dB higher. The traditional transformers and CM inductors are also used. As a result, its high frequency performance is degraded.

References

- [1] C. R. Paul and K. B. Hardin, "Diagnosis and reduction of conducted Noise Emissions," *IEEE Transactions, Electromagnetic Compatibility*, Volume 30, Issue 4, Nov. 1988, pp. 553 – 560.
- [2] Hsin-Lung Su and Ken-Huang Lin, "Computer-aided design of power line filters with a low cost common and differential-mode noise diagnostic circuit," In *proc. IEEE Electromagnetic Compatibility International Symposium*, Montreal, Canada, 13-17 Aug. 2001, pp. 511 – 516.
- [3] M. C. Caponet, F. Profumo, L. Ferraris, A. Bertoz and D. Marzella, "Common and differential mode noise separation: comparison of two different approaches," In *proc. IEEE Power Electronics Specialist Conference*, Vancouver, Canada, 17-21 June 2001, pp. 1383 – 1388.
- [4] M.C. Caponet and F. Profumo, "Devices for the separation of the common and differential mode noise: design and realization," In *proc. IEEE Applied Power Electronics Conference and Exposition*, Dallas, TX, 10-14 March 2002, pp. 100 –105.
- [5] M. J. Nave, "A novel differential mode rejection network for conducted emissions diagnostics," In *proc. IEEE Electromagnetic Compatibility National Symposium*, Denver, CO, 23-25 May 1989, pp. 223 – 227.
- [6] Guo Ting, D. Y. Chen and F. C. Lee, "Separation of the common-mode and differential-mode conducted EMI noise," *IEEE Transactions, Power Electronics*, Volume 11, Issue 3, May 1996, pp. 480 – 488.
- [7] See Kye Yak and Ng Chee Sum, "Diagnosis of conducted interference with discrimination network," In *proc. IEEE Power Electronics and Drive Systems International Conference*, Singapore, 21-24 Feb. 1995, pp. 433 – 437.
- [8] Yu-Kang Lo, Huang-Jen Chiu and Tzu-Herng Song, "A software-based CM and DM measurement system for the conducted EMI," *IEEE Transactions, Industrial Electronics*, Volume 47, Issue 4, Aug. 2000, pp. 977 – 978.

- [9] Mark J. Nave, *Power line filter design for switched-mode power supply*, Van Nostrand Reinhold, New York, 1991.
- [10] David M. Pozar, *Microwave Engineering*, John Wiley & Sons, Inc., 1998.
- [11] Norman Balabanian and Theodore Bickart, *Linear Network Theory: Analysis, Properties, Design and Synthesis*, Matrix Publishers, Inc., 1981.
- [12] W. Medley, *Microwave and RF Circuits: Analysis, Synthesis, and Design*, Artech House, Inc., 1993.
- [13] Agilent AN154 S-Parameters Design Application Note, Agilent Technologies, 2000.
- [14] Zhang, Dongbing, D.Y. Chen and D. Sable, "A New Method to Characterize EMI Filters," in *proc. IEEE Applied Power Electronics Conference and Exposition*, Anaheim, CA, 15-19 Feb. 1998, pp. 929-933.
- [15] Richard Anderson, "Test and Measurement Application Note 95-1 S-Parameters Techniques," Hewlett-Packard, 1997.
- [16] A. Nagel, R. W. De Donker, "Separating Common Mode and Differential Mode Noise in EMI Measurements," In *EPE conf proc.*, Lusanne, 1999, pp.1-8.
- [17] Jerry Sevick, *Transmission Line Transformers*, American Radio Relay League, 1987.
- [18] Guo Ting, *Separation of the common-mode and the differential-mode conducted electromagnetic interference noise*, Master thesis, Virginia Tech, 1994.

VITA

The author, Shuo Wang, was born in November 1972 in Puge, Sichuan, China. He received his B.S. degree from Southwest Jiaotong University, Chengdu, China in 1994, and M.S. degree from Zhejiang University, Hangzhou, China in 1997, both in electrical engineering. He started his Ph.D. study at Center for Power Electronics Systems (CPES), Virginia Polytechnic Institute and State University in January, 2001. He completed his work in Summer, 2005.